Probing Nonadiabatic Dynamics in Isolated Molecules with Ultrafast Velocity Map Imaging

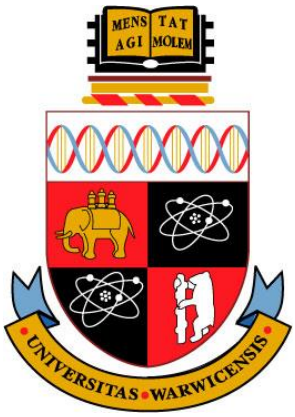

Adam Simon Chatterley

Submitted for the Qualification of Doctor of Philosophy in Chemistry

Universities of Warwick and Durham, Departments of Chemistry

October 2013

Table of Contents

List of Figures ..... **iv**
List of Tables ..... **v**
Acknowledgements ..... **vi**
Declaration ..... **vii**
Abstract ..... **viii**
1 Introduction **1**
1.1 Femtochemistry 2
1.2 Molecular Relaxation 9
1.3 Femtosecond Probing 16
1.4 Photostability 25
1.5 Summary 32
1.6 References 33
2 Experimental **38**
2.1 Introduction 39
2.2 Velocity Map Imaging 39
2.3 Femtosecond Laser System 44
2.4 Time-Resolved Hydrogen Imaging in Warwick 46
2.5 Time-Resolved Photoelectron Imaging in Durham 52
2.6 Data Fitting and Analysis 57
2.7 References 60
3 Relaxation Dynamics of Phenol and Catechol **63**
3.1 Introduction 64
3.2 Methods 66
3.3 Tunnelling in Phenol 66
3.4 Hydrogen Dissociation in Catechol 71
3.5 Discussion 92
3.6 Conclusions 95
3.7 References 96
4 Intrinsic Decay Dynamics of Indigo Carmine **99**
4.1 Introduction 100
4.2 Methods 103

4.3 Results and Analysis 103
4.4 Discussion 111
4.5 Conclusions 114
4.6 References 114
5 Relaxation Dynamics of Gas Phase DNA Subunits 116
5.1 Introduction 117
5.2 Methods 118
5.3 Base-Specific Ionization of Nucleotides 119
5.4 Dynamics of Isolated Nucleotides 128
5.5 Conclusions 150
5.6 References 151
6 Construction of a New Instrument for VMI and Laser Desorption 156
6.1 Introduction 157
6.2 Source Chamber 158
6.3 Interaction Chamber 160
6.4 Conclusions 164
6.5 References 165
7 Conclusions and Outlook 166
7.1 Summary 167
7.2 Outlook 168
7.3 References 170
Appendix A: List of Abbreviations ..... a
Appendix B: Global Fitting MATLAB code c
Appendix C: Drawings for New Instrument ..... h

List of Figures

1.1 Sketch of pump-probe process 4
1.2 Summation of cosine waves 6
1.3 The Franck-Condon Principle 7
1.4 Jablonski diagram 9
1.5 Conical intersections and avoided crossings 13
1.6 Quantum tunnelling 15
1.7 Koopmans' correlations 17
1.8 Time resolved photoelectron spectroscopy diagram 18
1.9 Time resolved photoelectron spectrum of I_2^- 20
1.10 Time resolved ICN dissociation 21
1.11 Processes to create ionic fragments 22
1.12 Resonance enhanced multi-photon ionization of hydrogen 23
1.13 Guaiacol CH_3^+ yield on- or off- resonance 24
1.14 Phenol potential energy cuts and total kinetic energy release spectra 27
1.15 Structures of DNA bases 29
1.16 Nucleobase ion yield dynamics 30
1.17 Lifetimes of adenine oligonucleotides 32
2.1 Time-of-flight mass spectrometry 40
2.2 Eppink and Parker's velocity map imaging setup 41
2.3 VMI angular distributions 42
2.4 Schematic of Warwick instrument 47
2.5 Schematic of Warwick laser setup 49
2.6 Calibration image of HBr 50
2.7 Electrospray mechanism 52
2.8 Schamatic of Durham instrument 53
2.9 Schamatic of Durham laser setup 55
2.10 Calibration image of I^- 57
2.11 Global fit simulation 58
3.1 Potential energy cut of phenol 64
3.2 Time-resolved total kinetic energy release spectra of phenol 67
3.3 Phenol parent ion transients 68
3.4 Potential energy cut and absorption spectrum of catechol 72
3.5 Total kinetic energy release spectrum of catechol 75
3.6 Time-resolved total kinetic energy release spectra of catechol 77
3.7 H^+ and parent transients of catechol pumped at 280.5 nm 79

3.8 Power dependency of catechol$^+$ transients 80
3.9 Schematic of out-of-plane potentials in catechol 81
3.10 Guaiacol$^+$ parent ion transient at 278 nm 83
3.12 Catechol$^+$ parent ion transients at many wavelengths 86
3.13 H^+ transients from catechol at many wavelengths 87
3.14 Catechol lifetimes as a function of excess energy 88
3.15 H^+ transient from catechol at 237 nm 90
3.16 H^+ transients from catechol with short pump wavelengths 91
3.17 Calculated vibrations for catechol S_1 state 95
4.1 Molecular structures of indigo and indigo carmine^{2-} 100
4.2 Photoelectron specrtra of indigo carmine^{2-} 104
4.3 Energy level diagram for indigo carmine^{2-} 105
4.4 Photoelectrom images of indigo carmine^{2-} 106
4.5 Action (absorption) spectrum of indigo carmine^{2-} 108
4.6 Time-resolved photoelectron spectra of indigo carmine^{2-} 109
4.7 Mass spectra of indigo carmine^{2-} and deuterated indigo carmine^{2-} 110
5.1 Structures of the four DNA bases 117
5.2 Nucleotide ionization scheme 121
5.3 Photodetachment spectra of nucleotide anions 122
5.4 Complete photodetachment spectrum for dGMP$^-$ 124
5.5 Time-resolved photoelectron spectra for dAMP$^-$ 132
5.6 Comparison of time-resolved spectra for dAMP$^-$ and adenine 133
5.7 Time-resolved photoelectron spectra for dGMP$^-$ 137
5.8 Time-resolved anisotropy parameters for dAMP$^-$ and dGMP$^-$ 138
5.9 Time-resolved photoelectron spectra for dTMP$^-$ 141
5.10 Structures of cytosine tautomers 144
5.11 Time-resolved photoelectron spectra for dCMP$^-$ 146
6.1 Rendering of new instrument in Warwick 158
6.2 Rendering of source chamber in new instrument 159
6.3 Rendering of interaction chamber in new instrument 162
6.4 Simulation of new VMI setup 163

List of Tables

3.1 Lifetimes of excited catechol 85
5.1 Detachment energies of nucleotides 125
5.2 Calculated dAMP$^-$ and adenine energies 134

Acknowledgements

This thesis is the result of three years of work, at two completely separated locations, and so there are an awful lot of people who supported me and helped me get through it:

Firstly, I must express enormous gratitude to my two supervisors, Vas Stavros and Jan Verlet. You are both amongst the most patient, understanding, helpful and fun bosses anyone could ask for. If either of you were my sole supervisor I would have considered myself to be in a very fortunate position; the fact that I had full support from both of you was truly exceptional.

Next, I would like to thank everyone I have directly worked with over the years, all of whom are superb scientists and (perhaps) more importantly great fun to be around. In no particular order, these are (Durham) Daniel Horke and Chris West; and (Warwick) David Hadden, Craig Williams, Gareth Roberts, Jamie Young and Michael 'Mick' Staniforth. Especial thanks go to Gareth Roberts, for being something of an academic and scientific mentor to me.

Thanks also to everyone who made universities such great places to be. In Durham I'm grateful to Oliver Willis, Scott Sanders and Adrian Rowland for making lunch time interesting. In Warwick, the office was made always interesting by the 'wet chemists', Ed Greenough and Michael 'Crazy Mitch' Horbury; and by the Costantini group. In particular, thanks to Ada Della Pia, for sharing the purgatory of writing up with me, and the frenetic coffee fuelled adventures that entails.

This work would have been possible without the help and support of many collaborators, in particular Dave Townsend, Justyna Zurek and Martin Paterson from Heriot Watt. Many thanks also to the electronic and mechanical workshops in both Warwick and Durham, for happily fixing the (many) things I broke over the years. Thanks of course also to the Leverhulme Trust for funding the project.

Outside of work, there have been many family and friends who have supported me the whole way, particularly my parents and Rachel for being so loving and supportive, despite many a grump.

Finally, I shall close with an unsorted (and incomplete) list of people/places/things which have made the past three years so enjoyable: David Greenwood, Tom Hollins, Will Dale, Ben Wilkins, Eddy Larkin, Katrina Georgiades, Calum Darling, Andy Summerhill, Adam 'Patty' Patterson, the pinball machine at the Duck, Fishtank, Arnold the giraffe, absent friends, board games in general, the people's chair, old gods, lost loves, Samurai sauce, The Bilash, Falafel Alhana, everyone at the SDG meetings, Inspire Cafe, The Big Mussel, Snickers the dog, Skol lager, ham, Legends Newcastle, The Kasbah, Scotch eggs, the season of mists, moocow, matrices, Battlestar Galactica, Kornstep (as a genre), black pudding, White Wolf Publishing, Grouse & Bru, my umbrella, the Leybold vacuum book, Squid brand fish sauce, and finally pallet wrap, without which travel between the two universities would be impossible.

Declaration

This thesis is submitted to the University of Warwick in support of my application for the degree of Doctor of Philosophy. It has been composed by myself and has not been submitted in any previous application for any degree. The work presented (including data generated and data analysis) was carried out by the author except in the cases outlined below:

i) The theory in Section 3.4.1 was performed by Justyna M. Żurek, and Martin J. Paterson at Heriot-Watt University.

ii) The theory in Section 5.5.4 was performed by Gareth M. Roberts at the University of Warwick.

Parts of this thesis have been published by the author:

Chapter 3

G.M. Roberts, A.S. Chatterley, J.D. Young and V.G. Stavros, Direct Observation of Hydrogen Tunneling Dynamics in Photoexcited Phenol, *J. Phys. Chem. Lett.*, 2012, **3**, 348

A.S. Chatterley, J.D. Young, D. Townsend, J.M. Żurek, M.J. Paterson, G.M. Roberts and V.G. Stavros, Manipulating Dynamics with Chemical Structure: Probing Vibrationally-Enhanced Tunnelling in Photoexcited Catechol, *Phys. Chem. Chem. Phys.*, 2013, **15**, 6879

Chapter 4

A. S. Chatterley, D. A. Horke and J. R. R. Verlet, On the intrinsic photophysics of indigo: a time-resolved photoelectron spectroscopy study of the indigo carmine dianion, *Phys. Chem. Chem. Phys.,* 2012, **14**, 16155

Chapter 5

A. S. Chatterley, A. S. Johns, V. G. Stavros and J. R. R. Verlet, Base-Specific Ionization of Deprotonated Nucleotides by Resonance Enhanced Two-Photon Detachment. *J. Phys. Chem. A,* 2013, **117,** 5299

A. S. Chatterley, C. W. West, G. M. Roberts, V. G. Stavros and J. R. R. Verlet, Mapping the ultrafast dynamics of adenine onto its nucleotide and oligonucleotides, **submitted**

Abstract

Two complementary experiments were used to study the ultrafast dynamics of large molecules in the gas phase. Both experiments used time-resolved pump-probe velocity map imaging to monitor energetically dispersed spectra of isolated systems on a femtosecond timescale. A 'bottom-up' methodology is applied, whereby initially simple, small, systems are studied in a high level of detail, and then the complexity of system studied is gradually increased. The overall goal was to explore the concept of photostability, the mechanism whereby molecules can withstand bombardment by visible and ultraviolet light, especially in biomolecules.

In the first set of experiments, based in Warwick University, the dissociation of hydrogen atoms from neutral phenol and 2-hydroxy phenol (catechol) following ultraviolet excitation was measured with femtosecond resolution. These experiments give unprecedented insight into the electronic structure of phenolic systems, and in particular hydrogen atom tunnelling underneath a conical intersection was directly observed. Varying the excitation energy allowed the transition from tunnelling dynamics to direct dissociation dynamics to be observed.

The second set of experiments, completed at Durham University, performed time-resolved photoelectron spectroscopy on large gaseous anions from an electrospray source. The electrospray technique allows very large ions to be introduced into the gas phase, so the bottom-up methodology can be continued. First, the dynamics of the common dye indigo carmine were explored, demonstrating that excited state proton transfer accounts for its photostability. Secondly, the dynamics of the nucleotides making up DNA were explored. The dynamics of nucleobase chromophores were shown to map onto larger nucleotide and oligonucleotide systems, retaining ultrafast photostable properties.

Finally, a new instrument was designed and constructed in Warwick. This machine will use laser desorption techniques to help further extend the size range isolated dynamics can be studied in, this time for neutrals. Overall, the bottom-up methodology grants insight into the excited state dynamics of real-world relevant molecules, at an extremely high level of detail.

"In the age of swine, these would be called whispers"

- Florentine Saying

1 Introduction

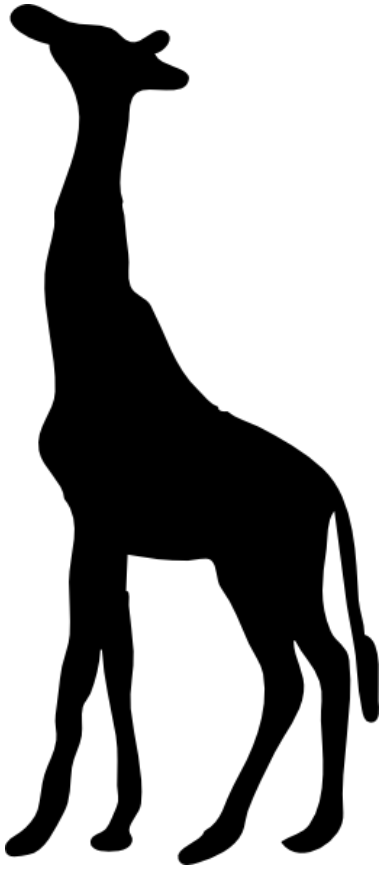

1.1 Femtochemistry

The fundamental goal of chemistry is to understand the behaviour of molecules, both in terms of structures and dynamics. The former relates to the unique combination of atoms which leads to a particular stable molecule, while the latter, which is the focus of this thesis, studies how a molecule can change over time to create new chemical species – a chemical reaction. The basic premise of any dynamics study is that a reaction is initiated at some precise time, and then some aspect of the system is measured as a function of reaction time.

Dynamics, in its simplest form, involves two reactants being mixed, and a clock simultaneously started. When the reaction has completed, the clock is stopped and the reaction time for this particular set of experimental parameters is retrieved. Such techniques were employed throughout the 19th century, and formed the basis of chemical kinetics.[1, 2] The time resolution of these experiments is dependent on both the speed with which the reagents can be mixed, and the reaction times of the experimentalist observing the end point, ultimately resulting in a time resolution on the order of a few seconds. In the 20th century, inventions such as using the stopped flow mixing technique with spectroscopic measurements made millisecond time resolution available,[3] but ultimately the limiting factor for the quickest reaction that can be measured is determined by the speed with which reactants can be mixed. In 1949, Eigen, Porter and Norrish realized that if light is used as one of the 'reactants', then the time for these reagents to mix is defined solely by the duration of the incident light pulse.[4-6] Likewise, if a spectroscopic interrogation tool is used, the time resolution for determining the reaction progress is also limited solely by the duration of light pulse which can be obtained.

The duration of pulses attainable from laser systems has continually decreased since the first laser, created in 1960, which produced microsecond long pulses.[7] The innovation of mode-locking, whereby the phase of each mode within the laser cavity is held in a fixed relationship, allows extremely short pulses to be produced. Using mode-locked systems, femtosecond (10^{-15} s) pulses were created for the first time in 1974,[8] and by now laser systems producing pulses a few tens of femtoseconds are readily available. The femtosecond regime is a particularly important milestone in reaction dynamics, as this is the typical timescale of nuclear motion within a molecule, for example molecular vibrations or bond breaking.[9] Hence, if a reaction can be tracked with femtosecond resolution, then it is possible to observe the motion of each atom and track their precise movements as the molecule transitions from reactant to product.

The technique of using femtosecond lasers to monitor 'real time' photo-initiated chemical reactions has been termed 'femtochemistry', and in 1999 the Nobel Prize in chemistry was awarded to Ahmed Zewail for his pioneering contributions to the field.[9, 10] Early femtochemistry work by Zewail was applied to myriad systems, from simple di- and tri-atomics,[11-15] through larger molecules.[16-18] Recently, even shorter pulses (in the attosecond regime (10^{-18} s)) have been obtained, using high harmonic generation techniques.[19, 20]

The work presented in this thesis is on applying femtochemistry techniques to study the relaxation dynamics of electronically excited molecules in the gas phase. Two separate but complementary experiments were employed; in Warwick time resolved H atom imaging was performed on cold neutral molecules, whilst in Durham time resolved photoelectron spectroscopy was performed on isolated anionic systems. The overall theme is 'building up'; that is, starting with simple molecular systems, and once they are well understood gradually increasing the complexity. As such, the introduction to this thesis is structured as follows: firstly a brief introduction to pump-probe spectroscopy is given, focussing on the initial 'pump' step. Next, some of the available relaxation pathways available to excited molecules are reviewed. Thirdly, the two main probe techniques employed in this thesis, photoelectron spectroscopy and photofragment imaging, are introduced. Finally, the topic of photostability is reviewed, which sets the scene for the later chapters.

1.1.1 Pump-Probe Spectroscopy

The fundamental mechanism by which femtochemistry (and indeed all flash photolysis techniques) operates is based on pump-probe spectroscopy.[9] In the simplest terms, an initial 'pump' laser pulse excites the molecule to some reactive state, then after an evolution time, *t,* a 'probe' pulse interrogates the system spectroscopically. By repeating the experiment with varying *t*, the spectroscopic response of the system can be determined as a function of time after the pump pulse is absorbed. As an example, illustrated in Fig. 1.1, consider a simple system where a molecule can be optically excited to an electronic state which is dissociative along some bond A-B. The pump pulse prepares the molecule in this state, and then at a series of different values of *t*, the probe pulse (via some spectroscopic technique) measures the total population of excited AB molecules (AB*). When pump and probe pulses arrive simultaneously (t_0), the maximum population of AB* is measured. As *t* increases, the population will decrease as the system relaxes into its fragment components. Finally, the reported

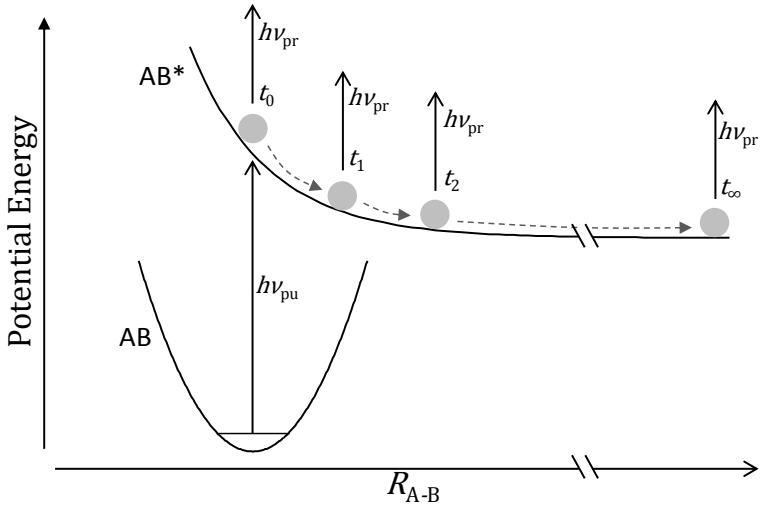

Figure 1.1 Sketch of a basic pump-probe experiment. The bound species AB is excited to a dissociative state by the pump pulse, $h\nu_{pu}$. After time t, the probe pulse $h\nu_{pr}$ measures population of excited AB. As a function of time, this value will decrease, reflecting the transformation from excited AB* into A and B fragments.

population will reach an asymptote at t_∞ when the reaction is completed and A and B no longer interact.

1.1.1.1 Born-Oppenheimer Approximation

This simple picture, though very intuitive, is purely classical and of course a correct mechanism on a molecular scale must invoke quantum mechanics. To perform any quantum mechanical treatment of a molecule, however, an approximation must be made at the outset – the *Born-Oppenheimer* (BO) approximation. The BO approximation states that, as electrons are orders of magnitude lighter than nuclei (m_{proton} / $m_{electron} \approx 1800$), we can assume the nuclei to be stationary on the timescale of electron motion.

The complete description of any system can be found by solving the Schrödinger equation for all nuclei and electrons, which, for a one electron system, is given by:[21]

$$H\psi(q,Q_1,Q_2,...Q_N) = E\psi(q,Q_1,Q_2,...Q_N) \tag{1.1}$$

where ψ is the total wavefunction, q is the position of the electron, Q_N the position of the N^{th} nucleus, E is the total energy and the H is the Hamiltonian of the system,

$$H = T_e + T_N + V \tag{1.2}$$

which depends on the kinetic energy of both the nuclei, T_N; and electron, T_e; and on the potential energy of the system, V. Eqn. (1.1) cannot be solved analytically for any system with more than one nucleus in it, *i.e.* molecules, and so we introduce the BO approximation to simplify the problem.[22, 23] This simplifies the problem such that now

we only need to find the wavefunction of the electron in the static field of the nuclei. The Schrödinger equation can now be written as[21]

$$T_e\psi + V\psi = E_e(Q_1, Q_2, ...Q_N)\psi \tag{1.3}$$

where E_e gives the eigenstates of the molecule, taking into account the kinetic energy of the electron as well as Coulombic interactions between all particles. It is worth noting that Eqn. (1.3) is still only exactly solvable when there is a single electron, however the BO approximation is still exceedingly useful for many electron systems, and it shall be employed extensively.

A concept which appears in the above equations and is of significant value is the existence of the potential energy, *V*, which for a given electronic state depends solely on the nuclear geometry. This concept has already been introduced in Fig. 1.1, where the potential energy was plotted as a function of a bond length, *R*. For an *N* atom non-linear molecule, *V* can be described by a 3*N*–6 dimensional surface (the –6 is to take account of rotations and translations which do not affect the energy). These potential energy surfaces (PES) are essential to understanding and visualizing molecular dynamics, although generally only the coordinates involved in the reaction at hand are considered.

1.1.1.2 Uncertainty Principle

There is a secondary consideration before we can consider a pump-probe spectroscopy experiment from a quantum perspective – *the uncertainty principle*.[21, 24, 25] Fig. 1.2 shows a series of summations of cosine waves, of the form

$$f(x) = \sum_{k=1}^{n} \cos(kx) \tag{1.4}$$

for $1 \leq n \leq 5$. As *n* increases, we see that $f(x)$ tends towards a train of short pulses, each with a broad frequency. This is a simple demonstration of Fourier's theorem,

$$f(x) = \sum_{n=-\infty}^{\infty} c_n e^{inx} \tag{1.5}$$

which states that any function can be composed as an infinite sum of sine and cosine functions. Thus, any non-sinusoidal function must contain multiple frequency components. Fourier's theorem shows that a necessary result of particle-wave duality is that one cannot precisely define both the energy of a state and its lifetime simultaneously, as for a state to be localized in time it must be composed of many frequencies, or formally

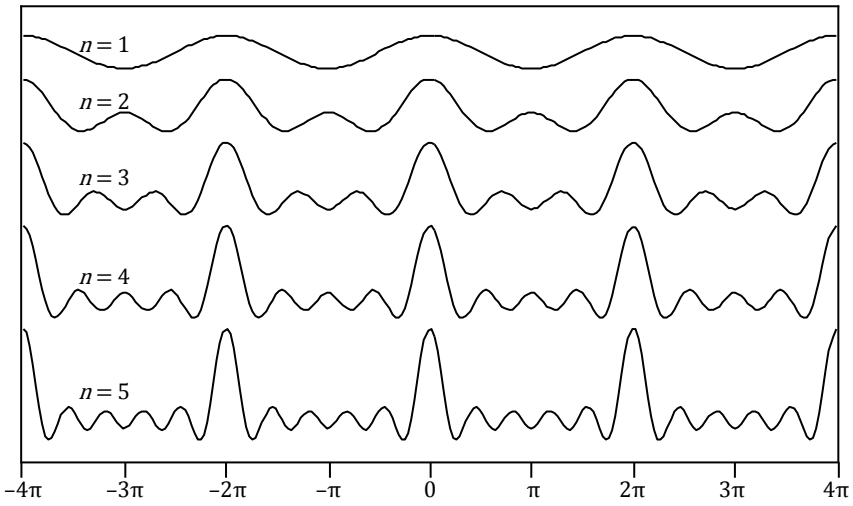

Figure 1.2 Demonstration of how a coherent sum of cosine waves results in localised regions of high amplitude. Each curve is a sum of the first n in-phase harmonics of a cosine wave; as n increases, the sum tends towards a train of localised spikes. The sum of waves in this manner is responsible for the uncertainty principle, mode-locking in ultrafast lasers, and the creation of wavepackets from coherent superpositions of eigenstates.

$$\Delta t \Delta E \geq \hbar / 2 \tag{1.6}$$

where Δt and ΔE are uncertainties in time and energy respectively. The uncertainty principle is a general feature of quantum mechanics, and many other relationships of the same form exist, although for femtochemistry the time-energy uncertainty principle is the most commonly encountered.† This result has extremely important implications for very short laser pulses; if the pulse has a known short temporal profile, then the energy (or wavelength; frequency) profile of the pulse must be broad.

In fact, it is by precisely the mechanism shown in Fig. 1.2 that mode-locking allows a broadband laser to generate ultrafast pulses;[26, 27] the summation of many individual in-phase modes leads to a single pulse that is short in time, but broad in frequency.

1.1.1.3 Franck-Condon Principle

We are now in a position to consider the first step of the pump-probe experiment – the pump step. In this step we use a pulse of light to excite the molecule from its ground state into an electronically excited state. We shall first consider excitation using only a single frequency (a continuous wave), then expand this to broadband ultrafast laser pulses. Consider the potential energy surface (PES) of the ground and an excited state of a molecule, viewed along a single coordinate, q, illustrated in Fig. 1.3. The excited state PES will differ from the ground state, generally due to lower occupation of

† Strictly, as time is a quantum mechanical parameter, not an observable, the time-energy uncertainty relationship is of a different classification than those from a pair of complementary variables, although this does not generally affect the treatment.

bonding molecular orbitals, and hence the equilibrium geometry of the ground state is likely to be different in the excited state. As electronic excitation is a movement of electrons, within the BO approximation there can be no nuclear rearrangement, and the transition is said to be vertical (only the energy changes and all other coordinates remain fixed). The transition probability depends on the interaction of the electric dipole moment, $\vec{\mu_e}$, with the electric field of the photon, $\vec{E}$, to account for electron motion, however the fixed nuclear positions of the two states must be considered also. The total transition moment, *d*, is then given symbolically as: [21, 26]

$$d = S(v', v)\left\langle \psi'(q) \middle| \vec{\mu} \cdot \vec{E} \middle| \psi(q) \right\rangle$$
$$S(v', v) = \left\langle \psi_{v'}(\mathrm{Q}) \middle| \psi_{v}(Q) \right\rangle \tag{1.7}$$

using Dirac bra-ket notation where $\psi_v(Q)$ and $\psi_{v'}(Q)$ are the initial and final vibrational wavefunctions, as a function of nuclear geometry, and $\psi(\mathrm{q})$ and $\psi'(q)$ are the initial and final electronic wavefunctions. The overlap integral *S* is known as the Franck-Condon (FC) factor for the given transition. Pictorially, Fig. 1.3 shows this principal – the wavefunction with the greatest overlap with the ground state has the greatest probability amplitude and thus is the strongest absorber. This is known as the Franck-Condon principle, and it is a cornerstone of molecular spectroscopy.[28-30] The general

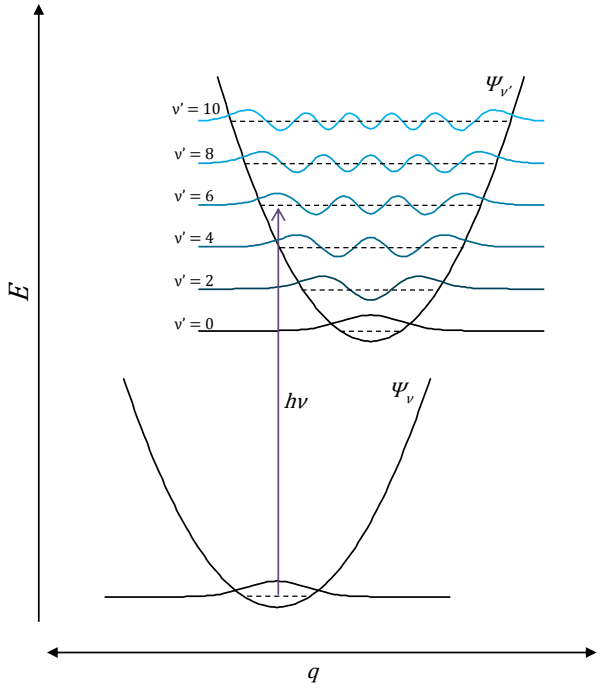

Figure 1.3 The Franck-Condon principle. Electronic excitation is most favourable when there is overlap of the ground and excited vibrational wavefunctions. In this example, the most favourable (and thus highest intensity) transition from the v = 0 level of the ground state is to the v' = 6 level of the excited state. For clarity, only even values of v' are shown.

result is that a progression of vibronic (electronic and vibrational) excitations is available, with the greatest amplitude located on the transition that perturbs the nuclear geometry the least.

1.1.1.4 Wavepackets

The description of vibronic excitation above is valid if only a single frequency is involved. In femtochemistry, where an ultrafast broadband excitation pulse is employed, rather than just one state being excited there will likely be a coherent superposition of excited vibrational states with energies within the spectral bandwidth of the laser pulse. Mathematically, such a superposition takes the form:[21, 31, 32]

$$\Psi(t) = \sum_n A_n \psi_n e^{-iE_n t/h} \tag{1.8}$$

where ψ_n is the n^{th} vibrational wavefunction, E_n is the energy of this function and t is the evolution time of the system. A_n is a weighting factor, to account for the shape of the excitation pulse (generally Gaussian), the differing Franck-Condon factors, and the transition dipole moment. Essentially, each stationary state wavefunction is multiplied by a time-varying sinusoidal factor, with a frequency dependant only on its energy. The overall picture is then very much reminiscent of Fig. 1.2, which shows how the sum of sinusoidal functions results in a localized region of high amplitude, with near zero amplitude elsewhere. This local feature is known as a wavepacket. Crucially, wavepackets display time-dependant behaviour: as t varies, the position at which all the component wavefunctions constructively interfere will evolve, and effectively the wavepacket moves as a coherent entity, oscillating back and forth across the PES as the position of constructive interference moves. In fact, in the limit of infinitesimal spacing between wavefunctions, the wavepacket will behave entirely as a classical particle – an example of the correspondence principle linking the quantum and macroscopic worlds.[21, 31]

The evolution of wavepackets is essentially the fundamental process that femtochemistry is observing. If the wavepacket is formed of wavefunctions with equal energetic spacing, as in a harmonic oscillator, then the wavepacket will retain the shape imposed by the A_n factors, and simply oscillate indefinitely (in the absence of the relaxation schemes discussed below). The frequency of this oscillation reveals the energy spacing between vibrational levels, and hence if observed it can be used to extract vibrational frequency information.[33] On the other hand, in more complex systems, as in the case of an anharmonic oscillator, the spacing between vibrational levels is not equal. Evolution in the shape of the wavepacket can thus occur, leading to

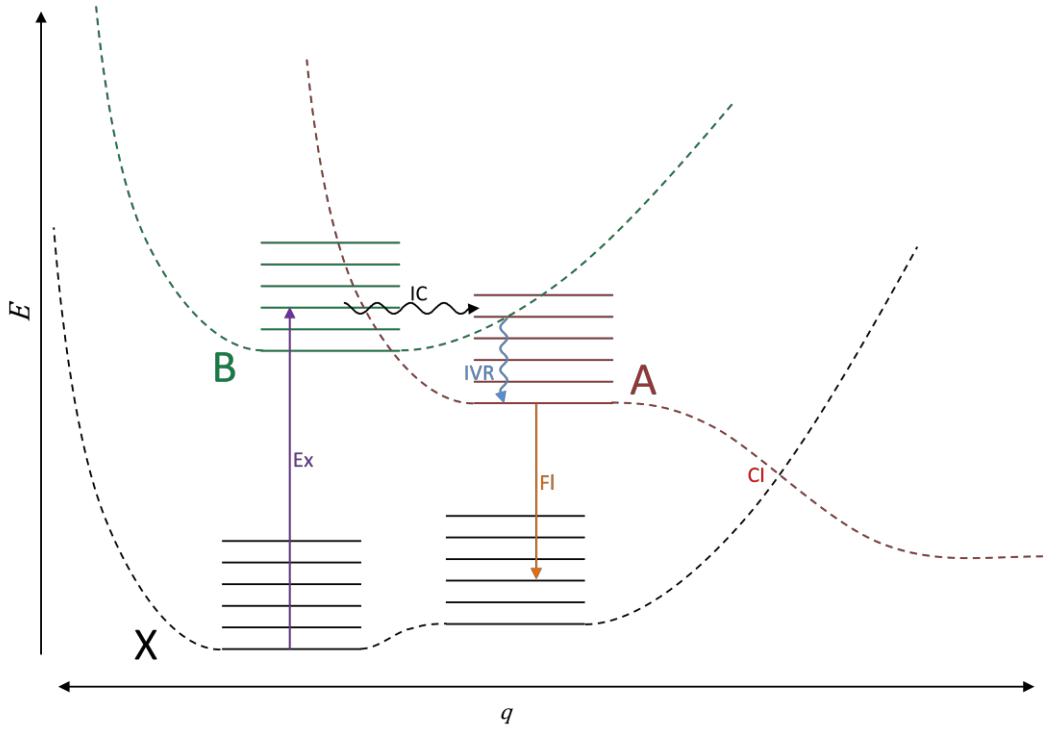

Figure 1.4 Jablonski diagram illustrating some available photophysical processes for a molecule. The processes shown are: i) excitation from the ground (X) state to an excited (B) state in the vertical Franck-Condon region, ii) internal conversion from the B state to the A state, iii) intramolecular vibrational redistribution to disperse energy to orthogonal modes (note that the potential energy only decreases along the *q* coordinate, and is redistributed to orthogonal modes to maintain conservation of energy), and iv) fluorescence from the lowest excited state back to the ground state. Also shown is a conical intersection where the A and X states cross.

dephasing and subsequent revivals of the wavepacket as the phase of the component wavefunctions differ.[34]

1.2 Molecular Relaxation

Following excitation with the pump pulse, the system is allowed to evolve until time *t*, generally by relaxing in some manner. It is the behaviour during this evolution process we are attempting to discern, and we shall now discuss some of the available relaxation pathways a complex polyatomic system may take. Fig. 1.4, a *Jablonski diagram*,[35] forms the basis of this discussion. In the diagram, radiative processes (those involving a photon) are represented by straight arrows whilst non-radiative processes are represented by wiggly arrows. Three different electronic states are shown, with the vibrational manifold expanded in a few regions, and a dotted line representing the zero-point energy elsewhere. The axis denoted by *q* is some (arbitrary) reaction coordinate, along which the energy of our three states varies.

The simplest relaxation processes involve radiative decay, where the energy is lost by the emission of a photon.[36] This process, which can either be spontaneous or

stimulated by an initial photon,† is essentially analogous to excitation in reverse, *i.e.* the process is vertical and governed by Franck-Condon factors. Spontaneous emission generally occurs on the order of nanoseconds,[36] and although it is one of the most common relaxation processes, this thesis will not explore it in any detail here and instead focus shall be paid exclusively to the non-radiative relaxation pathways available.

1.2.1 Intramolecular Vibrational Redistribution

Intramolecular vibrational redistribution (IVR) is a mechanism whereby energy located in a few (or one) highly energetic vibrational modes can be redistributed into other, lower lying, modes. The primary cause for this redistribution is anharmonic coupling between the various vibrational modes.[37-39] In very small molecules, there are few enough vibrational modes that IVR is a reversible process and periodicity will be seen in the mode population as the wavepacket dephases and revives.[37] On the other hand, in larger systems, such as those dealt with in this thesis, the density of vibrational modes is high enough that they form a 'bath' and energy flow into this bath is overall irreversible (and hence incoherent). In these cases, we can approximate the IVR process as a transition into a continuum of states, and the probability and therefore rate of the transition occurring becomes proportional to the strength of the coupling between states, V, and to the density of final states, ρ_M. This is known as *Fermi's golden rule*, symbolically given as:[21, 38]

$$k_{IVR} = \frac{2\pi}{\hbar}|V|^2 \rho_M \tag{1.9}$$

The rate of IVR as presented here is only valid in cases where the coupling between the initial and all final modes is identical. However, taking it as an average of all modes, in many cases, provides a perfectly good approximation, resulting in a simple first order kinetic model with statistical origin.

It is important to make the distinction between intramolecular vibration *redistribution* and *relaxation*; in the gas phase the system is completely isolated and so, due to conservation of energy, the overall potential energy of the system cannot decrease, meaning potential energy is simply redistributed to other modes. It is then important to note that in Fig. 1.4, for an isolated system the IVR arrow is only correct when viewed along a single coordinate, the energy is redistributed into other 'bath' modes to compensate. On the other hand, in a condensed system, the entire solvent can

† In fact, we can think of spontaneous emission as the same as stimulated emission, but stimulated by a virtual photon.

act as the bath, effectively taking energy away from the molecule irreversibly. In this case, the moniker intramolecular vibrational relaxation is more appropriate, as the potential energy of the excited molecule has decreased, with the energy dispersed as heat in the solvent.[36]

The timescale for IVR processes is typically on the order of tens to hundreds of picoseconds for reasonably large systems,[37] which is considerably faster than spontaneous emission, and hence efficiently outcompetes it. The result is that, particularly in solution, fluorescence is observed from a lower vibrational level than the excitation energy. The difference between excitation and emission energies is known as the *Stokes shift*.[36]

1.2.2 Internal Conversion and Intersystem Crossing

IVR dealt with the non-radiative redistribution of energy within a given electronic state. The possibility also exists, for non-radiative transitions to occur between two different electronic states. When both electronic states are of the same spin, this is known as internal conversion (IC). In IC, a vibrational mode on the initial electronic state couples to a mode or modes of equivalent energy on a lower lying final electronic state. To a first approximation, the mechanism follows that of IVR, and eq. (1.9) applies equally well to calculating the rate of IC to a continuum of states. The coupling between any two vibronic states is dependent on the energy gap between the electronic states, ΔE, and hence the overall rate has been shown to display the proportionality:[40]

$$k \propto \exp[-\Delta E / (\mathrm{h}\nu)] \tag{1.10}$$

where ν is the vibrational frequency. The important outcome of this law is that IC is most probable in cases where the two electronic states lie close in energy to each other. To successfully couple the two electronic states, usually specific *promoting modes* are required,[38] in symmetry terms it is required that the promoting mode have the correct symmetry to couple the initial and final states, *i.e.* the product of all three representations must be totally symmetric, symbolically:[41]

$$\Gamma_m \otimes \Gamma_W \otimes \Gamma_l \supset A \tag{1.11}$$

where Γ is an irreducible representation, m and l label the initial and final states, W labels the promoting mode, and A is the totally symmetric representation of the relevant point group or molecular symmetry group.

In cases where the initial and final electronic states have different spin, IC is formally forbidden. However, if there is sufficient spin-orbit coupling then this rule may break down and allow conversion into a state with different spin.[21] This process is

called intersystem crossing (ISC), and as it depends on spin-orbit coupling, its occurrence is favoured by the presence of heavy atoms. Radiative decay with a change in spin (phosphorescence) is also possible by the same arguments, although the forbidden nature of the transition means lifetimes of phosphorescence can be seconds to hours.[21] Phosphorescent species with long radiative lifetimes are responsible for glow-in-the-dark materials, and a phosphor screen is used as the anode of the detector in the experiments described in this thesis.

1.2.2.1 Conical Intersections and Avoided Crossings

Eq. (1.10) shows that as two electronic states approach in energy, the rate of conversion between them increases. In the special case where ΔE becomes zero, the two states are crossing in what is termed a *conical intersection* (CI).[34, 38, 42-45] The CI is a ubiquitous feature of polyatomic potential energy surfaces, and drives much of the excited state dynamics observed in these systems. If we consider a two state system, for a crossing to occur there must exist some nuclear configuration where both states are degenerate. We shall start by assuming that each state ψ_n can be composed as a linear combination of two diabatic states, ϕ_n, so that[42, 45]

$$\begin{pmatrix}\psi_1\\ \psi_2\end{pmatrix}=\begin{pmatrix}c_{11} & c_{12}\\ c_{21} & c_{22}\end{pmatrix}\begin{pmatrix}\phi_1\\ \phi_2\end{pmatrix} \tag{1.12}$$

The energies of the two states ψ_n can then be determined by the corresponding Hamiltonians, $H_{mn}=\langle\phi_n|H|\phi_m\rangle$, using the secular determinant

$$\begin{vmatrix}H_{11}-E & H_{12}\\ H_{21} & H_{22}-E\end{vmatrix}=0 \tag{1.13}$$

so

$$E_{1,2}=(H_{11}+H_{22})/2\pm\sqrt{(H_{11}-H_{22})^2/4+(H_{12}+H_{21})^2} \tag{1.14}$$

Since $E_1=E_2$,

$$(H_{11}-H_{22})^2/4+(H_{12}+H_{21})^2=-(H_{11}-H_{22})^2/4-(H_{12}+H_{21})^2 \tag{1.15}$$

then

$$\begin{aligned}H_{11}&=H_{22}\\ H_{12}&=H_{21}=0\end{aligned} \tag{1.16}$$

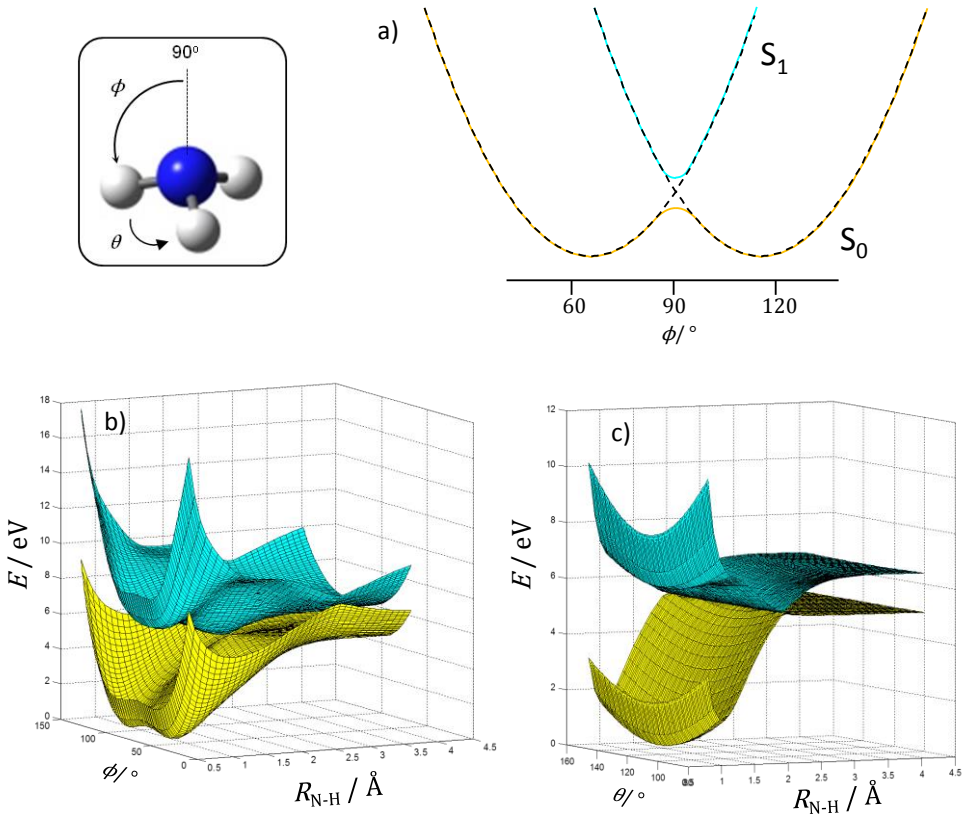

Figure 1.5 Examples non crossing and conical intersections using ammonia (coordinates employed are inscribed on the inset). a) Sketch demonstrating the non-crossing rule. The two dashed diabats cross in a planar geometry, however the upper and lower state avoid crossing and hence form a double well instead, b) when viewed along the ϕ and $r_{N\text{-}H}$ coordinates, a point of conical intersection is visible. These two coordinates form the branching space. c) When viewed along only one branching vector (with ϕ fixed at 90°), the CI manifests as a seam. Potentials are from refs 47, 50.

H_{12} is the coupling between states, which must be zero. If the two diabatic states have different spins or symmetry, then this condition is trivially met, and such intersections are known as accidental crossings. On the other hand, if the diabatic states share spin and symmetry, it has been shown that zero off-diagonals can only be produced in an $N - 2$ dimensioned subspace, where N is the number of degrees of freedom of the system.[46] As a diatomic system only possesses a single degree of freedom, this condition can never be met and states cannot cross, a rule known as the *non-crossing rule*. Fig. 1.5(a) shows a situation where two diabatic harmonic states can create a double well ground state with a harmonic upper state, as an example of the kind of richly featured potential energy surfaces which can arise from the non-crossing rule. In this example, the two diabats are formed by considering the potential energy of ammonia as the inversion angle is varied. If electronic rearrangement is forbidden, then repulsion between the electron lone pair on the nitrogen atom and the hydrogen atoms increase the energy as the molecule is inverted. In an adiabatic framework, the

two diabatic curves form an avoided crossing to give a double well, with a maximum at the degenerate planar configuration.[47-49]

In polyatomic systems, there are enough available degrees of freedom that an $N-2$ subspace can be formed, and the two diabatic states may cross.[42] The two dimensions not involved in this subspace are known as the branching[45] (or **g** & **h**)[43, 44] vectors, and the branching space formed by them is responsible for lifting the degeneracy, allowing the states to cross. When the potential energy surface is viewed along these two dimensions, the surface where the two states cross resembles a cone, hence the term *conical intersection* (CI). At the CI, nuclear and electronic motions are strongly coupled, leading to a breakdown of the BO approximation, and dynamics employing them are termed nonadiabatic – the dynamics are not adiabatic (as the states cross), but they are also not purely diabatic (as they form a CI). It is important to note that although the CI appears as a single point when viewed along the branching space, in actuality it is an $N-2$ dimensional seam. This is illustrated in Fig. 1.5(b) and (c), where the PES of ammonia (NH_3) is viewed along two different sets of coordinates.[47, 50] The first, the branching space, clearly shows the cone shape of the CI. On the other hand, when viewed along one of the branching vectors and one non-branching coordinate, the intersection appears as a seam.

Nonadiabatic dynamics through a CI can occur very rapidly, often limited only by the vibrational period of the modes which bring the wavepacket towards it, along with any barriers on the PES. Timescales <1000 fs are typical for dynamics proceeding through CIs.[42] Upon reaching a CI, a wavepacket can then fall onto either side of the lower adiabatic state, arriving into a highly vibrational state such that energy is conserved.

1.2.3 Dissociative States

One final relaxation pathway we shall consider is dissociation. This is the conceptually simple process whereby the system accesses a state which is antibonding with respect to the bond between two fragments. A simple schematic of such a process was already given in Fig. 1.1, where molecule AB is excited to AB*, which goes on to dissociate to give fragments A and B. Excess energy is converted into either internal energy in the fragments, or translational energy (which is partitioned between the fragments according to their masses). The total kinetic energy release (TKER) is given by

$$TKER = h\nu + E_{AB} - (D_0 + E_A + E_B) \tag{1.17}$$

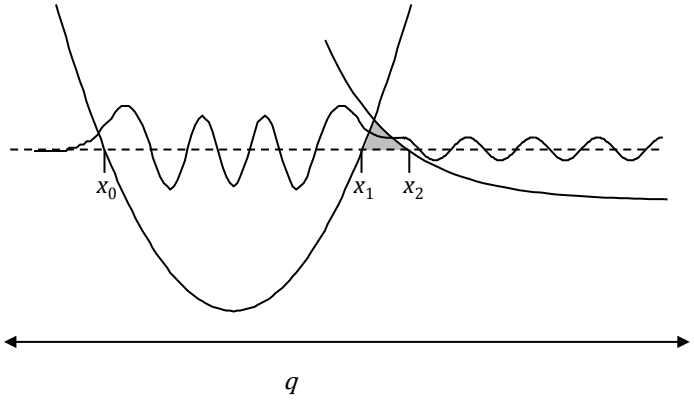

Figure 1.6 Schematic of a wavefunction tunnelling through a barrier. In the bound region, x_0-x_1, a standard harmonic wavefunction is observed. In the classically forbidden region, x_1 - x_2, the wavefunction undergoes an exponential decay, before emerging in the continuum > x_2.

where E_x gives the internal energy of the molecule (AB) or fragment *X*, $h\nu$ is the excitation energy and D_0 is the bond dissociation energy (assuming we have accessed the lowest dissociative state).[51] Dissociative states are particularly convenient for monitoring photoreactive processes; see Section 1.3.3.

1.2.4 Tunnelling

In all of the above discussions of wavepacket motion across a PES, we have assumed that no barriers to reaction exist, and the dynamics can be thought of as a 'ball rolling down a slope'. This classical description, though often very useful, neglects the quantum phenomenon of tunnelling, where there is a non-zero probability that a wavefunction (and hence wavepacket) can penetrate *through* a barrier to appear on the other side without possessing enough energy to surmount it.[21] Fig. 1.6 shows a schematic of an example system where a wavefunction tunnels through a barrier into the continuum, along some coordinate *q*.

The rate of tunnelling can be approximated in one dimension using the semiclassical Wentzel–Kramers–Brillouin (WKB)† approximation.[21, 52-54] The WKB approximation for tunnelling can be derived by considering the potential as an infinite series of square barriers. The probability of tunnelling through a square barrier, T_{sq}, well below the barrier top, is given by:[21]

$$T_{sq} = \frac{16E}{V}\left(1-\frac{E}{V}\right)\exp\left[\frac{-2l}{\hbar}\sqrt{2m(V-E)}\right] \qquad (1.18)$$

where *E* is the energy of the wavefunction, *V* is the potential energy of the barrier, *m* is the mass of the tunnelling particle and *l* is the width of the barrier. To approximate a

† or BKW or JWKB, all these abbreviations are seen in the literature.

varying barrier, we simply take the product of transmission probabilities for a series of square barriers with height $V(x)$ and width Δx:

$$T \propto \prod_x \exp\left[\frac{-2\Delta x}{\hbar}\sqrt{2m(V(x)-E)}\right] \tag{1.19}$$

Using the rules of logarithms, we can then write:

$$T \propto \exp\left[\sum_x \frac{-2\Delta x}{\hbar}\sqrt{2m(V(x)-E)}\right] \tag{1.20}$$

Then in the limit $\Delta x \to 0$:

$$T \approx \exp\left[\int_{x_1}^{x_2} \frac{-2}{\hbar}\sqrt{2m(V(x)-E)}dx\right] \tag{1.21}$$

with x_1 and x_2 given in Fig. 1.6. From here, producing a tunnelling rate is simply a matter of combining T with the frequency the barrier is approached, *i.e.* the vibrational frequency ν of the mode we are viewing the barrier along,

$$k_{tunnel} = \nu T \ . \tag{1.22}$$

Crucially, k_{tunnel} depends exponentially on both the mass of the tunnelling particle and on the size of the barrier, so a short lifetime is only observed for very light particles tunnelling through small barriers. In practical terms, this means only electrons and protons are commonly observed to tunnel. A common experimental technique to determine whether a proton transfer or loss is occurring by tunnelling is to deuterate the molecule at the site of the suspected proton, and observe the resultant change in lifetime. A very large increase in lifetime strongly suggests that tunnelling is the operative mechanism,[55] if no tunnelling is occurring then we might expect a change in rate proportional to the different vibrational frequencies of H and D contained bonds, *i.e.* $\sqrt{2}$.

1.3 Femtosecond Probing

Following temporal evolution, the final step in a femtochemistry experiment is the probe step. There is a vast array of techniques available for probing the system with femtosecond resolution,[38] however two of the most common in the gas phase, and the two which are employed in this thesis, are photoelectron (PE) spectroscopy[56, 57] and photofragment spectroscopy.[38] These two schemes shall now be discussed in some detail. As the PE work is performed on anions, and the photofragment work on neutrals, the focus of discussion is aligned accordingly, however it should be noted that time resolved PE spectroscopy is regularly performed on neutral species,[31, 37, 58] and

femtosecond photofragment studies have been performed on anions[59, 60] (and cations[61]).

1.3.1 Photoelectron Spectroscopy

The basis for photoelectron spectroscopy comes from the photoelectric effect, discovered by Hertz[62] and theoretically explained by Einstein[63] (for which he received the Nobel prize). The photoelectric effect is the simple phenomenon where a photon with sufficient energy is able to eject an electron from a system if it is bound by less than the photon energy. In the case of anion PE spectroscopy, this leaves a neutral parent behind, usually in a doublet spin state (if the initial anion was a singlet). As energy must be conserved, if the energy of the photon is known then the electron binding energy (eBE) can easily be calculated by measuring the electron kinetic energy (eKE):[56]

$$h\nu = eBE + eKE \tag{1.23}$$

From a molecular perspective, the electron is projected onto an unbound continuum state, while the parent anion is projected onto the corresponding neutral. As an interrogation technique, PE spectroscopy is particularly attractive as the selection rules for photodetachment are extremely relaxed, and it is always an allowed process, so any state can in principle be probed if there is sufficient photon energy. In addition, photoelectrons are readily detected using electron multiplier apparatus.[64]

As with excitation, the BO approximation applies and the detachment is a vertical process. The vertical nature imposes two conditions on the detachment. Firstly, just as with excitation, Franck-Condon factors apply; there must be overlap between the vibrational wavefunctions of the initial anion and the final neutral. The detachment cross section will then echo this overlap, just as in excitation. Secondly, when an

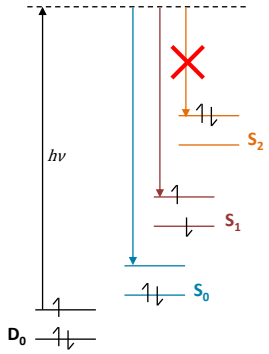

Figure 1.7 Diagram illustrating Koopmans' correlations. Electron detachment must correlate to an energy level where a single electron has been lost, and no rearrangement of the remaining 'core' electrons has taken place.

electron is lost there can be no rearrangement of the other electrons in the system. Fig. 1.7 illustrates this idea: any electron can be lost if there is sufficient probe energy, even if this results in an excited state of the resultant neutral. On the other hand, rearrangement cannot occur in the remaining electrons and so the final state must be correlated with the initial state. These are known as *Koopmans' correlations*,[31, 65] and importantly they can often provide information as to the electronic structure of the state from which the detachment occurs.[66, 67] A final rule worth mentioning for anion PE spectroscopy is the Wigner threshold law. Essentially, this states that a small centrifugal barrier is created by the ensemble of the parent neutral and outgoing electron, which must be overcome for electron detachment to occur. Symbolically, the threshold law is given by:

$$\sigma \propto eKE^{l+1/2} \tag{1.24}$$

where σ is the detachment cross section, and l the oribital angular momentum. The upshot is that the detachment cross section drops as *eKE* approaches zero, and *eKE* = 0 photoelectrons cannot be observed (from anions).[68, 69]

1.3.2 Time-Resolved Photoelectron Spectroscopy

Time-resolved PE spectroscopy (TRPES) utilises PE spectroscopy as the probe and detection step in a pump-probe experiment.[31, 58, 70-73] Due to the relaxed selection rules, TRPES is ideally suited to tracking a wavepacket throughout the molecular decay

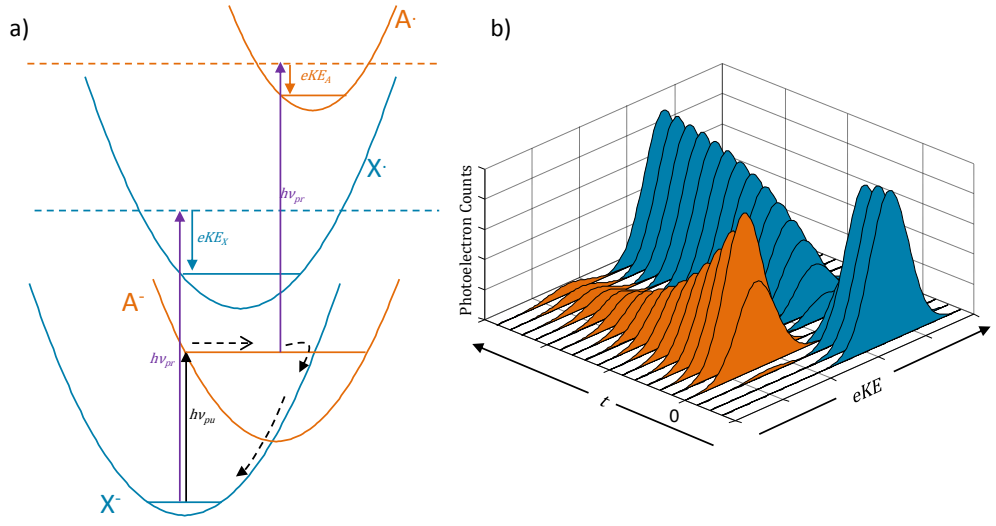

Figure 1.8 a) An example system where Koopmans' correlations will lead to two different features in the TRPES spectrum from the ground and excited state. The excited state relaxes back to the ground state, and hence the excited feature decays whilst the ground state feature grows in. The resultant TRPES is shown in b). This example shows type I correlations, where the different anion states are correlated with different neutral states, with Franck-Condon factors determining where on each neutral manifold to detach to. An alternative are type II correlations, where both states correlate to the same final state, and Franck-Condon factors solely determine the *eKE* of emitted photoelectrons.

process. The electron signal from the experiment, *I(t)*, is given by the projection of the time dependant initial wavepacket, $\Psi_i(t)$, onto the final state, ψ_f, by means of the interaction of the electric field of the photon, $\vec{E}$, with the ion's electric dipole moment, $\vec{\mu}_e$:[58]

$$I(t) = \left\langle \psi_f \left| \vec{E} \cdot \vec{\mu}_e \right| \Psi_i(t) \right\rangle \tag{1.25}$$

The initial wavepacket $\Psi_i(t)$ will evolve in accordance with Eq. (1.8), hence TRPES allows for real time monitoring of the projection onto the final state, and with it any changes in Franck-Condon factors and Koopmans' correlations.[66, 67] Owing to the relaxed selection rules, there is no 'optical window', and hence the entire reaction can be monitored using TRPES. Fig. 1.8(a) shows a schematic of a simple TRPES experiment. Immediately after the pump pulse (t = 0), the wavepacket is located on the excited state, A^-, which correlates to state A•. The probe pulse will therefore produce a feature with a kinetic energy eKE_A, corresponding to ionization of the excited state, with appropriate FC factors for detachment to the correlated state. As t evolves, population returns to the ground X^- state, via *e.g.* internal conversion. The ground state of the anion correlates with the ground state of the neutral, so electrons detached from here have a different kinetic energy, eKE_X. As a function of time, one would observe the A state feature decay away, with the X state feature growing in concomitantly. Fig. 1.8(b) shows the resultant time resolved PE spectrum. In this example, the different anionic electronic states are correlated to different neutral states, in what is termed type I Koopmans' correlations. Alternatively, if both anionic states correlate to the same neutral state, then FC factors will dominate in the spectral differences between PEs from the two states, in what is termed type II correlations.[58, 66, 67]

A simple example of TRPES is shown in Fig. 1.9, presenting the spectra of I_2^- when pumped at 780 nm (1.59 eV), and probed at 260 nm (4 .77 eV).[59, 74] Initially, three features are observed (labelled A, B & C), which arise from three different accessible excited electronic states of the diatomic ion, all of which are dissociative. As t evolves, the molecule dissociates to give one atom as a neutral and the other as an ion. The probe energy is sufficient to detach from the atomic anion into two spin-orbit states of the doublet neutral ($^2P_{3/2}$ and $^2P_{1/2}$), labelled D and E. As the bond breaks, the features from the molecular ion decay, while the atomic features grow in. This example is for a dissociation, so there is no 'recovery' of a ground state observed, however the general principle holds: tracking the appearance and decay of PE features allows the population of different states or species to be tracked as the molecule makes its way

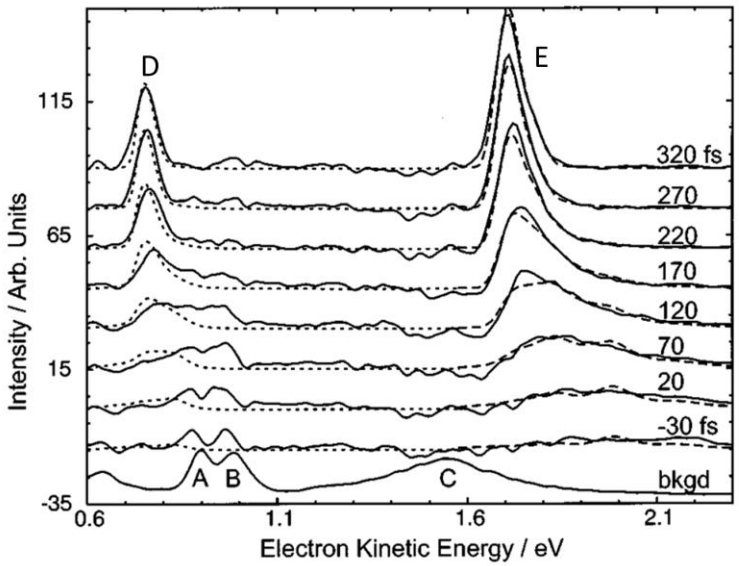

Figure 1.9 The time resolved photoelectron spectrum of I_2^-, showing the initial features (A, B & C) from the excited I_2^- system decaying away while product features from I^- atomic ions (D & E) grow in. Adapted with permission from ref. 74.

down the PES. It also elegantly demonstrates how TRPES can monitor the entire reaction coordinate.

1.3.3 Time Resolved Photofragment Spectroscopy

The previous I_2^- example touched upon a further method of ultrafast probing, which is of photofragment detection. This technique, which can be employed only in photoreactions where a bond breaks, monitors the fragments released from the parent molecule as a function of time. For this section of the introduction, our focus shall switch back to neutral molecules, as these techniques are applied to neutrals in this work.

The earliest femtosecond spectroscopy was of this nature; in 1987 Zewail and co-workers published the first femtochemistry paper, on the excited state dissociation of iodine cyanide.[11, 75, 76] They monitored the appearance of CN fragments as a function of pump-probe delay, using laser induced fluorescence as the detection means, to give the kinetic traces in Fig. 1.10. By tuning the probe wavelength, they were able to map out the dynamics at different points along the dissociative potential; 388.9 nm corresponds to ionization of free CN and hence shows a rise followed by a plateau, measuring the total progress of the dissociation whilst longer wavelengths are only resonant during the dissocation process, so the signal decays away again.

In modern experiments, mass spectrometry is often used to detect charged fragments in time resolved photofragment spectroscopy.[38, 77-80] This process, also known as time resolved ion yield spectroscopy, follows the same ionization principles

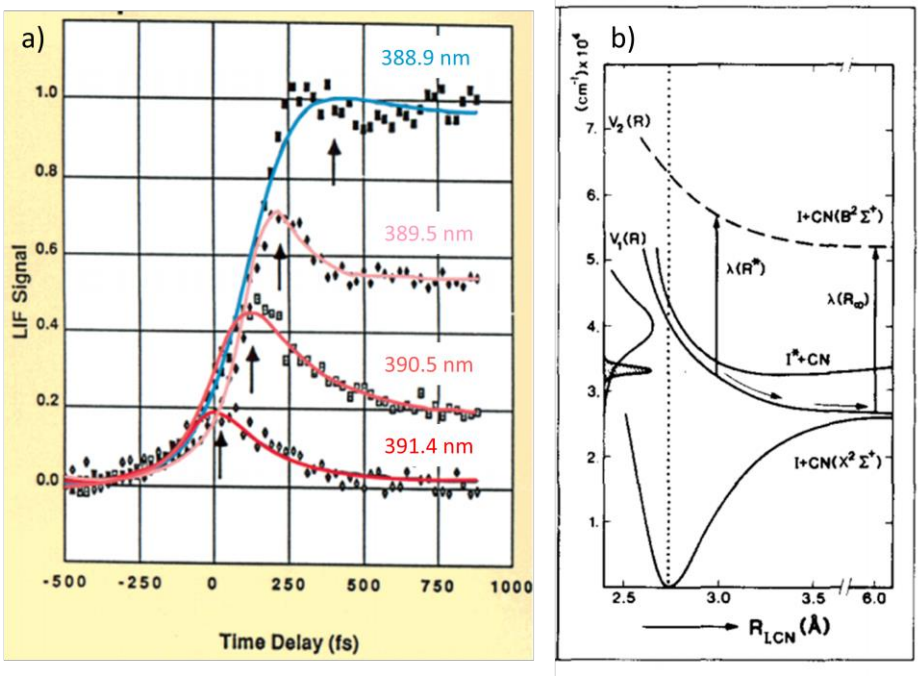

Figure 1.10 Time resolved study of the dissociation of ICN, by monitoring the creation of CN fragments. Tuning the probe wavelength changes where on the potential ionization occurs, allowing the potential to be mapped in time. This early femtochemistry experiment nicely illustrates the use of photofragment detection for reaction monitoring. a) Shows the CN yield at various probe energies, b) shows the PES for the reaction. Adapted with permission from ref. 75, 76.

as photoelectron spectroscopy, however rather than monitoring yield of photoelectrons, photoions are recorded instead. Unlike TRPES, which is a differential measurement, ion yield spectroscopy only gives a measure of the *total* ionization yield and no information about the *eKE* of emitted photoelectrons is collected.

There are a number of important advantages these techniques confer: firstly, detection of charged particles is easily achieved; single ion detection is readily attained, and the detection is generally universally applicable to all possible fragments.[64, 81] Secondly, mass spectrometry techniques such as time-of-flight or quadrupole filters allow for separation by mass of photofragments, which allow the experiment to easily be tuned to observe different fragments. In the case of time-of-flight techniques, the entire mass spectrum can be collected in one shot and all channels can be monitored simultaneously.[81]

Finally, by implementing techniques such as velocity map imaging[82] (discussed in Chapter 2), it is possible to measure the translational energy imparted to fragments, and hence the *TKER,* from Eq. (1.17). Such 'dispersed' measurements provide an extra dimension of information, just as with photoelectron spectroscopy, and information about the state of the system may be extracted from the *TKER*. In the frequency domain, such photofragment translational spectroscopy is frequently employed to

monitor the distribution of energy upon dissociation, as a function of excitation modes for the parent molecule. Velocity map imaging[78, 82, 83] and Rydberg tagging techniques[51, 84] have been employed to perform these measurements.

In general, there are two mechanisms by which fragment ion yields may vary as a function of *t* (from a neutral molecule).[38, 85, 86] After excitation with the pump pulse, a dissociative state may be accessed which yields two neutral fragments. The probe laser then ionizes one (or both) of these fragments and the ions are mass separated and detected. In this scenario, the yield of ions as a function of time reflects the cumulative yield of neutral fragments up until *t*. Fig. 1.11(a) demonstrates a schematic for this process, termed absorption-dissociation-ionization (A-D-I). Alternatively, the probe pulse could ionize the excited state, to produce some dissociative state. This ionic state will then dissociate to produce a neutral and a cationic fragment, which is detected. In this scheme, illustrated in Fig. 1.11(b), the fragment ion yield reflects the ionizable population of the excited state, following the same rules for ionization as photoelectron spectroscopy, and hence will usually decay to the baseline as *t* increases. This process is referred to as absorption-ionization-dissociation (A-I-D). The timescale for dissociation of the ionic species need not be particularly quick: typical time-of-flight for ionic fragments is nanoseconds to microseconds, and so it is feasible for the

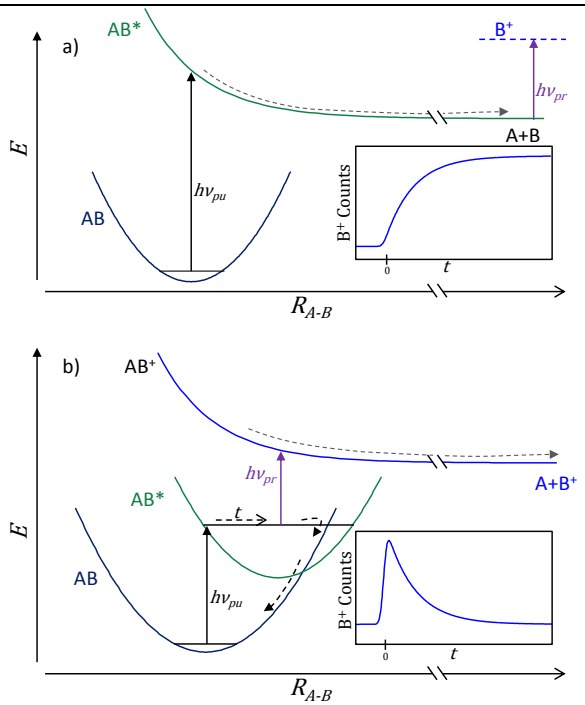

Figure 1.11 Schematic of the two possible channels which lead to time resolved fragment ion signal from molecules – a) absorption-dissociation-ionization, where AB* fragments to give A + B, and the probe pulse then ionizes B; b) absorption-ionization-dissociation, where the probe pulse ionizes AB* to AB^+, which then goes on to dissociate to give A + B^+. In each case, the expected ion yield as a function of time is shown.

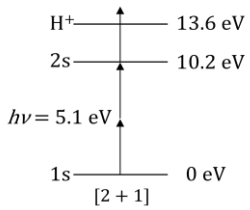

Figure 1.12 Schematic for a [2 + 1] REMPI scheme on a hydrogen atom. Two photons at 5.1 eV excite to the 2s level, and a third then ionizes.

fragmentation to occur from a slow statistical process (e.g. from a vibrationally hot state), rather than a direct dissociation pathway.[87] Standard two pulse pump-probe experiments do not have any means of measuring this timescale.

1.3.4 Resonance Enhanced Multi-Photon Ionization

In many systems, the two channels for pump-probe fragment ion production, discussed above, are in competition with each other; however, here we shall briefly review the resonance-enhanced multi-photon ionization (REMPI) technique,[26, 88] borrowed from high resolution spectroscopy, which allows some differentiation as to whether the observed ions originate from neutral or cationic species. The basic premise of REMPI is that a resonant transition to an excited state in the species to be probed is selected, and a laser with a photon energy matching the transition energy (or any other integer multiple fraction of this difference) is incident onto the molecule. In the case of excitation using multiple photons, the photon energy is insufficient to one-photon ionize the molecule, or even excite it. On the other hand, it is possible for two photons to be absorbed simultaneously via a *virtual state*.[89] The virtual state does not exist as an eigenfunction of the system, and cannot be populated, however if both photons arrive (near) simultaneously then it may act as an intermediate to a real resonance.† This two photon absorption takes the molecule into its excited state, and from here absorption of one (or more) additional photon allows the continuum to be accessed and the molecule ionized. REMPI schemes are labelled [n + m], where n is the number of photons required to reach the resonant state, and m is the number of photons required to ionize this state. The excitation and ionization wavelengths need not be identical; if they are not the label [n + m'] is employed.[88] In this work, [2 + 1] REMPI is used to ionize H atoms; the schematic for this process is shown in Fig. 1.12.

Crucially, the ionization is entirely dependent on the presence of the initial resonance. For frequency resolved spectroscopy, this allows very high resolution

† One can be convinced of this fact by considering the time-energy uncertainty principle – the virtual state has a near zero lifetime and hence near infinite imprecision in energy. As long as both photons arrive within its lifetime, the state can thus be utilized.

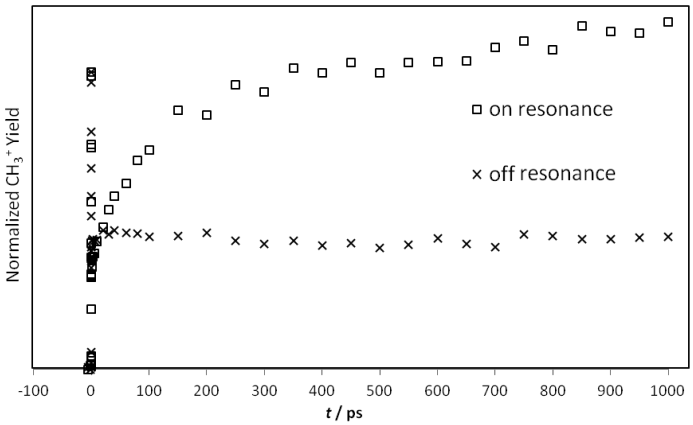

Figure 1.13 Comparison of total CH_3^+ yield for 2-methoxyphenol, excited at 238 nm and probed at either 333.3 nm (resonant) or 338 nm (off-resonance) to ionize CH_3 fragments. A slow component is visible only in the on-resonance data; hence this feature must be from A-D-I. On the other hand, a very fast initial spike is seen with both on- and off-resonance probes, so this feature must be from A-I-D.

absorption spectra to be recorded in the gas phase by monitoring ion production as a function of wavelength.[88, 90] In the case of time resolved photofragment spectroscopy, REMPI can be used to distinguish between A-D-I and A-I-D.[87, 91] If the probe wavelength is set to be resonant with a transition in the fragment we wish to ionize, then both A-D-I and A-I-D processes will be visible. On the other hand, if the wavelength is set to be just off resonance, then the neutral species cannot be ionized and only A-I-D is observed. The off-resonance A-I-D dynamics should differ little from on-resonance, due to the minimal change in probe energy. The difference between the two spectra thus reveals the A-D-I component. Fig. 1.13 shows an example from the Warwick lab of the total CH_3^+ yield from 2-methoxyphenol, exciting at 238 nm, and probing with either 333.3 nm, which is two-photon resonant with the $3p^2A_2'' \leftarrow X^2A_2''$ excitation in CH_3, or 338 nm, which is below the resonance. The on resonance spectrum clearly shows an additional slow component, which must come from A-D-I. It is worth noting, however, that if dissociation is sufficiently fast then the fragment may dissociate and be ionized all within the duration of the probe pulse, which means dissociation may not have 'naturally' occurred by this point in time, giving misleading ion signal. Measurements which disperse the energy of the ions (as in the work here) are less susceptible to these problems as the kinetic energy of fragments can often guide interpretation as to their origin.

1.3.5 Coincidence Measurements

Finally, it is worth mentioning a technique that can combine both photoelectron and photofragment spectroscopies – photoelectron-photoion coincidence spectroscopy

(PEPICO).[38, 92-94] In a PEPICO experiment, ion optics are employed such that photoelectrons are sent in one direction, while cations are sent in the other. If there are few enough events (*e.g.* by attenuating laser powers), then each electron event can be correlated with a corresponding cation event. PEPICO experiments allow the species which the electron was born from to be precisely defined, making them extremely useful for distinguishing between different sized clusters in a neutral beam, or for more precisely mapping out decay pathways of excited states.

1.4 Photostability

The previous sections gave an overview of the techniques and fundamentals of femtochemistry. Now we shall turn to looking at the application of these to exploring photostability, which is one of the core goals of this thesis. Electronic excitations are often damaging to molecules, as they can easily induce cleavage across structural covalent bonds.[95] In the absence of any non-radiative decay pathways, the system will have to spend nanoseconds in its excited state, during which time irreversible reactions may occur. On the other hand, if there is a rapid non-raditive decay pathway then the excess energy of the electronic excitation can rapidly be converted into heat, which may be dissipated into the surroundings in non-isolated environments. One obvious example where photostability is a desirable quality is in dyes; if exposure to light damages the dye molecule then the colour will fade and the applications of the dye are limited. This principle is readily observed in the everyday world: many 'classic' textile dyes, such as Perkins' mauve[96, 97] or indigo,[98-103] show strong photostable properties: mauve dye has a fluorescence lifetime < 5 ps.[96] Significant efforts have been devoted to the synthesis of dyes with photostable properties, often for applications such as biomedical imaging,[104, 105] and in Chapter 4 we explore the mechanism by which the indigo dye is imparted photostability.

Another area of active research is photostability in biomolecules. All life is made, at its core, of surprisingly few different molecules: the four DNA bases, the RNA base uracil, and the twenty natural amino acids, along with some other moieties such as carbohydrates. In the prebiotic world, the ozone layer was not present[106] and hence there was a significantly greater flux of UV light on the earth's surface. It has been hypothesized that the increased UV flux led to natural selection of biomolecules which are resistant to this radiation, as non-resistant molecules would lack the stability required for reproduction.[95, 106-109] In fact, there have even been proposals that life itself was started by photochemical reactions in this environment, leading to the creation of the first self-replicating RNA strands.[110] Photochemistry and the origins of life may

then be inseparably linked. In more recent times and in more complex organisms, photostability still plays a major role. For example, eumelanin, the pigment responsible for skin colour, has extremely complex photophysics and plays a major role in preventing UV damage.[108, 111, 112]

Any photostable mechanism depends on rapid non-radiative relaxation pathways. In practice, this usually amounts to saying that the dynamics of photostable systems are driven by nonadiabatic features – CIs.[95] In the past decade or so, there has been a flurry of activity in the field of identifying CIs in molecular systems. This has been driven both by more powerful computational techniques, such as CASSCF,[113, 114] which have made locating CIs routine, along with advanced experimental practices to explore larger molecules in greater detail.[42, 45] These studies have shown that CIs are ubiquitous in medium and larger sized systems, where the potential landscape is large and complex enough to support them. Note that for the purposes of this review, 'medium' refers to a molecule with $\gtrsim 10$ atoms, which is of course minute in comparison with complex biomolecules such as proteins. The comparatively small size of the species being studied does not completely invalidate their application to realistic systems, however. In practice, the electronic absorption properties of very large systems tend to be dominated by smaller *chromophores*, moieties with large absorption cross sections.[115] To a first approximation, the photophysics are thus controlled mainly by the chromophores, and the surrounding system can often be thought of simply as an environment to host the chromophore, with no active part taken in the absorption processes. The dynamics of the system are less likely to be completely driven by the chromophore, as both electronic and steric effects of the environment may greatly perturb the dynamics. Despite this, it is still important to understand the intrinsic dynamics so that the effect of the surroundings can be better understood. The logical means of studying the photophysics of very large systems is then to initially elucidate the properties of the chromophore, and then begin increasing the complexity of the system to better emulate the true environment. On the other hand, care must be taken that one does not apply the chromophore approximation overzealously. In systems such as eumelanin,[111, 112] proteins[116-118] or helical DNA (discussed below), chromophores strongly couple to each other or the environment and thus produce very different photophysical effects in larger systems, compared to isolated environments. As a pertinent example, the green fluorescent protein has an exceedingly high fluorescence yield which accounts for its wide use as a biomarker.[119] The isolated chromophore, however, has almost zero fluorescence quantum yield because the lack

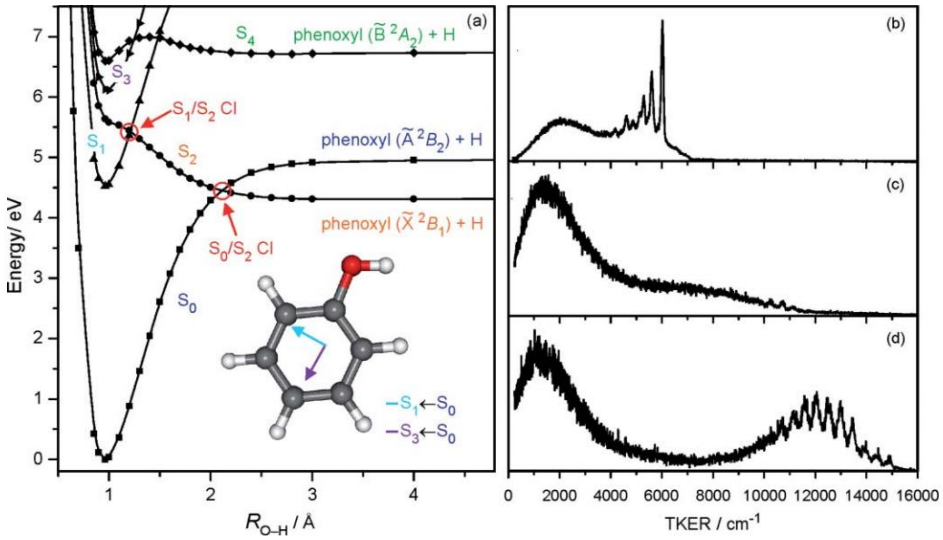

Figure 1.14 a) Potential energies of the first five states in phenol, as a function of $R_{O\text{-}H}$. The two $^1\pi\pi^*$ states are bound in all dimensions, while the $^1\pi\sigma^*$ states are unbound with respect to dissociation of the H atom. b), c) and d) Total kinetic energy release spectra for O-H bond fission in phenol at 275.113, 240 and 218 nm, respectively. Beneath the S_2/S_1 CI, structured peaks are observed indicating a slow decay process, however above CI these broaden out to indicate an ultrafast process occurring. Reproduced with permission from ref. 133.

of a restrictive protein environment allows a conical intersection to be accessed by a bond twist.[116, 117, 120, 121]

1.4.1 $^1\pi\sigma^*$ States as Relaxation Pathways

In 2002, Sobolewski and Domcke *et al.* published a seminal work proposing that a significant proportion of small aromatic species can non-radiatively relax by the employ of a $^1\pi\sigma^*$ state (a state formed from a $\sigma^* \leftarrow \pi$ transition).[84, 122†] These states are ubiquitous in aromatic systems with protonated heteroatoms, for example phenols,[91, 123-134] anilines,[135-138] pyrroles,[139-150] indoles,[151-156] etc. Many of these systems are directly relevant to biology, for example the amino acids tyrosine[157] and tryptophan have sidechains of phenol and indole, respectively; and the DNA and RNA bases are all heteroaromatics (see Fig. 1.15(a)).

As a representative example, Fig. 1.14(a) shows the potential energy of the first five electronic states of phenol, as a function of the O-H bond length.[133] Phenol, which is explored in further detail in Chapter 3, shall be used as the prototypical species to discuss $^1\pi\sigma^*$ states. The 0–0 transition (between zero-point vibrational levels) lies at 4.507 eV (275.113 nm),[158] which is to a bound $^1\pi\pi^*$ state (S_1). This transition is optically allowed, possessing a sizable absorption cross section (>2×10^{-17} cm^{-1} at the maximum),[159] and is termed 'bright'. Lying slightly higher in the vertical Franck-

† $^1n\sigma^*$ states essentially follow the same principles as $^1\pi\sigma^*$ states, so for convenience we shall not distinguish between the two.

Condon region is the first $^1\pi\sigma^*$ state (S_2), which corresponds to an electron populating the antibonding σ* orbital along the O–H bond, and hence is dissociative with respect to H loss. Unlike the first $^1\pi\pi^*$ state, the $^1\pi\sigma^*$ state is 'dark' as optical excitation to it is symmetry forbidden. Despite this, there is still a non-zero oscillator strength to this state, due to intensity borrowing from higher states and vibronic coupling.[84, 133] The shape of $^1\pi\sigma^*$ states generally shows a kink at short internuclear separation, which is due to mixing with the Rydberg like non-bonding orbital of the heteroatom.[84] Crucially, a CI is formed between S_1 and S_2, and another at longer bond length between S_2 and S_0 (the latter is necessary on symmetry grounds).[84] The postulated photostabilizing mechanism is then that the $^1\pi\sigma^*$ state could be employed as a direct route from the bright S_1 state back to the ground state. At the lower CI, the molecule can either recombine to give vibrationally hot S_0 or dissociate to lose an H atom.[122] Note that in the latter case, although a bond has been broken this can still provide a protective mechanism, as in a solvent or protein environment the hydrogen can easily recombine.[160]

Direct participation of the $^1\pi\sigma^*$ state in the photochemistry of phenol was first shown using frequency resolved photofragment translational energy spectroscopy by the Ashfold group,[134] who observed the appearance of a distinct high *TKER* peak in the H atom energy spectrum when excited to the first $^1\pi\pi^*$ state. Fig. 1.14(b) shows the resultant *TKER* spectra at three wavelengths. With wavelengths longer than 248 nm, structured features are observed, indicating a relatively slow dissociation, whilst above this energy the features become significantly broadened. The transition from a structured to a broad feature indicates that either a rapid enhancing in dissociation timescale is observed, or the potential becomes much broader. The CI was thus deduced to lie 5 eV (248 nm) above the S_0 ground state. Iqbal *et al.* then used time domain measurements to demonstrate that photoexcitation far above the S_2/S_1 CI, H loss is indeed ultrafast.[91, 128] Since then, a plethora of studies have been performed to explore $^1\pi\sigma^*$ states, ranging from theoretical, to frequency resolved and time resolved studies on phenol based systems. These have included halogenated phenols to modify electronic properties and symmetry;[126, 161] thiophenols,[129, 162-166] which have very different $^1\pi\sigma^*$ states; and methoxyphenols, from where CH_3 elimination can also be observed.[167] A number of intriguing questions have emerged, such as the nature of $^1\pi\sigma^*$ participation in excited state dynamics *below* the CI, and the contribution of the S_2/S_1 CI to the dynamics. Chapter 3 looks at these two issues in detail, and demonstrates how time resolved photofragment spectroscopy can go a significant way towards addressing these questions.

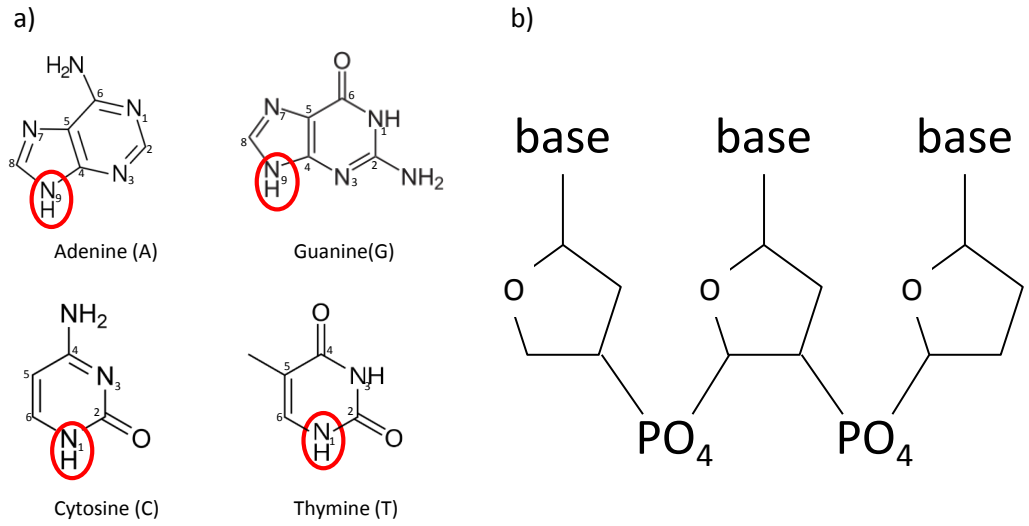

Figure 1.15 a) the structure of the four naturally occurring DNA bases. In oligonucleotides, the sugar/phosphate backbone connects via the red circled nitrogen atom in each case. A and G are the purine bases, while C and T are the pyrimidine bases. b) Schematic of the structure of oligonucleotides.

1.4.2 DNA Photostability

Finally, we shall tie together all of the previously considered topics with a very brief discussion of DNA relaxation dynamics. This provides some background for Chapter 5, but also presents a nice overview of the current state of the art in biomolecule relaxation dynamics.[168-170] As discussed earlier, the photostability of DNA and RNA may have been critical for the formation of life under primordial conditions. The issue is still of major importance in the modern day, however, as damage to DNA from solar UV radiation is a major cause of skin cancer, one of the most prevalent forms of cancer.[171] From a fundamental research point of view, studying DNA dynamics is a tremendous challenge due to the size of systems involved. DNA is composed of the four nucleobases, adenine (A / Ade), guanine (G / Gua), cytosine (C / Cyt) and thymine (T / Thy); structures shown in Fig. 1.15(a). These bases are connected to a deoxyribose ring, which are connected via phosphate groups to form a polymeric backbone (Fig. 1.15(b)). We shall begin by considering the dynamics of just the bases in the gas phase (*i.e.* applying the chromophore approximation), however as larger systems are considered we quickly find that the limits of size for (neutral) gas phase spectroscopy are reached, and so we shall instead turn to the solution phase to consider the dynamics of larger DNA strands.

1.4.2.1 Gas Phase DNA Bases

In the gas phase, all four nucleobases exhibit rapid relaxation from their first bright electronic excited state, which in all cases possesses $^1\pi\pi^*$ character and absorbs strongly in the UV from around 230 to 280 nm (4.4 - 5.4 eV).[168, 172] Time resolved ion

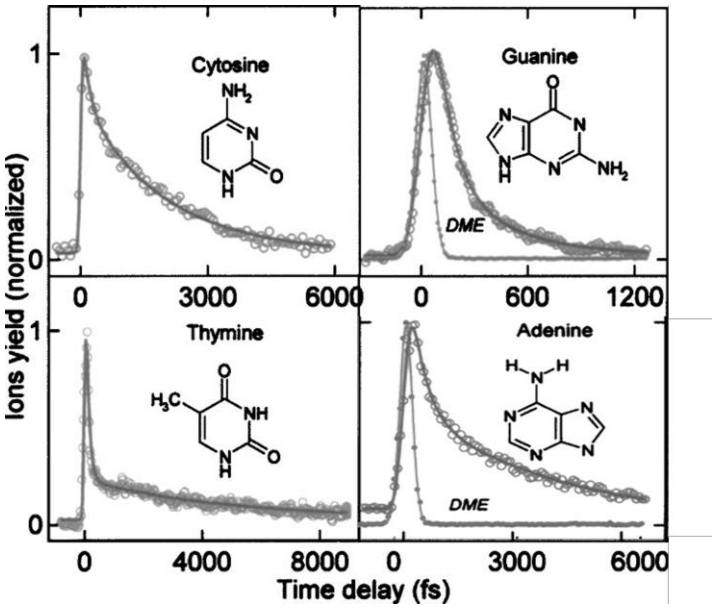

Figure 1.16 The time resolved ion yield of the four DNA bases, when excited with a 266 nm pump photon and probed with two photons at 400 nm. All four bases reveal biexponential decay, with an initial decay < 200 fs, followed by a second, picosecond, decay. The traces labelled DME give the cross correlation of the two lasers, determined by non-resonant ionization of dimethyl ether. Adapted with permission from ref. 173.

yield traces for the four bases, when photoexcited at 266 nm and probed with two photons at 400 nm,[173] are shown in Fig. 1.16. Similar dynamics had earlier been obtained when using a multiphoton 800 nm probe.[174] The rapid decay processes observed clearly implicate nonadiabatic relaxation pathways, and the challenge to the community has been to rationalize these. TRPES by the Stolow group found evidence of sequential kinetics in the decays of the bases, *i.e.* population flowing from one state to another before finally relaxing to the ground state.[175-177] Numerous theory studies have confirmed that there are accessible CIs in the excited states of all the bases, *e.g.*[45, 122, 178-185]

A $^1\pi\sigma^*$ state has been implicated in the decay of adenine,[122, 183, 186-188] however with excitation wavelengths > 233 nm, no high *TKER* H atoms are observed, meaning that if the $^1\pi\sigma^*$ state is an active participant, the dissociation must be fully aborted at the S_2/S_0 CI, and no H atoms released.[189-192] Regardless, in biological adenine the N-H bond responsible for this $^1\pi\sigma^*$ state (the 9-N, circled in Fig. 1.15(a)) is where the deoxyribose attaches, and so this $^1\pi\sigma^*$ state is perhaps unlikely to contribute. This has been confirmed by studies on 9-methyl adenine, which still shows rapid relaxation, with TRPES suggesting that the $^1\pi\sigma^*$ is no longer active (unlike 9-H adenine), and instead that perhaps a lower lying $^1n\pi^*$ state drives the relaxation.[169, 175-177, 192]

The remaining bases (G, C & T) have received less attention in the gas phase than A, although a sizable body of work remains. Guanine is particularly difficult to seed into

a molecular beam without decomposition; hence only ion yield dynamics studies have been performed on it.[173, 174] On the theory side, however, more studies have been performed,[179, 193-197] although theoretical works shall not be discussed in depth in this (experimental) thesis. Laser desorption sources (such as that designed in Chapter 6) should help overcome the experiment-theory gap.[198] The pyrimidine bases, cytosine and thymine, are both easily seeded into molecular beams, but in cytosine there are multiple tautomers to contend with.[199] Despite this, a small body of experimental[173, 174, 177, 199, 200] work exists along with the (much more extensive) theory, *e.g.*[178, 181, 182, 184, 200-206]

1.4.2.2 Base Stacking and Oligomeric DNA

Moving away from individual nucleobases to complete DNA strands, additional complexities begin to emerge.[168, 169] So far, all DNA gas phase dynamics studies have used molecular beam pulsed valve technologies, which creates an upper limit on the size of molecule that can be sublimated without thermal degradation occurring.[207] As a result, all dynamics studies on nucleosides, nucleotides or larger (a nucleoside is a base with a sugar; a nucleotide is a base with sugar and phosphate) have been performed in the solution phase, and results may not necessarily be directly comparable due to solvent effects altering the stability of different states, or impeding motions. The question of comparability between the isolated and condensed phases is key to assessing the applicability of gas-phase spectroscopy, and is a key question this thesis hopes to answer. The most common experimental technique is transient absorption,[33, 208-211] where the UV/vis spectrum absorption is measured as a function of pump-probe delay, however fluorescence upconversion has also been employed.[212, 213] Going from isolated bases to nucleotides, in general the dynamics seem to be mostly preserved, however some long lived population has been detected in pyrimidine nucleotides.[208]

When multiple bases are present in the same oligonucleotide, however, a significant change in relaxation dynamics is observed. Fig. 1.17 shows a recent transient absorption study on DNA strands composed of increasing numbers of A bases.[214] A long lived (> 150 ps) state is observed in the dimer, which increases in intensity as the number of bases increases. These effects have been attributed to excimer states formed between parallel stacked bases, and there has been a vast volume of research into these states, since their discovery in 1966,[215] *e.g.*[168, 169, 211, 216-218] Excimers are observed between not just A-A stacked pairs, but also most other dimer combinations and in disordered 'natural' DNA.[218] The exact nature of

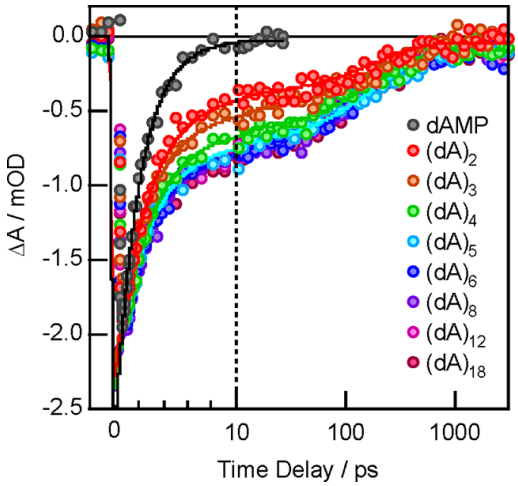

Figure 1.17 Lifetimes of A containing oligonucleotides, measured by transient absorption. Going from the mononucleotide to the dimer, a very long-lived component is observed. This long-lived state grows in intensity as the number of bases is increased, reaching an asymptote at around six bases. Reproduced with permission from ref. 214.

the excimer states is still under considerable debate, for example there is the question as to how many bases the exciton is delocalized over: predictions have ranged from just two bases, to as many as eight involved in the delocalization.[219-222] Structure, of course, plays a strong role in excimer dynamics; altering the pH of solution to break stacked configurations results in the excimers disappearing.[214] Moving briefly back to the gas phase, experiments have been performed on base dimers (which can readily be created in supersonic expansions),[223-225] however, long lived states are generally not observed, as the dimer tends to form in an 'end-on' configuration, as opposed to a parallel stacked configuration. The exception to this is a recent study where A_2 was hydrated with three water molecules, inducing a stacked configuration. In this instance, a long lived component was observed in the TRPES.[94] In Chapter 5 we demonstrate how electrospray ionization can potentially be used to continue exploring gas phase DNA base stacking excimers.

1.5 Summary

This chapter has aimed to introduce the fundamental concepts behind this thesis. After a brief historical perspective, the critical aspects of femtochemistry as they apply to this work were reviewed, by considering the pump, evolution, and probe steps in sequence. The two probe techniques considered, photoelectron spectroscopy and photofragment spectroscopy were employed in the two laboratories in which this work was carried out, and are used consistently throughout this thesis. Finally, a short introduction to the (vast) topic of photostability was given. Particular detail was given

to the emerging topic of $^1\pi\sigma^*$ mediated photostability, and to the crucial topic of DNA photodynamics.

The remainder of the thesis is structured as follows: the details of both experiments are presented in Chapter 2. Chapter 3 begins by looking at phenol, the simplest aromatic alcohol, and introduces complexity in the form of catechol, which possesses an additional hydroxyl group. Chapter 4 then moves onto studying a still larger system, the anionic dye indigo carmine, the photodynamics of which are crucial to its use both historical and modern day. Chapter 5 then continues the increase of both complexity and relevance of application by studying anionic DNA fragments, starting at single nucleotides and building to an oligonucleotide trimer. Finally, Chapter 6 presents a new instrument which has been constructed in Warwick for the purposes of studying isolated neutral molecules of ever larger size and complexity.

1.6 References

1. K. J. Laidler, *J. Chem. Educ.*, 1984, **61**, 494.
2. H. Landolt, *Berichte der deutschen chemischen Gesellschaft*, 1886, **19**, 1317.
3. B. Chance, *Journal of the Franklin Institute*, 1940, **229**, 455.
4. R. G. W. Norrish and G. Porter, *Nature*, 1949, **164**, 658.
5. R. G. W. Norrish, Nobel Lecture, 1967.
6. J. Van Houten, *J. Chem. Educ.*, 2002, **79**, 548.
7. T. H. Maiman, *Nature*, 1960, **187**, 493.
8. C. V. Shank and E. P. Ippen, *Appl. Phys. Lett.*, 1974, **24**, 373.
9. A. H. Zewail, Nobel Lecture, Stockholm, Sweden, 1999.
10. A. H. Zewail, *Femtochemistry: Ultrafast Dynamics of the Chemical Bond*, World Scientific Publishing, Singapore, 1994.
11. M. Dantus, M. J. Rosker and A. H. Zewail, *J. Chem. Phys.*, 1988, **89**, 6128.
12. T. S. Rose, M. J. Rosker and A. H. Zewail, *J. Chem. Phys.*, 1989, **91**, 7415.
13. M. Dantus, R. M. Bowman, M. Gruebele and A. H. Zewail, *J. Chem. Phys.*, 1989, **91**, 7437.
14. A. Mokhtari, P. Cong, J. L. Herek and A. H. Zewail, *Nature*, 1990, **348**, 225.
15. T. Baumert, J. L. Herek and A. H. Zewail, *J. Chem. Phys.*, 1993, **99**, 4430.
16. M. H. M. Janssen, M. Dantus, H. Guo and A. H. Zewail, *Chem. Phys. Lett.*, 1993, **214**, 281.
17. J. L. Herek, S. Pedersen, L. Banares and A. H. Zewail, *J. Chem. Phys.*, 1992, **97**, 9046.
18. S. Pedersen, L. Banares and A. H. Zewail, *J. Chem. Phys.*, 1992, **97**, 8801.
19. I. P. Christov, M. M. Murnane and H. C. Kapteyn, *Phys. Rev. Lett.*, 1997, **78**, 1251.
20. P. M. Paul, E. S. Toma, P. Breger, G. Mullot, F. Augé, P. Balcou, H. G. Muller and P. Agostini, *Science*, 2001, **292**, 1689.
21. P. Atkins and R. Friedman, *Molecular Quantum Mechanics*, Oxford University Press, Oxford, 2011.
22. M. Born and R. Oppenheimer, *Annalen der Physik*, 1927, **389**, 457.
23. C. Eckart, *Phys. Rev.*, 1934, **46**, 383.
24. W. Heisenberg, *Z. Phys. A*, 1927, **43**, 172.
25. E. H. Kennard, *Zeitschrift für Physik*, 1927, **44**, 326.
26. W. Demtroder, *Laser Spectroscopy*, Springer-Verlag, Berlin, 1981.
27. R. Paschotta, *Encyclopedia of Laser Physics and Technology*, Wiley, Berlin, 2008.
28. E. U. Condon, *Phys. Rev.*, 1928, **32**, 858.
29. E. Condon, *Phys. Rev.*, 1926, **28**, 1182.
30. J. Franck and E. G. Dymond, *Trans. Faraday Soc.*, 1926, **21**, 536.
31. G. Wu, P. Hockett and A. Stolow, *Phys. Chem. Chem. Phys.*, 2011, **13**, 18447.
32. E. J. Heller, *J. Chem. Phys.*, 1975, **62**, 1544.
33. T. Kobayashi and Y. Kida, *Phys. Chem. Chem. Phys.*, 2012, **14**, 6200.
34. G. A. Worth and L. S. Cederbaum, *Annu. Rev. Phys. Chem.*, 2004, **55**, 127.
35. A. Jablonski, *Nature*, 1933, **131**, 839.
36. J. R. Lakowicz, *Principles of Fluorescence Spectroscopy*, Kluwer Academic, New York, 1999.
37. K. L. Reid, *Int. Rev. Phys. Chem.*, 2008, **27**, 607.
38. I. V. Hertel and W. Radloff, *Rep. Prog. Phys.*, 2006, **69**, 1897.

39. A. M. Aleksandr, L. M. Aleksandr and A. R. Evgenii, *Physics-Uspekhi*, 2012, **55**, 977.
40. R. Englman and J. Jortner, *Mol. Phys.*, 1970, **18**, 145.
41. T. S. Kuhlman, S. P. A. Sauer, T. I. Solling and K. B. Moller, *J. Chem. Phys.*, 2012, **137**, 22A522.
42. W. Domcke, D. R. Yarkony and H. Koppel, eds., *Conical Intersections: Theory Computation and Experiment*, World Scientific Publishing, Singapore, 2011.
43. D. R. Yarkony, *Acc. Chem. Res.*, 1998, **31**, 511.
44. D. R. Yarkony, *Rev. Mod. Phys.*, 1996, **68**, 985.
45. S. Matsika and P. Krause, *Annu. Rev. Phys. Chem.*, 2011, **62**, 621.
46. J. von Neumann and E. P. Wigner, *Phys. Z.*, 1929, **30**, 467.
47. Z. H. Li, R. Valero and D. G. Truhlar, *Theor. Chem. Acc.*, 2007, **118**, 9.
48. J. Biesner, L. Schnieder, G. Ahlers, X. Xie, K. H. Welge, M. N. R. Ashfold and R. N. Dixon, *J. Chem. Phys.*, 1989, **91**, 2901.
49. J. Biesner, L. Schnieder, J. Schmeer, G. Ahlers, X. Xie, K. H. Welge, M. N. R. Ashfold and R. N. Dixon, *J. Chem. Phys.*, 1988, **88**, 3607.
50. R. J. Duchovic, Y. L. Volobuev, G. C. Lynch, A. W. Jasper, D. G. Truhlar, T. C. Allison, A. F. Wagner, B. C. Garrett, J. Espinosa-García, and J. C. Corchado, POTLIB, http://comp.chem.umn.edu/potlib
51. H. J. Krautwald, L. Schnieder, K. H. Welge and M. N. R. Ashfold, *Farady Discuss.*, 1986, **82**, 99.
52. M. S. Child, *Semiclassical Mechanics with Molecular Applications*, Oxford University Press, Oxford, 1991.
53. K. W. Ford, D. L. Hill, M. Wakano and J. A. Wheeler, *Annals of Physics*, 1959, **7**, 239.
54. R. J. L. Roy and R. B. Bernstein, *J. Chem. Phys.*, 1971, **54**, 5114.
55. D. Borgis and J. T. Hynes, *Chem. Phys.*, 1993, **170**, 315.
56. T. A. Carlson, *Annu. Rev. Phys. Chem.*, 1975, **26**, 211.
57. R. R. Corderman and W. C. Lineberger, *Annu. Rev. Phys. Chem.*, 1979, **30**, 347.
58. A. Stolow, A. E. Bragg and D. M. Neumark, *Chem. Rev.*, 2004, **104**, 1719.
59. B. Jefferys Greenblatt, M. T. Zanni and D. M. Neumark, *Chem. Phys. Lett.*, 1996, **258**, 523.
60. V. Vorsa, S. Nandi, P. J. Campagnola, M. Larsson and W. C. Lineberger, *J. Chem. Phys.*, 1997, **106**, 1402.
61. J.-W. Ho, W.-K. Chen and P.-Y. Cheng, *J. Chem. Phys.*, 2009, **131**, 134308.
62. H. Hertz, *Annalen der Physik*, 1887, **267**, 983.
63. A. Einstein, *Annalen der Physik*, 1905, **322**, 132.
64. J. H. Moore, C. C. Davis, M. A. Coplan and S. C. Greer, *Building Scientific Apparatus*, Cambridge University Press, Cambridge, 2009.
65. T. Koopmans, *Physica*, 1934, **1**, 104.
66. M. Seel and W. Domcke, *Chem. Phys.*, 1991, **151**, 59.
67. M. Seel and W. Domcke, *J. Chem. Phys.*, 1991, **95**, 7806.
68. E. P. Wigner, *Phys. Rev.*, 1948, **73**, 1002.
69. J. P. David, *Rep. Prog. Phys.*, 2004, **67**, 857.
70. D. M. Neumark, *Annu. Rev. Phys. Chem.*, 2001, **52**, 255.
71. T. Baumert, R. Thalweiser and G. Gerber, *Chem. Phys. Lett.*, 1993, **209**, 29.
72. T. Suzuki, *Annu. Rev. Phys. Chem.*, 2006, **57**, 555.
73. A. Stolow, *Annu. Rev. Phys. Chem.*, 2003, **54**, 89.
74. M. T. Zanni, V. S. Batista, B. J. Greenblatt, W. H. Miller and D. M. Neumark, *J. Chem. Phys.*, 1999, **110**, 3748.
75. M. Dantus, M. J. Rosker and A. H. Zewail, *J. Chem. Phys.*, 1987, **87**, 2395.
76. A. H. Zewail, *J. Phys. Chem. A*, 2000, **104**, 5660.
77. D. Zhong and A. H. Zewail, *J. Phys. Chem. A*, 1998, **102**, 4031.
78. R. d. Nalda, J. G. Izquierdo, J. Dura and L. Banares, *J. Chem. Phys.*, 2007, **126**, 021101.
79. H. Kang, K. T. Lee and S. K. Kim, *Chem. Phys. Lett.*, 2002, **359**, 213.
80. P. C. Samartzis, B. L. G. Bakker, D. H. Parker and T. N. Kitsopoulos, *J. Phys. Chem. A*, 1999, **103**, 6106.
81. J. O. Watson and O. D. Sparkman, *Introduction to Mass Spectrometry*, Wiley and Sons, Chichester, 2007.
82. A. T. J. B. Eppink and D. H. Parker, *Rev. Sci. Instrum.*, 1997, **68**, 3477.
83. B. Whitaker, ed., *Imaging in Molecular Dynamics: Technology and Applications*, Cambridge University Press, New York, 2003.
84. M. N. R. Ashfold, G. A. King, D. Murdock, M. G. D. Nix, T. A. A. Oliver and A. G. Sage, *Phys. Chem. Chem. Phys.*, 2010, **12**, 1218.
85. E. M. Snyder, J. Purnell, S. Wei, S. A. Buzza and A. W. Castleman Jr, *Chem. Phys.*, 1996, **207**, 355.
86. J. Purnell, S. Wei, S. A. Buzza and A. W. Castleman, *J. Phys. Chem.*, 1993, **97**, 12530.
87. D. J. Hadden, C. A. Williams, G. M. Roberts and V. G. Stavros, *Phys. Chem. Chem. Phys.*, 2011, **13**, 4494.
88. M. N. R. Ashfold and J. D. Howe, *Annu. Rev. Phys. Chem.*, 1994, **45**, 57.
89. M. Goppert-Mayer, *Ann. Physik.*, 1931, **401**, 273.
90. N. C. Polfer and J. Oomens, *Phys. Chem. Chem. Phys.*, 2007, **9**, 3804.

91. A. Iqbal, M. S. Y. Cheung, M. G. D. Nix and V. G. Stavros, *J. Phys. Chem. A*, 2009, **113**, 8157.
92. C. Dedonder-Lardeux, I. Dimicoli, C. Jouvet, S. Martrenchard-Barra, M. Richard-Viard, D. Solgadi and M. Vervloet, *Chem. Phys. Lett.*, 1995, **240**, 97.
93. V. Stert, W. Radloff, C. P. Schulz and I. V. Hertel, *Eur. Phys. J. D*, 1999, **5**, 97.
94. V. R. Smith, E. Samoylova, H. H. Ritze, W. Radloff and T. Schultz, *Phys. Chem. Chem. Phys.*, 2010, **12**, 9632.
95. W. Domcke, *Phys. Chem. Chem. Phys.*, 2010, **12**, 4897.
96. M. M. Sousa, M. J. Melo, A. J. Parola, P. J. T. Morris, H. S. Rzepa and J. S. S. de Melo, *Chemistry – A European Journal*, 2008, **14**, 8507.
97. J. Seixas de Melo, S. Takato, M. Sousa, M. J. Melo and A. J. Parola, *Chem. Commun.*, 2007, **0**, 2624.
98. A. S. Chatterley, D. A. Horke and J. R. R. Verlet, *Phys. Chem. Chem. Phys.*, 2012, **14**, 16155.
99. S. Yamazaki, A. L. Sobolewski and W. Domcke, *Phys. Chem. Chem. Phys.*, 2011, **13**, 1618.
100. I. Iwakura, A. Yabushita and T. Kobayashi, *Chem. Phys. Lett.*, 2010, **484**, 354.
101. I. Iwakura, A. Yabushita and T. Kobayashi, *Chem. Lett.*, 2009, **38**, 1020.
102. J. Seixas de Melo, R. Rondão, H. D. Burrows, M. J. Melo, S. Navaratnam, R. Edge and G. Voss, *ChemPhysChem*, 2006, **7**, 2303.
103. J. Seixas de Melo, A. P. Moura and M. J. Melo, *J. Phys. Chem. A*, 2004, **108**, 6975.
104. C. Jung, B. K. Müller, D. C. Lamb, F. Nolde, K. Müllen and C. Bräuchle, *J. Am. Chem. Soc.*, 2006, **128**, 5283.
105. A. Dubois, M. Canva, A. Brun, F. Chaput and J.-P. Boilot, *Appl. Opt.*, 1996, **35**, 3193.
106. H. Bernhardt, *Biology Direct*, 2012, **7**, 23.
107. N. Balucani, *Int. J. Mol. Sci.*, 2009, **10**, 2304.
108. C. S. Cockell and J. Knowland, *Bio. Rev.*, 1999, **74**, 311.
109. C. Sagan, *J. Theor. Biol.*, 1973, **39**, 195.
110. M. W. Powner, B. Gerland and J. D. Sutherland, *Nature*, 2009, **459**, 239.
111. A. Huijser, A. Pezzella and V. Sundstrom, *Phys. Chem. Chem. Phys.*, 2011, **13**, 9119.
112. P. Meredith and T. Sarna, *Pigment Cell Research*, 2006, **19**, 572.
113. J. Olsen, *Int. J. Quantum Chem*, 2011, **111**, 3267.
114. B. O. Roos, P. R. Taylor and P. E. M. Siegbahn, *Chem. Phys.*, 1980, **48**, 157.
115. A. D. McNaught and A. Wilkinson, eds., *IUPAC. Compendium of Chemical Terminology (the "Gold Book")*, Blackwell Scientific Publications, Oxford, 1997.
116. C. R. S. Mooney, D. A. Horke, A. S. Chatterley, A. Simperler, H. H. Fielding and J. R. R. Verlet, *Chem. Sci.*, 2013, **4**, 921.
117. M. W. Forbes and R. A. Jockusch, *J. Am. Chem. Soc.*, 2009, **131**, 17038.
118. D. Polli, P. Altoe, O. Weingart, K. M. Spillane, C. Manzoni, D. Brida, G. Tomasello, G. Orlandi, P. Kukura, R. A. Mathies, M. Garavelli and G. Cerullo, *Nature*, 2010, **467**, 440.
119. O. Shimomura, F. H. Johnson and Y. Saiga, *J. Cell. Comp. Phys.*, 1962, **59**, 223.
120. M. Chattoraj, B. A. King, G. U. Bublitz and S. G. Boxer, *Proc. Natl. Acad. Sci. USA*, 1996, **93**, 8362.
121. M. Zimmer, *Chem. Rev.*, 2002, **102**, 759.
122. A. L. Sobolewski, W. Domcke, C. Dedonder-Lardeux and C. Jouvet, *Phys. Chem. Chem. Phys.*, 2002, **4**, 1093.
123. G. M. Roberts, A. S. Chatterley, J. D. Young and V. G. Stavros, *J. Phys. Chem. Lett.*, 2012, **3**, 348.
124. R. A. Livingstone, J. O. F. Thompson, M. Iljina, R. J. Donaldson, B. J. Sussman, M. J. Paterson and D. Townsend, *J. Chem. Phys.*, 2012, **137**, 184304.
125. G. A. King, T. A. A. Oliver, R. N. Dixon and M. N. R. Ashfold, *Phys. Chem. Chem. Phys.*, 2012, **14**, 3338.
126. G. A. Pino, A. N. Oldani, E. Marceca, M. Fujii, S. I. Ishiuchi, M. Miyazaki, M. Broquier, C. Dedonder and C. Jouvet, *J. Chem. Phys.*, 2010, **133**, 124313.
127. G. A. King, T. A. A. Oliver, M. G. D. Nix and M. N. R. Ashfold, *J. Phys. Chem. A*, 2009, **113**, 7984.
128. A. Iqbal, L. J. Pegg and V. G. Stavros, *J. Phys. Chem. A*, 2008, **112**, 9531.
129. M. N. R. Ashfold, A. L. Devine, R. N. Dixon, G. A. King, M. G. D. Nix and T. A. A. Oliver, *Proc. Natl. Acad. Sci. USA*, 2008, **105**, 12701.
130. G. A. King, A. L. Devine, M. G. D. Nix, D. E. Kelly and M. N. R. Ashfold, *Phys. Chem. Chem. Phys.*, 2008, **10**, 6417.
131. M. G. D. Nix, A. L. Devine, R. N. Dixon and M. N. R. Ashfold, *Chem. Phys. Lett.*, 2008, **463**, 305.
132. C. M. Tseng, Y. T. Lee, M. F. Lin, C. K. Ni, S. Y. Liu, Y. P. Lee, Z. F. Xu and M. C. Lin, *J. Phys. Chem. A*, 2007, **111**, 9463.
133. R. N. Dixon, T. A. A. Oliver and M. N. R. Ashfold, *J. Chem. Phys.*, 2011, **134**, 194303.
134. M. N. R. Ashfold, B. Cronin, A. L. Devine, R. N. Dixon and M. G. D. Nix, *Science*, 2006, **312**, 1637.
135. G. M. Roberts, C. A. Williams, J. D. Young, S. Ullrich, M. J. Paterson and V. G. Stavros, *J. Am. Chem. Soc.*, 2012, **134**, 12578.
136. R. Spesyvtsev, O. M. Kirkby and H. H. Fielding, *Faraday Discuss.*, 2012, **157**, 165.
137. R. Montero, A. P. Conde, V. Ovejas, R. Martinez, F. Castano and A. Longarte, *J. Chem. Phys.*, 2011, **135**, 054308.
138. G. A. King, T. A. A. Oliver and M. N. R. Ashfold, *J. Chem. Phys.*, 2010, **132**, 214307.

139. G. M. Roberts, C. A. Williams, H. Yu, A. S. Chatterley, J. D. Young, S. Ullrich and V. G. Stavros, *Faraday Discuss.*, 2013, DOI:10.1039/C2FD20140B.
140. B. Sellner, M. Barbatti and H. Lischka, *J. Chem. Phys.*, 2009, **131**, 024312.
141. M. Vazdar, M. Eckert-Maksic, M. Barbatti and H. Lischka, *Mol. Phys.*, 2009, **107**, 845.
142. H. Lischka, M. Vazdar, M. Eckert-Maksic and M. Barbatti, *Mol. Phys.*, 2009, **107**, 845.
143. V. Poterya, V. Profant, M. Farnik, P. Slavicek and U. Buck, *J. Chem. Phys.*, 2007, **127**, 064307.
144. B. Cronin, A. L. Devine, M. G. D. Nix and M. N. R. Ashfold, *Phys. Chem. Chem. Phys.*, 2006, **8**, 3440.
145. M. Barbatti, M. Vazdar, A. J. A. Aquino, M. Eckert-Maksic and H. Lischka, *J. Chem. Phys.*, 2006, **125**, 164323.
146. B. Cronin, M. G. D. Nix, A. L. Devine, R. N. Dixon and M. N. R. Ashfold, *Phys. Chem. Chem. Phys.*, 2005, **8**, 599.
147. H. Lippert, H. H. Ritze, I. V. Hertel and W. Radloff, *ChemPhysChem*, 2004, **5**, 1423.
148. J. Wei, A. Kuczmann, J. Riedel, F. Renth and F. Temps, *Phys. Chem. Chem. Phys.*, 2003, **5**, 315.
149. A. L. Sobolewski and W. Domcke, *Chem. Phys.*, 2000, **259**, 181.
150. D. A. Blank, S. W. North and Y. T. Lee, *Chem. Phys.*, 1994, **187**, 35.
151. R. Montero, A. P. Conde, V. Ovejas, F. Castano and A. Longarte, *J. Phys. Chem. A*, 2012, **116**, 2698.
152. T. A. A. Oliver, G. A. King and M. N. R. Ashfold, *Phys. Chem. Chem. Phys.*, 2011, **13**, 14646.
153. R. Livingstone, O. Schalk, A. E. Boguslavskiy, G. R. Wu, L. T. Bergendahl, A. Stolow, M. J. Paterson and D. Townsend, *J. Chem. Phys.*, 2011, **135**, 194307.
154. A. Iqbal and V. G. Stavros, *J. Phys. Chem. A*, 2010, **114**, 68.
155. A. L. Sobolewski and W. Domcke, *ChemPhysChem*, 2007, **8**, 756.
156. H. Lippert, H. H. Ritze, I. V. Hertel and W. Radloff, *Chem. Phys. Lett.*, 2004, **398**, 526.
157. A. Iqbal and V. G. Stavros, *J. Phys. Chem. Lett.*, 2010, **1**, 2274.
158. G. Berden, W. L. Meerts, M. Schmitt and K. Kleinermanns, *J. Chem. Phys.*, 1996, **104**, 972.
159. T. Etzkorn, B. Klotz, S. Sørensen, I. V. Patroescu, I. Barnes, K. H. Becker and U. Platt, *Atmos. Environ.*, 1999, **33**, 525.
160. Y. Zhang, T. A. A. Oliver, M. N. R. Ashfold and S. E. Bradforth, *Faraday Discuss.*, 2012, **157**, 141.
161. A. L. Devine, M. G. D. Nix, B. Cronin and M. N. R. Ashfold, *Phys. Chem. Chem. Phys.*, 2007, **9**, 3749.
162. T. S. Venkatesan, S. G. Ramesh, Z. Lan and W. Domcke, *J. Chem. Phys.*, 2012, **136**, 174312.
163. T. A. A. Oliver, Y. Zhang, M. N. R. Ashfold and S. E. Bradforth, *Faraday Discuss.*, 2011, **150**, 439.
164. A. L. Devine, M. G. D. Nix, R. N. Dixon and M. N. R. Ashfold, *J. Phys. Chem. A*, 2008, **112**, 9563.
165. J. S. Lim, Y. S. Lee and S. K. Kim, *Angew. Chem. Int. Ed.*, 2008, **47**, 1853.
166. I. S. Lim, J. S. Lim, Y. S. Lee and S. K. Kim, *J. Chem. Phys.*, 2007, **126**, 034306.
167. D. J. Hadden, G. M. Roberts, T. N. V. Karsili, M. N. R. Ashfold and V. G. Stavros, *Phys. Chem. Chem. Phys.*, 2012, **14**, 13415.
168. C. T. Middleton, K. de La Harpe, C. Su, Y. K. Law, C. E. Crespo-Hernández and B. Kohler, *Annu. Rev. Phys. Chem.*, 2009, **60**, 217.
169. C. E. Crespo-Hernández, B. Cohen, P. M. Hare and B. Kohler, *Chem. Rev.*, 2004, **104**, 1977.
170. K. Kleinermanns, D. Nachtigallová and M. S. de Vries, *Int. Rev. Phys. Chem.*, 2013, **32**, 308.
171. D. M. Parkin, D. Mesher and P. Sasieni, *Br J Cancer*, 2011, **105**, S66.
172. M. K. Shukla and J. Leszczynski, *J. Biomol. Struct. Dyn.*, 2007, **25**, 93.
173. C. Canuel, M. Mons, F. Piuzzi, B. Tardivel, I. Dimicoli and M. Elhanine, *J. Chem. Phys.*, 2005, **122**, 074316.
174. H. Kang, K. T. Lee, B. Jung, Y. J. Ko and S. K. Kim, *J. Am. Chem. Soc.*, 2002, **124**, 12958.
175. H. Satzger, D. Townsend, M. Z. Zgierski, S. Patchkovskii, S. Ullrich and A. Stolow, *Proc. Natl. Acad. Sci. USA*, 2006, **103**, 10196.
176. H. Satzger, D. Townsend and A. Stolow, *Chem. Phys. Lett.*, 2006, **430**, 144.
177. S. Ullrich, T. Schultz, M. Z. Zgierski and A. Stolow, *Phys. Chem. Chem. Phys.*, 2004, **6**, 2796.
178. L. Serrano-Andrés and M. Merchán, *J. Photochem. Photobiol. C*, 2009, **10**, 21.
179. L. Serrano-Andrés, M. Merchán and A. C. Borin, *J. Am. Chem. Soc.*, 2008, **130**, 2473.
180. L. Serrano-Andrés, M. Merchán and A. C. Borin, *Proc. Natl. Acad. Sci. USA*, 2006, **103**, 8691.
181. M. Merchán, R. González-Luque, T. Climent, L. Serrano-Andrés, E. Rodríguez, M. Reguero and D. Peláez, *J. Phys. Chem. B*, 2006, **110**, 26471.
182. S. Perun, A. L. Sobolewski and W. Domcke, *J. Phys. Chem. A*, 2006, **110**, 13238.
183. S. Perun, A. L. Sobolewski and W. Domcke, *J. Am. Chem. Soc.*, 2005, **127**, 6257.
184. K. A. Kistler and S. Matsika, *J. Phys. Chem. A*, 2007, **111**, 2650.
185. L. Blancafort, *J. Am. Chem. Soc.*, 2005, **128**, 210.
186. W. Credo Chung, Z. Lan, Y. Ohtsuki, N. Shimakura, W. Domcke and Y. Fujimura, *Phys. Chem. Chem. Phys.*, 2007, **9**, 2075.
187. S. Perun, A. L. Sobolewski and W. Domcke, *Chem. Phys.*, 2005, **313**, 107.
188. S. Ullrich, T. Schultz, M. Z. Zgierski and A. Stolow, *J. Am. Chem. Soc.*, 2004, **126**, 2262.
189. K. L. Wells, D. J. Hadden, M. G. D. Nix and V. G. Stavros, *Journal of Physical Chemistry Letters*, 2010, **1**, 993.
190. K. L. Wells, G. M. Roberts and V. G. Stavros, *Chem. Phys. Lett.*, 2007, **446**, 20.
191. M. G. D. Nix, A. L. Devine, B. Cronin and M. N. R. Ashfold, *J. Chem. Phys.*, 2007, **126**, 124312.

192. C. Z. Bisgaard, H. Satzger, S. Ullrich and A. Stolow, *ChemPhysChem*, 2009, **10**, 101.
193. M. Barbatti, J. J. Szymczak, A. J. A. Aquino, D. Nachtigallova and H. Lischka, *J. Chem. Phys.*, 2011, **134**, 014304.
194. H. Chen and S. Li, *J. Chem. Phys.*, 2006, **124**, 154315.
195. B. Heggen, Z. Lan and W. Thiel, *Phys. Chem. Chem. Phys.*, 2012, **14**, 8137.
196. C. M. Marian, *J. Phys. Chem. A*, 2007, **111**, 1545.
197. Z. Lan, E. Fabiano and W. Thiel, *ChemPhysChem*, 2009, **10**, 1225.
198. M. Smits, C. A. de Lange, S. Ullrich, T. Schultz, M. Schmitt, J. G. Underwood, J. P. Shaffer, D. M. Rayner and A. Stolow, *Rev. Sci. Instrum.*, 2003, **74**, 4812.
199. K. Kosma, C. Schröter, E. Samoylova, I. V. Hertel and T. Schultz, *J. Am. Chem. Soc.*, 2009, **131**, 16939.
200. J. Gonzalez-Vazquez, L. Gonzalez, E. Samoylova and T. Schultz, *Phys. Chem. Chem. Phys.*, 2009, **11**, 3927.
201. K. A. Kistler and S. Matsika, *J. Chem. Phys.*, 2008, **128**.
202. V. B. Delchev, *Monatsh. Chem.*, 2011, **142**, 251.
203. D. Picconi, V. Barone, A. Lami, F. Santoro and R. Improta, *ChemPhysChem*, 2011, **12**, 1957.
204. J. J. Szymczak, M. Barbatti, J. T. S. Hoo, J. A. Adkins, T. L. Windus, D. Nachtigallova and H. Lischka, *J. Phys. Chem. A*, 2009, **113**, 12686.
205. S. Yamazaki and T. Taketsugu, *J. Phys. Chem. A*, 2012, **116**, 491.
206. G. Zechmann and M. Barbatti, *J. Phys. Chem. A*, 2008, **112**, 8273.
207. J. Richard Behrens, *Rev. Sci. Instrum.*, 1987, **58**, 451.
208. P. M. Hare, C. E. Crespo-Hernández and B. Kohler, *Proc. Natl. Acad. Sci. USA*, 2007, **104**, 435.
209. J.-M. L. Pecourt, J. Peon and B. Kohler, *J. Am. Chem. Soc.*, 2000, **122**, 9348.
210. J.-M. L. Pecourt, J. Peon and B. Kohler, *J. Am. Chem. Soc.*, 2001, **123**, 10370.
211. M. C. Stuhldreier and F. Temps, *Faraday Discuss.*, 2013.
212. T. Gustavsson, A. Sharonov, D. Onidas and D. Markovitsi, *Chem. Phys. Lett.*, 2002, **356**, 49.
213. J. Peon and A. H. Zewail, *Chem. Phys. Lett.*, 2001, **348**, 255.
214. C. Su, C. T. Middleton and B. Kohler, *J. Phys. Chem. B*, 2012, **116**, 10266.
215. J. Eisinger, M. Guéron, R. G. Shulman and T. Yamane, *Proc. Natl. Acad. Sci. USA*, 1966, **55**, 1015.
216. T. Takaya, C. Su, K. de La Harpe, C. E. Crespo-Hernández and B. Kohler, *Proc. Natl. Acad. Sci. USA*, 2008, **105**, 10285.
217. C. E. Crespo-Hernandez, B. Cohen and B. Kohler, *Nature*, 2005, **436**, 1141.
218. K. de La Harpe and B. Kohler, *J. Phys. Chem. Lett.*, 2011, **2**, 133.
219. B. Bouvier, J.-P. Dognon, R. Lavery, D. Markovitsi, P. Millié, D. Onidas and K. Zakrzewska, *J. Phys. Chem. B*, 2003, **107**, 13512.
220. I. Buchvarov, Q. Wang, M. Raytchev, A. Trifonov and T. Fiebig, *Proc. Natl. Acad. Sci. USA*, 2007, **104**, 4794.
221. E. Emanuele, K. Zakrzewska, D. Markovitsi, R. Lavery and P. Millié, *J. Phys. Chem. B*, 2005, **109**, 16109.
222. U. Kadhane, A. I. S. Holm, S. V. Hoffmann and S. B. Nielsen, *Phys. Rev. E*, 2008, **77**, 021901.
223. N. J. Kim, J. Chang, H. M. Kim, H. Kang, T. K. Ahn, J. Heo and S. K. Kim, *ChemPhysChem*, 2011, **12**, 1935.
224. E. Samoylova, H. Lippert, S. Ullrich, I. V. Hertel, W. Radloff and T. Schultz, *J. Am. Chem. Soc.*, 2005, **127**, 1782.
225. E. Samoylova, T. Schultz, I. V. Hertel and W. Radloff, *Chem. Phys.*, 2008, **347**, 376.

2 Experimental

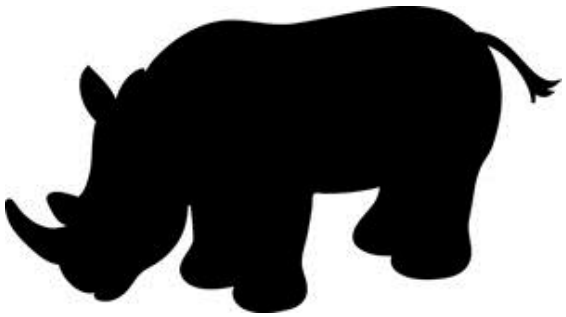

2.1 Introduction

The work described in this thesis is the result of two separate experiments, carried out in Warwick and in Durham. Despite their differences, the two experiments share a number of similarities: they both perform gas phase ultrafast time resolved spectroscopy using the same model of laser system, and they both use velocity map imaging (VMI) as the detection scheme. The fundamentals of the two spectroscopic techniques, time resolved photofragment and photoelectron spectroscopies, were reviewed in Chapter 1. What follows are the experimental details; firstly those which are general to both experiments (velocity map imaging and the femtosecond laser system), and then the specifics of each experiment in turn. As both these instruments were designed and operational before the start of this doctorate, this chapter serves only as an overview of their operation. For a more comprehensive treatment of each experiment design, the reader is directed to the theses of Dr Kym Wells (Warwick)[1] and Dr Gareth Roberts (Durham).[2] Following the discussion of the experimental aspect, the data fitting procedure employed is described.

2.2 Velocity Map Imaging

2.2.1 Time-of-Flight Mass Spectrometry

Before we discuss VMI, it is worth exploring time-of-flight (TOF) mass spectrometry, which is a technique employed in both laboratories. In Warwick, TOF is used as a diagnostic tool to measure constituents of the molecular beam, and also identify generated photofragments, whilst in Durham TOF is used to mass select ions prior to interaction with the laser. Conceptually, TOF mass spectrometry is an extremely intuitive means of mass separation.[3, 4] We shall first consider an idealized system, before expanding to realistic TOF setups. All the ions to be analysed are initially located in the same plane, then at a precise time, t_0, all ions are given an equal amount of kinetic energy, E, perpendicular to their plane. The ions are allowed to fly some distance, D, in a field free region, before impacting a time sensitive detector. This setup is shown in Fig. 2.1(a). The time of flight of an ion of mass m is then simply given by:

$$TOF = D \Big/ \left(\frac{2E}{m} \right)^{1/2} \tag{2.1}$$

Practically, this is implemented by pulsing an electric field, V, (from a metal grid) across the ions, imparting energy, $E = Vz$, where z is the charge on the ion. Such a scheme is simple; however it assumes that all ions have an equal position and initial kinetic energy. In reality, there will be a spread in these properties, so the mass

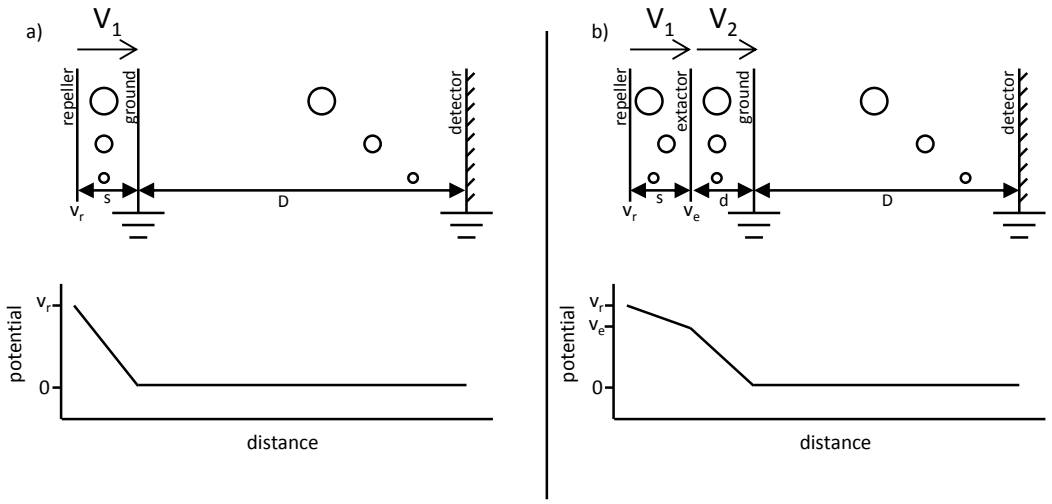

Figure 2.1 Schematic for a TOF mass spectrometer with a) only one acceleration region, and b) two acceleration regions as in a Wiley-McLaren setup. Above: schematic of the ion optics as well as representative particles positions for three different masses of ion. Below: the electric potential as a function of distance.

resolution of such a system is limited. In 1955, Wiley and McLaren demonstrated that this spread can be compensated for by using two acceleration regions, rather than one, in a setup shown in Fig. 2.1(b).[5] The first region is responsible for compensating for differences in position and energy, so the second field can focus them independently of these factors. The focusing mechanism of this first field is intuitive; ions which are further back will spend more time in this region, and so be accelerated more than those near the front. The ratio of voltages on the two plates (named the repeller and extractor) is selected such that the *TOF* is independent of the initial position of the ion. For a given distance, *D*, from the secondary plate to the detector, the focusing condition is:[5]

$$D = 2sk^{3/2}\left(1 - \frac{d}{s\left(k + k^{1/2}\right)}\right)$$
$$k = \frac{sV_1 + dV_2}{sV_1} \tag{2.2}$$

where V_1 and V_2 gives the electric field across the two regions, and s and d give their lengths (see Fig. 2.1(b)). The focusing is independent of mass, and so the complete mass spectrum can be recorded in one shot by recording ion signal as a function of flight time.

2.2.2 Velocity Map Imaging

In both experiments, the energy and angular distribution of the charged particles of interest (protons or electrons) is measured using VMI.[6] VMI as a technique has

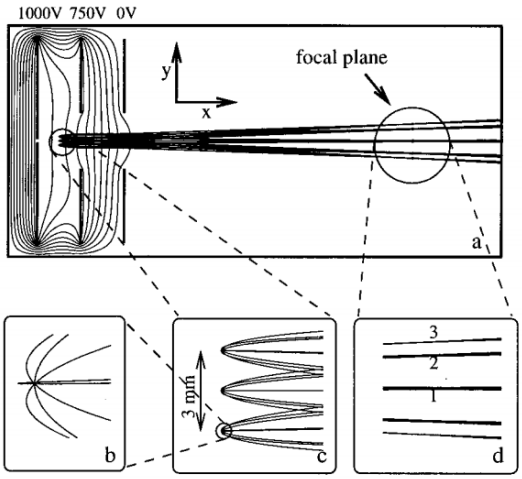

Figure 2.2 Ion trajectory simulation demonstrating velocity mapping. The electrostatic lens shown in (a) results in conditions whereby particles with different initial positions (c) are mapped to a final position dependant only on their velocity (d). The particles all have equal speeds, but are ejected at varying angles. Reproduced with permission from ref. 11.

revolutionized the field of gas phase spectroscopy, and is currently extensively used.[6-9] The essential goal of VMI is to project the velocity of charged particles into position space. When a molecular dissociation or electron detachment event occurs, the departing particles will have a spherical distribution of velocities, known as a *Newton sphere*, which we intend to image. We shall consider isotropic distributions initially; the concept of angular distributions is introduced in the following section. In a Wiley-McLaren TOF mass spectrometer, Eq. (2.2) showed how stationary particles may be projected onto a distant plane. We can then imagine that if the particles have some initial velocity, U_0, this will translate to a displacement on the detector, proportional to U_0. This precise setup was first attempted in the 1980s by Houston and Chandler; however resolution was severely limited because the initial position of the particle is also translated onto the detector, which meant the size of the initial interaction region (several mm) controlled the final resolution, and the presence of grids in the ions path resulted in distortions, as well as limited ion transmission.[10]

In 1997 Eppink and Parker realized that if the grids in a Wiley-McLaren arrangement are removed, and a simple plate with a hole used instead, then an electrostatic lens is generated which has the remarkable property of mapping velocity onto the detector, independent of the initial position.[11, 12] Thus, by removing the grids, both major sources of poor resolution in charged particle imaging were removed. Fig. 2.2 is a reproduction of the ion simulation from the original paper,[11] clearly demonstrating the capability for velocity mapping independent of initial ion/electron position.

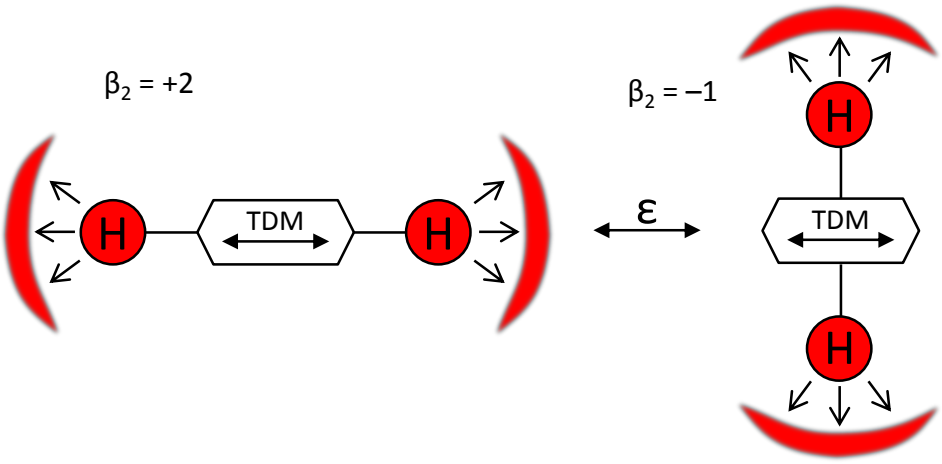

Figure 2.3 Simple example demonstrating the origins of angular distributions in VMI. If the transition dipole moment which leads to dissociation is aligned parallel with the electric field, ϵ, of the laser, departing fragments will be parallel to ϵ in the lab frame. If the transition dipole moment is perpendicular, we will then see perpendicular fragments in the lab frame.

2.2.3 Angular Distributions

A major advantage of VMI over other charged particle energy resolving techniques (*e.g.* TOF), is the ability to measure angular distributions in the dissociation/detachment event, *i.e.* the direction particles leave relative to electric field vector of the dissociation laser.[6] This process is more intuitive for H dissociation than electrons, as H atoms behave relatively classically under photolysis. Fig. 2.3 illustrates a simple example, where H atoms may depart from a molecule either parallel, or perpendicular to the transition dipole moment leading to their dissociation. The result is that, when projected onto a detector parallel to the laser polarization, the relative dissociation vector is revealed. Recalling Eq. (1.7), the transition probability for excitation is given by an overlap integral which includes product of the transition dipole moment and the electric field polarization, $\vec{\mu}\cdot\vec{E}$. This dot-product results in a cosine distribution around the angle between these two vectors, which is squared to give a $\cos^2$ distribution of initially excited molecules. The $\cos^2$ distribution is then mapped into the Newton sphere when dissocation occurs. The Newton sphere created in these events possesses cylindrical symmetry, as electric field vector is time-averaged zero (equal intensities in opposing directions).

Quantitatively, the angular distribution, $I(\theta)$, can be described using spherical harmonic functions:[6]

$$I(\theta)=\frac{\sigma}{4\pi}\left[1+\sum_n \beta_n P_n(\cos\theta)\right] \tag{2.3}$$

where P_n is the n^{th} order Legendre polynomial, and β_n is a coefficient known as the *anisotropy parameter*.[6] In general (excluding strong orientation effects), $I(\theta)$ can be

described completely by even values of n up to twice the total number of photons involved in the dissociation. The first term in the sum, corresponding to $\beta_0 P_0(\cos\theta)$ has been taken out of the summation and describes the total cross section, σ. In our pump-probe experiments then only β_2 and β_4 need be considered, however in none of the experiments in this work was a significant non-zero β_4 parameter recorded. Hence, the angular distribution can be modelled as (expanding the Legendre polynomial to the second order):

$$I(\theta) = \frac{\sigma}{4\pi}\left[1 + \beta_2 \frac{1}{2}(3cos^2\theta - 1)\right] \tag{2.4}$$

The β_2 parameter may vary from –1 to +2, where –1 represents a transition in which the transition dipole moment is completely perpendicular to the electric field polarization, +2 is completely parallel, and 0 is a perfectly isotropic distribution.

In a photoelectron imaging experiment, angular distributions are less intuitive, as we must consider the wave-nature of electrons. For very small systems, angular distributions can be modelled by considering the interference between outgoing electrons of varying angular momentums,[13] however for larger systems such as those explored in this work, a quantitative description is not possible and instead we can only make qualitative statements about changes in the distribution. This is still a highly useful technique, as it allows some indication of which orbital detachment occurs from.[13, 14] Finally, in polyanionic systems, such as indigo carmine, (see Chapter 4) the potential from multiple interacting charges can lead to enforced anisotropy – electrons may only leave through the lowest part of the Coulombic barrier, resulting in strongly anisotropic distribution.[15-19]

2.2.4 Deconvolution

Previous discussion only considered the properties of the full three-dimensional Newton sphere. The detectors used in VMI are two-dimensional, but the full sphere is projected onto it; hence, it is necessary to reconstruct the original 3D sphere from the 'pancaked' 2D data. As the sphere possesses cylindrical symmetry, it can be described using only two coordinates, and so there is no loss of information. Note that for reconstruction to be performed, the plane of laser polarization must be parallel to the detector, so that the axis of cylindrical symmetry is along the vector of electric field polarization. The reconstruction can be achieved physically by slice imaging, a technique where pulsed detectors are used so that only a central slice of the sphere is recorded, and the rest is discarded.[20-22] More commonly, a deconvolution algorithm is used to perform the reconstruction on the 2D data as this does not require specialist

ion optics and fast pulsers. Many deconvolution algorithms are in use,[6, 23-28] however all the reconstructions in this thesis were performed using the Polar Onion Peeling (POP) algorithm,[29] developed in Durham.

POP is attractive as it is a fast, but also very intuitive algorithm. Full details can be found in the original publication for it;[29] only a brief introduction is presented here. Firstly, the 2D Cartesian image data are converted into polar coordinates. Then, beginning at the outer most radius, r, the data at that r are fit to Eq. (2.3), to return the intensity, σ, and anisotropy parameters, β_2 and β_4. For this r, the full sphere as it appears on a 2D detector is then reconstructed (using a precomputed lookup table to reduce computation time), and the reconstructed sphere is subtracted from every smaller radius. This process is repeated for each decreasing r, at each step reconstructing and removing the outer most layer, hence the name *onion peeling*. The algorithm returns the intensity and β parameters of each r, in velocity space. Transformation into energy space requires the intensity to be plotted against r^2 (with a calibration factor, see below), and the intensity must be divided through by the Jacobian r, to account for the change in coordinate space.

In practical terms, the original POP algorithm was developed using LabVIEW. Recently, in collaboration with Dr Adi Natan (Stanford), POP has been ported to Matlab. The Matlab verison offers the advantage of faster computation, and supports arbitrary (even) β parameters. The LabVIEW POP code was used for all works presented, except for Chapter 5, which used the Matlab version.

2.3 Femtosecond Laser System

Both experiments use the same model of laser, and employ the same frequency conversion techniques, so these shall be briefly described here. Femtosecond pulses are generated from a *Tsunami* series passively mode-locked Ti:Sapphire oscillator (Spectra-Physics), which is pumped by a 5 W continuous wave frequency-doubled Nd:YAG laser (Spectra-Physics, *Millenia*). The oscillator produces a train of < 100 fs pulses, with ~6.6 nJ energy each at a repetition rate of 76 MHz. The oscillator wavelength is centred at 800 nm, and it has a bandwidth of 35 – 50 nm (full width half max, dependant on precise tuning).

The output from the oscillator is amplified using a Ti:Sapphire regenerative amplifier (Spectra-Physics, *Spitfire XP*). The amplifier picks out pulses from the oscillator input at a 1 KHz repetition rate. These pulses are stretched in time using a diffraction grating, amplified in a Ti:Sapphire cavity (pumped by a pulsed 25 W Nd:YLF laser (Spectra-Physics, *Empower*)), then switched out by a Pockels cell and

recompressed by a second grating. The amplifier outputs a fundamental beam centred at 800 nm, with 3 mJ pulse energy and 35 fs pulse duration.

The precise laser arrangement differs throughout the experiments performed; however, the same basic scheme is used. The fundamental is split into two separate beams, one of which is directed onto a motorized delay line (Physik Intrumente), which creates a temporal delay between the pump and probe pulses. The maximum time delay we can observe (barring multipass setups) is dictated by the length of this stage which is 20 cm (Warwick) or 15 cm (Durham), giving maximum time delays of ~1.3 ns (Warwick) or ~1 ns (Durham). Frequency conversion is then performed on the two beams, and they are recombined in the VMI arrangement.

2.3.1 Frequency Conversion

The photon energy of the fundamental beam (1.55 eV, 800 nm) is generally too low for use in experiments, so frequency conversion must be performed on the two laser pulses before they are used for spectroscopy. This is achieved using non-linear processes, from a combination of beta barium oxide (BBO) crystals, or an optical parametric amplifier (OPA). When high intensity light impacts the BBO crystals (which are non-centrosymmetric materials), 2nd order non-linear effects are observed which can result in the combination of two input photons to yield a single photon with a frequency equal to the sum of the input frequencies.[30, 31] If the two photons are of the same frequency, this is known as *second harmonic generation* (SHG), whilst if they differ it is *sum frequency generation* (SFG). The process a BBO performs is dependent on the orientation of the crystal relative to the laser. A combination of SHG and SFG processes can readily create pulses with wavelengths centred at 400 nm, 266 nm or 200 nm, hence the prolificacy of these wavelengths in this work and others.

A more tunable source of frequency conversion comes from the TOPAS-C OPAs (Light Conversion). The OPA also uses BBO crystals, but this time rather than summing two photons to give one, an input photon is divided into two output photons, with frequencies such that energy is conserved. This is known as *parametric generation*, as the output frequencies can be altered parametrically.[31, 32] In the OPA, a white light continuum is created via non-linear processes from focussing a small portion of the fundamental into a sapphire plate, and this broadband light acts as a seed for the parametric amplification process. The remaining fundamental then amplifies this output in another BBO, to give two tunable output beams (perpendicularly polarized) in the near IR (1150 – 2600 nm). Changing the angle of the BBOs allows the output wavelength to be tuned, and subsequent SHG or SFG (with the fundamental) allows for

effectively continuous output from ~240 nm to 2600 nm. The energy per pulse decreases steeply with wavelength; typical values are 4 μJ at 240 nm, up to 70 μJ at 540 nm.

2.4 Time-Resolved Hydrogen Imaging in Warwick

2.4.1 Molecular Beams

For the experiment in Warwick (and most other spectroscopic techniques on neutrals), a source of isolated, cold molecules is essential. The molecules must be in a high vacuum environment, as background gas will severely interfere with the measurements, and working on cold molecules simplifies the spectroscopy significantly as only the lowest rotational and vibrational levels can be populated. Both conditions are readily obtained by means of supersonic expansion into a vacuum.[33, 34] The general technique is to seed the molecule of interest into a high pressure source of an inert gas, and expand this into a vacuum. Initially, there will be a very high frequency of collisions with the seed gas, which collisionally cools the molecules by converting energy from the vibrational and rotational into translational degrees of freedom. After cooling, if the resultant beam of molecules is rapid enough to exceed the speed of sound, then no more collisions will take place and the result is a cold molecular beam. The beam is coldest in the centre, so a skimmer (a cone shaped orifice) is used to select only this part and to remove the hotter outer beam.[34] The skimmer also makes for a convenient pinhole for differential pumping. The properties of the molecular beam can be altered by changing the seed gas: a heavier gas will result in more energy being carried away in collisions, so cooling will be more efficient, increasing the rate of cluster formation. The terminal velocity, v_0, of the molecular beam is also related to the mass, m, of the backing gas by:[33, 35]

$$\begin{aligned} v_0 &= \sqrt{\frac{2k_BT}{m}\frac{\gamma}{\gamma-1}} \\ &= \sqrt{\frac{5k_BT}{m}} \text{ (for a monatomic ideal gas)} \end{aligned} \tag{2.5}$$

where k_B is the Boltzmann constant, T is the temperature of the gas before expansion and γ is the heat capacity ratio, which corresponds to $5/3$ for an ideal monatomic gas.

In practice, a continuous beam is not used, and instead a pulsed valve is operated to deploy short bursts of gas in pulses. Typically, the valve is opened for < 20 μs, at a frequency of around 10 to 1000 Hz. This has the advantage that a much smaller amount of gas enters the vacuum system, so the chamber pressure will be lower for a given

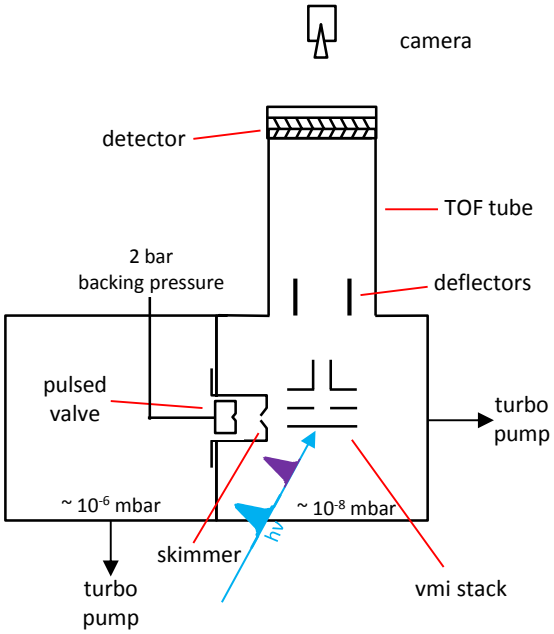

Figure 2.4 Schematic of the instrument used in the Warwick experiments. Two chambers, separated by a skimmer are used. The pulsed valve is mounted in the source region, and fires a molecular beam into the interaction region, where photolysis and VMI is performed.

vacuum pump. In the Warwick instrument, the molecular beam source is an Even-Lavie solenoid pulsed valve,[36] backed by helium at a pressure of 2 bar and pulsed open for ~13 μs at a frequency of 125 Hz. The sample is introduced from a heated cartridge in the valve assembly, filled with the sample in either solid or liquid form. The choice of helium as a backing gas is an attempt to minimize cluster formation; using a heavier gas would result in more energy being carried away in collisions, so cooling would be more efficient and the rate of Van der Waal's cluster formation increases.[34] By Eq. (2.5), the terminal velocity of our beam is ~1800 ms^{-1} for a valve temperature of 50 °C. We cannot directly probe the temperature of our beam, however the Even-Lavie valve has been shown to be capable of producing rotational temperatures < 1 K,[36] albeit in a setup optimized for maximum cooling, with very high backing pressure, as opposed to our setup which is for maximum signal and uses a lower backing pressure.

2.4.2 Instrument Overview

The Warwick experiment is time resolved H atom imaging.[1, 37] As reviewed in Chapter 1, the basis of the experiment is that a pump pulse induces H atom dissociation in a molecule, and then the probe pulse ionizes this atom using [2 + 1] REMPI prior to energy resolved detection by VMI. The instrument, diagrammed in Fig. 2.4, consists of two differentially pumped regions. The first, the source region, houses an Even-Lavie pulsed valve as the molecular beam source.[36] The valve pulses at 125 Hz, and is synchronized to the laser, such that the laser will intersect the molecular beam pulse in

the interaction region. The timing for this is controlled by a digital delay generator (Stanford, *DG-535*). The valve is mounted 25 mm away from a skimmer, which forms the orifice into the interaction region. The valve and skimmer are mounted to an insertion can to provide the minimum distance to the interaction region, increasing sample density. The interaction region consists of a VMI stack, oriented orthogonal to both the molecular beam and laser, directing ions upwards. The VMI setup is exactly as described by Eppink and Parker[11] (electrodes 15 mm apart with 20 mm openings), and is operated with potentials of 5.00 and 3.57 kV on the repeller and extractor, respectively. A small grounded metal tube extends off the ground plate, to increase the homogeneity of the field outside the VMI stack. A thin (2 mm) calcium fluoride window allows access by the laser to the interaction region, and a second window allows for subsequent alignment through the back.

Mounted above the VMI stack is a TOF tube (0.27 m long), with the detector at its terminus. The detector consists of two multichannel plates (MCPs) in a v-stack arrangement, with a phosphor screen behind the second MCP. Events are recorded by a CCD camera (Basler, *A312f*) mounted above the screen. During H^+ imaging experiments, a potential of 800 V across each MCP is typical, with 5 kV on the phosphor screen; lower MCP voltages are employed for parent ion imaging experiments. The detector diameter is 40 mm, and the camera resolution is 512×512 pixels, so each pixel corresponds to ~80 μm in real space.

An output from the front face of the phosphor screen has been added, which allows a signal to be displayed on an oscilloscope to record TOF spectra of all fragments produced by laser interaction. The back MCP is kept at a low voltage, and then pulsed to operational voltage for a short time, so that we can ignore all impacts of ions heavier than hydrogen. Unfortunately, even if the detector is not at full potential, a large number of ion impacts can still desensitize it, causing 'burns'. In the case of H^+ imaging experiments, far more cations from photoionized parent molecules are created than protons, and so to avoid the parent cations damaging the detector a pair of deflector plates are used. The deflectors are situated at the entrance to the TOF tube, and one plate is pulsed to 400 V after protons have passed, to deflect all heavier ions into the walls of the vacuum chamber. In cases where the parent ion yield is to be monitored, the relative timing of the laser and gas pulses was detuned so to reduce the number of ions created and thus avoid burns on the channel plates.

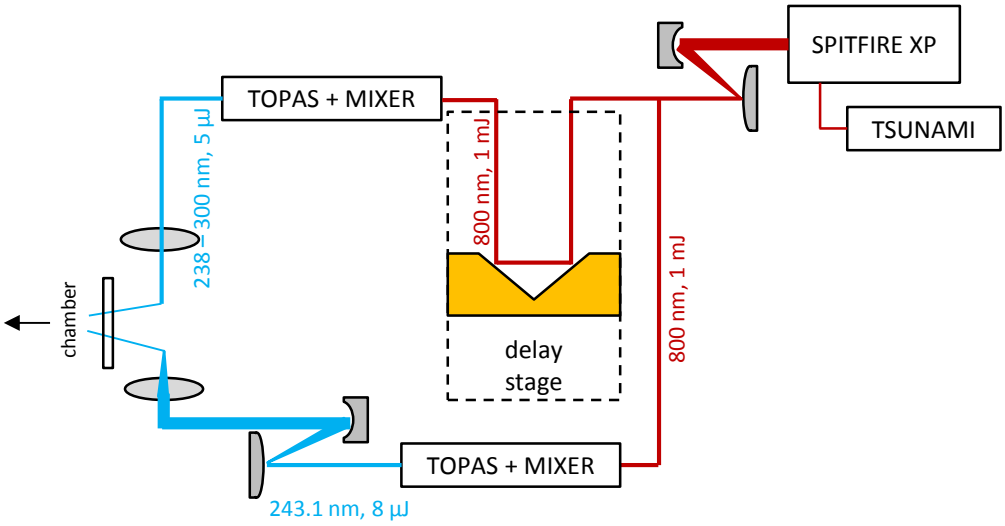

Figure 2.5 Simplified schematic of the laser setup for the Warwick experiment. A motorized translation stage generates the delay between the pump and probe pulses, which are generated using two OPAs. Pump and probe pulses are focused and combined non-collinearly in the chamber.

2.4.3 Laser Setup

The optical setup for the Warwick experiment (Fig. 2.5) consists of a tuneable UV pump pulse, and a probe pulse fixed at 243.1 nm. The 800 nm fundamental from the amplifier is reduced in size with a telescope, and then divided equally into three beams by beamsplitters (1 mJ pulse^{-1} each, one of the beams is not used for these experiments). The first beam, the pump beam, is directed onto a gold retro-reflector mounted on the delay stage to create the temporal delay between pump and probe, and then converted using a TOPAS-C OPA. The OPA is fitted with two motorized mixing stages after its output, each containing a BBO crystal. IR output from the OPA is mixed in these two crystals (using either SHG or SFG with the fundamental), to create UV light which is tuneable from 238 nm to >300 nm. Alternatively, three BBO crystals may be used to generate a 200 nm pump, using a combination of SHG and SFG.

The second beam, the probe beam, is directed into a second TOPAS-C unit, which is also fitted with two mixing stages. This OPA outputs 1239.5 nm light, which is mixed with the fundamental in the first crystal to give 486.2 nm, then doubled in the second crystal to give the 243.1 nm probe, which is two-photon resonant with the 2s ← 1s transition in atomic hydrogen. Both the pump and probe beams are tightly focused with convex lenses (f = 500 mm), then overlapped non-collinearly in the chamber using a half mirror as the final optic for the pump beam.

As the probe step is strongly non-linear (a 3-photon process), the greatest possible photon flux density (intensity) of the probe is required. The intensity at the focus is

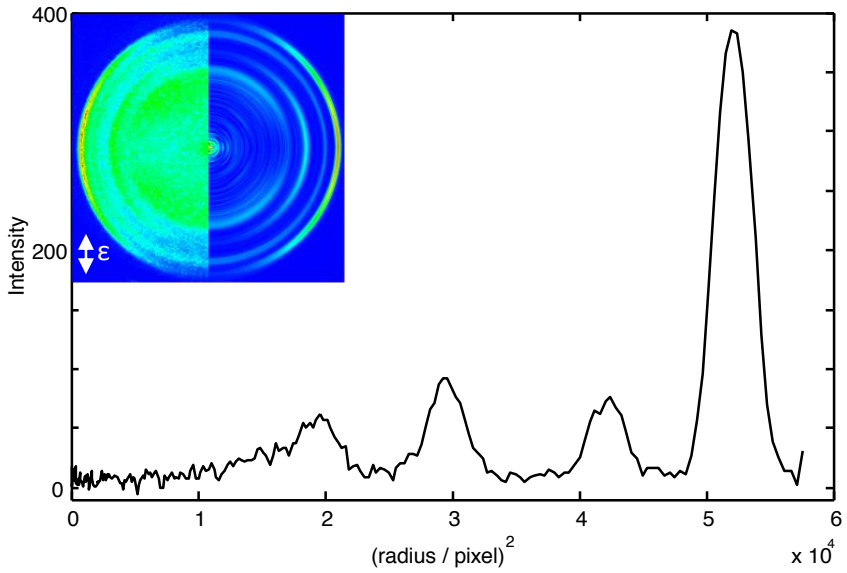

Figure 2.6 An example of the image (left, convoluted; right, deconvoluted central slice) and resultant spectrum for H atom imaging of HBr with a 200 nm (6.2 eV) dissociation laser, and a 243.1 nm (5.101 eV) probe laser, separated by 1 ps. The two peaks at large radius are the fragmententation leading to the two spin orbit states ($^2P_{3/2}$ and $^2P_{1/2}$), induced by the 200 nm laser, whilst the two peaks at shorter wavelength come from the 243.1 nm probe laser alone. The splitting between peaks allows the energy scale to be calibrated.

dependent on the pulse duration, the pulse energy, and the beam diameter at the focus, D_f, which, for a Gaussian beam, is given by:[31]

$$D_f = \frac{4\lambda F}{\pi D_0} \tag{2.6}$$

where λ is the wavelength, F is the focal length of the focussing optic, and D_0 is the initial beam diameter. A convex-concave matched pair of mirrors is used to expand the probe beam to ~15 mm diameter before focussing; Eq. (2.6) shows that this results in a tighter beam waist and so a higher photon flux. Typical pulse energies are 4 μJ and 8 μJ for the pump and probe beams respectively, giving photon fluxes on the order of 10^{12} and 10^{13} W cm^{-2}, respectively.

As discussed in Chapter 1, it is essential to distinguish between protons born from a dissociative ionization process, and those ionized from neutrals by the probe pulse. To perform this check, the probe wavelength is shifted away from 243.1 nm so that they will no longer be resonant with the 2s ← 1s transition, and an image is recorded. In all the molecules studued in this thesis, the peaks at high kinetic energy disappeared when this test was performed, indicating that we are observing neutral hydrogen atoms.

The cross correlation between the pump and probe beams (which gives the instrument response function) is found through non-resonant two photon ionization of

methanol. Methanol is used because it is facile to introduce to the pulsed valve, and because it exhibits no absorption at wavelengths ≥ 200 nm,[38] so the process is always off-resonance. It is important that measurements are taken off resonance to avoid influence of dynamics on the peak shape and centre.[39] The cross correlation is extracted by recording the yield of $MeOH^+$ as a function of *t*, and fitting this response to a Gaussian function to obtain the precise width and centre (t_0). Typically, the cross correlation was ~120 fs full width at half maximum (FWHM).

2.4.4 Calibration

Calibration of the VMI arrangement is performed using photodissociation of HBr with a 200 nm photolysis beam. HBr is used because removal of an H atom can lead to either the $^2P_{3/2}$ or the $^2P_{1/2}$ state of the remaining bromine atom, both of which have a narrow (atomic) linewidth, and are split by a well-known energy (3685.24 cm^{-1}) through spin-orbit coupling.[40] Fig. 2.6 shows the image and resultant radial intensity spectrum with a 200 nm (6.2 eV) pump and 243.1 nm (5.1 eV) H atom REMPI probe, separated by a 1 ps delay. Four peaks are visible; the two at large radii are from photolysis with the 200 nm laser, whilst the two peaks at smaller radii are from photolysis and probing all within the duration of the 243.1 nm probe pulse. The presence of the two pairs of peaks means that calibration can be performed with both pairs, and the result averaged. To perform the calibration, a Gaussian function is fit to each peak (in radius^2 space), and the centre for each peak in a pair, r_1^2 and r_2^2 are extracted. The calibration factor, *k*, is simply the bromine spin orbit splitting, ΔE, divided by the difference in peak centres:

$$k = \frac{\Delta E}{\left(r_2^2 - r_1^2\right)} \tag{2.7}$$

A typical calibration factor for H imaging on the Warwick experiment is 0.3751 cm^{-1} $pixel^{-2}$. The instrument resolution can also be extracted directly from the peak widths in these calibration images, and a resolution of ~10 % (FWHM / peak energy) is extracted. The poor resolution is partly due to the bandwidth of the laser (~400 cm^{-1}) and partly due to fringe fields from the connectors to the VMI optics.

The mass of ions striking the detector can be evaluated using their TOF, which must also be calibrated. The calibration is performed in a similar manner to the VMI calibration, by using the difference between two known peaks, but this time in $(TOF)^2$ space (see Section 2.2.1). Typically, the species currently in the system is used, along with $TOF = 0$, however a two point calibration can also be performed if there are two

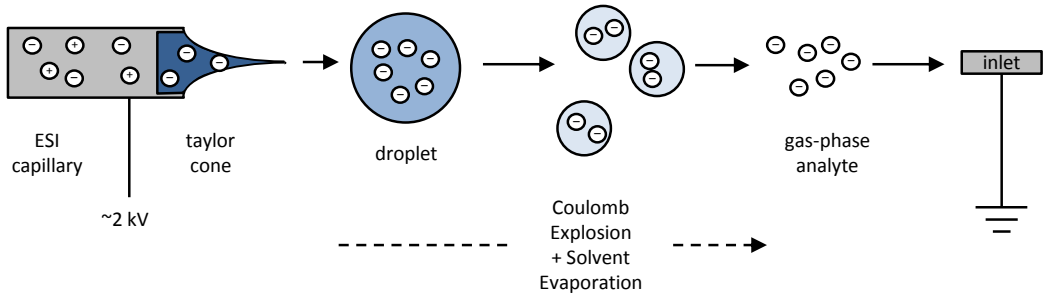

Figure 2.7 - Schematic of the electrospray process. A solution containing the ion of interest is injected through a small capillary, which is at a potential of several kV relative to the instrument inlet a short distance away. The high potential induces Coulomb explosion, repeatedly fragmenting charged droplets until isolated ions remain, which are transported into the vacuum system.

well-known species within the molecular beam (residual water often serves this task well).

2.5 Time-Resolved Photoelectron Imaging in Durham

2.5.1 Electrospray

The experiment in Durham performs photoelectron spectroscopy on gas phase anions, using electrospray ionization (ESI) as the ion source. The technique of electrospray has revolutionized mass spectrometry, as it allows virtually any solvated ion to be transported intact directly from solution to the gas phase.[4, 41-43] Anions (or cations) ranging in size from single atoms, to molecules, all the way through proteins and oligonucleotides can be electrosprayed. At the far end of the scale, entire viruses have been mass analyzed using ESI.[44]

A schematic of the ESI process is shown in Fig. 2.7. A solution containing the analyte of interest (generally 0.1 – 0.01 mM in our experiments) is pushed through a stainless steel capillary by a syringe pump (World Precision Instruments) at a flow rate of ~200 μL hour^{-1}. A large potential difference (–2 to –3kV) is held between the ESI capillary and machine inlet by a constant current power supply (Applied Kilovolts). This large electric field leads to the accumulation of ions at the end of the capillary in a *Taylor cone*,[43] which then breaks down to produce a fine aerosol of solution. The droplets of this aerosol undergo further fission from Coulomb explosion, with some solvent evaporating off at each stage, until bare ions remain. These ions are sampled by the inlet capillary (600 μm ID) into the first vacuum stage of the instrument.

2.5.2 Instrument Overview

The Durham instrument, shown schematically in Fig. 2.8(a) is composed of six differentially pumped vacuum regions, which shall now be briefly described in turn. For a more comprehensive treatment, details are available in refs. [2, 14, 45]

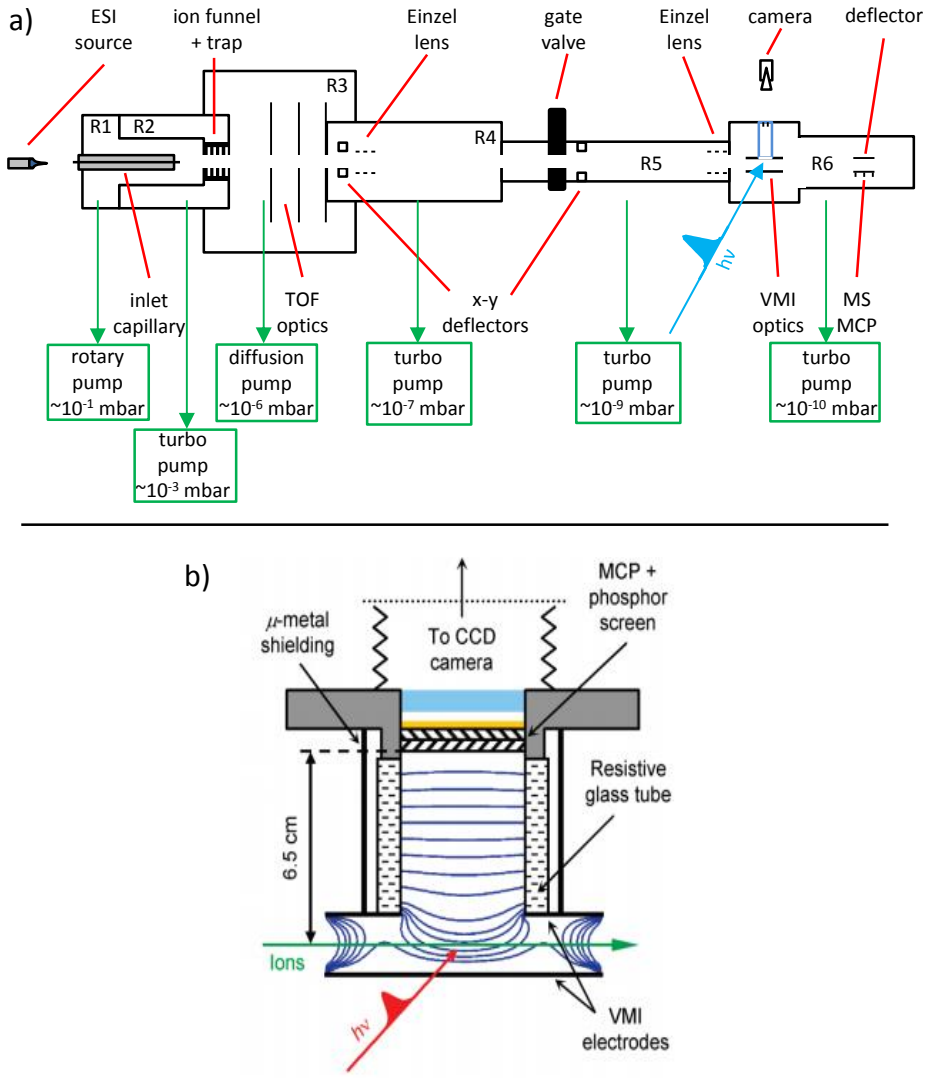

Figure 2.8 a) Simplified schematic of the anion photoelectron spectroscopy machine in Durham. b) Expanded view of the VMI optics in the instrument, along with the electric field lines. b) was reproduced with permission from ref. 45.

Anions enter the instrument through a biased transfer capillary (~ – 80 V) into region 1 (R1), which operates at a pressure of ~2 – 4 mbar. R1 leads to R2 via a 1 mm pinhole, biased at ~ –60 V. R2 holds a radial ion funnel/trap, where ions are accumulated. The funnel is composed of 33 ring electrodes, with a DC voltage gradient (from ~ –60 to –20 V) pulling ions towards the end. Radial confinement is achieved by superimposing a radio frequency field on the electrodes, (~1.5 MHz, 300 V peak-to-peak) with adjacent electrodes 180° out of phase. The final electrode is maintained at a higher potential, and serves to trap ions. At the experimental repetition rate (typically 50 – 500 Hz), the voltage on this last electrode is pulsed to a lower potential, emptying the trap into R3. The trap can hold a maximum of around 1000 ions.

R3 houses a set of on-axis Wiley-McLaren time-of-flight optics, formed from stainless steel rings with high transmission (88% optical transparency) steel mesh

glued over the central hole. The plates are separated by 30 mm, and are initially at ground, however are pulsed to voltages of –2.3 and –1.95 kV on the repeller and extractor respectively shortly after emptying of the trap. Ions are accelerated from the TOF through a pinhole into R4. The precise timing of the TOF pulsing is dependent on the mass of the species in question, as well as the chosen potentials for the trap; typical delays are 8 – 15 μs. All timings on the ion machine are performed by a digital delay generator (Highland Technology, *P400*), synchronised with the laser, such that the laser intersects the ions in the VMI stack.

R4 houses a set of steering optics in the form of flat *x*-*y* deflectors, which can have potentials up to ± 40 V to correct for any ion drift off away from the central axis due to stray fields or misalignments. Following the deflectors is an Einzel lens, which focuses ions spatially. The Einzel lens is composed of three open, tubular electrodes, with a 30 mm inner diameter. The outer two electrodes are 20 mm long, and kept at ground, whilst the inner electrode is 16 mm long, and is held at ~1.5 kV. This arrangement of ion optics results in fields with a shape reminiscent of a convex lens, and the overall effect is similar. Varying the voltage of the inner electrode allows the focal point to be adjusted.

R4 is separated from R5 via a pneumatically actuated gate valve, which allows the high vacuum end to be isolated from the low vacuum end of the machine. R5 is composed primarily of a TOF tube, which allows sufficient distance for mass separation of ions. The total TOF length is 1.3 m. Mounted at the entrance to R5 is another set of *x*-*y* deflectors, for final course correction, and at the other end is a second Einzel lens. This secondary lens allows the ions to be tightly focused into the interaction region to give the maximum ion density at the overlap with the laser beam.

R6 houses the VMI stack and ion detection apparatus. The VMI arrangement, shown in Fig. 2.8(b), is a novel setup with a resistive glass tube to provide a smooth field gradient towards the (grounded) front of the detector.[45] The ratio of electrode distance to opening size has been carefully chosen for the repeller and extractor, such that focussing conditions are obtained when they have identical voltages applied. There are two advantages to using an equal potential on these plates. Firstly, the deflection experienced by ions passing through the VMI stack is minimal, which allows continuous monitoring of ions signals whilst the imaging system is running. Secondly, the size of image produced, and therefore the resolution and maximum energy range, can be controlled simply by altering the potential fed to both plates. Increasing the voltage shrinks the image, whilst lowering it enlarges it, and focusing conditions are

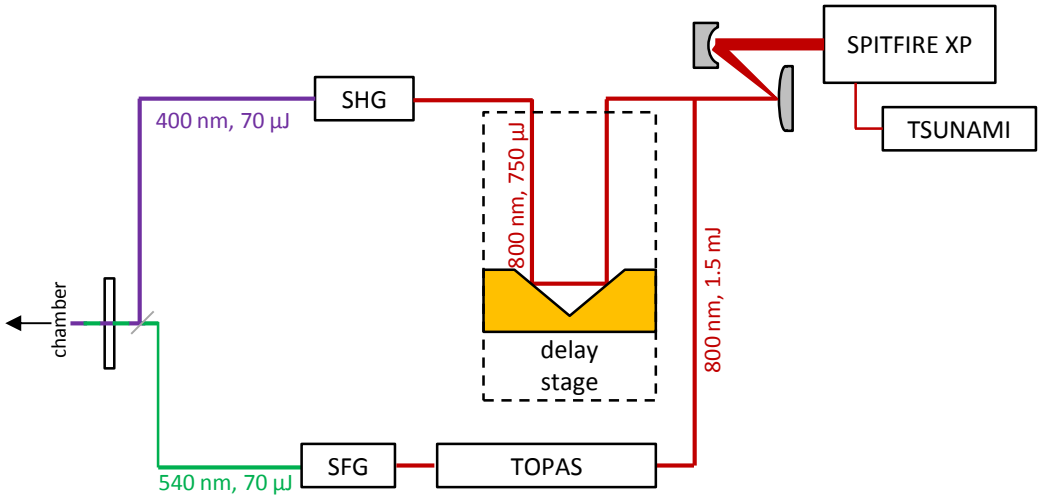

Figure 2.9 An example of a beamline used in the Durham experiment. In this instance the experiment is 540 nm pump (from the TOPAS) and 400 nm probe (from SHG). The 400 nm beamline has a variable length from the delay stage, allowing the temporal delay to be altered, and the beams are combined collinearly with a dichroic mirror before intersecting the ion packet in the instrument.

always met. For the indigo carmine work (Chapter 4), the VMI stack was operated at 500 V, while for DNA (Chapter 5) it ran at 750 V, to enhance collection efficiency at the expense of resolution. The electrodes for the VMI stack are made of mu-metal, which has very low magnetic permittivity, to reduce the effect of magnetic fields on the imaging. The detector and camera is exactly as with that in Warwick; however typical operating voltages were 0.725 kV across each MCP, and 4.5 kV on the phosphor screen. The detector was pulsed on for only 50 ns after the laser fires, to minimize dark counts.

Behind the VMI stack lies the ion detection MCP. This is mounted horizontally, underneath the ion beam, and so a high voltage (~ −1kV) deflector plate is mounted above to push ions onto the MCP. The output of the MCP is fed into an oscilloscope, synchronized to the pulsing of the TOF plates, so the mass spectrum of ions in the instrument may be recorded and the laser can be correctly timed to mass select the ion to experiment upon. This arrangement is designed so that instead ions may pass over the MCP into a reflectron, which turns them back around before being pulsed onto the MCP. The reflectron allows product ions to be measured, although it was not used in any of these experiments.[46]

2.5.3 Laser Setup

The laser arrangement in Durham is flexible, allowing for a variety of experiments to be performed. As a prototypical example, a simplified schematic of one optical arrangement used (in this case for indigo carmine, Chapter 4) is shown in Fig. 2.9. In this instance, the optics are set up to perform a 540 + 400 nm pump-probe experiment. The fundamental output of the amplifier is resized with a reflecting telescope, and then

split in two by a 50:50 beam splitter. Half the beam (1.5 mJ pulse^{-1}) is directed into a TOPAS-C OPA, to produce IR light, which is then mixed with residual fundamental in a BBO to produce 540 nm light (~70 μJ pulse^{-1}). The remaining half of the fundamental is reduced in intensity with another beamsplitter (to produce 750 μJ pulse^{-1}), and then directed onto a gold retro-reflector mounted on the motorized delay line. After the delay line, the frequency is doubled to 400 nm (~70 μJ pulse^{-1}) in a BBO crystal, then the two beams are combined collinearly by a dichroic mirror, and subsequently directed unfocused into the instrument through a thin calcium fluoride window.

For the experiments on DNA, a similar setup was employed; however an additional BBO crystal (with a waveplate for polarization correction) was used after the SHG process, to produce 266 nm light by SFG. Instead of using the OPA, the secondary beam was simply frequency doubled to 400 nm, for a 266 + 400 nm experiment. For the DNA experiments, the beam was loosely focused into the interaction region to enhance signal levels.

Unlike the Warwick instrument, measuring cross correlations of the pump and probe is non-trivial, as non-resonant two photon electron detachment from anions is usually vastly outcompeted by one photon detachment, especially if 4.66 eV (or more energetic) photons are used. Instead, the cross correlation can be measured using SFG in a BBO outside the chamber. It is important to note that, prior to SFG, we send both beams through a window of identical thickness to that in the entrance of the chamber, in order to create a similar amount of dispersion in both beams. Alternatively, cross correlations can be extracted from the fitting procedure, using the rising edge of signals. The cross correlation was generally ~120 fs.

2.5.4 Calibration

The VMI arrangement was calibrated using I^-, in a similar manner to hydrogen imaging calibration using HBr in Warwick. As iodide is an atomic ion, very sharp photoelectron peaks are produced from photodetachment. When 266 nm (4.66 eV) detachment radiation is used, two peaks are observed, corresponding to detachment to the $^2P_{3/2}$ and $^2P_{1/2}$ spin orbit states, separated by a well-known splitting of 0.9426 eV[40]. Fig. 2.10 shows a typical iodide calibration image. The splitting between the two peaks (in r^2 space) allows a calibration factor to be computed, in the exact same manner as for the HBr calibration, using Eq. (2.7). As varying VMI repeller and extractor voltages are used, a calibration must be performed for each potential to be employed. The resolution of the instrument is ~ 5%.

In principle, the ion TOF mass spectrometry may be calibrated to provide accurate masses, by measuring a series of flight times of ions of known mass. In practice, however, most voltages on the instrument slightly alter the TOF calibration, and as these are always optimized for maximum signal, the calibration varies on a day-to-day basis. Rather than a precise calibration factor then, approximate ion timings can be calculated using previous flight times (±1 μs), which is perfectly acceptable for uncongested mass spectra (*i.e.* those from a pure solution).

2.6 Data Fitting and Analysis

2.6.1 Fit Functions

Fitting of time resolved photoelectron and H^+ transients in Chapters 3 and 4 was all performed by integrating slices of the spectra and fitting these to appropriate functions. After a feature of interest is identified, a suitable spectral window is chosen, and the intensity of the feature, $I(t)$, is found by numerically integrating in this window as a function of pump-probe delay, t. In general, there are two processes that may be observed in $I(t)$. Firstly, in cases where a signal arises at t_0 (when pump and probe temporally overlap), which then drops to zero, an exponential decay function is used:

$$I(t) = G(t) * A\exp\left(-\frac{t-t_0}{\tau}\right) \tag{2.8}$$

where τ is the lifetime of the decay and A gives the intensity of this feature. $G(t)$ is the

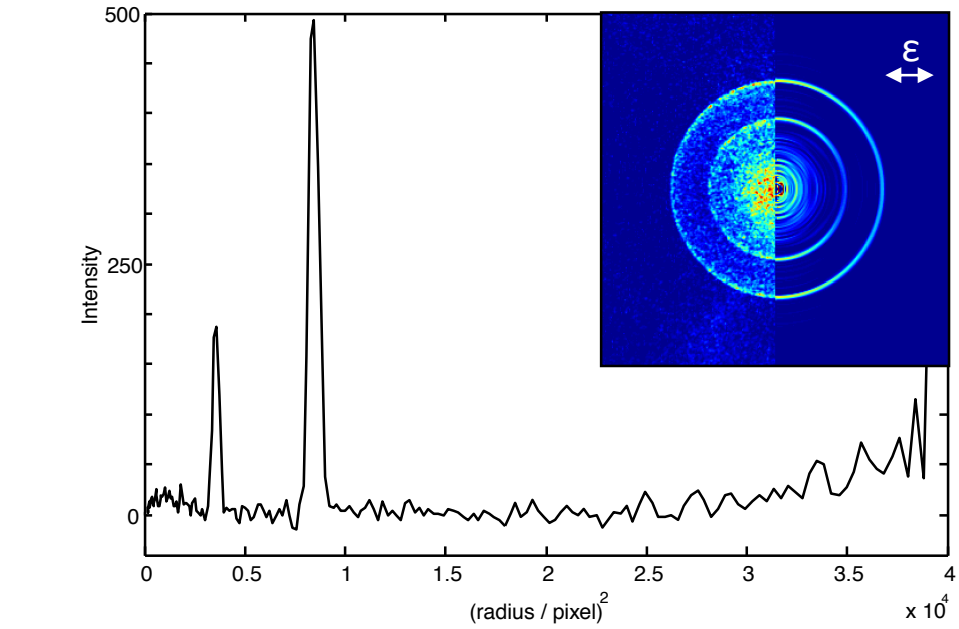

Figure 2.10 An example of the image (left, convoluted; right, deconvoluted central slice) and resultant spectrum for photodetachment from I^- with 4.66 eV photons. The spacing between the peaks allows the VMI setup to be calibrated.

instrument response function, discussed below. Exponential decays are usually the appropriate function for photoelectron signals, as well as ionic fragments produced from absorption-ionization-detachment processes (see Chapter 1). The parent ion spectra presented in Chapter 3 are fit with the exponential decay, as these are essentially photoelectron yields. On the other hand, in situations where a signal is produced which does not decay away, an exponential rise is more appropriate:

$$I(t) = G(t) * A\left[1 - \exp\left(-\frac{t - t_0}{\tau}\right)\right] \tag{2.9}$$

The exponential rise is typically used for signals arising from ionization of neutral hydrogen atoms. Note that often several processes will overlap within the same spectral window, so a combination of exponential rises and exponential decays may be appropriate to fit the entire transient.

In each case, the function was convoluted with $G(t)$, the instrument response function. $G(t)$ is simply a Gaussian function, centred at t_0:[47]

$$G(t) = A\exp\left(-\frac{(t - t_0)^2}{2\sigma^2}\right) \tag{2.10}$$

where the width is given by σ, related to the pump-probe cross correlation FHWM by:

$$\sigma = \frac{FWHM}{2\sqrt{2\ln 2}} \tag{2.11}$$

Fitting was then performed by the Levenberg-Marquardt algorithm (as implemented by the Origin software package) to minimize the squares of the difference between the data and fits from Eqs. (2.8) and (2.9).

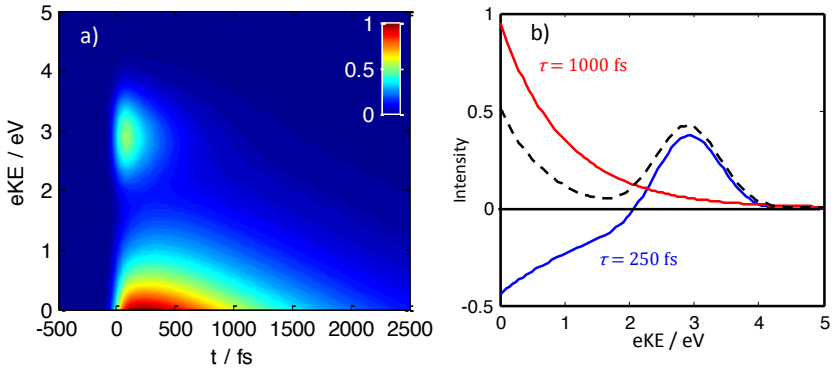

Figure 2.11 Simulated intensity plot (a) and component decay associated spectra (b) of a TRPES experiment with two spectral components, a feature ~ 3 eV which transfers to < 2 eV on a 250 fs timescale, and a 1000 fs decay of this secondary feature. The dashed line in b) shows the sum of the two DAS componenents. The negative going signal in the DAS shows population transfer, which can also be seen as a later onset in the signal maximum in the TRPES at low *eKE*.

2.6.2 Global Fitting

For the TRPES fits in Chapter 5, a global fitting algorithm was employed.[48, 49] In essence, global fitting operates by fitting all energies at all time delays simultaneously to the same set of time constants for a sum of *i* exponential decays:

$$S(eKE,t)=\sum_i G(t)*c_i(eKE)e^{\frac{-(t-t_0)}{\tau_i}} \tag{2.12}$$

where $c_i(eKE)$ is the intensity of the i^{th} exponential decay component as a function of kinetic energy, which has a decay constant of τ_i. The global fit is performed by a squares fit of $S(eKE, t)$ to the experimental data, with $c_i(eKE)$ and τ_i as parameters to be determined by the fit. The number of decay components to include, *i*, must be selected as a parameter of the fitting procedure; in general the smallest *i* which produces an acceptable fit is desirable.

The coefficients $c_i(eKE)$ give the spectral shape of the feature associated with the exponential decay time constant τ_i, and for this reason are also known as *decay associated spectra* (DAS). Intriguingly, there is no stipulation that DAS must be universally positive; negative going DAS may be produced by the fitting procedure. A negative DAS feature in isolation is unphysical – it corresponds to a *gain* in photoelectron signal from a negative starting position. On the other hand, if it is superimposed on top of a positive feature with a different τ, then we can interpret it in terms of a flow of population. The negative component means that this spectral region is being populated with one time constant, and then a DAS with a positive component at this region shows this population decaying away at a second time constant. In the DAS with a negative going feature, positive features then likely correspond to decay away from that spectral region, into the negative going region. An example simulated TRPES experiment is shown in Fig. 2.11, along with the constituent DAS. In this example, there is a negative going feature in the DAS of the faster component, representing population transferring from the high *eKE* region to the lower *eKE* region. The second time component is responsible for this lower *eKE* feature decaying away again. The population transfer is visible by eye in the TRPES intensity plot as a shift to later time of the feature of maximum intensity. Whilst powerful, it is important to keep in mind that global fitting can be a delicate process; as the number of parameters employed in the fitting process is so high, a good fit can often be found even if it is not physically meaningful. The fit is always constrained by the initial model (number of time constants and starting parameters), and so care should be taken if there is not an obvious physical explanation for fit results. Additionally, this algorithm can only fit data

for which each state has a static spectrum. If the *eKE* of a given state shifts over time (e.g. due to wavepacket motion), then the global fitting algorithm cannot exactly fit the data, instead approximating it with a static state model. For datasets with large amplitude motions, the global fitting procedure is not applicable.[50]

To obtain confidence intervals for parameters produced by global fits, the support plane analysis technique can be used.[51-53] To perform this procedure, the parameter whose confidence interval we are interested in is fixed to a set value and the square of the residuals between the data sat and model (χ^2) is minimized. The fixed parameter is scanned across the region of interest, and χ^2 is computed at each step. This then provides insight as to the region in parameter space (generally time constants) where an acceptable fit is produced. A numerical confidence interval can also be determined by the points at which χ^2 deviates statistically significantly from its minimum point. The point, *x,* of significant deviation for 95% confidence intervals can be calculated by: [53]

$$\frac{\chi_x^2}{\chi_{min}^2} = 1 + \frac{p}{\nu} F(0.95, p, \nu)$$

where p is the number of parameters in the fit, *i.e.* the sum of the number of time constants, components in each DAS, and t_0 and σ values. ν gives the degrees of freedom (total number of data points – p), and F is the inverse F cumulative distribution function (implemented in Matlab as finv).

In practical terms, the global fitting algorithm has been implemented using Matlab. The program takes as parameters the experimental matrix of intensity as a function of time and energy, the two respective axes for this matrix, and the cross correlation for the experiment. The number of time components to fit is determined by the length of a $\boldsymbol{\tau}$ vector, where each element is the initial trial value. The DAS are represented by a $m \times n$ matrix, where m is the size of the *eKE* scale used, and n is the number of decay components to fit. The DAS are initially flat. From these, a trial $S(eKE, t)$ is generated, and the Levenberg-Marquardt algorithm is used, as implemented by the Matlab optimization toolbox, to minimize χ^2. If the output of an imaging experiment is to be used directly in the global fitting algorithm, then the nonlinear *eKE* axis (proportional to r^2) means that a weighting factor of r should be used to prevent overfitting at lower energies. The code for the global fitting algorithm is presented in Appendix B.

2.7 References

1. K. L. Wells, PhD. Thesis, Warwick University, 2010.
2. G. M. Roberts, PhD. Thesis, Durham University, 2010.
3. J. Gross, in *Mass Spectrometry*, Springer Berlin Heidelberg, 2011, ch. 4, pp. 117.

4. J. T. Watson and O. D. Sparkman, *Introduction to Mass Spectrometry*, Wiley, 2008.
5. W. C. Wiley and I. H. McLaren, *Rev. Sci. Instrum.*, 1955, **26**, 1150.
6. B. Whitaker, ed., *Imaging in Molecular Dynamics: Technology and Applications*, Cambridge University Press, New York, 2003.
7. M. N. R. Ashfold, N. H. Nahler, A. J. Orr-Ewing, O. P. J. Vieuxmaire, R. L. Toomes, T. N. Kitsopoulos, I. A. Garcia, D. A. Chestakov, S. M. Wu and D. H. Parker, *Phys. Chem. Chem. Phys.*, 2006, **8**, 26.
8. S. J. Greaves, R. A. Rose and A. J. Orr-Ewing, *Phys. Chem. Chem. Phys.*, 2010, **12**, 9129.
9. T. Suzuki and B. J. Whitaker, *Int. Rev. Phys. Chem.*, 2001, **20**, 313.
10. D. W. Chandler and P. L. Houston, *J. Chem. Phys.*, 1987, **87**, 1445.
11. A. T. J. B. Eppink and D. H. Parker, *Rev. Sci. Instrum.*, 1997, **68**, 3477.
12. D. H. Parker and A. T. J. B. Eppink, *J. Chem. Phys.*, 1997, **107**, 2357.
13. K. L. Reid, *Annu. Rev. Phys. Chem.*, 2003, **54**, 397.
14. J. Lecointre, G. M. Roberts, D. A. Horke and J. R. R. Verlet, *J. Phys. Chem. A*, 2010, **114**, 11216.
15. A. S. Chatterley, D. A. Horke and J. R. R. Verlet, *Phys. Chem. Chem. Phys.*, 2012, **14**, 16155.
16. D. A. Horke, A. S. Chatterley and J. R. Verlet, *J. Phys. Chem. Lett.*, 2012, **3**, 834.
17. C.-G. Ning, P. D. Dau and L.-S. Wang, *Phys. Rev. Lett.*, 2010, **105**, 263001.
18. X.-P. Xing, X.-B. Wang and L.-S. Wang, *Phys. Rev. Lett.*, 2008, **101**, 083003.
19. X.-P. Xing, X.-B. Wang and L.-S. Wang, *J. Phys. Chem. A*, 2008, **113**, 945.
20. C. R. Gebhardt, T. P. Rakitzis, P. C. Samartzis, V. Ladopoulos and T. N. Kitsopoulos, *Rev. Sci. Instrum.*, 2001, **72**, 3848.
21. J. J. Lin, J. Zhou, W. Shiu and K. Liu, *Rev. Sci. Instrum.*, 2003, **74**, 2495.
22. D. Townsend, M. P. Minitti and A. G. Suits, *Rev. Sci. Instrum.*, 2003, **74**, 2530.
23. A. J. R. Heck and D. W. Chandler, *Annu. Rev. Phys. Chem.*, 1995, **46**, 335.
24. V. Dribinski, A. Ossadtchi, V. A. Mandelshtam and H. Reisler, *Rev. Sci. Instrum.*, 2002, **73**, 2634.
25. M. J. J. Vrakking, *Rev. Sci. Instrum.*, 2001, **72**, 4084.
26. J. Winterhalter, D. Maier, J. Honerkamp, V. Schyja and H. Helm, *J. Chem. Phys.*, 1999, **110**, 11187.
27. G. A. Garcia, L. Nahon and I. Powis, *Rev. Sci. Instrum.*, 2004, **75**, 4989.
28. T. Gerber, Y. Z. Liu, G. Knopp, P. Hemberger, A. Bodi, P. Radi and Y. Sych, *Rev. Sci. Instrum.*, 2013, **84**, 10.
29. G. M. Roberts, J. L. Nixon, J. Lecointre, E. Wrede and J. R. R. Verlet, *Rev. Sci. Instrum.*, 2009, **80**, 053104.
30. P. A. Franken, A. E. Hill, C. W. Peters and G. Weinreich, *Phys. Rev. Lett.*, 1961, **7**, 118.
31. E. Hecht, *Optics*, Addison-Wesley Longman, Incorporated, 2002.
32. R. Paschotta, *Encyclopedia of Laser Physics and Technology*, Wiley, Berlin, 2008.
33. N. F. Ramsey, *Molecular Beams*, Oxford University Press, Oxford, 1956.
34. G. Scoles, ed., *Atomic and Molecular Beam Methods*, Oxford University Press, Oxford, 1988.
35. W. Christen and K. Rademann, *Phys. Rev. A*, 2008, **77**, 012702.
36. U. Even, J. Jortner, D. Noy, N. Lavie and C. Cossart-Magos, *J. Chem. Phys.*, 2000, **112**, 8068.
37. K. L. Wells, G. Perriam and V. G. Stavros, *J. Chem. Phys.*, 2009, **130**, 074308.
38. J. G. Philis, *Chem. Phys. Lett.*, 2007, **449**, 291.
39. I. V. Hertel and W. Radloff, *Rep. Prog. Phys.*, 2006, **69**, 1897.
40. A. Karmida, Y. Ralchenko and J. Reader, NIST atomic spectra database [electronic resource], Accessed from http://nla.gov.au/nla.cat-vn4265688.
41. R. L. Hines, *J. Appl. Phys.*, 1966, **37**, 2730.

42. J. Fenn, M. Mann, C. Meng, S. Wong and C. Whitehouse, *Science*, 1989, **246**, 64.
43. J. B. Fenn, M. Mann, C. K. Meng, S. F. Wong and C. M. Whitehouse, *Mass Spectrom. Rev.*, 1990, **9**, 37.
44. B. Bothner and G. Siuzdak, *ChemBioChem*, 2004, **5**, 258.
45. D. A. Horke, G. M. Roberts, J. Lecointre and J. R. R. Verlet, *Rev. Sci. Instrum.*, 2012, **83**, 063101.
46. D. A. Horke, PhD. Thesis, Durham University, 2010.
47. D. Hanggi and P. W. Carr, *Anal. Chem.*, 1985, **57**, 2394.
48. C. R. S. Mooney, D. A. Horke, A. S. Chatterley, A. Simperler, H. H. Fielding and J. R. R. Verlet, *Chem. Sci.*, 2013, **4**, 921.
49. S. Ullrich, T. Schultz, M. Z. Zgierski and A. Stolow, *Phys. Chem. Chem. Phys.*, 2004, **6**, 2796.
50. P. Hockett, *Faraday Discuss.*, 2013, **163**, 513.
51. S. C. Warren, A. Margineanu, D. Alibhai, D. J. Kelly, C. Talbot, Y. Alexandrov, I. Munro, M. Katan, C. Dunsby and P. M. W. French, *PLoS ONE*, 2013, **8**, e70687.
52. T. A. Roelofs, C. H. Lee and A. R. Holzwarth, *Biophys. J.*, 1992, **61**, 1147.
53. J. R. Lakowicz, *Principles of Fluorescence Spectroscopy*, Kluwer Academic, New York, 1999.

3 Relaxation Dynamics of Phenol and Catechol

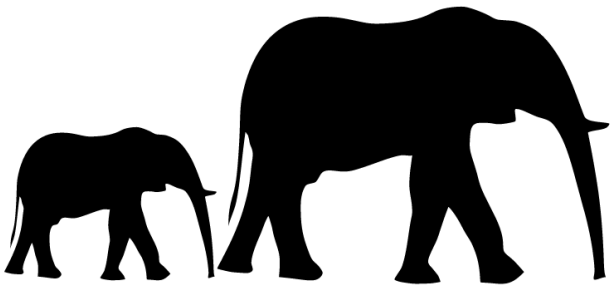

This chapter is based on the following publications:

G.M. Roberts, A.S. Chatterley, J.D. Young and V.G. Stavros, Direct Observation of Hydrogen Tunneling Dynamics in Photoexcited Phenol, *J. Phys. Chem. Lett.*, 2012, **3**, 348

A.S. Chatterley, J.D. Young, D. Townsend, J.M. Żurek, M.J. Paterson, G.M. Roberts and V.G. Stavros, Manipulating Dynamics with Chemical Structure: Probing Vibrationally-Enhanced Tunnelling in Photoexcited Catechol, *Phys. Chem. Chem. Phys.*, 2013, **15**, 6879

The theory in Section 3.4.1 was performed by Justyna M. Żurek, and Martin J. Paterson.

3.1 Introduction

Throughout the last decade, the (electronic) excited state dynamics of phenol have received considerable attention from both experimental[1-8] and theoretical[9-14] standpoints. Fig. 3.1 shows calculated one-dimensional (diabatic) potential energy cuts[8] along the O-H coordinate ($R_{O\text{-}H}$) for the first two singlet electronic excited states, S_1 ($^1\pi\pi^*$) and S_2 ($^1\pi\sigma^*$), together with the S_0 ($^1\pi\pi$) ground state. At $R_{O\text{-}H} \approx 1.2$ Å the S_1 and S_2 states cross, resulting in the formation of an S_1/S_2 conical intersection (CI) (see Chapter 1).[15] Following excitation at wavelengths (λ) < 248 nm (~5 eV), the role of the S_1/S_2 CI in the excited state dynamics has been comprehensively investigated. This has been achieved using a variety of techniques, including multi-mass ion imaging,[1, 4] high resolution H atom Rydberg tagging methods[2, 16] and ultrafast time-resolved velocity map ion imaging.[7] In combination, the results of these studies implicate that population of the dissociative S_2 state causes rapid O-H bond scission through non-adiabatic crossing at the S_2/S_0 CI ($R_{O\text{-}H} \approx 2.1$ Å, see Fig. 3.1). This process predominantly yields H atoms in conjunction with ground state phenoxyl radicals (C_6H_5O ($\tilde{X}$)), correlated with the diabatic dissociation asymptote of S_2.[2, 7] The mechanism of population was

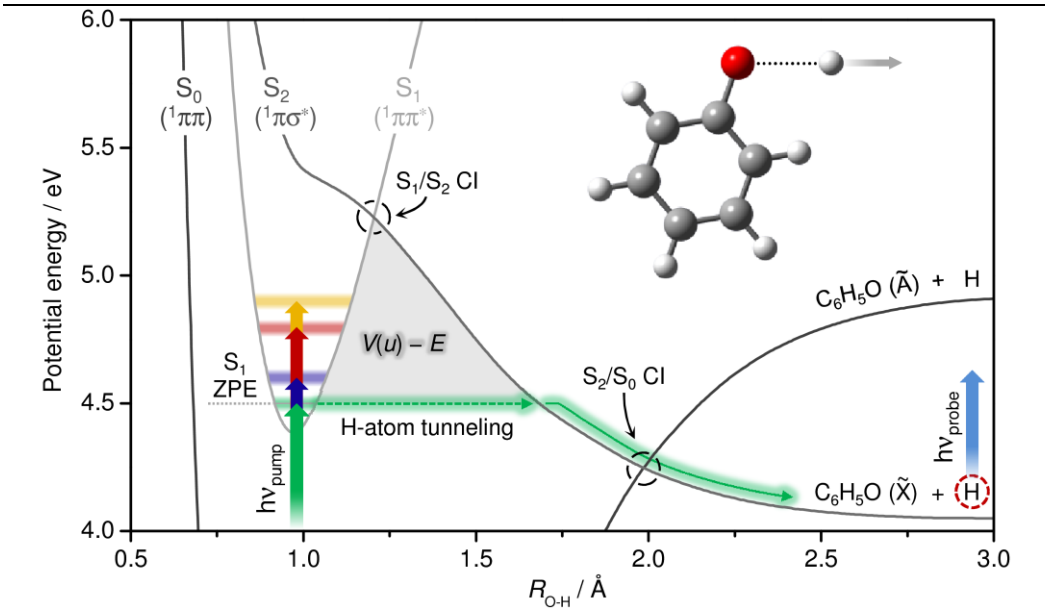

Figure 3.1 Calculated potential energy cuts along the O-H coordinate in phenol (molecular structure inset), for the first two electronic excited states, S_1 ($^1\pi\pi^*$) and S_2 ($^1\pi\sigma^*$), together with the S_0 ($^1\pi\pi$) ground state. These cuts are adapted from those calculated at the CASSPT2(10,10)/aug(O)-AVTZ level of theory in ref. 8. Excitation ($h\nu_{pump}$) to S_1 is shown for four different excitation wavelengths: 275 (green), 268 (blue), 258 (red) and 253 nm (orange). Shaded regions in the S_1 potential represent the energy bandwidth of the femtosecond pump pulses. Excitation of S_1 at all wavelengths results in H tunneling under the S_1/S_2 conical intersection (CI) and S_2 mediated O-H bond fission, proceeding exclusively from the zero point energy (ZPE) region of S_1 (green arrows). H atoms (produced in coincidence with C_6H_5O ($\tilde{X}$) radicals) are subsequently probed using fs probe pulses ($h\nu_{probe}$). The shaded gray area, labeled $V(u) - E$, represents the potential barrier used in WKB tunneling calculations (see text for details).

originally postulated to be a transfer from the optically bright S_1 state via the S_1/S_2 CI.[10] Recently, however, some doubt has been shed on the participation of the S_1/S_2 CI in the dynamics at $\lambda < 248$ nm, and instead direct excitation to the S_2 state has been proposed.[8]

Below the S_1/S_2 CI ($\lambda > 248$ nm), population transfer between the S_1 and S_2 states is hindered by an energy barrier (see Fig. 3.1). However, after excitation to the zero-point energy (ZPE) of S_1 ($\lambda = 275.113$ nm), frequency domain measurements reveal that O-H bond fission mediated by S_2 still persists.[2] This remains the case as the excitation energy is incrementally increased to just below the S_1/S_2 CI. Two schools of thought have been developed to explain these observations: (i) following population of S_1, $S_1 \rightarrow S_0$ internal conversion (IC) is driven by O-H stretch acceptor modes in S_0 (hereon, termed S_0*), which subsequently promotes predissociation through efficient $S_0^* \rightarrow S_2$ coupling at extended $R_{O\text{-}H}$, finally resulting in H elimination on S_2;[2, 17] (ii) more recently, new dynamical calculations,[8, 10, 14] in addition to experiments on substituted phenols (and their H bonded complexes with NH_3),[18] implicate that O-H fission proceeds through H tunnelling under the S_1/S_2 CI, facilitated by the ν_{16a} motion[13] (a ring torsional mode[5]). Furthermore, selective deuteration of the O-H bond (C_6H_5OD) leads to an increase in the fluorescence lifetime of the S_1 ZPE level from ~2.4 ns to ~13.3 ns,[19] and full deuteration (C_6D_5OD) produces no D atom signature for O-D scission along S_2 in Rydberg tagging experiments conducted below the S_1/S_2 CI.[2] These observations are consistent with either of the aforementioned mechanisms, as the probability for D tunnelling is $\sim 10^3$ less than H atoms[8] while the O-D stretch is hypothesized to be a less efficient acceptor for $S_1 \rightarrow S_0$* IC.[2, 17]

In this chapter, we use time resolved H atom imaging to answer the questions of the origin of H atom dissociation, both energetically above and below and the CI, in phenolic compounds. Below the CI, the question to be answered is whether H atoms are born from tunnelling or internal conversion processes, and above the CI the question is whether the S_2 state is directly excited, or if it is populated via the S_1/S_2 CI. We start by studying phenol itself, which gives tantalizing hints as to the below barrier mechanism, but the length of timescales involves rules out anything conclusive. To overcome these problems, and in the spirit of 'building up', we then look at the dynamics of catechol (1,2-dihydroxybenzene). Catechol has significantly quicker dynamics than phenol and allows us to comprehensively study the dynamics both above and below the CI, demonstrating that tunnelling is the mechanism beneath the CI, whilst direct excitation to the S_2 state occurs above it. As well as solving the

question of the nature of H atom dissociation, we observe a very rapid tunnelling lifetime, which is attributed to vibrational effects on the multi-dimensional potential energy surface of catechol.

3.2 Methods

The experiments on both phenol and catechol were performed using the time-resolved H atom imaging experiment in Warwick (see Chapter 2). All samples were obtained from Sigma-Aldrich (>99% purity), and used without further purification. The valve opening time was set to 13 μs in all cases. To obtain sufficient vapour pressure to seed the molecular beam, the solids phenol and catechol were heated to 100 °C, whilst guaiacol (2-methoxyphenol, see Section 3.4.4) is a liquid and was only heated to 60 °C. Doubly deuterated catechol (catechol-d_2) was produced by stirring catechol in D_2O for ~48 hours, then removing the D_2O under reduced pressure. Vapour phase absorption spectra were produced by heating the compounds in a fused silica cell to obtain sufficient vapour pressure, and measured using a commercial UV-vis absorption spectrometer (Perkin-Elmer, Lambda 25) at a 1 nm resolution.

3.3 Tunnelling in Phenol

To explore the mechanism of $^1\pi\sigma^*$ mediated H hydrogen loss in phenol below the S_1/S_2 CI, we have measured the time resolved H atom photodissocation spectra at four wavelengths, λ > 248 nm, the location of the CI.[5] Shown inset in Fig. 3.2(a) is a representative H^+ velocity map image recorded after broadband excitation around the S_1 ZPE, using a pump wavelength centred at 275 nm and a pump-probe delay (Δt) of 1.2 ns; *i.e.* the pump precedes the probe by 1.2 ns. The image in Fig. 3.2(a) is dominated by a single ring at larger radius. This feature possesses a near isotropic angular distribution ($\beta_2 \approx 0$), tentatively suggesting that this H^+ signal is generated on a timescale slower than the rotational period of parent phenol species, although this is by no means definitive as the recoil may be insufficiently axial for a well defined anisotropy to be observed.[20]

Total kinetic energy release (TKER) spectra were derived from the velocity map images using the POP algorithm (see Chapter 2).[21] In Fig. 3.2(a), TKER spectra recorded at Δt = 1.2 ns are presented for four different pump wavelengths (275, 268, 258 and 253 nm), all of which are beneath the S_1/S_2 CI. The TKER spectra in fact reveal that there are two features present at all wavelengths: a broad underlying signal with a Boltzmann-like' distribution and a Gaussian signal centered at higher TKER (~5500 – 6500 cm^{-1}). Previously, it has been suggested that the Boltzmann-like feature is multi-

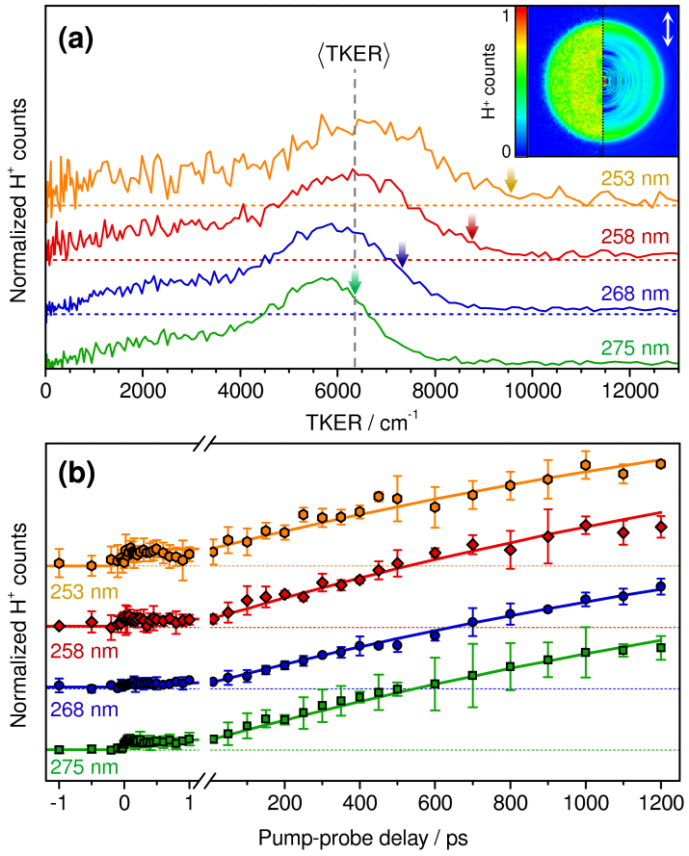

Figure 3.2 (a) TKER spectra in phenol obtained following excitation at 275 (green), 268 (blue), 258 (red) and 253 nm (orange). All spectra were recorded at Δt = 1.2 ns. Horizontal dotted lines correlate to zero signal baselines. Vertical arrows represent predicted $TKER_{max}$ values at each pump wavelength, while the dashed gray line shows a predicted $\langle TKER \rangle$ for dissociation from the S_1 ZPE (see text for details). Inset: raw H^+ velocity map image (left) and reconstructed slice through the centre of the H^+ distribution (right) at 275 nm and Δt = 1.2 ns. The white arrow indicates the polarization of $h\nu_{pump}$. (b) H^+ signal transients for the high TKER (Gaussian) features at each pump wavelength. Solid lines through the data present a predicted kinetic model for H tunnelling.

component in nature, with contributions from both statistical[2] and multiphoton processes,[22] while the Gaussian component is assigned to O-H fission via S_2 forming C_6H_5O ($\tilde{X}$) + H.[2] The

latter assignment is confirmed by determining the maximum TKER ($TKER_{max}$) for the O-H dissociation process at each pump wavelength using the relationship $TKER_{max} = h\nu_{pump} - D_0$, where D_0 is the adiabatic O-H dissociation energy (previously determined as 30015 cm^{-1}).[2] The predicted $TKER_{max}$ at each wavelength is indicated by the vertical arrows in Fig. 3.2(a). The increase in $TKER_{max}$ with increasing $h\nu_{pump}$ is approximately mirrored by the broadening of the Gaussian features towards higher TKER.[23] However, the mean TKERs, $\langle TKER \rangle$, of these high TKER features are approximately unchanged between the four excitation wavelengths, in line with results from frequency domain studies.[2] Within the context of the one-dimensional cuts through the full multi-dimensional potential energy surfaces in Fig. 3.1 (*i.e.* the O-H

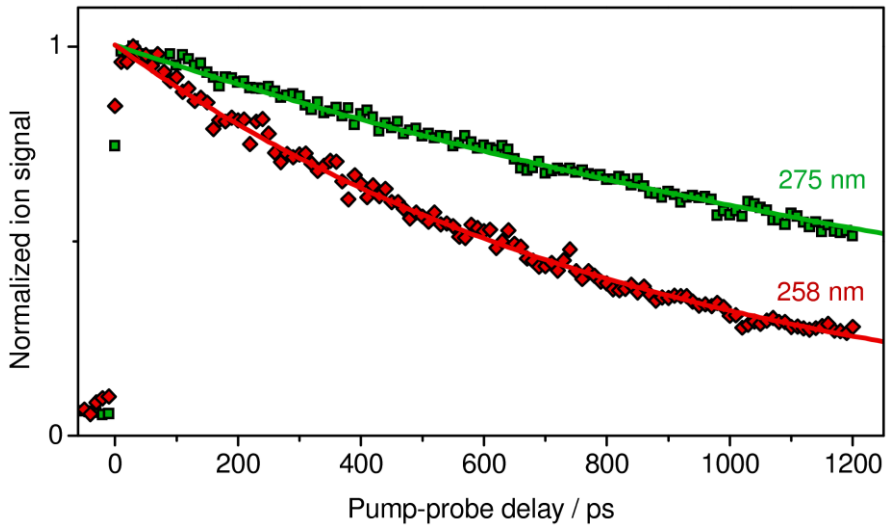

Figure 3.3 Representative parent ion (phenol$^+$) signal transients. Transients were recorded using [1 + 1′] REMPI, following excitation at 275 (green squares) and 258 nm (red diamonds) and probing (ionization) at 243.1 nm. Solid lines correspond to fits with a single exponential decay.

stretch coordinate only), this provides some initial indication that: (i) after populating S_1, O-H dissociation dynamics below the S_1/S_2 CI are seemingly independent of $h\nu_{pump}$ and proceed from approximately the same vibronic region of S_1, nominally around the S_1 ZPE (this is based on the observation that $TKER_{max}$ for 275 nm predicts the observed $\langle TKER \rangle$ at other wavelengths reasonably well (dashed gray line, Fig. 3.2(a))); and (ii) with increasing $h\nu_{pump}$, populated vibrational modes in S_1 which are *orthogonal* to the O-H dissociation coordinate represented in Fig. 3.1 (spectator modes), are mapped into vibrational excitation of the C_6H_5O ($\tilde{X}$) co-fragment.

Fig. 3.2(b) shows normalized H^+ signal transients of the high TKER features out to Δt = 1.2 ns at the four pump wavelengths: 275 (green), 268 (blue), 258 (red) and 253 nm (orange). These are obtained by generating a series of TKER spectra at each Δt and integrating the high TKER feature. In all cases there is an initial rapid step at Δt = 0, which appears within our instrument response window (~160 fs), and correlates to the appearance of the underlying Boltzmann-like signal. This feature is likely due to unintended multiphoton effects. This is then followed by a slower signal rise, due to growth of the high TKER feature, corresponding to S_2 mediated O-H fission. At all four excitation wavelengths the transients show no indication that the dynamics have terminated by the temporal limit of our experiments, which is currently 1.2 ns. As such, it is tenuous to extract *definitive* appearance time constants for the high TKER features via kinetic fits. Instead, we conservatively quote a lower limit for the H elimination dynamics of ≥ 0.8 ns, in all cases.

At this stage, it appears that as more excess internal energy is imparted to S_1 (increasing $h\nu_{pump}$), there is no noticeable increase in the rate of S_2 driven H formation, but rather an apparent invariance in the H elimination timescales. Such an observation is inconsistent with a model whereby the high TKER features originate through successive $S_1 \rightarrow S_0^* \rightarrow S_2$ couplings and the production of C_6H_5O ($\tilde{X}$) + H. Rather, within Fermi's golden rule, one would anticipate that as the density of vibrational states (orthogonal to the O-H coordinate) in S_1 is enhanced with increasing $h\nu_{pump}$, the rate of $S_1 \rightarrow S_0^*$ IC and concomitantly the (predissociative) O-H fission rate, should notably increase.[24] To confirm this, we have performed time-resolved ion yield experiments on the parent cation (phenol$^+$) using [1 + 1′] REMPI, which provide a measure of S_1 population decay (from the Franck-Condon excitation window) through *all* available relaxation processes (*e.g*. fluorescence, IC, intersystem crossing, tunnelling *etc*.). Crucially, as decay processes have a definitive end point (0 at $\Delta t = \infty$), it is possible to fit these dynamics even if they outlive the temporal window afforded by the length of our delay stage. Fig. 3.3 presents two representative parent ion transients for excitation at 275 and 258 nm and probing (ionization) at 243.1 nm. Fits to these transients with a single exponential decay (solid lines) provide time constants of 1.9 and 0.9 ns at 275 and 258 nm, respectively. This is in-line with the expectation that the overall lifetime of S_1 at the excited Franck-Condon window (containing modes orthogonal to the O-H coordinate) will decrease with increasing $h\nu_{pump}$ through an enhanced propensity for $S_1 \rightarrow S_0^*$ IC. By arguments of competing kinetics, the H^+ appearance lifetime should mirror the S_1 lifetime, and thus it appears that the constrained maximum of Δt is restricting our ability to correctly assign the H^+ dynamics. At this stage, the dynamics do not appear to favour either mechanism, although the apparent invariance in H^+ appearance time is intriguing.

Despite the inconclusiveness of the dynamics, we can still attempt to reconcile the observed H^+ transients in Fig. 3.2(b) with the H tunnelling mechanism. To begin, we focus on H tunnelling to S_2 from the S_1 ZPE (275 nm). Within a one-dimensional approximation, the tunnelling lifetime, τ, at the ZPE of the O-H stretch mode in S_1 can be estimated using a semi-classical WKB method (see Chapter 1):[25]

$$\tau \approx \left[\nu_{OH} \exp\left(\int_{u_1}^{u_2} \frac{-2}{\hbar} \sqrt{2m(V(u) - E)}\, du \right) \right]^{-1} \qquad (3.1)$$

where u is the O-H bond coordinate, ν_{OH} is the O-H stretch frequency (3582 cm^{-1}), m is the mass of H, $V(u)$ is the potential barrier (obtained from the S_1 and S_2 one-dimensional potential energy cuts shown in Fig. 3.1) and E is the kinetic energy of the H

atom (in this case the ZPE of the O-H stretch in S_1, $\frac{1}{2}\nu_{OH}$). The potential energy cuts in Fig. 3.1 generate a value of t = 2.5 ns for H tunnelling onto S_2 from the ZPE of ν_{OH} in S_1. This is in excellent agreement with the value for t empirically derived by Pino *et al*. (~2.4 ns).[18] A kinetic *model* of the 275 nm H^+ transient, where t has been fixed to 2.5 ns, is shown in Fig. 3.2(b) by the solid green line through the experimental data points. The model represents the data exceptionally well and adds weight to an argument that following excitation around the S_1 ZPE, H elimination via S_2 is promoted by H tunnelling from S_1. This is in line with predictions by Dixon *et al*.[8] who, at the S_1 ZPE, model H tunnelling dynamics using two-dimensional wavepacket calculations in ν_{16a} and O-H stretch coordinates. These authors reveal that the ν_{16a} (a_2) motion is required for vibronically coupling S_1 ($^1B_2$) and S_2 ($^1B_1$) within phenol's non-rigid G_4 (isomorphous with C_{2v}) symmetry group ($B_2 \otimes a_2 \otimes B_1 = A_1$). We, however, emphasize that our broadband pump-probe measurements presented here cannot provide us with information regarding mode-specific behaviour.

Similar kinetic models, with H tunnelling time constants of 2.5 ns, can also be used to represent the H^+ transients resulting from a vibrationally excited S_1 state, at 268, 258 and 253 nm (solid lines, Fig. 3.2(b)). In each case, the models fit the experimental data very well, however given the changing parent ion lifetime, this model should not be considered reliable, and the data are simply not of sufficient quality to be accurately fit. On the other hand, we would not expect the rate of tunnelling alone to vary with excess internal energy imported in S_1: by populating modes orthogonal to the O-H dissociation coordinate, O-H fission dynamics should still primarily proceed from the ZPE of the O-H stretch mode in S_1. This confers with the following expectations. Firstly, excitation to orthogonal modes in S_1 has a minimal impact on the observed tunnelling rate, although we concede that in the current experiments this cannot be directly observed due to the long tunnelling time compared to the maximum Δt observable. Secondly, as the ν = 1 level of ν_{OH} is not energetically accessible at the wavelengths used here ($S_1(\nu_{OH} = 1) \approx 250$ nm),[26] either through direct excitation or internal vibrational energy redistribution (IVR) from orthogonal modes, a major change in rate should not be observed. Rather, H tunnelling along the O-H coordinate should always proceed from the ZPE of ν_{OH} in S_1 over our excitation range. The reduction in the overall S_1 lifetime with increasing $h\nu_{pump}$ (see Fig. 3.3) likely results from an increase in the $S_1 \rightarrow S_0$* IC rate, driven from the orthogonal modes excited (and following IVR) within the Franck-Condon window, and this reduction presumably carries through into the H^+ appearance lifetime, even if the rate of tunnelling alone is constant. Moreover, exclusive tunnelling from the S_1 ZPE region consolidates with our earlier hypothesis for

why the $\langle \mathrm{TKER} \rangle$ of the Gaussian features in all four TKER spectra (Fig. 3.2(b)) appear close to the predicted TKER_{max} for O-H dissociation from the S_1 ZPE. We therefore tentatively propose, that below the S_1/S_2 CI, O-H bond cleavage via S_2 in phenol proceeds purely by H tunnelling from the S_1 ZPE, reinforcing previous postulates by Sobolweski *et al.*,[10] Dixon *et al*.[8] and Pino *et al*.[18]

Unfortunately, the very slow dynamics of phenol prevent us from making any concrete assignments. Our observations are consistent with a tunnelling mechanism, but do not in any way contradict a scheme whereby neutral H atoms are borne from an $S_1 \rightarrow S_0^* \rightarrow S_2 \rightarrow C_6H_5O$ ($\tilde{X}$) + H dissociation mechanism. To settle this ambiguity, instead of studying phenol, we must move to a derivative with more rapid dynamics, such that all processes can be accurately quantified. In the following section we have done precisely this, building up to the more complex catechol molecule (ortho-hydroxyphenol). In catechol, tunnelling is fast enough that it can be definitely assigned, and we find by analogy that the tentative prediction of tunnelling in phenol was indeed correct.

3.4 Hydrogen Dissociation in Catechol

Catechol moieties are found in a diverse variety of biologically active molecules, including hormones and neurotransmitters, such as epinephrine and dopamine, as well as subunits of natural (eu)melanin co-polymer pigments – the latter are implicated in UV photoprotection within human skin, although its exact macromolecular structure and photophysics still remain poorly characterised.[27, 28] Catechol can also be viewed as a derivative of phenol (hydroxybenzene) – the UV chromophore of the amino acid tyrosine. Within the context of the present work, past studies into the photochemistry of phenols[2, 5, 6, 8, 16, 18, 29-34] serve as an excellent benchmark for understanding how simple modifications to the chemical structure of a bio-molecular subunit, such as phenol, can manipulate its excited state dynamics, and in turn the potential impact this may have on its specific function in biological systems. Indeed, this so-called 'structure-dynamics-function' relationship has proved to be central for building towards a more intimate understanding of dynamics in a number of photoactivated biomolecules, including rhodopsins[35-37] and fluorescent proteins.[38, 39]

Calculated 1-D potential energy cuts (PECs) along the O–H bond distance of catechol are shown in Fig. 3.4(a). The excited state structure closely mirrors that of phenol, and so we might expect it have similar dynamical properties. Fig. 3.4(b) shows the vapour phase absorption spectrum of ~80 °C catechol. The S_1 state is responsible

for the large absorption onset at 280.5 nm, whilst excitation to the S_2 state must occur via intensity borrowing, and so is much weaker.[8]

Relative to phenol, the excited state dynamics of catechol have received significantly less attention. Early gas phase spectroscopy[40-44] and *ab initio* studies[42, 44-46] on catechol determined that the only stable tautomer in S_0 (within a molecular beam) is the planar structure presented in Fig. 3.4(a), where the O^2-H bond is involved in an intramolecular hydrogen bond with the O^1 atom, and O^1-H is 'free'. In addition to this, it was noted that the two O-H torsion motions are strongly coupled[43, 44] and that, unlike phenol, the minimum energy geometry of the S_1 state ($S_{1\ min}$) is not planar;[46] the latter proposal was further supported by more recent calculations of $S_{1\ min}$ at the RI-CC2/aug-cc-pVTZ level by King *et al.*[47]

It is only very recently that there have been two separate studies investigating the excited state dynamics of catechol in the gas phase, using frequency-resolved H(Rydberg) atom photofragment translational spectroscopy (HRA-PTS)[47] and ultrafast time-resolved photoelectron imaging (TR-PEI)[31] techniques, both of which draw heavily on the $^1\pi\sigma^*$ (S_2) oriented dynamics observed in phenol. The former HRA-PTS studies by King *et al.*[47] found that following excitation to $S_1(v = 0)$ at 280.5 nm, coupling

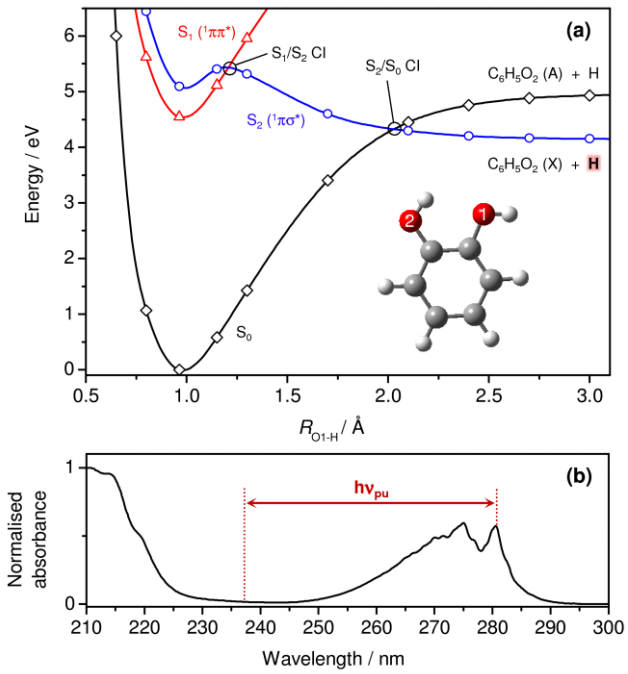

Figure 3.4 (a) Calculated 1-D potential energy cuts of the S_0, S_1 ($^1\pi\pi^*$) and S_2 ($^1\pi\sigma^*$) electronic states along the O^1-H bond dissociation coordinate ($R_{O1\text{-}H}$) in catechol (molecular structure and atom labelling shown inset). Cuts are calculated at the CASPT2(12,10)/aug-cc-pVDZ level. (b) Vapour-phase absorption spectrum of catechol between 300 – 210 nm, indicating the excitation wavelength range ($h\nu_{pu}$) investigated in this study.

onto the repulsive S_2 surface is active, evidenced by the formation of translationally excited H-atoms (~7500 cm^{-1}). By analogy with phenol, these high KE H-atoms were assigned to a tunnelling process under the S_1/S_2 CI. It was also found that the vibrational product distribution of the ground state catechoxyl radical co-fragments ($C_6H_5O_2(X)$) was highly sensitive to initial excitation of the 'free' O^1-H torsion mode in the S_1 state, although the exact mode assignments in the $C_6H_5O_2(X)$ photoproducts were by no means definitive.[47] Nonetheless, this led these authors to postulate that the O^1-H torsion undergoes strong mode mixing with both in- and out-of-plane ring distortion motions prior to/during tunnelling. Support for this interpretation was garnered by their RI-CC2 calculations of $S_{1\ min}$, which exhibits a 'buckled' structure of the phenyl ring, as well as both of the C-O-H groups lying out-of-plane. However, unlike prior HRA-PTS on phenol, the studies on catechol were unable to assign the precise location of S_1/S_2 CI. Instead it was proposed that the S_1/S_2 CI lies within the broad range of 265 – 230 nm.[47]

More recently, ultrafast TR-PEI experiments by Livingstone *et al*.[31] have probed the excited dynamics of catechol, as well as phenol, resorcinol (1,3-dihydroxybenzene) and hydroquinone (1,4-dihydroxybenzene), in the time-domain, following excitation to the S_1 state at 267 nm. Relative to phenol, resorcinol and hydroquinone, catechol was found to exhibit a significantly reduced S_1 state lifetime of ~12 ps (*cf.* 0.4 – 1.0 ns).[31] Livingstone *et al*. noted that 1-D PECs along $R_{O1\text{-}H}$ (calculated at the EOM-CCSD/aug-cc-pVDZ level) suggest the barrier area under the S_1/S_2 CI in catechol may be notably reduced compared to phenol, resorcinol and hydroquinone, which could contribute to its reduced S_1 state lifetime.[31] However, these authors duly highlight that the 1-D barrier area to tunnelling along $R_{O1\text{-}H}$ was not suppressed anywhere near enough to account for the two orders of magnitude reduction in the S_1 state lifetime of catechol.[31]

Herein, we present new and comprehensive results, which probe the excited state dynamics of catechol in intimate detail, and by analogy answer the questions of phenols dynamics also. This is achieved by simultaneously monitoring both the kinetic energy release and appearance timescales of the H-atom photoproducts with ultrafast time-resolved velocity map ion imaging (TR-VMI), as well as corresponding decay times of the photoexcited catechol parent species using ultrafast time-resolved ion yield (TR-IY) measurements. Firstly, we definitively confirm that tunnelling ensues from the photoprepared S_1 state to the S_2 state, when excitation occurs below the S_1/S_2 CI. The combined time and energy information allows us, for the first time, to determine an energetic onset for accessing the S_1/S_2 CI, revealing that the barrier

height for tunnelling is comparable to phenol. Yet, somewhat remarkably, the tunnelling rate in catechol is found to be orders of magnitude greater, which we interpret in terms of a highly 'vibrationally-enhanced' tunnelling phenomenon. Secondly, we conclusively demonstrate that H atoms dissociating from above the S_1/S_2 CI are borne from direct excitation to the S_2, rather than participation of the CI from the S_1. From a broader perspective, these studies further demonstrate how detailed insights into the intimate relationship between molecular structure and function in biomolecules and their subunits could be attained through a more rigorous structure-dynamics-function picture. Here, this is exemplified by the fact that even a simple chemical modification (*ortho*-hydroxy substitution) to the structure of a fundamental biologically relevant UV chromophore, such as phenol, yields dramatic modifications to/control over its excited state dynamics.

3.4.1 *Ab initio* calculations

The PECs shown in Fig. 3.4(a) were generated by Justyna M. Żurek and Martin J. Paterson as follows: density functional theory was used to generate an initial S_0 ground state structure for catechol. The B3LYP functional with an aug-cc-pVDZ basis set was used for structure optimisation, with C_s symmetry imposed. This structure was then used to generate 1-D PECs for the S_0, S_1 ($^1\pi\pi^*$) and S_2 ($^1\pi\sigma^*$) electronic states of catechol along the $R_{O1\text{-}H}$ bond coordinate using a combination of the multi-configurational complete active space self-consistent field (CASSCF)[48, 49] method and its second-order perturbation theory extension (CASPT2),[50, 51] as implemented in the Molpro 2012.1 package.[52] Specifically, restricted Hartree-Fock orbitals were used as starting 'trial' orbitals for the CASSCF calculations with an active space consisting of 12 electrons in 10 orbitals (12,10). This (12,10) active space contains the 3 π bonding orbitals, 3 π* anti-bonding orbitals, the 2 n_p lone pair orbitals on the O^1 and O^2 atoms, and the correlated σ and σ* orbitals associated with the O^1-H bond. After generating a proper active space for the system, energies of the S_0, S_1 and S_2 states were computed as a function of $R_{O1\text{-}H}$ at the CASPT2(12,10)/aug-cc-pVDZ level, taking some account of dynamic correlation effects. The RS2C option[51] for CASPT2 calculations was implemented, which uses internally contracted configurations as a basis for subspaces, for which the overlap matrix depends on the first- and second-order density matrix of the reference function. This method is more compact and efficient than RS2, especially for larger molecules or for larger active spaces (as is the case here). A level shift of 0.5 au for each state was used to improve the convergence of the calculations.

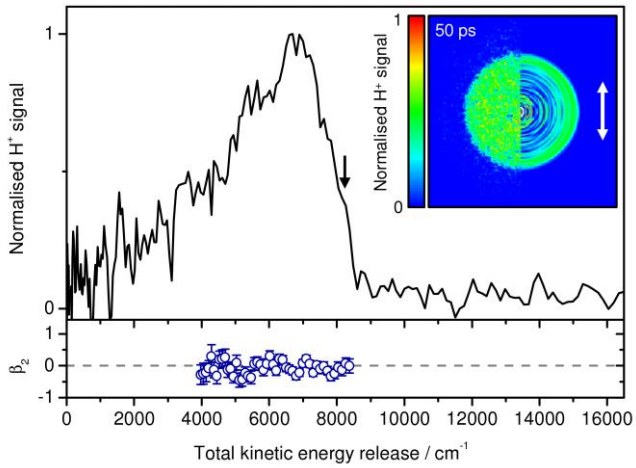

Figure 3.5 TKER spectrum recorded after excitation around S_1(v = 0) at 280.5 nm and probing H-atom photoproducts using a time-delayed 243.1 nm probe pulse at Δt = 50 ps. The predicted $TKER_{max}$ for O^1-H bond fission is indicated by the vertical black arrow. β_2 recoil anisotropy parameters (blue circles) are presented as a function of TKER below. Inset: H^+ velocity map image from which the TKER spectrum is derived (left half) together with a reconstructed slice through the centre of the original 3-D ion distribution (right half). The vertical white arrow indicated the electric field polarisation of the pump pulse, **ϵ**.

3.4.2 H^+ image and TKER spectrum at S_1(v = 0): λ = 280.5 nm

Fig. 3.5 shows an H^+ image (inset) and the TKER spectrum derived therefrom, recorded following photoexcitation to S_1(v = 0) at 280.5 nm, and selectively probing any H-atom photoproducts with a time-delayed 243.1 nm fs probe pulse at Δt = 50 ps. Both the image and derived spectrum have a one-colour 243.1 nm probe only background signal subtracted. The spectrum displays a feature which rises in intensity with increasing TKER, peaking at a maximum intensity around 7000 cm^{-1}, and then sharply decays back to the baseline signal level by ~8500 cm^{-1}. This feature correlates with the dominant isotropic signal at large radii in the inset H^+ image. The isotropic nature of this feature is confirmed by the extracted β_2 anisotropy parameters between 4000 – 8500 cm^{-1} (Fig. 3.5, lower panel), which possess an average value of $\beta_2 \approx 0$.

The profile of the TKER spectrum is in qualitative agreement with that previously reported by Ashfold and co-workers,[47] using the HRA-PTS method (at $\Delta t \sim 10$ ns), although we observe much less signal at low TKER (< 4000 cm^{-1}), due to the shorter Δt. Previously, these authors attributed the signal peaking at ~7000 cm^{-1} to O^1-H bond fission, forming H-atoms in coincidence with $C_6H_5O_2$(X) radicals, mediated by coupling onto the dissociative S_2 surface from S_1(v = 0). This interpretation is supported by considering the energetics of the O^1-H bond scission process after excitation at 280.5 nm. Based on a photon energy, $h\nu_{pu}$, of 35650 cm^{-1} and a (maximum) adiabatic O^1-H bond strength, $D_0(O^1\text{-H})$, of 27480 cm^{-1},[47] a predicted maximum TKER for this process, $TKER_{max}$, can be determined according to:

$$\mathrm{TKER}_{\max} = h\nu_{pu} - D_0\left(\mathrm{O}^1\text{-H}\right) \tag{3.2}$$

Eq. (3.2) returns a value of TKER_{max} = 8170 cm^{-1}, corresponding to a scenario where the $C_6H_5O_2(X)$ co-fragments are formed in their ZPE vibrational level (v = 0). This value for TKER_{max}, indicated by the vertical arrow in Fig. 3.5, agrees very well with the high TKER cut-off of the observed signal (within the energy resolution of our VMI spectrometer), adding weight to the proposal that this signal is associated with O^1–H bond fission along the S_2 surface. From a mechanistic perspective, after excitation to S_1(v = 0), coupling on to the S_2 surface has been postulated to occur through tunnelling under the S_1/S_2 CI;[47] a conclusion largely drawn by analogy with more comprehensive studies on phenol.[8, 29, 53] The same conclusion was also reached by Livingstone *et al*. in TR-PEI measurements after excitation at the shorter wavelength of 267 nm.[31] Below, we provide strong evidence that tunnelling from the S_1 state to the S_2 state is indeed active when catechol is excited below the S_1/S_2 CI.

As noted above, the profile of the TKER spectrum in Fig. 3.5 displays a significant degree of asymmetry, peaking at ~7000 cm^{-1} and monotonically decaying back towards the baseline signal by ~2000 cm^{-1}. This suggests that a significant fraction of $C_6H_5O_2(X)$ radical co-fragments are born with a large degree of internal vibrational energy (peaked at E_{vib} ~ 1000 cm^{-1}). Given that negligible excess vibrational energy is imparted to S_1 at 280.5 nm, it is unlikely that the 'hot' $C_6H_5O_2(X)$ fragments are formed as a consequence of initially prepared 'spectator modes' in S_1 (modes which are orthogonal to the $R_{O1\text{-}H}$ coordinate shown in Fig. 3.4(a)) mapping directly through into $C_6H_5O_2(X)$ photoproducts (*cf*. phenol[8, 29]). Instead, this observation suggests that vibrationally hot $C_6H_5O_2(X)$ radicals arise through Franck-Condon effects, due to a significant change in nuclear geometry between $S_{1\ min}$ and $C_6H_5O_2(X)$ during the S_1(v = 0) → S_2 → O^1-H bond fission process. Such an interpretation is supported by previous theoretical calculations of a highly non-planar $S_{1\ min}$ geometry,[46, 47] which contrasts the planar structure of the $C_6H_5O_2(X)$ radical species.[47, 54]

Studies on related heteroaromatic species, also containing O-H groups bound within an intramolecular hydrogen bond, have suggested that H-atom atom loss from sites such as O^2-H in catechol may also occur (as a minor dissociation channel),[55] and before proceeding further, we also consider possible contributions from cleavage of the hydrogen bonded O^2-H group to the spectrum in Fig. 3.5. In previous measurements by Ashfold and co-workers,[47] they acknowledged that although they did not observe any firm evidence for H-atom elimination from the hydrogen bonded O^2-H group, they could not definitively rule out signal contributions from such a process. We also

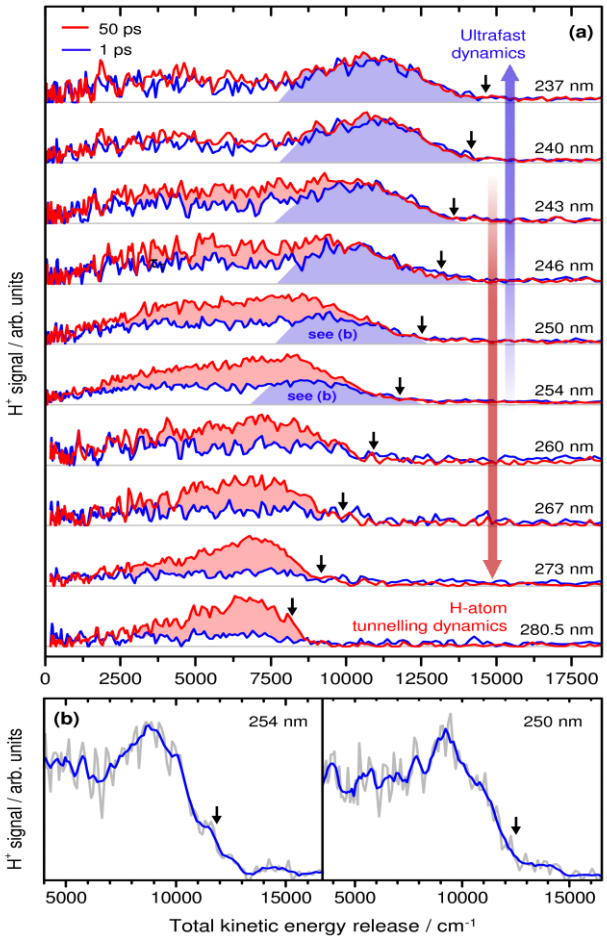

Figure 3.6 (a) Time-resolved TKER spectra at Δt = 1 (blue line) and 50 ps (red line) recorded after excitation at a series of wavelengths over the range 280.5 – 237 nm. Vertical black arrows indicate the predicted $TKER_{max}$ value for O^1-H bond fission at a given wavelength. Red shading indicates signal arising from H-atom tunnelling dynamics under the S_1/S_2 CI, whereas blue shading indicated signal associated with ultrafast O^1-H bond fission after coupling directly through the S_1/S_2 CI (see main text for further details). (b) Enlarged sections of the TKER spectra (between ~4000 – 16000 cm^{-1}) recorded after excitation at 254 nm and 250 nm at Δt = 1 ps. Grey lines are the raw spectrum, while the blue lines indicate a 5-point average.

concede that based on the results in Fig. 3.5 alone, this could in principle be the case here, although we present results below which support the idea that O^1-H bond fission is primarily (if not exclusively) responsible for the signal peaked around ~7000 cm^{-1} in Fig. 3.5. Furthermore, we note that the electronically excited $C_6H_5O_2$(A) + H photoproduct channel (see Fig. 3.4(a)), which lies ~12900 cm^{-1} above the $C_6H_5O_2$(X) + H channel,[54] is energetically closed following excitation to S_1(v = 0) and remains closed until ~248 nm.

3.4.3 Time-resolved TKER spectra

Fig. 3.6(a) shows time-resolved TKER spectra at Δt = 1 ps (blue) and 50 ps (red), recorded at a series of excitation wavelengths over the range 280.5 – 237 nm (as with 3.5, a one-colour signal originating from the 243.1 nm pulses has been subtracted from all TKER spectra). After excitation to S_1(v = 0) at 280.5 nm a very small two-colour

'background' signal (extending to ~7000 cm^{-1}) is observed by Δt = 1 ps. In a similar vein to previous studies on related heteroaromatic species,[7, 29, 56, 57] we assign this signal to undesired multiphoton induced dissociation processes via $catechol^+$ (*e.g.* dissociative ionisation). Upon extending these measurements out to Δt = 50 ps a sizeable peak associated with O^1-H bond cleavage along the S_2 state appears (see above), highlighted by the red shading in Fig. 3.6(a). This provides some provisional insight that coupling from around S_1(v = 0) on to the S_2 surface, occurs over a timeframe of tens of picoseconds.

At wavelengths between 273 – 260 nm, similar behaviour to S_1(v = 0) is observed in the recorded time-resolved TKER spectra, although we note that the peak associated with O^1-H fission at Δt = 50 ps broadens towards higher TKER with increasing excitation energy, approximately mirroring the predicted increase in $TKER_{max}$ (shown by the vertical black arrows in Fig. 3.6(a)). However, the maximum intensity of this peak remains located around ~7000 – 7500 cm^{-1}, similar to the location of the maximum intensity of this feature in the TKER spectrum recorded after excitation around S_1(v = 0). Analogous behaviour was observed previously in phenol[8, 29] (following excitation to the S_1 state below the S_1/S_2 CI) and suggests that: (*i*) a large amount of the excess vibrational energy initially imparted to the S_1 state at these shorter wavelengths (which will be localised in coordinates orthogonal to $R_{O1\text{-}H}$) projects directly through into the $C_6H_5O_2$(X) co-fragment, essentially behaving as a 'spectator' to the O^1-H bond scission process; and (*ii*) tunnelling onto the dissociative S_2 surface occurs from a similar energy within the S_1 state (with respect to the $R_{O1\text{-}H}$ coordinate), irrespective of λ. As the excitation wavelength is decreased further (λ < 254 nm), more signal is present by Δt = 1 ps and the relative signal increase by Δt = 50 ps, associated with tunnelling under the S_1/S_2 CI and dissociation along the S_2 state, reduces until there is no signal difference between the two time-resolved spectra measured at 240 and 237 nm, indicating that this mechanism is inactive at λ < 243 nm.

We now focus on the spectra recorded at Δt = 1 ps with excitation wavelengths <254 nm. As above, the signal at less than ~7000 cm^{-1} is primarily attributed to rapid undesired multiphoton induced processes. More importantly though, close inspection of the TKER spectra at Δt = 1 ps between 254 – 237 nm reveals that a new peak is present, centred between 9500 – 11000 cm^{-1}, highlighted by the blue shading in Fig 3.6(a); at 254 and 250 nm this is more clearly seen in Fig. 3.6(b), which presents enlarged portions of these TKER spectra at Δt = 1 ps between ~4000 – 16000 cm^{-1}. The high energy tail of this new feature accords reasonably well with the predicted $TKER_{max}$

for S_2 mediated O^1-H dissociation at these wavelengths, leading us to provisionally propose that this peak arises through a new rapid O^1-H bond fission pathway facilitated by direct dissociation along the S_2 surface. At $\lambda < 243$ nm this becomes the dominant mechanism for S_2 mediated O^1-H fission and is complete by $\Delta t = 1$ ps, as evidenced by the fact that there is no further evolution of the amplitude of this feature by $\Delta t = 50$ ps.

From these time- and frequency-resolved TKER spectra alone, recorded at just two time-delays, it is apparent that between 280.5 – 237 nm two different photophysical mechanisms drive excited state O^1-H bond fission, which we provisionally assign to quantum tunnelling under the S_1/S_2 CI and direct dissociation via the S_2 surface. Additionally, the relative quantum yields for these two processes show a pronounced dependence on the initial excitation energy and take place over two distinctly different

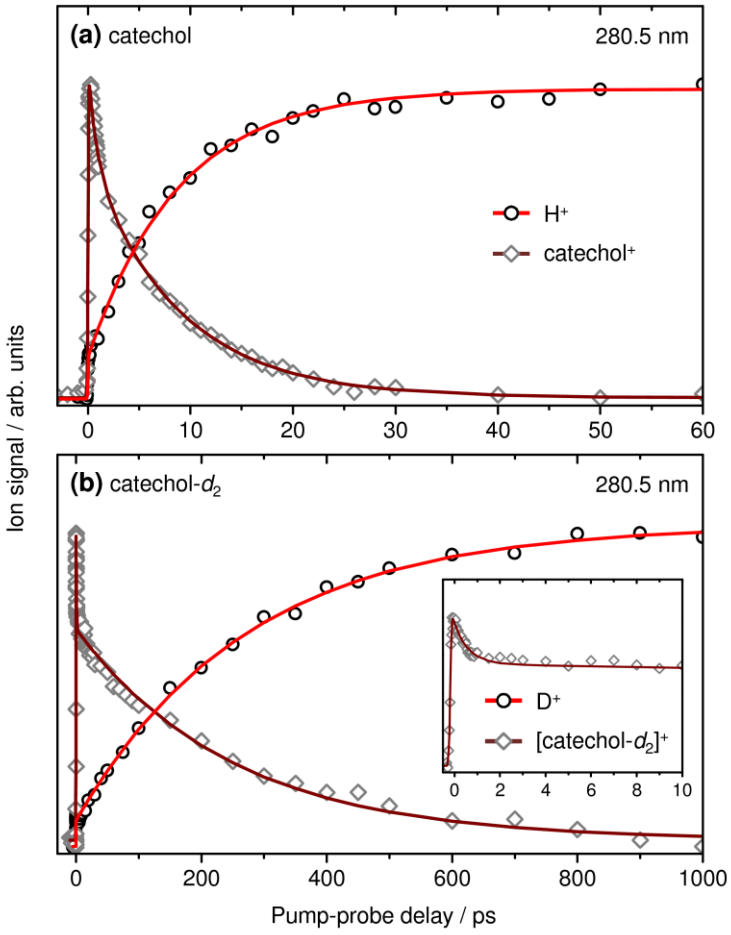

Figure 3.7 (a) Normalised integrated H^+ signal transient after excitation to $S_1(v = 0)$ at 280.5 nm (black circles), obtained by integrating signal between 5000 – 8000 cm^{-1} in TKER spectra recorded at many Δt. Also shown is the corresponding normalised catechol$^+$ parent ion signal transient (grey diamonds) at the same excitation wavelength. Kinetic fits to these transients are indicated by the solid lines (see Chapter 2 for details). (b) Analogous normalised D^+ and [catechol-d_2]$^+$ signal transients (together with kinetic fits) recorded after excitation of catechol-d_2 around $S_1(v = 0)$. Transients associated with catechol-d_2 are presented over a longer Δt window out to 1 ns and the initial rapid decay in [catechol-d_2]$^+$ signal is shown inset (up to 10 ps).

timeframes. Below, we turn to investigate the dynamics of these two processes in a more quantitative manner.

3.4.4 H-atom tunnelling dynamics: λ = 280.5–243 nm

3.4.4.1 Dynamics after excitation to S_1 (v = 0)

Fig. 3.7(a) presents a normalised H^+ signal transient, recorded following excitation around $S_1(v = 0)$ at 280.5 nm (open circles). This transient is obtained by integrating signal over the range 5000 – 8000 cm^{-1} in (one-colour background subtracted) TKER spectra extracted at many Δt between –1 to 60 ps. At $\Delta t < 0$ ps, where excitation occurs at 243.1 nm and 280.5 nm acts as the 'probe' step, we observe negligible 'probe-pump' H^+ signal, in line with the fact that 280.5 nm is unable to resonantly ionize any eliminated H-atoms. Around $\Delta t = 0$ ps there is a sharp rise in signal, which corresponds to the appearance of the small background signal observed in Fig. 3.6(a) at $\Delta t = 1$ ps. The H^+ signal then continues to steadily rise and finally plateaus by ~30 ps, which we attribute to the appearance of H-atoms formed through an $S_1(v = 0) \rightarrow S_2 \rightarrow O^1$-H bond fission mechanism via tunnelling under the S_1/S_2 CI.

In order to extract a time constant for the S_2 mediated O^1-H bond cleavage process after excitation to $S_1(v = 0)$, a kinetic fit to the H^+ transient in Fig. 3.7(a) is performed (red line) using two exponential rise functions each convoluted with our Gaussian IRF (~120 fs FWHM) – see Chapter 2. This fit returns time constants of $\tau_r < 30$ fs,[58] associated with the sharp rise in underlying background signal around $\Delta t = 0$ ps, and $\tau_T = 8.8 \pm 0.3$ ps for tunnelling under the S_1/S_2 CI and subsequent O^1-H bond rupture

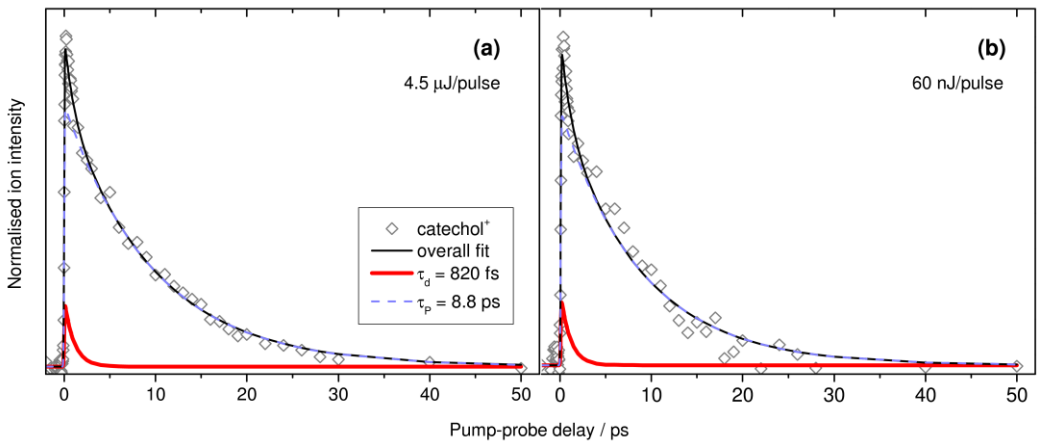

Figure 3.8 Catechol$^+$ parent ion signal transients (grey diamonds) obtained following excitation at 280.5 nm with pump pulse energies of (a) 4.5 mJ/pulse and (b) 60 nJ/pulse. Overall kinetic fits are shown by the black lines. The individual fit components associated with the τ_d and τ_P time constants are shown by the bold red and dashed blue lines, respectively. No change to the amplitude of the t_d component is observed upon reducing the power density of the pump to ~1×10^{10} W cm^{-2}.

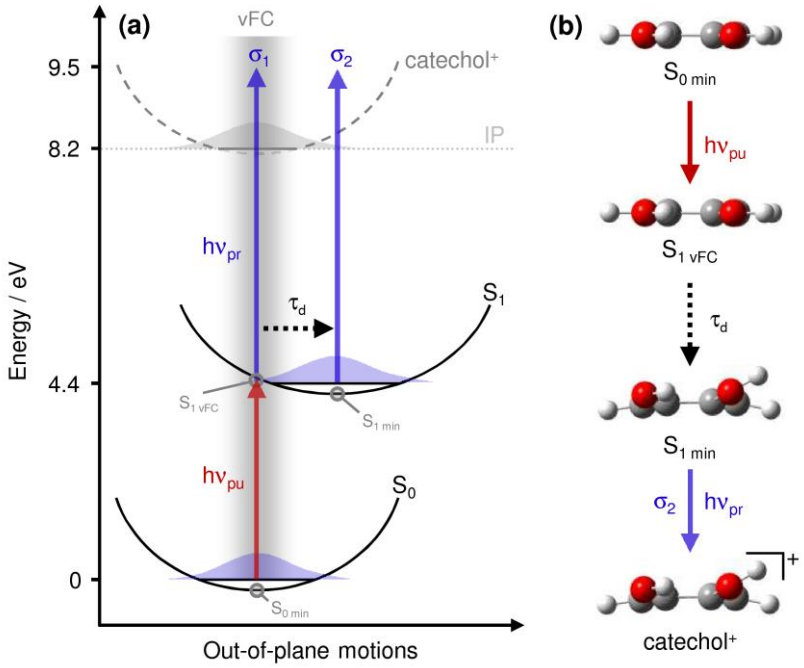

Figure 3.9 (a) Schematic potentials of the S_0 and S_1 electronic states of catechol (as well as the ground state of catechol$^+$) with respect to a general 'out-of-plane' coordinate. After excitation with $h\nu_{pu}$ from the planar $S_{0\ min}$ structure, the planar $S_{1\ vFC}$ structure is prepared in the vertical Franck-Condon (vFC) excitation region of S_1, which subsequently evolves towards the non-planar $S_{1\ min}$ structure on a timescale τ_d. Ionisation of the $S_{1\ vFC}$ and $S_{1\ min}$ structures to catechol$^+$ with $h\nu_{pr}$ occurs with cross-sections of σ_1 and σ_2, respectively. The adiabatic ionisation potential (IP) of catechol (8.2 eV) is also given.[31] (b) Schematics of nuclear geometries associated with $S_{0\ min}$, $S_{1\ vFC}$ and $S_{1\ min}$, based on previous calculated geometries.[49]

along the S_2 state.

In addition to the H^+ signal transient, Fig. 3.7(a) also presents a complementary TR-IY trace of the catechol$^+$ parent ion signal as a function of Δt (grey diamonds), which provides a measure of the dynamics occurring in the initially populated S_1 state after photoexcitation at 280.5 nm (and ionisation with 243.1 nm). Cursory inspection of this catechol$^+$ signal transient, relative to the corresponding H^+ transient, reveals that the S_1 state population decays on a timescale comparable to the appearance of H-atoms associated with O^1-H dissociation into the $C_6H_5O_2(X)$ + H photoproduct channel via the S_2 surface. However, a biexponential decay function (dark red line) is required to model this parent ion trace accurately (see Fig. 3.8), returning time constants of τ_d = 820 ± 120 fs and τ_P = 8.7 ± 0.3 ps.

We first consider the origins of the τ_d = 820 ± 120 fs time constant. In earlier TR-PEI experiments by Livingstone *et al.* at 267 nm (~1800 cm^{-1} above $S_1(v = 0)$), a sub-picosecond decay component (~320 fs) was also observed in the S_1 state dynamics and was attributed to rapid intramolecular vibrational energy redistribution (IVR) through a vibrational 'doorway' state.[31] However, following excitation around $S_1(v = 0)$ it is extremely unlikely that τ_d is associated with a similar process, given the very low

density of vibrational states accessed in S_1 at this energy. Alternatively, τ_d may result from two-photon induced formation (with $h\nu_{pu}$) and decay of 'super-excited' states in catechol (rather than dynamics in S_1), which has previously been observed to occur over a comparable timeframe in phenol.[22] To investigate this further, we have also recorded TR-IY traces of the catechol$^+$ signal with significantly lower $h\nu_{pu}$ intensities (~60 nJ/pulse, ~1×10^{10} W cm^{-2}) and observed no significant reduction in the amplitude of this signal component (see Fig. 3.8), suggesting that two-photon excitation and decay of super-excited states is not responsible for τ_d. We note that, based on energy conservation grounds, Livingstone *et al*. were also able to rule out the formation of super-excited states at 267 nm in their TR-PEI measurements.[31] At this stage, we recall from previous studies that the nuclear geometry of $S_{1\,min}$ is highly non-planar, whereas the S_0 minimum geometry ($S_{0\,min}$), as well as that of the catechol$^+$ ion (to which ionisation occurs), are both planar.[46, 47] With reference to the schematic in Fig. 3.9, immediately following excitation from the planar $S_{0\,min}$ geometry, S_1 will be prepared in a planar geometry ($S_{1\,vFC}$), away from $S_{1\,min}$. Subsequent evolution towards $S_{1\,min}$ may then result in a modification of the cross-section for ionisation to catechol$^+$ ($S_1 \rightarrow S_2$).[59] Based on this reasoning, we therefore propose that τ_d represents the timescale for an initial geometry rearrangement out of the vertical Franck-Condon (vFC) region in the photoprepared S_1 state, towards $S_{1\,min}$. Additional support for this interpretation can be garnered through a comparison with previous TR-IY measurements on phenol around $S_1(v = 0)$, which only exhibit a single exponential decay,[29] consistent with the fact that its $S_{0\,min}$ and $S_{1\,min}$ geometries are both planar.[8] We acknowledge though, that further time-resolved photoelectron spectroscopy measurements after excitation around $S_1(v = 0)$ are ultimately required to fully validate this hypothesis.[59]

The second time constant of τ_P = 8.7 ± 0.3 ps extracted from the TR-IY trace in Fig. 3.7(a) is ascribed to population decaying out of the S_1 state, and shows a clear correlation with the appearance time constant for $C_6H_5O_2(X)$ + H photoproducts born through tunnelling onto the S_2 state under the S_1/S_2 CI (τ_T = 8.8 ± 0.3 ps). This observation is in line with sequential first-order kinetics for a unimolecular reaction, where the appearance of the 'product', $C_6H_5O_2(X)$ + H, mirrors the decay of the 'reactant', $S_1(v = 0)$.

To definitively confirm the role of tunnelling in the ensuing dynamics after excitation around $S_1(v = 0)$, we have also performed measurements on the deuterated isotopomer, catechol-d_2 (selective deuteration of both O-H bonds). A TR-IY trace of the

[catechol-d_2]$^+$ signal, as well as a normalised D$^+$ signal transient (obtained by integrating time-resolved TKER spectra derived from measured D$^+$ velocity map images, between 5000 – 8000 cm^{-1}), are presented in Fig. 3.7(b). Kinetic fits to these traces return time constants of τ_P = 250 ± 10 ps and τ_T = 270 ± 10 ps, and in turn an (average) kinetic isotope effect (k_H/k_D) of ~30. Such a large kinetic isotope effect provides extremely strong evidence that coupling onto the S_2 state, prior to O^1-H dissociation in catechol, does indeed proceed through tunnelling under the S_1/S_2 CI. We also briefly state that the [catechol-d_2]$^+$ signal trace returns a τ_d value of 620 ± 140 fs (see Fig. 3.7(b), inset), which (within the associated uncertainties) is comparable to the value extracted from the undeuterated species (820 ± 120 fs). With reference to Fig. 3.9 once more, the apparent minimal impact of selective O-H deuteration on the τ_d time constant confers with a picture where evolution away from the planar $S_{1\ vFC}$ structure towards $S_{1\ min}$, not only involves out-of-plane O-H torsion motion,[46] but is also dominated by significant distortion of the heavier ring framework and C-O bonds.[47]

Analogous to the undeuterated species, depletion of the S_1 state population, τ_P, mirrors the concomitant increase in the photoproducts resulting from O^1-D bond rupture via S_2, τ_T, in catechol-d_2. This observation of sequential first-order kinetics in *both* catechol-d_2 and catechol leads us to speculate that tunnelling onto the S_2 state could be the primary process driving population loss out of S_1(v = 0) in catechol, kinetically outcompeting slower radiative decay pathways such as fluorescence. However, up to this stage we have neglected to consider the participation of possible

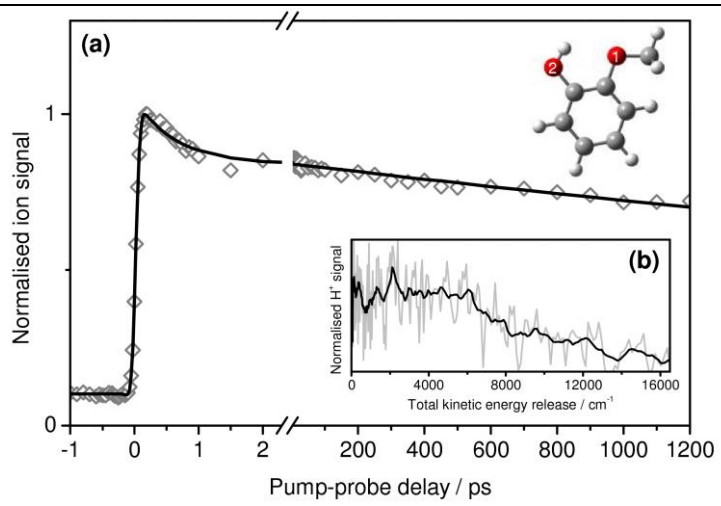

Figure 3.10 (a) Normalised guaiacol$^+$ parent ion signal transient (grey diamonds) recorded after excitation to S_1(v = 0) at 278 nm and probing (ionisation) with 243.1 nm (molecular structure of guaiacol shown inset). A kinetic fit to the transient is shown by the solid black line. (b) TKER spectrum (grey line) recorded after excitation of guaiacol at 278 nm and probing H-atom photoproducts using a time-delayed 243.1 nm probe pulse at Δt = 1.2 ns. A 5-point average through the raw TKER spectrum is shown by the black line.

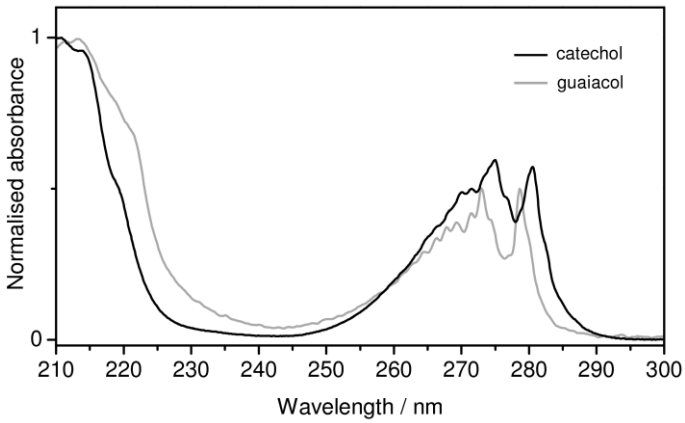

Figure 3.11 Vapour-phase UV absorption spectrum of guaiacol (grey) recorded over the range 210 – 300 nm. The $S_1(v = 0)$ origin band of guaiacol is determined to lie at ~278 nm.[64,65] The vapour-phase UV absorption spectrum of catechol is shown for comparison (black).

alternative decay pathways, which may also play a role in defining the S_1 state lifetime of catechol, τ_P (and in turn τ_T). In particular, excited state intramolecular proton transfer (ESIPT) has been recognised to play a key role in the relaxation dynamics of many species containing intramolecular hydrogen bonds.[60, 61] In catechol, this pathway may, in principle, proceed via H^+ transfer from the O^2-H group onto the O^1 site through the intramolecular hydrogen bond, offering an alternative method for rapid repopulation of the S_0 ground state from S_1 (*cf*. ESIPT in the prototypical system malonaldehyde[62]). If the measured S_1 state lifetime, τ_P, is instead a reflection of the timescale for ESIPT, then branched kinetics dictate that the appearance time of any H-atoms eliminated through O^1-H bond cleavage via the S_2 surface, τ_T, would still match τ_P, consistent with our results presented in Fig. 3.7 (we note though that any ESIPT process must also occur via tunnelling, given the measured kinetic isotope effect of ~30). Thus, to determine whether an ESIPT mechanism is instead responsible for defining τ_P and τ_T in catechol, we have performed comparative TR-IY measurements on the related species guaiacol (structure shown inset in Fig. 3.10). In guaiacol, H-atom elimination from the O^1-H site is blocked as a result of methylation, and its vapour-phase UV absorption spectrum is very comparable to that of catechol's (see Fig. 3.11), suggesting that methylation does not dramatically perturb the electronic structure ($S_1(v = 0)$ is only blue-shifted by ~2 nm in guaiacol, relative to catechol).[63, 64] If ESIPT is the primary process for S_1 state relaxation in catechol, we may also anticipate similar rapid S_1 state decay dynamics in guaiacol.

Fig. 3.10(a) displays the guaiacol$^+$ parent signal transient after excitation to $S_1(v = 0)$ at 278 nm, and probing with 243.1 nm (grey diamonds). As with catechol, there is also a sub-picosecond decay component to the S_1 state dynamics of guaiacol. However, most strikingly, the transient in Fig. 3.10(a) clearly demonstrates that the S_1

Table 3.1 Time constants extracted from kinetic fits to catechol$^+$ parent ion signal transients (τ_d and τ_P) and integrated H^+ signal transients (τ_T and τ_{CI}), recorded at excitation wavelengths (λ) across the range 280.5 – 237 nm. τ_T and τ_{CI} were extracted from H^+ signal transients, which are generated via integration across the TKER ranges of 5000 – 8000 cm^{-1} and 10000 – 14000 cm^{-1}, respectively. Quoted errors correspond to two standard deviations (2σ). τ_d = ultrafast IVR lifetimes on the S_1 surface (at $S_1(v = 0)$ τ_d is assigned to a geometry rearrangement away from the planar $S_{1\ vFC}$ geometry); τ_P = S_1 state lifetimes; τ_T = hydrogen tunnelling lifetimes; τ_{CI} = lifetimes for ultrafast O^1-H fission after direct excitation to the S_2 surface.

		Extracted time constants			
λ / nm	S_1 excess internal energy[a] / cm^{-1}	τ_d / fs	τ_P / ps	τ_T / ps	τ_{CI} / fs
280.5	0	820 ± 120	8.7 ± 0.3	8.8 ± 0.3	…
273	980	620 ± 40	11.8 ± 0.3	9.7 ± 0.3	…
267	1800	535 ± 80	11.5 ± 0.4	10.5 ± 0.3	…
260	2810	460 ± 70	9.4 ± 0.4	9.2 ± 0.5	…
254	3720	200 ± 50	7.0 ± 0.4	5.4 ± 0.4	88 ± 42
250	4350	300 ± 80	7.1 ± 0.7	6.6 ± 0.4	85 ± 22
246	5000	130 ± 70	5.9 ± 0.4	5.4 ± 0.5	89 ± 24
243	5500	< 30	7.6 ± 1.5	5.5 ± 1.2	99 ± 22
240	6020	…	…	…	120 ± 15
237	6540	…	…	…	125 ± 18

[a] Quoted energies correspond to 'mean' excess internal energies, given the ~500 cm^{-1} bandwidth of the fs excitation pulses, $h\nu_{pu}$.

state lifetime of guaiacol is orders of magnitude longer than catechol's, extending further than the maximum Δt attainable with our current experimental setup (>1.2 ns). A kinetic fit to this transient (black line) returns an approximate S_1 state lifetime for guaiacol of $\tau_P \approx 7$ ns. This observation supports a conclusion that the S_1 state lifetime of τ_P = 8.7 ± 0.3 ps in catechol is not due to ESIPT from the hydrogen bonded O^2-H coordinate, but rather tunnelling under the S_1/S_2 CI on to the S_2 state and subsequent O^1-H bond fission. Furthermore, we have also studied H-atom elimination from photoexcited guaiacol at 278 nm, with a TKER spectrum taken at Δt = 1.2 ns shown in Fig. 3.10(b). Only a broad 'Boltzmann-like' profile of H-atoms is observed, with no obvious signature for O^2-H bond fission via a dissociative ($^1\pi\sigma^*$) state, adding weight to our earlier conclusion that the H-atom signal assigned to dissociation via the repulsive S_2 state in catechol, primarily results from O^1-H fission.

3.4.4.2 Effects of excess internal energy

Further to measurements around $S_1(v = 0)$, we have also extracted values for τ_T, τ_P and τ_d from kinetic fits to H^+ and catechol$^+$ signal transients at a number of shorter wavelengths across the range 273 – 243 nm, where tunnelling dynamics under the S_1/S_2 CI remain active, shown in Fig. 3.12 and Fig. 3.13. These time constants are collated in Table 3.1 and are also presented as a function of the excess internal energy imparted to the S_1 state in Fig. 3.14, where $S_1(v = 0)$ correlates to 0 cm^{-1}. We note that: (*i*) at 267 nm the extracted τ_P and τ_T time constants are in good agreement with the S_1 state lifetime previously measured through TR-PEI (12 ps);[31] and (*ii*) below 254 nm, tunnelling dynamics from the S_1 state begin to deactivate, most likely a reflection of a poor Franck-Condon overlap for initial population of a highly vibrationally excited S_1

state,[65] which manifests as a very weak absorbance between ~245 – 230 nm in Fig. 3.4(b).

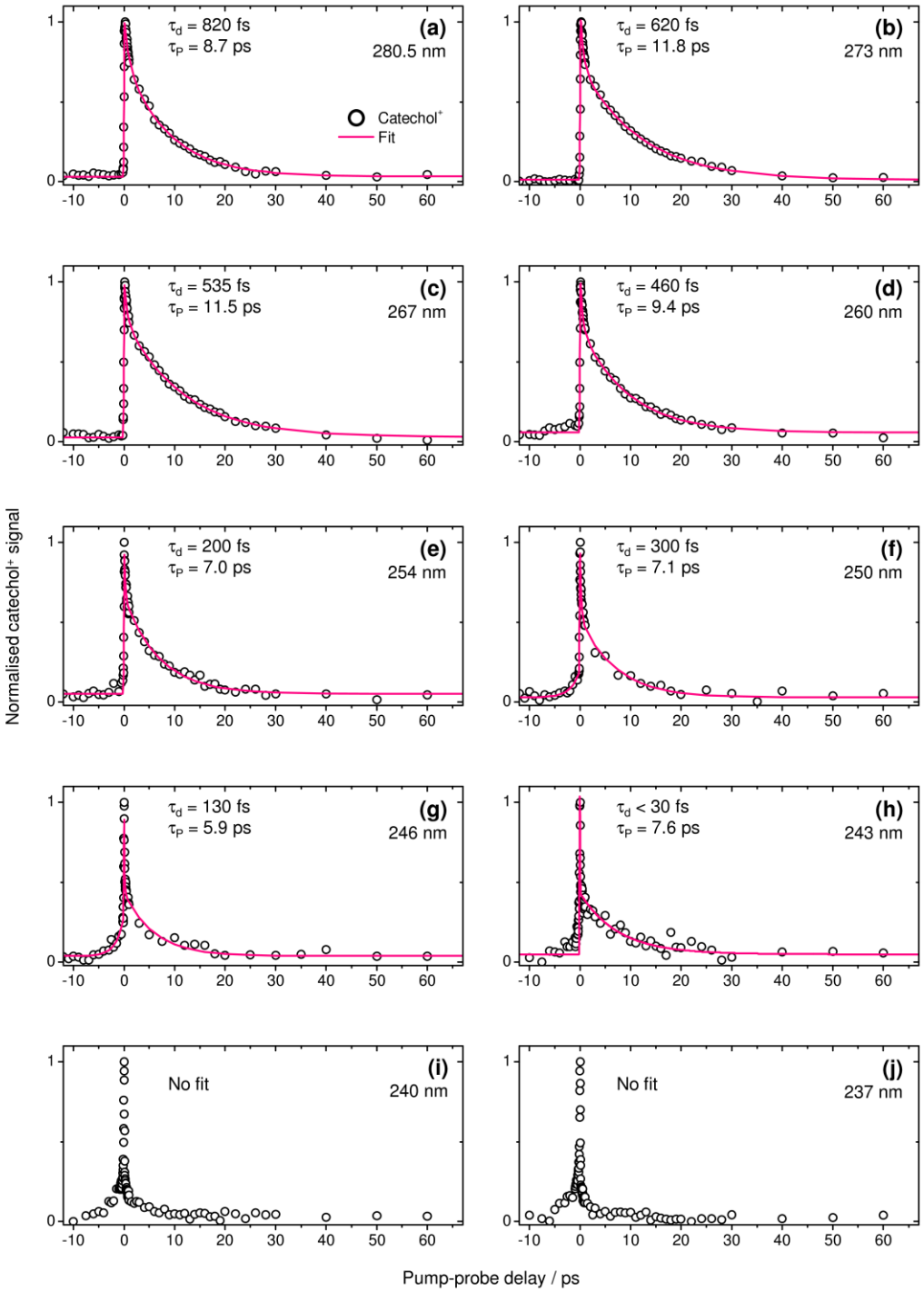

Figure 3.12 Catechol+ parent ion signal transients (open circles) recorded at many wavelengths over the range 280.5 – 237 nm. Associated kinetic fits to the data are indicated by the pink lines. Extracted time constants at each excitation wavelength are also provided.

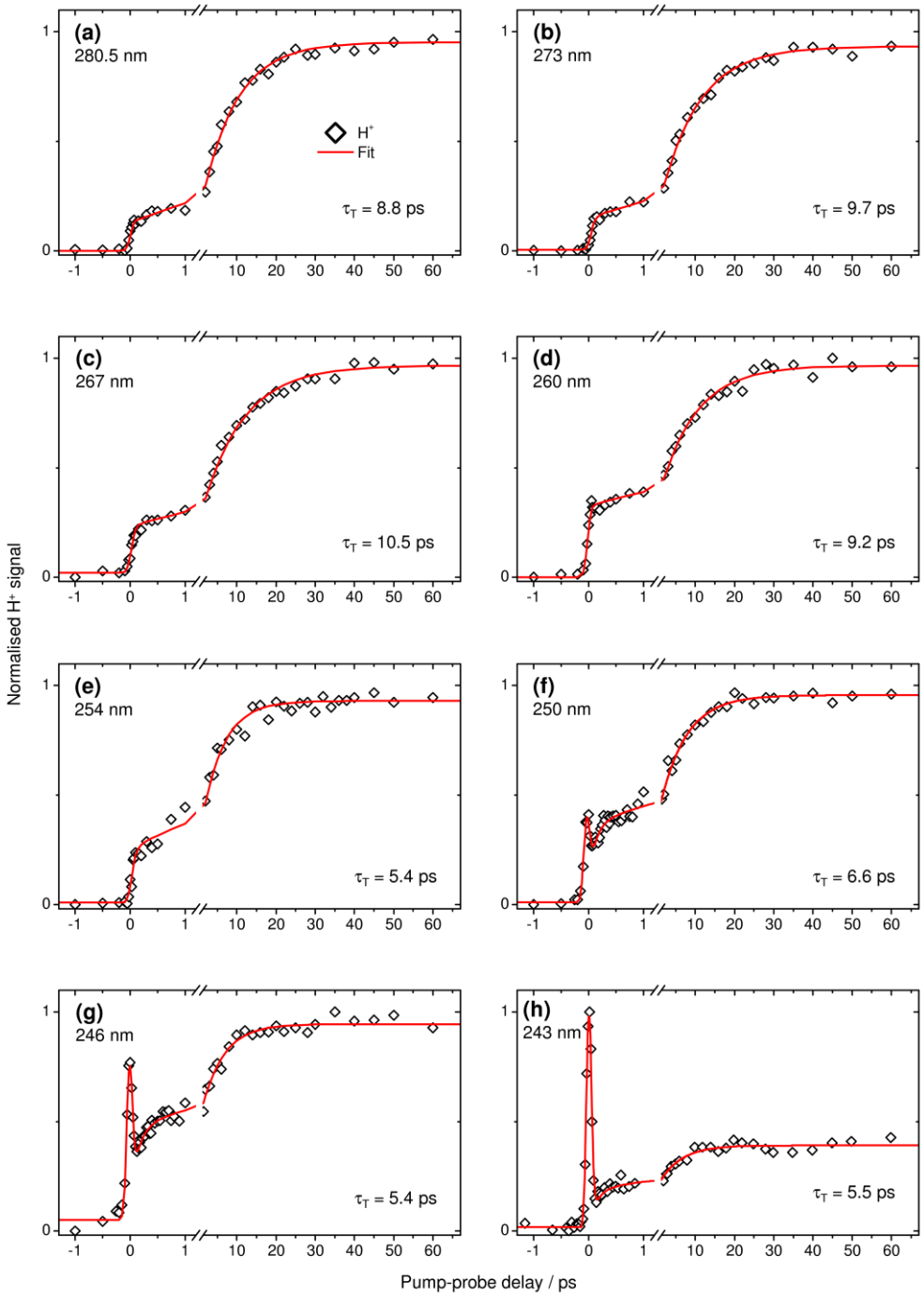

Figure 3.13 H^+ signal transients obtained by integrating signal in TKER spectra over the range 5000 – 8000 cm^{-1} at many Δt (open diamonds), over the excitation wavelength range 280.5 – 243 nm (where tunnelling dynamics are observed to be active). Kinetic fits to the transients using either two rises (280.5 – 254 nm) or two rises and a decay (250 – 243 nm) are indicated by the red lines. Extracted τ_T time constants are also provided.

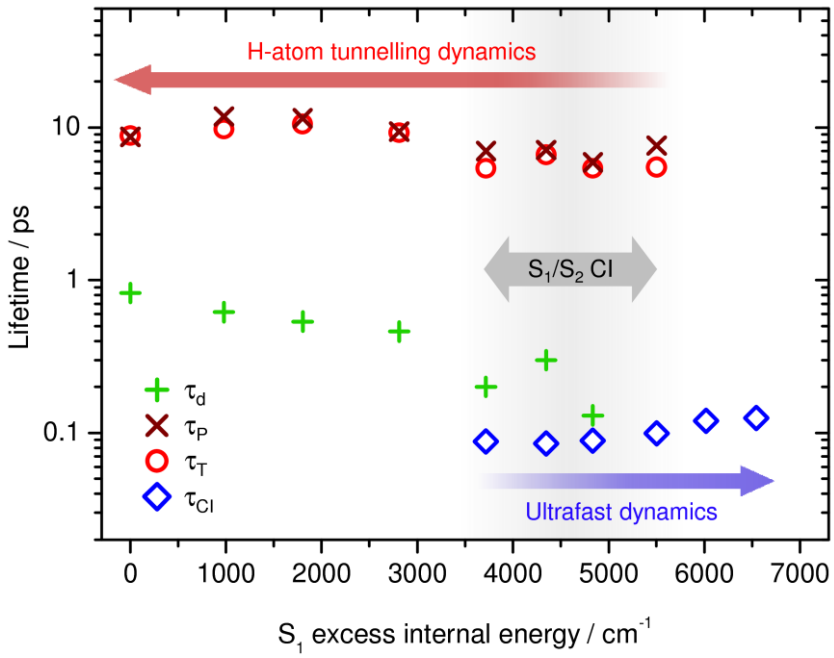

Figure 3.14 Time constants extracted from kinetic fits to H^+ and catechol$^+$ ion signal transients (across the excitation wavelength range 280.5 – 237 nm), shown as a function of excess internal energy imparted to the S_1 state. Excitation at $S_1(v = 0)$ correlates to 0 cm^{-1}. τ_d = ultrafast IVR lifetimes on the S_1 surface (at $S_1(v = 0)$ τ_d is assigned to a geometry rearrangement away from the planar $S_{1\,vFC}$ geometry); τ_P = S_1 state lifetimes; τ_T = hydrogen tunnelling lifetimes; τ_{CI} = lifetimes for ultrafast O^1-H fission after direct excitation to the S_2 surface.

Briefly, we consider the τ_d time constants. At $S_1(v = 0)$ we assigned this to evolution of the nuclear geometry away from a planar structure in the vFC window towards the non-planar $S_{1\,min}$ structure (see Fig. 3.9). At $\lambda \leq 273$ nm however, excitation is now likely to be above the threshold for IVR in catechol's S_1 state and, as with previous TR-PEI studies by Livingstone *et al.*, we speculate that there may be contributions from 'ultrafast' IVR in the S_1 potential surface, mediated by vibrational 'doorway' states.[31] If such a mechanism were operative at $\lambda \leq 273$ nm one may anticipate that τ_d will decrease as the density of available vibrational states in the S_1 potential surface grows with increasing excitation energy. Indeed, Fig. 3.14 clearly shows an overall decrease in τ_d as the amount of excess internal energy imparted to S_1 increases, decreasing from ~820 fs at 280.5 nm to ~130 fs at 246 nm,[2] lending support to a mechanism involving IVR.

We now return to the extracted τ_P and τ_T time constants. As with excitation at $S_1(v = 0)$, the values for τ_P and τ_T, at a given wavelength, are in excellent agreement with each other across the entire excitation range. However, what is perhaps most striking from Fig. 3.14 is that, unlike the τ_d time constants, there is minimal change to

[2] We acknowledge that at excitation wavelengths below 254 nm, the extracted τ_d time constants may contain contributions from rapid population decay out of the S_2 state, which can be directly populated below 254 nm

τ_P and τ_T up to ~3000 cm^{-1} above $S_1(v = 0)$ (280.5 – 260 nm), only spanning between ~9 – 11 ps. This accords with the proposed mechanism from our earlier investigations of tunnelling dynamics in photoexcited phenol[29] (as well as other related species[65]), which suggest that the tunnelling lifetime under an analogous S_1/S_2 CI is largely independent of the amount of excess vibrational energy initially imparted into the S_1 state. As with these previous studies, the near-invariance of τ_P and τ_T over this excitation range can be rationalised by recognising that, with respect to the $R_{O1\text{-}H}$ dissociation coordinate (Fig. 3.4(a)), tunnelling under the S_1/S_2 CI proceeds from an energy which is around the ZPE point energy of the O^1-H stretch in S_1, and any excess vibrational energy (located in modes orthogonal to $R_{O1\text{-}H}$) is mapped directly through into the $C_6H_5O_2(X)$ photoproducts. We note that this interpretation is also consistent with our earlier conclusions drawn from the observed energy disposal in the time-resolved TKER spectra between 273 – 260 nm in Fig. 3.6(a).

Above ~3000 cm^{-1} in Fig. 3.14 (254 – 243 nm), there is a small decrease in τ_P and τ_T from ~9 – 11 ps to ~5 – 7 ps. This energy threshold corresponds to the approximate location of a single quantum of the O^1-H stretch in the S_1 state, $S_1(v_{O1\text{-}H} = 1)$.[66] Although direct excitation to the $S_1(v_{O1\text{-}H} = 1)$ level is improbable across the entire 254 – 243 nm excitation range, we recall that 'ultrafast' IVR likely plays a role in the S_1 excited state dynamics.[31] This leads us to assign the decrease in τ_P and τ_T to a reduction in the overall tunnelling lifetime via contributions from tunnelling out of the $S_1(v_{O1\text{-}H} = 1)$ level, after it is populated through rapid IVR. Once again, just considering the tunnelling process with respect to the $R_{O1\text{-}H}$ coordinate (Fig. 3.4(a)), the barrier to tunnelling under the S_1/S_2 CI from $S_1(v_{O1\text{-}H} = 1)$ will be considerably less that at $S_1(v = 0)$, resulting in a significant (orders of magnitude) reduction in the effective tunnelling lifetime (*cf*. potentials in Fig. 3.4(a)), given the tunnelling lifetime decreases exponentially as the size of the barrier area reduces.[8, 25, 29] Here however, we only observe a decrease of approximately half in the recorded values of τ_P and τ_T, relative to excitation at energies <3000 cm^{-1} above $S_1(v = 0)$, suggesting that tunnelling from the zero-point level of the O^1-H stretch in the S_1 state remains the dominate tunnelling pathway even at >3000 cm^{-1} above $S_1(v = 0)$, with only a small contribution from the $S_1(v_{O1\text{-}H} = 1)$ level.

3.4.5 Ultrafast dissociation dynamics via the S_2 state: λ = 254–237 nm

At excitation wavelengths between 254 – 237 nm, a new rapid O^1-H bond cleavage process along the S_2 surface becomes an open channel, as evidenced by the time-resolved TKER spectra in Fig. 3.6. In Fig. 3.15 a representative H^+ signal transient

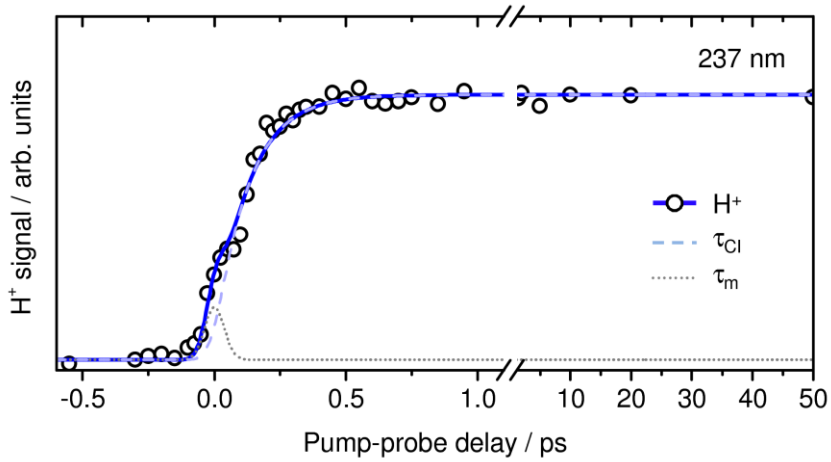

Figure 3.15 H^+ signal transient after excitation at 237 nm (circles), obtained by integrated signal between 10000 – 14000 cm^{-1} in TKER spectra recorded at many Δt. An overall kinetic fit to the trace is shown by the solid blue line, with the individual τ_m < 30 fs (dotted line) and τ_{CI} = 125 fs (dashed line) components also shown (see main text for details).

associated with this feature at 237 nm is presented (circles). This has been obtained by integrating over the high energy edge of this feature (10000 – 14000 cm^{-1}) in a series of time-resolved TKER spectra between –0.5 to 50 ps. Unlike the H^+ signal transient arising from tunnelling under the S_1/S_2 CI (Fig. 3.7(a)), the signal associated with O^1-H bond rupture along the S_2 state at 237 nm rises rapidly around Δt = 0 ps and then plateaus by ~0.5 ps, with no further signal increase out to Δt = 50 ps; this confirms our earlier interpretation that these O^1-H bond fission dynamics are indeed ultrafast and are complete within less than 1 ps. This H^+ transient has been fitted with an exponential rise function, in addition to an exponential decay function; the latter accounts for signal arising from undesired multiphoton effects when the pump and probe pulses are temporally overlapped, manifesting as a small 'kink' in the recorded H^+ signal transient around Δt = 0 ps in Fig. 3.15 (also see Fig. 3.16). This overall kinetic fit is shown by the solid blue line in Fig. 3.15, generating time constants of t_m < 30 fs (dotted line) for the decay of the multiphoton induced signal component around Δt = 0 ps, and τ_{CI} = 125 ± 18 fs (dashed line) for the appearance of H-atoms formed through O^1-H dissociation along the S_2 surface.

In Table 3.1 and Fig. 3.14 we have also collated the values for τ_{CI} extracted at other wavelengths where these ultrafast S_2 mediated O^1–H bond fission dynamics are active (254–237 nm). All values for τ_{CI} are on the order of ~100 fs (ranging from 85–125 fs). The associated H^+ signal transients and kinetic fits at these additional wavelengths are provided in Fig. 3.16.

We now consider in more detail the photophysical mechanism which gives rise to this ultrafast O^1–H bond fission along the S_2 surface at these shorter excitation wavelengths. Intuitively, there are two possible pathways: (i) initial excitation to the S_1 state followed by coupling onto the S_2 state at the S_1/S_2 CI; or (ii) direct excitation to the S_2 state and subsequent evolution through the S_1/S_2 CI. With respect to the former, there is a key experimental observation which makes it difficult to reconcile these ultrafast dissociation dynamics with an $S_1 \rightarrow S_2 \rightarrow O^1$–H bond fission mechanism: Fig. 3.6 and Fig. 3.14 demonstrate that, between 254–243 nm, ultrafast dissociation along the S_2 surface and tunnelling under the S_1/S_2 CI are both active processes. If both processes originate from the S_1 state, then the S_1 state lifetime should be defined solely

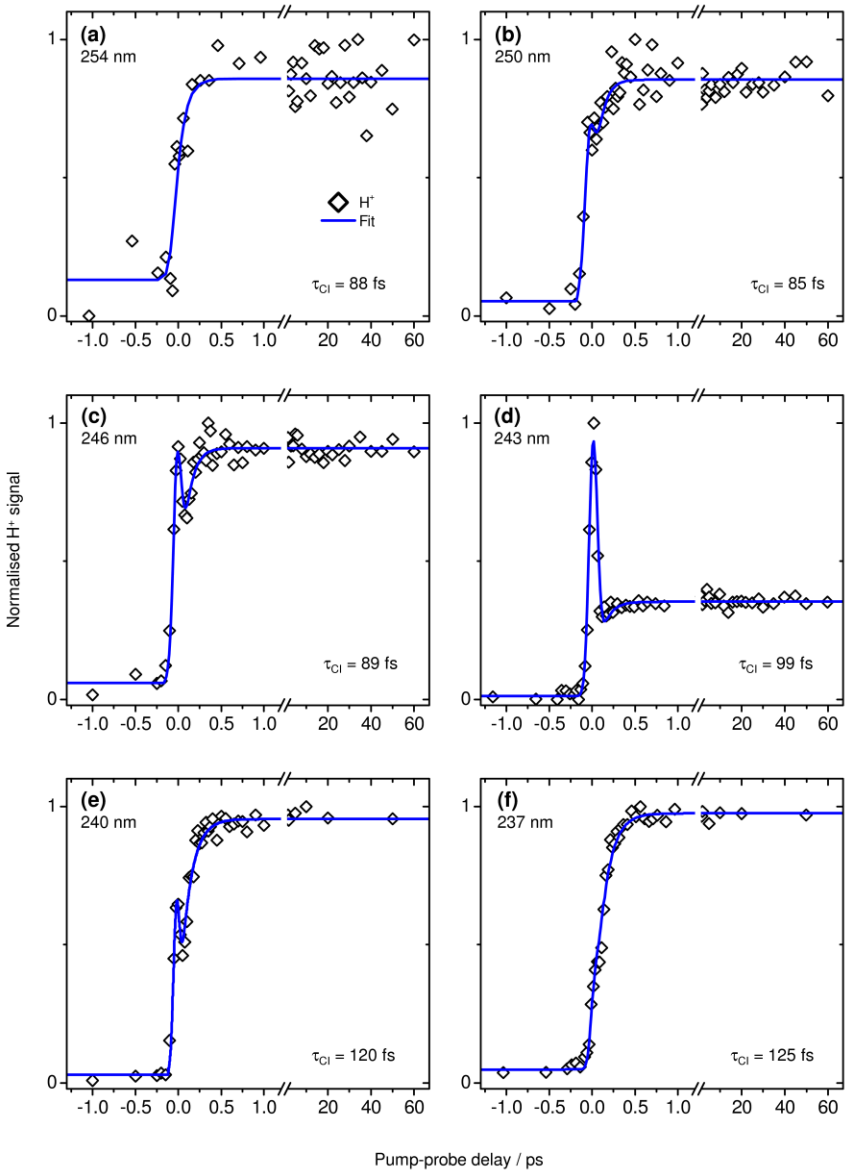

Figure 3.16 H^+ signal transients obtained by integrating signal in TKER spectra over the range 10000 – 14000 cm^{-1} at many Δt (open diamonds), over the excitation wavelength range 254 – 237 nm (where ultrafast O^1-H fission dynamics are observed to be active). Kinetic fits to the transients using one rise and one decay function are indicated by the blue lines. Extracted τ_{CI} time constants are also provided.

by the timescale for ultrafast $S_1 \rightarrow S_2 \rightarrow O^1$–H bond fission (~100 fs), effectively deactivating the slower tunnelling process (~5–7 ps), as dictated by simple branched kinetics. However, this behaviour is clearly not observed here, leading us to propose that the ultrafast O^1–H fission dynamics are instead born through direct excitation to the S_2 surface.

In principle, an analysis of the H-atom photofragment angular recoil distribution for this feature, between 254 – 237 nm, could aid to confirm direct excitation to the S_2 state. Unfortunately, in catechol we observe a consistently isotropic recoil distribution ($\beta_2 = 0$) for this feature across this excitation range, making it difficult to gain any additional information from β_2 (we note though that this isotropic distribution cannot be due to rotational dephasing of the parent molecule,[20] given the ultrafast nature of the O^1-H dissociation dynamics). In spite of this, support for such a mechanism can be found through a comparison with O-H bond fission dynamics in phenol, which below 248 nm have also been assigned to a mechanism involving direct excitation to the S_2 surface;[8] similar reasoning was also used by Ashfold and co-workers to interpret their earlier HRA-PTS studies on catechol.[47] In addition to this, the calculated 1-D PECs in Fig. 3.4(a) suggest that there may be a small 'quasi-bound' well in the vFC region of the S_2 surface in catechol (formed as a result of mixing with a $^1\pi 3s$ manifold, where the 3s Rydberg character is associated with the O^1 heteroatom[67, 68]). The presence of quasi-bound vibrational levels in the vFC region of the S_2 state could very well enhance the probability for its direct excitation, as observed in studies of analogous dissociation dynamics in other heteroaromatic species.[65, 69] Based on the combined reasoning above, we therefore conclude that the τ_{CI} time constants represent the timescale for an ultrafast O^1-H fission mechanism, driven by direct excitation to the dissociative S_2 state and subsequent evolution through the S_2/S_0 CI.

3.5 Discussion

3.5.1 Location of the S_1/S_2 CI

In previous HRA-PTS studies by King *et al*., it was proposed that the onset for accessing the S_1/S_2 CI in catechol lies within the broad excitation range of 265 – 230 nm.[47] This is in contrast to phenol, where HRA-PTS measurements have accurately placed the CI at 248 nm.[5] From our present results on catechol (Fig. 3.14 and Table 3.1), we find that the onset for direct excitation to the S_2 state occurs at ~254 nm, and that between 254 – 243 nm excitation results in population of both the S_1 and S_2 states (a superposition), manifesting in the experimental observation of both tunnelling dynamics under the

S_1/S_2 CI and ultrafast O^1-H dissociation along the S_2 surface. The observed contribution of tunnelling under the S_1/S_2 CI from the $S_1(v_{O1\text{-}H} = 1)$ level from below ~254 nm (see above) indicates that the S_1/S_2 CI must lie at λ < 254 nm for this process to be active. This leads us to propose a refined narrower excitation range of <254 to 243 nm for the location of the S_1/S_2 CI (highlighted in Fig. 3.14 by the grey arrow) and by extension a corresponding barrier height for tunnelling from $S_1(v = 0) \rightarrow S_2$ of between ~3700 – 5500 cm^{-1}.

Guided by calculated 1-D PECs along the O^1-H coordinate at the EOM-CCSD/aug-cc-pVDZ level and findings from TR-PEI experiments conducted at 267 nm, Livingstone *et al*. proposed that a smaller 1-D barrier to tunnelling under the S_1/S_2 CI in catechol may contribute to the shorter S_1 state lifetime of ~12 ps (*cf*. ~1 ns in phenol), although they acknowledge that interpreting such tunnelling behaviour with a simple 1-D model is likely to be insufficient to fully rationalise catechol's significantly reduced S_1 state lifetime.[31] Indeed, the present more comprehensive experimental studies ultimately imply that the barrier height to tunnelling under the S_1/S_2 CI in catechol is comparable to that measured for phenol (~4000 cm^{-1}).[2] These new findings therefore lead us to explore the possible causes of the significantly enhanced tunnelling rate observed in catechol, relative to phenol.

3.5.2 Origins of the enhanced tunnelling rate in catechol

In the TR-VMI studies on phenol, we demonstrated that the timescales for H-atom tunnelling under the S_1/S_2 CI could, to first-order, be modelled reasonably adequately using a simple 1-D tunnelling picture along the O-H stretch coordinate only[29] (similar conclusions were also drawn through TR-IY studies by Pino *et al*.[18]). Given our experimental observation that the barrier heights to tunnelling in catechol and phenol are comparable, invoking a similar 1-D model along the $R_{O1\text{-}H}$ coordinate in catechol would require a much steeper gradient of the S_2 potential (beyond the S_1/S_2 CI) and, in turn, a notable reduction in the barrier *width* (along $R_{O1\text{-}H}$), to account for the sizeable reduction in catechol's tunnelling lifetime, relative to phenol. Our present calculated 1-D PECs along $R_{O1\text{-}H}$ shown in Fig. 3.4(a), suggest that, when compared to earlier calculated 1-D PECs for phenol (see refs. [8] and [29]), there is no major difference in the gradient of the dissociative S_2 potential beyond the S_1/S_2 CI in catechol. This leads us to conclude that applying a 1-D tunnelling model to catechol is simply inadequate for describing the observed tunnelling dynamics, in-line with previous postulates by Livingstone *et al*.,[31] and that the origins of the enhanced tunnelling rate in catechol occur as a result of alternative behaviour.

Experimental observations from HRA-PTS measurements, together with symmetry considerations, led Dixon *et al*. to demonstrate that a more comprehensive description of the tunnelling dynamics in phenol can be attained using a 2-D model along both the O-H stretch and ν_{16a} coordinates,[8] the latter of which is a ring torsion motion and is responsible for vibronically coupling population from $S_1 \rightarrow S_2$. These calculations demonstrate that, even with the inclusion of just one key additional nuclear degree of freedom (ν_{16a}), the effective barrier area to tunnelling under the S_1/S_2 CI is reduced, leading to a greater 'vibrationally-enhanced' tunnelling probability of up to ~40 % (relative to a 1-D picture).[8, 32]

In phenol, the planar minimum energy structures of both the S_0 ground state and the S_1 state conform to a non-rigid G_4 (isomorphous with C_{2v}) symmetry, as evidenced by the presence of peak splitting due to torsional tunnelling in high-resolution spectroscopy studies.[66, 70] Based on these symmetry restraints, only modes of a_2 symmetry have the potential to couple population from the S_1 ($^1B_2$) state onto the S_2 ($^1B_1$) state in phenol, of which ν_{16a} has the lowest frequency in S_1 (out of a total of only three available a_2 modes).[8] In catechol however, the geometry of $S_{1\ min}$ is known to be highly non-planar and as a result, possesses much lower C_1 symmetry,[46, 47] meaning that any low frequency vibrations may *a priori* reduce the multidimensional barrier width, and so enhance tunnelling from the S_1 state. We also note that *ab initio* calculations (see Fig. 3.17) suggest many of these lowest frequency vibrations in the S_1 state exhibit strongly mode-mixed character (sharing O-H torsion and in- and out-of-plane ring distortion), supporting earlier interpretations drawn by King *et al*.[47] This therefore leads us to propose that the reduced tunnelling lifetime observed for catechol, relative to phenol, largely arises through a highly 'vibrationally-enhanced' tunnelling process. This is a direct result of the relaxed C_1 symmetry constraints in catechol's S_1 state, leading to a significant *effective* reduction of the *multi-dimensional barrier area* under the S_1/S_2 CI; such a process can be viewed as an extreme multi-dimensional analogue of the 2-D tunnelling model adopted by Dixon *et al*. to describe the tunnelling behaviour in phenol.[8] We acknowledge that any more detailed rationale for understanding such a process would require a treatment of these tunnelling dynamics with calculated fully multi-dimensional potential energy surfaces, extending far beyond the scope of these present studies.

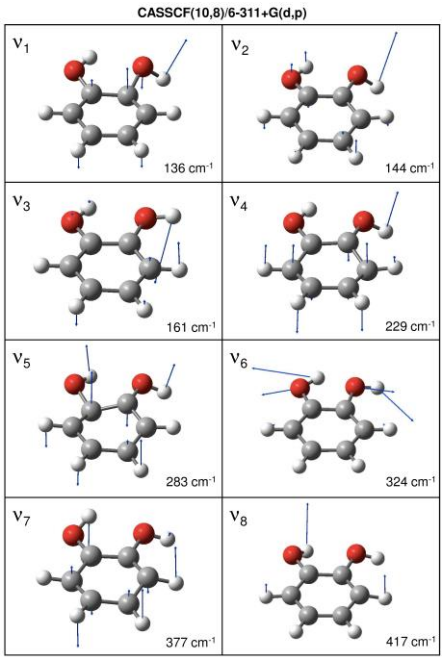

Figure 3.17 Calculated harmonic frequencies for catechol in its S_1 state at the CASSCF(10,8)/6-311+G(d,p) level. The eight lowest frequency modes are presented (labelled ν_1 to ν_8). All eight vibrations exhibit significant mode-mixed character, including O-H torsion and in- and out-of-plane motions.

3.6 Conclusions

The nature of hydrogen dissociation in both phenol and catechol has been comprehensively explored using time-resolved H atom imaging and time resolved ion yield techniques. By direct measurement in catechol, and inference in phenol, we can directly assign the loss of H atoms to tunnelling when the excitation is beneath the S_1/S_2 CI. This assignment is confirmed by the large kinetic isotope effect upon deuteration of catechol, and from the constant hydrogen appearance lifetime. Compared to phenol, catechol has a greatly enhanced tunnelling rate, despite similar 1-D PECs, demonstrating the need for consideration of full dimensionality in tunnelling problems.

After excitation with $\lambda \leq 254$ nm in catechol an additional O^1-H fission channel opens up with ultrafast dynamics. This channel coexists with the tunnelling pathway, and so both cannot be borne from the same state; instead we assign the fast dynamics to direct excitation to the dissociative S_2 state. At higher still energies, $\lambda < 243$ nm, excitation to the S_1 decreases enough that direct dissociation is the only measurable H dissociation pathway. The demonstration that dissociation above the S_1/S_2 CI occurs without direct involvement of the CI answers a question long posed in the literature.

The combination of experiments on these two phenols has nicely answered two of the major questions regarding the participation of $^1\pi\sigma^*$ states in relaxation dynamics of

phenolic systems. The gradual increase in complexity, from phenol to catechol (and guaiacol) serves as an example of how chemical modifications can complement spectroscopy to give a complete picture of excited state processes. Additionally, this is a simple demonstration of the 'building up' principle, where complexity is gradually added to systems so that larger systems can be understood in terms of concepts explored in simpler molecules.

3.7 References

1. C. M. Tseng, Y. T. Lee and C. K. Ni, *J. Chem. Phys.*, 2004, **121**, 2459.
2. M. G. D. Nix, A. L. Devine, B. Cronin, R. N. Dixon and M. N. R. Ashfold, *J. Chem. Phys.*, 2006, **125**, 133318.
3. M. N. R. Ashfold, B. Cronin, A. L. Devine, R. N. Dixon and M. G. D. Nix, *Science*, 2006, **312**, 1637.
4. C. M. Tseng, Y. T. Lee, M. F. Lin, C. K. Ni, S. Y. Liu, Y. P. Lee, Z. F. Xu and M. C. Lin, *J. Phys. Chem. A*, 2007, **111**, 9463.
5. M. N. R. Ashfold, A. L. Devine, R. N. Dixon, G. A. King, M. G. D. Nix and T. A. A. Oliver, *Proc. Natl. Acad. Sci. USA*, 2008, **105**, 12701.
6. M. L. Hause, Y. H. Yoon, A. S. Case and F. F. Crim, *J. Chem. Phys.*, 2008, **128**, 104307.
7. A. Iqbal, M. S. Y. Cheung, M. G. D. Nix and V. G. Stavros, *J. Phys. Chem. A*, 2009, **113**, 8157.
8. R. N. Dixon, T. A. A. Oliver and M. N. R. Ashfold, *J. Chem. Phys.*, 2011, **134**, 194303.
9. A. L. Sobolewski and W. Domcke, *J. Phys. Chem. A*, 2001, **105**, 9275.
10. A. L. Sobolewski, W. Domcke, C. Dedonder-Lardeux and C. Jouvet, *Phys. Chem. Chem. Phys.*, 2002, **4**, 1093.
11. Z. G. Lan, W. Domcke, V. Vallet, A. L. Sobolewski and S. Mahapatra, *J. Chem. Phys.*, 2005, **122**, 224315.
12. M. Abe, Y. Ohtsuki, Y. Fujimura, Z. G. Lan and W. Domcke, *J. Chem. Phys.*, 2006, **124**, 224316.
13. M. G. D. Nix, A. L. Devine, R. N. Dixon and M. N. R. Ashfold, *Chem. Phys. Lett.*, 2008, **463**, 305.
14. H. An and K. K. Baeck, *J. Phys. Chem. A*, 2011, **115**, 13309.
15. D. R. Yarkony, *Rev. Mod. Phys.*, 1996, **68**, 985.
16. G. A. King, T. A. A. Oliver, M. G. D. Nix and M. N. R. Ashfold, *J. Phys. Chem. A*, 2009, **113**, 7984.
17. A. Sur and P. M. Johnson, *J. Chem. Phys.*, 1986, **84**, 1206.
18. G. A. Pino, A. N. Oldani, E. Marceca, M. Fujii, S. I. Ishiuchi, M. Miyazaki, M. Broquier, C. Dedonder and C. Jouvet, *J. Chem. Phys.*, 2010, **133**, 124313.
19. C. Ratzer, J. Kupper, D. Spangenberg and M. Schmitt, *Chem. Phys.*, 2002, **283**, 153.
20. R. N. Zare, *Angular Momentum: Understanding Spatial Aspects in Chemistry and Physics*, Wiley, New York, 1988.
21. G. M. Roberts, J. L. Nixon, J. Lecointre, E. Wrede and J. R. R. Verlet, *Rev. Sci. Instrum.*, 2009, **80**, 053104.
22. C. P. Schick and P. M. Weber, *J. Phys. Chem. A*, 2001, **105**, 3725.
23. T. A. A. Oliver, Y. Zhang, M. N. R. Ashfold and S. E. Bradforth, *Faraday Discuss.*, 2011, **150**, 439.
24. G. S. Beddard, G. R. Fleming, O. L. Gijzeman and G. Porter, *Chem. Phys. Lett.*, 1973, **18**, 481.

25. R. J. Le Roy and W. K. Liu, *J. Chem. Phys.*, 1978, **69**, 3622.
26. H. Kang, K. T. Lee, B. Jung, Y. J. Ko and S. K. Kim, *J. Am. Chem. Soc.*, 2002, **124**, 12958.
27. P. Meredith and T. Sarna, *Pigment Cell Research*, 2006, **19**, 572.
28. A. Huijser, A. Pezzella and V. Sundstrom, *Phys. Chem. Chem. Phys.*, 2011, **13**, 9119.
29. G. M. Roberts, A. S. Chatterley, J. D. Young and V. G. Stavros, *J. Phys. Chem. Lett.*, 2012, **3**, 348.
30. A. Iqbal, M. S. Y. Cheung, M. G. D. Nix and V. G. Stavros, *J. Phys. Chem. A*, 2009, **113**, 8157.
31. R. A. Livingstone, J. O. F. Thompson, M. Iljina, R. J. Donaldson, B. J. Sussman, M. J. Paterson and D. Townsend, *J. Chem. Phys.*, 2012, **137**, 184304.
32. Y. Zhang, T. A. A. Oliver, M. N. R. Ashfold and S. E. Bradforth, *Faraday Discuss.*, 2012, **157**, 141.
33. G. A. King, A. L. Devine, M. G. D. Nix, D. E. Kelly and M. N. R. Ashfold, *Phys. Chem. Chem. Phys.*, 2008, **10**, 6417.
34. A. Iqbal and V. G. Stavros, *J. Phys. Chem. Lett.*, 2010, **1**, 2274.
35. T. Sovdat, G. Bassolino, M. Liebel, C. Schnedermann, S. P. Fletcher and P. Kukura, *J. Am. Chem. Soc.*, 2012, **134**, 8318.
36. M. Garavelli, D. Polli, P. Altoe, O. Weingart, K. M. Spillane, C. Manzoni, D. Brida, G. Tomasello, G. Orlandi, P. Kukura, R. A. Mathies and G. Cerullo, *Nature*, 2010, **467**, 440.
37. P. Kukura, D. W. McCamant, S. Yoon, D. B. Wandschneider and R. A. Mathies, *Science*, 2005, **310**, 1006.
38. S. R. Meech, *Chem. Soc. Rev.*, 2009, **38**, 2922.
39. C. R. S. Mooney, D. A. Horke, A. S. Chatterley, A. Simperler, H. H. Fielding and J. R. R. Verlet, *Chem. Sci.*, 2013, **4**, 921.
40. T. M. Dunn, R. Tembreull and D. M. Lubman, *Chem. Phys. Lett.*, 1985, **121**, 453.
41. M. Onda, K. Hasunuma, T. Hashimoto and I. Yamaguchi, *J. Mol. Struct.*, 1987, **159**, 243.
42. W. Caminati, S. Dibernardo, L. Schafer, S. Q. Kulpnewton and K. Siam, *J. Mol. Struct.*, 1990, **240**, 263.
43. T. Bürgi and S. Leutwyler, *J. Chem. Phys.*, 1994, **101**, 8418.
44. M. Gerhards, W. Perl, S. Schumm, U. Henrichs, C. Jacoby and K. Kleinermanns, *J. Chem. Phys.*, 1996, **104**, 9362.
45. C. Puebla and T. K. Ha, *Journal of Molecular Structure (Theochem)*, 1990, **63**, 337.
46. M. Gerhards, S. Schumm, C. Unterberg and K. Kleinermanns, *Chem. Phys. Lett.*, 1998, **294**, 65.
47. G. A. King, T. A. A. Oliver, R. N. Dixon and M. N. R. Ashfold, *Phys. Chem. Chem. Phys.*, 2012, **14**, 3338.
48. H. J. Werner and P. J. Knowles, *J. Chem. Phys.*, 1985, **82**, 5053.
49. P. J. Knowles and H. J. Werner, *Chem. Phys. Lett.*, 1985, **115**, 259.
50. H. J. Werner, *Mol. Phys.*, 1996, **89**, 645.
51. P. Celani and H. J. Werner, *J. Chem. Phys.*, 2000, **112**, 5546.
52. T. Gerber, Y. Z. Liu, G. Knopp, P. Hemberger, A. Bodi, P. Radi and Y. Sych, *Rev. Sci. Instrum.*, 2013, **84**, 10.
53. G. A. Pino, A. N. Oldani, E. Marceca, M. Fujii, S. I. Ishiuchi, M. Miyazaki, M. Broquier, C. Dedonder and C. Jouvet, *J. Chem. Phys.*, 2010, **133**, 124313.
54. X. B. Wang, Q. A. Fu and J. L. Yang, *J. Phys. Chem. A*, 2010, **114**, 9083.
55. Y. L. Yang, Y. Dyakov, Y. T. Lee, C. K. Ni, Y. L. Sun and W. P. Hu, *J. Chem. Phys.*, 2011, **134**, 034314.
56. G. M. Roberts, C. A. Williams, J. D. Young, S. Ullrich, M. J. Paterson and V. G. Stavros, *J. Am. Chem. Soc.*, 2012, **134**, 12578.

57. G. M. Roberts, C. A. Williams, M. J. Paterson, S. Ullrich and V. G. Stavros, *Chem. Sci.*, 2012, **3**, 1192.
58. S. Ullrich, T. Schultz, M. Z. Zgierski and A. Stolow, *Phys. Chem. Chem. Phys.*, 2004, **6**, 2796.
59. M. Schmitt, S. Lochbrunner, J. P. Shaffer, J. J. Larsen, M. Z. Zgierski and A. Stolow, *J. Chem. Phys.*, 2001, **114**, 1206.
60. J. Z. Zhao, S. M. Ji, Y. H. Chen, H. M. Guo and P. Yang, *Phys. Chem. Chem. Phys.*, 2012, **14**, 8803.
61. A. S. Chatterley, D. A. Horke and J. R. R. Verlet, *Phys. Chem. Chem. Phys.*, 2012, **14**, 16155.
62. A. L. Sobolewski and W. Domcke, *Chem. Phys.*, 2000, **259**, 181.
63. S. W. Konijn, R. J. J. M. Steenvoorden, P. G. Kistemaker and T. L. Weeding, *J. Phys. Chem.*, 1994, **98**, 5399.
64. E. R. E. Vanderhage, J. J. Boon, R. J. J. M. Steenvoorden and T. L. Weeding, *Anal. Chem.*, 1994, **66**, 543.
65. D. J. Hadden, G. M. Roberts, T. N. V. Karsili, M. N. R. Ashfold and V. G. Stavros, *Phys. Chem. Chem. Phys.*, 2012, **14**, 13415.
66. H. D. Bist, J. C. D. Brand and D. R. Williams, *J. Mol. Spectrosc.*, 1967, **24**, 413.
67. M. N. R. Ashfold, G. A. King, D. Murdock, M. G. D. Nix, T. A. A. Oliver and A. G. Sage, *Phys. Chem. Chem. Phys.*, 2010, **12**, 1218.
68. H. Reisler and A. I. Krylov, *Int. Rev. Phys. Chem.*, 2009, **28**, 267.
69. T. Ebata, C. Minejima and N. Mikami, *J. Phys. Chem. A*, 2002, **106**, 11070.
70. G. Berden, W. L. Meerts, M. Schmitt and K. Kleinermanns, *J. Chem. Phys.*, 1996, **104**, 972.

4 Intrinsic Decay Dynamics of Indigo Carmine

This chapter is based on the following publication:

A. S. Chatterley, D. A. Horke and J. R. R. Verlet, On the intrinsic photophysics of indigo: a time-resolved photoelectron spectroscopy study of the indigo carmine dianion, *Phys. Chem. Chem. Phys.,* 2012, **14**, 16155

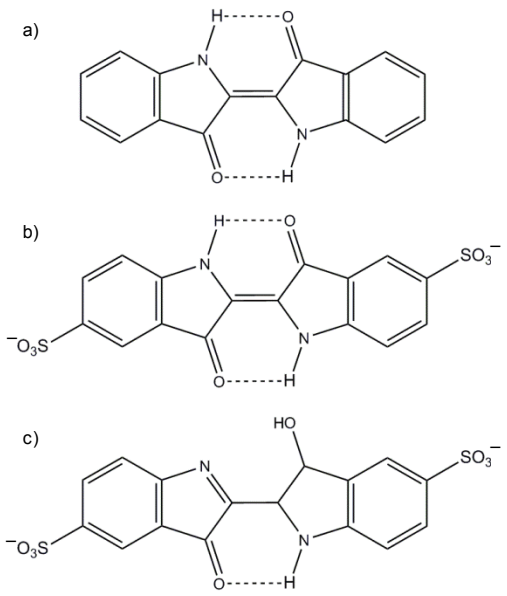

Figure 4.1 Molecular structures of a) indigo, b) indigo carmine dianion (InC^{2-}) and c) InC^{2-} in the mono-enol form following excited state single proton transfer.

4.1 Introduction

Following the work performed in Warwick on phenols, we now switch to the Durham anion experiment, where the dynamics and spectroscopy of the dye indigo carmine (InC) were studied. The move to InC from phenols elegantly demonstrates the concepts of bottom up spectroscopy – InC is a larger and more complex system, however core concepts like the kinetic isotope effect carry through. The photophysics of indigos also have consequences for their use as dyes, so this work is also 'building up' to more real-world applicable systems.

The organic dye, indigo (Fig. 4.1(a)), and its ring substituted derivatives have been used since ancient times as a distinctive blue stain in applications ranging from Egyptian mummies, to the blue 'war paint' of Celtic warriors and to modern day denim jeans.[1, 2] Historically, the dye was extracted from natural sources, such as the leaves of the *indigofera tinctoria* plant. Over a century ago, however, Adolf von Baeyer successfully synthesised indigo, for which he received the 1905 Nobel Prize. Since then, the synthetic route has been extensively used and currently well over 10,000 tons of indigo are produced globally each year.

The reason for the sustained importance of indigo as a dye is not solely due to its striking blue colour, but more importantly because of its resistance to fading after prolonged exposure to light. The blue colour of indigo arises from the strong $S_1 \leftarrow S_0$ transition centred at around 600 nm. However, the origin of the photo-resistivity of indigo is more intricate and has been extensively studied. In general, photo-resistive

chromophores are a topic of great interest and have, for example, been linked with the survival of primordial organisms on early Earth (see Chapter 1). The photo-resistive properties are related to the excited state dynamics of the chromophore and here we present a direct study of the S_1 dynamics of a disulfonated derivative, indigo carmine (InC^{2-}, Fig. 4.1(b)), using time-resolved photoelectron spectroscopy.

The luminescent properties of indigo provide clear evidence for its photo-resistance. In dimethylformamide (DMF) solution, the fluorescent quantum yield of indigo is $\Phi_F = 0.0023$, while for InC, it is even lower at $\Phi_F = 0.0015$, despite the large absorption cross section, $\sigma = 3.1 \times 10^{-17}$ cm^2.[3] Hence, a very efficient non-radiative process is operative that effectively out-competes radiative decay. Intersystem crossing has been determined to be almost entirely inactive, and so internal conversion accounts for >99% of the relaxation from the S_1 in indigo and its derivatives.[4] The S_1 lifetime has been determined to be on the order of tens or hundreds of picoseconds, dependent on the specific indigo derivative and the solvent. The reduced (leuco) form of indigo on the other hand has a much longer lived S_1 state, indicating that the keto structure is central to the photo-stability of indigo.[4]

Because of the inherent photo-resistance of indigo, its underlying molecular mechanism has been topical. There are three possible intra-molecular mechanisms that can lead to the rapid internal conversion, and thus photostability. Firstly, *trans* → *cis* isomerisation around the central C=C bond can occur. The $S_1 \leftarrow S_0$ transition corresponds to the promotion of an electron from a π to a π* orbital, which leads to a weakening of the central C=C bond[5, 6] and could in principle result in free rotation around this central carbon bond. Many other dyes with a C=C (stilbenes) or N=N bond (azobenzenes) show considerable *trans-cis* photo-isomerisation yields.[7-9] Indigo, however, does not isomerise,[10] which can be rationalised by the presence of two intra-molecular hydrogen bonds between the C=O and N–H groups in the *trans* form of the molecule (see Fig. 4.1(a) and (b)). Breaking these hydrogen bonds imposes a large barrier to isomerisation.

The second possible mechanism is excited state intra-molecular proton transfer (ESIPT).[11-13] In this, a proton transfers from an amine group to the adjacent oxygen on the C=O, producing an enol–structure (Fig. 4.1(c)). The third possible process is a double ESIPT process, in which both hydrogen atoms are transferred in the excited state.

Direct evidence that single ESIPT is operative on the S_1 state was recently provided by Kobayashi *et al*. by means of transient absorption of InC, using sub–5 fs pulses.[14-16]

By tracking the temporal evolution of vibronic signatures of InC following photoexcitation, they were able to demonstrate that an alcohol intermediate is formed, while at the same time, the C=O stretch could still be seen. This was taken as direct proof of single ESIPT (Fig. 4.1(c)). After this intermediate, the system reverts back to the keto-form on the S_1 excited state. The time for a full oscillation of the proton along the ESIPT coordinate was measured to take ~600 fs in methanol. Similar dynamics and timescales were observed in dimethyl sulfoxide (DMSO), indicating that the process is indeed intra-molecular and that the solvent polarity has no significant impact on the ESIPT dynamics. On the other hand, the lifetime of the S_1 excited state is very sensitive to the solvent environment. The fastest excited decay is observed in water, where the S_1 lifetime has been determined to be on average 2.7 ps. In methanol on average it is 23 ps and extends to 100s ps as the solvent polarity is decreased.[17] This suggests that the proton can shuttle back and forth a number of times on the excited state before internal conversion occurs.

Ab initio calculations by Yamazaki *et al*. agree with experiment and indicate that the single ESIPT is the more likely relaxation mechanism.[6] A negligible barrier was calculated for ESIPT on the S_1 potential energy surface and a conical intersection (CI) with the ground state was identified near the enol form that is energetically accessible. A viable CI was also identified along the *trans-cis* isomerisation coordinate; however, a large barrier to isomerisation inhibits this process, in agreement with measurements that indicate that no isomerisation occurs. The possibility of the double ESIPT was also investigated. Although a CI could be identified that would lead to internal conversion, its energy was calculated to be too high to be accessible following excitation to the S_1 state. Hence, it was concluded that single ESIPT was the most likely mechanism by which indigo attains its photo-stability. However, no information about the timescales of the S_1 internal conversion was calculated. Very recently, Cui and Thiel employed nonadiabatic trajectory surface hopping calculations to explore the relaxation mechanism of bispyrroleindigo, a truncated model of indigo.[5] In agreement with the work by Yamazaki *et al*., all population in the excited state was found to decay via near barrierless ESIPT, followed by internal conversion and back-transfer of the proton on the ground state. However, the S_1 lifetime was calculated to be around 700 fs for bispyrroleindigo, significantly shorter than that observed in solution. Moreover, as the calculations assume an isolated system, calculated timescales may be expected to be closer to that in a non-polar solvent and, for indigo, the internal conversion timescales span 100s of ps.

The calculations of Yamazaki *et al*. are considered at the frontier of the size for which excited state surfaces can be calculated at a high level of theory. However, at present, there is no experimental data that allows these calculations to be benchmarked against. Specifically, only studies on solvated indigo derivatives have been performed to date, while the calculations are in vacuum. The same is true for the dynamics study of Cui and Thiel and their extracted timescales do not compare well with those for indigo in aprotic solvents. This chapter provides this benchmark and highlights the strong influence of the solvent on the excited state lifetimes. Specifically, time-resolved photoelectron spectroscopy[18-20] is employed to study the intrinsic excited state dynamics of the InC^{2-} derivative as a model system of indigo. Moreover, through isotopic substitution, we show conclusively that ESIPT is the primary motion on the excited state and leads to internal conversion. The timescales for decay from the S_1 observed in the gas-phase are significantly faster than all timescales observed in solution and agree moderately well with those calculated by Cui and Thiel for a truncated indigo model in the gas phase.[5] Our results indicate that the solvent plays no constructive role to the photo-stability of indigo, and may in fact impede the relaxation.

4.2 Methods

The experiments were performed using the time-resolved photoelectron imaging setup in Durham. InC sodium salt (Sigma-Aldrich) was dissolved in a 20:80 (*v:v*) water:acetonitrile mixture, and the dianion was produced by electrospray at a –2.5 kV potential. The femtosecond laser setup was as described in Chapter 2, with a visible pump beam produced by SFG/OPA, and the 400 nm probe beam produced by SHG. The absorption action spectrum presented in Section 4.3.4 was produced using nanosecond pulses from an optical parametric oscillator (Continuum, *Panther Ex*), pumped by the 3rd harmonic of an Nd:YAG laser (Continuum, *Surelight;* 355 nm) at 10 Hz. The pulses were tunable across the visible and have energies of ~5 mJ / pulse. Both lasers were used unfocussed and laser intensities were on the order of 10^{10} W cm^{-2} and 10^{7} W cm^{-2} for the femtosecond and nanosecond lasers, respectively.

4.3 Results and Analysis

4.3.1 Photoelectron spectroscopy at 4.66 eV

In order to determine the relative energies of the isolated InC^{2-} dianion relative to the anion (radical), the one-colour PE spectrum at 4.66 eV (266 nm) has been acquired with a femtosecond laser and is presented in Fig. 4.2(a). Two PE features are observed around *eKE* = 1.2 eV and *eKE* = 1.7 eV. The feature at highest *eKE* can normally be

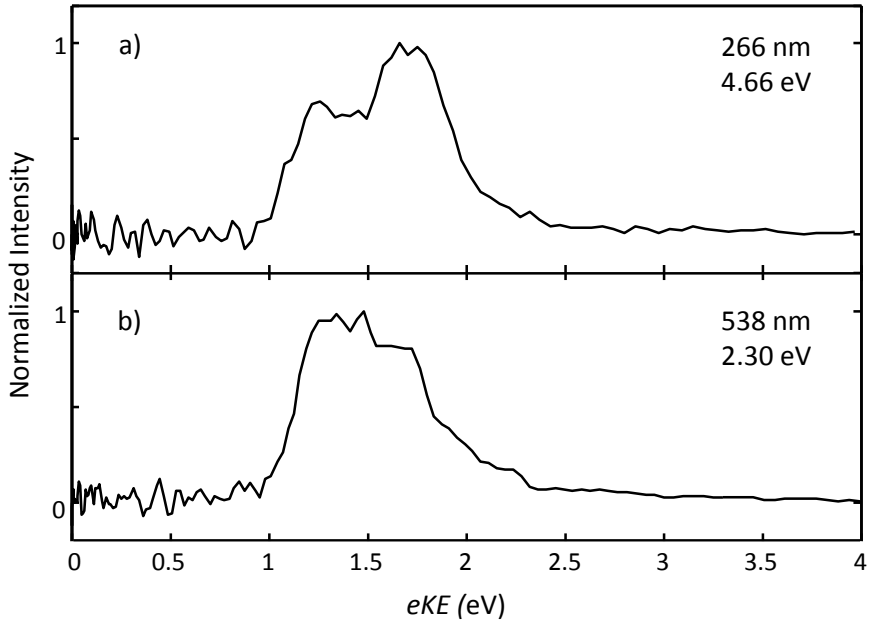

Figure 4.2 Photoelectron spectrum of InC^{2-} taken with a) 1×4.66 eV (266 nm) and b)2×2.30 eV (538 nm) photons. A sharp cut-off is observed in both cases at low electron kinetic energy (*eKE*), arising from the repulsive Coulomb barrier.

assigned to the direct detachment from the dianion ground state to the ground state of the anion: $InC^{2-}(S_0) + h\nu \rightarrow InC^{-}(D_0) + e^{-}$. From this, the vertical detachment energy of InC^{2-} is estimated to be 3.0 eV. The adiabatic energy is commonly determined by considering the extrapolation of the steepest onset to the *eKE* axis, which for InC^{2-} gives an adiabatic binding energy of ~ 2.5 eV. The feature observed at *eKE* = 1.2 eV suggests that an excited state in the radical anion is accessed upon photodetachment. An alternative assignment for this feature is direct detachment from one of the charged sulphate groups. DFT calculations (see below) suggest that the molecular orbital for the SO_3^- group lies only ~0.1 eV below the HOMO, so direct detachment should be energetically available. Complete assignment of this peak is not facile, as the sharp cut-off of PE signal at lower *eKE* suggests that perhaps the entire feature has not been observed

The appearance of cut-offs in the PE spectra at low *eKE* is a common feature in polyanions. Photoelectrons can only escape from the dianion if the electron has sufficient energy to overcome the repulsive Coulomb barrier (RCB) that arises from the long-range Coulomb repulsion between the outgoing electron and the remaining anion.[21, 22] Below the RCB, photoelectrons can only escape through tunnelling, despite the fact that their kinetic energy is above the $InC^{-}(D_0) + e^{-}$ asymptote.[23] In the present case, the S_1 is lower in energy than this asymptote and no tunnelling feature is observed. The photoelectron cut-off provides a direct measure of the height of the RCB.

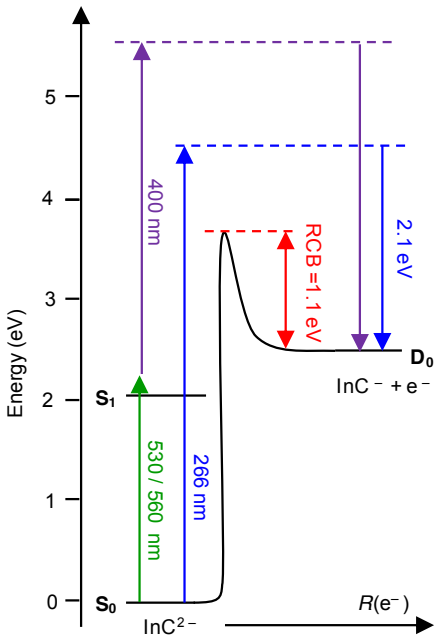

Figure 4.3 Energy levels and excitation scheme employed for InC^{2-}. Photoelectron spectra have been taken with 4.66 eV (Fig. 4.2(a)), leading to direct detachment to the D_0. In pump-probe experiments, a pump at 2.21 eV or 2.33 eV was used while a probe at 3.1 eV was employed to detach from the S_1 state.

For InC^{2-}, the RCB height is 1.1 eV as evidenced by the steep rise in photoelectron signal in Fig. 4.2(a).

To confirm the relative energies determined from the 4.66 eV PE spectrum, *ab initio* calculations have been performed using density functional theory. All calculations were done using the B3LYP functional,[24] with a 6-311++G** basis set,[25] using the Gaussian09 package.[26] The adiabatic detachment energy is defined as the difference in energy between the ground state of InC^{2-} and InC^- in their respectively optimised geometry and is found to be 2.57 eV (excluding zero-point energies). This is in excellent agreement with the extrapolated 2.5 eV from the PE spectrum. The vertical detachment energy, defined as the energy difference between InC^{2-} and InC^- in the dianion geometry, was calculated to be 2.61 eV. This is lower than the measured vertical detachment of 3.0 eV. This discrepancy could be attributed to the finite temperature of InC^{2-} in the current experiment ($T \approx 300$ K) or the fact that the observed spectral maximum does not necessarily coincide with the vertical detachment energy (which often becomes more pronounced with temperature). Nevertheless, the calculated values provide sufficient confidence that the assignment of the energy levels of InC^{2-} is correct. The intrinsic energy level diagram of InC^{2-} is shown in Fig. 4.3 including various excitation and detachment schemes used for time-and frequency-resolved PE spectroscopy.

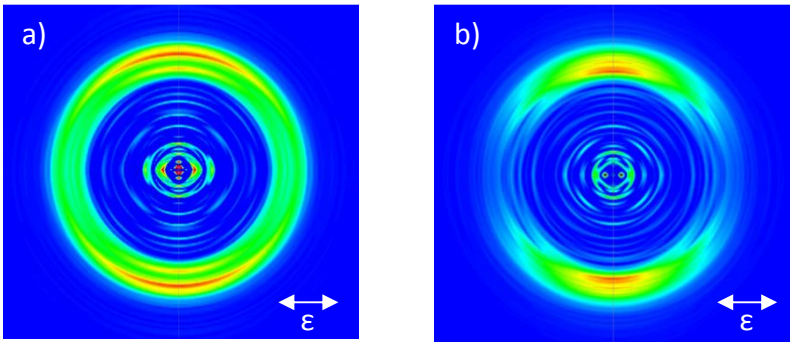

Figure 4.4 The reconstructed central slice of the photoelectron image produced from detachment with a) 1×4.66 eV and b) 2×2.30 eV photons. The direction of the excitation laser electric field is indicated by the arrows. The 2.30 eV image shows significantly more angular anisotropy, owing to pre-alignment by the first photon absorbed.

4.3.2 Photoelectron spectroscopy at 2.3 eV

In addition to the spectrum taken with 4.66 eV photons, we have performed PE spectroscopy using 2.30 eV (538 nm) photons. These are insufficient to one-photon detach InC^{2-}, however by utilizing the first excited state resonance enhanced two-photon detachment may be performed, and high signal levels are observed. Fig. 4.2(b) shows the resultant PE spectrum. The total energy imparted is 4.60 eV, so the maximum *eKE* observed should be approximately 0.1 eV below that from the 4.66 eV spectrum. The shape of the 2.30 eV PE spectrum is somewhat different to that of the spectrum taken at 4.66 eV. The bimodal structure in the 4.66 eV PE spectrum is not clearly reproduced in the two-photon spectrum. If the second feature arises from sulphate detachment, no resonance enhancement of this feature would occur and so it is highly unlikely to be observed, in agreement with our findings. The theoretical work by Yamazaki *et al*. suggests that the S_1 excited state surface is rather flat, which would be consistent with a very broad photoelectron distribution from the S_1 excited state if the final states are not similarly flat.[6]

4.3.3 Photoelectron angular distributions

In Fig. 4.4, the central slice through the PE cloud is presented for photodetachment at (a) 4.66 eV and (b) 2.30 eV with a femtosecond laser. The two images look markedly different, the one-photon 4.66 eV image shows less a less anisotropic photoelectron angular distribution (PAD) than the two-photon 2.30 eV image. Quantitatively, the β_2 parameters (see Chapter 2) for the features around *eKE* = 1.5 eV are –0.33 ± 0.03 and -0.89 ± 0.05 for the 4.66 eV and 2.30 images, respectively. The PADs of both images are dictated by both the presence of the RCB and of an aligning state.

In the case of the 4.66 eV image, detachment is a single photon process, directly over the RCB. The *eKE* is not very high above the RCB, and as has been demonstrated

before, PADs can be strongly influenced by the RCB in these cases.[27-29] This can be rationalised by considering the spatial profile of the RCB, which is significantly higher near to the two anionic sulfate groups. The determined 1.1 eV RCB is the *lowest* spatial RCB; it will be higher for electron detachment parallel to the SO_3 – SO_3 internuclear axis. The presence of the low lying RCB influences the outgoing electron to have a PAD preferentially perpendicular to this axis.

For the femtosecond image with 2.30 eV excitation, the process is two photon via a resonant state. The presence of a resonant state in detachment from an anion results in molecular alignment prior the absorption of the detaching photon, giving the much more pronounced anisotropy.[29, 30] The first photon absorbed will selectively excite dianions whose transition dipole moment (TDM) is aligned with the electric field of the laser (in a $\cos^2$ distribution, see Chapter 2). The TDM for the first excitation of InC^{2-} has been calculated using time dependent density functional theory, at the TD-B3LYP/6-311++G** level of theory. The calculated TDM lies roughly parallel with the central double bond of the InC^{2-} dianion, and so alignment of InC^{2-} by a single 2.30 eV photon will thus result in the two SO_3^- groups lying parallel with the electric field of the laser, and hence any detached electrons should be directed perpendicular to this direction by the presence of the two negative charges. In the case of InC^{2-}, this effect seems to be particularly pronounced and a near limiting perpendicular β_2 parameter is observed.

4.3.4 Absorption (action) spectroscopy

Direct photodetachment is only possible for photons with energy above ~3.6 eV (λ < 340 nm). Below this energy, PE emission can still be observed due to the resonance enhancement via the $S_1 \leftarrow S_0$ transition of InC^{2-} and the total PE yield measured as a function of photon energy can be used to provide an action spectrum of the absorption to the S_1 excited state. The (nanosecond) laser wavelength was scanned between 2.0 < $h\nu$ < 2.6 eV (620 > λ > 470 nm) and total electron yield on the imaging detector was monitored. Fig. 4.5 shows the resulting action spectrum, which has been scaled with the laser pulse energy to compensate for changes in intensity as the wavelength was tuned. Also shown is the absorption spectrum of InC^{2-} in methanol. The overall profile of the action spectrum is very similar to the absorption spectrum for InC^{2-} in solution, providing some confidence that the action spectrum faithfully represents the intrinsic absorption spectrum of InC^{2-}.

Solvation introduces a large red-shift in the $S_1 \leftarrow S_0$ absorption. The intrinsic maximum occurs at λ_{max} = 2.21 eV (560 nm), while in methanol, this is shifted to

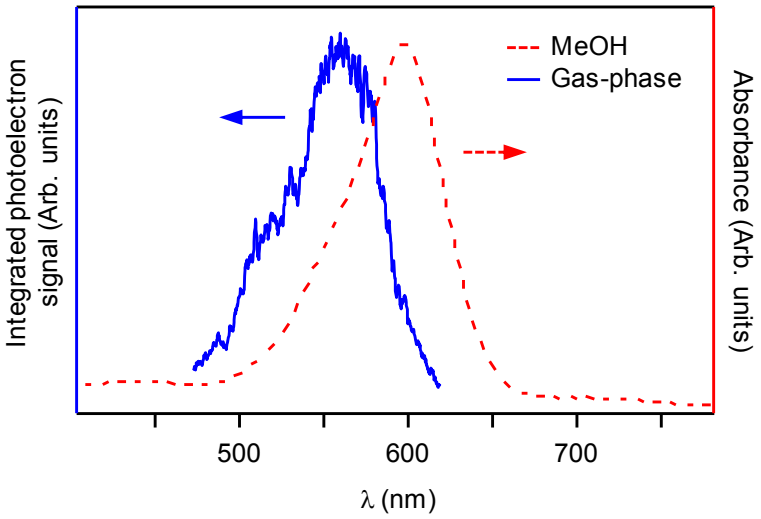

Figure 4.5 Action (absorption) spectrum of InC^{2-} in the gas phase (solid line) and absorption spectrum in a methanol solution (dashed line). The gas phase spectrum is similar to the solution-phase absorption spectrum, but blue-shifted by 40 nm.

λ_{max} = 2.07 eV (600 nm), corresponding to a shift of 0.14 eV (40 nm). These observations are comparable to those observed in neutral indigo for which the absorption maximum has been measured to be λ_{max} = 2.27 eV (546 nm) in the gas-phase, relative to λ_{max} = 2.05 eV (605 nm) in methanol (a 0.22 eV shift). [31, 32]

The bathochromic shift of indigo has been attributed to the unique arrangement of the N–H electron donor and C=O electron acceptor groups in the chromophore which has a structure resembling an "H" (see Fig. 4.1(a)). The LUMO is particularly well stabilised in polar solvents because it exhibits an increased charge separation relative to the HOMO.[33-36] Consequently, the HOMO-LUMO gap is larger in the gas-phase in the absence of the polar stabilisation of the LUMO. The same picture appears valid for the InC^{2-} system although the solvatochromism is perhaps slightly weaker than for neutral indigo. Nonetheless, it demonstrates that InC^{2-} is an appropriate system to study the photophysics of indigo in the gas-phase. Our choice of InC^{2-} has, however, primarily been motivated because of its more recent use in excited state dynamics studies compared to indigo which is much less readily dissolved (and also more difficult to electrospray).

4.3.5 Time-resolved photoelectron spectroscopy

To determine the intrinsic dynamics of InC^{2-}, time-resolved PE spectroscopy has been employed. A laser pulse centred at the maximum absorption of the $S_1 \leftarrow S_0$ transition (2.21 eV (560 nm)) was used as a pump pulse, while a 3.10 eV (400 nm) probe pulse was used to monitor the excited state population as a function of time-delay, *t*. The PE signal arising only from the 3.10 eV probe is very small compared to the signal from the

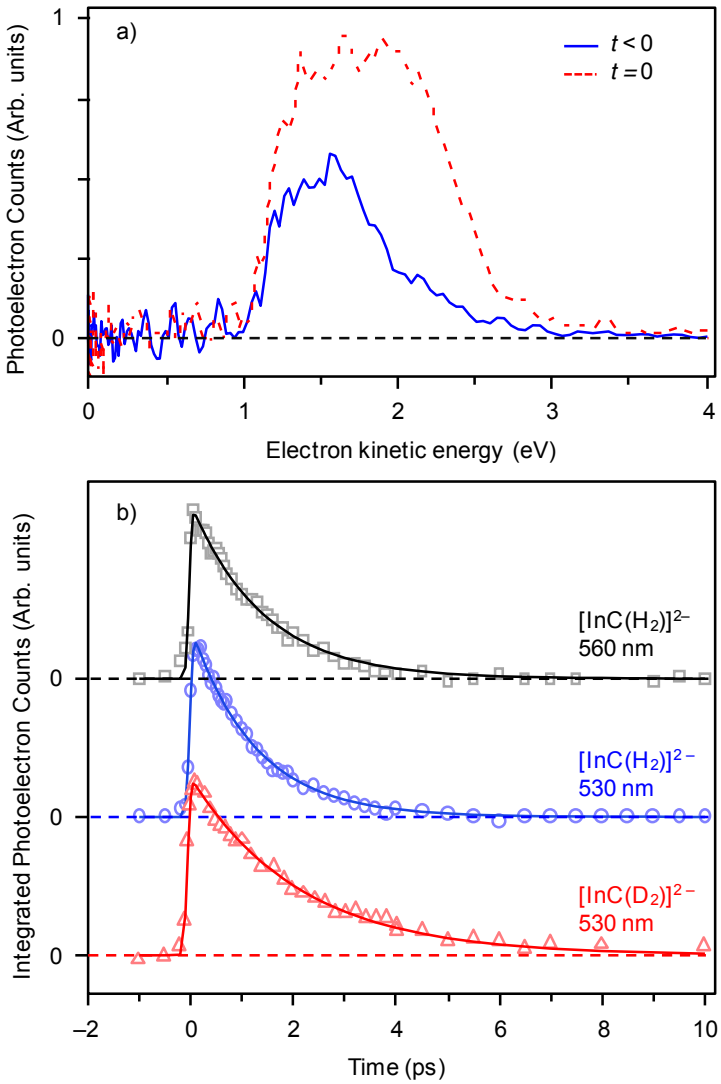

Figure 4.6 a) Photoelectron spectra of $[InC(D_2)]^{2-}$ with a 2.33 eV pump and 3.10 eV probe. Solid line represents a typical spectrum in which the probe is arriving before pump, while the dashed line is shortly after t_0. The difference in photoelectron signal is representative of the S_1 excited state population. b) Integrated photoelectron yields of the S_1 excited state signal as a function of time for $[InC(H_2)]^{2-}$ at pump energy of 2.21 eV (560 nm) (squares) and at 2.33 eV (530 nm) for $[InC(H_2)]^{2-}$ (circles) and $[InC(D_2)]^{2-}$ (triangles).

2.21 eV pump. At 3.10 eV, the photon energy is no longer resonant with the $S_1 \leftarrow S_0$ transition and is insufficient to directly detach an electron from the system (*i.e.* the RCB is too high – see Fig. 4.3). The 2.21 eV (560 nm) pump also has insufficient energy to induce direct single photon detachment. However, a relatively strong photoelectron signal is seen between 1 eV < *eKE* < 2 eV. This can be attributed to the resonance-enhanced 2-photon photo-detachment via the S_1 state.

The PE spectrum following 2-photon photodetachment from the pump centred at 2.33 eV (530 nm) is shown in Fig. 4.6(a), in which the probe arrives before pump pulse, $t < 0$. For comparison purposes, we show the spectrum at 2.33 eV rather than 2.21 eV, as the total energy imparted following two-photon absorption is equal to the 4.66 eV

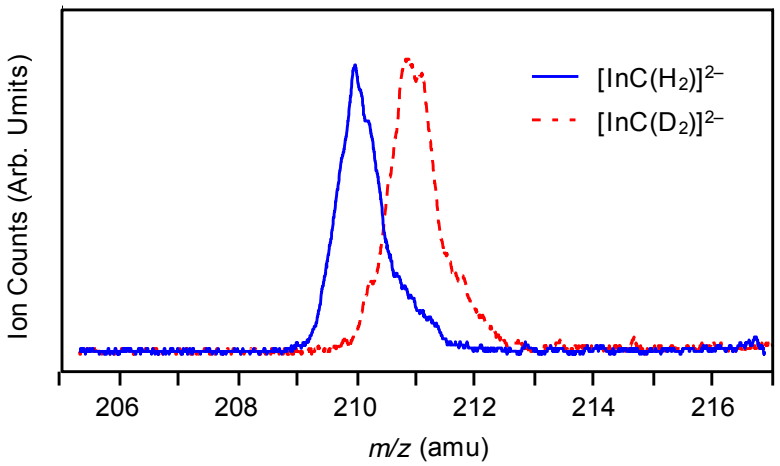

Figure 4.7 Mass spectra of $[InC(H_2)]^{2-}$ and $[InC(D_2)]^{2-}$. Complete deuteration is demonstrated by the increase of 1 *m/z* when InC is sprayed from D_2O:acetontrile.

PE spectrum (shown in Fig. 4.2(a)). The spectrum very well resembles that with 2.30 eV photons only (Fig. 4.2(b)), as may be expected for such a small change in energy. When the pump arrives before the probe, $t > 0$, a considerable increase in PE yield is observed as shown in Fig. 4.6(a). The enhanced feature is broad, structureless and similar in appearance to the spectrum at $t < 0$, but it extends to higher *eKE*, as expected from the extra energy imparted into the system (an additional 0.77 eV is imparted). As a function of time, the spectral shape of the PE distribution does not change significantly. The only observed change is a decrease in the PE yield as the delay is increased. The pump-probe PE spectra taken with a 2.21 eV pump are qualitatively the same as those taken with the 2.33 eV pump.

In order to determine the kinetics of the excited state dynamics following excitation at the absorption maximum (2.21 eV), the integrated PE signal has been plotted as function of *t*. For this we have taken only the pump-probe signal by subtracting a PE spectrum at $t < 0$ from all other spectra. The total PE yield as a function of time is shown as squares in Fig. 4.6(b). The kinetics appears first order and the data are well reproduced by a single exponential decay convoluted with the Gaussian instrument response function. The resulting fit is shown by a solid line Fig. 4.6(b), from which a lifetime has been deduced to be 1.4 ± 0.2 ps. Following excitation at 2.33 eV (Fig. 4.6(b), circles), a similar timescale of 1.2 ± 0.2 ps has been obtained. Although this is marginally faster, within our error bounds the timescales are effectively the same.

We have also performed time-resolved PE spectroscopy on deuterated InC^{2-}. The H atoms forming the intra-molecular hydrogen bonds can be exchanged for D atoms by dissolving the InC sodium salt in a 20:80 D_2O:acetonitrile solution instead of

H_2O:acetonitrile. The effective D exchange is verified by the mass-spectrum as shown in Fig. 4.7. The mass/charge separation between the two ion peaks is 1 amu, indicating that both H atoms have been exchanged forming the dianionic $[InC(D_2)]^{2-}$ species. The total integrated pump-probe PE signal as a function of time following excitation at 2.33 eV of $[InC(D_2)]^{2-}$ is shown in Fig. 4.6(b) as triangles and clearly shows that the lifetime is significantly longer. The data are fit to the same function as protonated InC^{2-} and the lifetime extracted is found to be 2.3 ± 0.2 ps, thus giving an isotope effect $\tau_D / \tau_H \approx 2$. This isotope effect is indicative of direct involvement of the hydrogen atom (pure ballistic motion would give a value of $\sqrt{2}$), however it rules out tunnelling, which would produce much larger effects (see Chapter 1).

4.4 Discussion

4.4.1 Intrinsic decay dynamics

In the absence of solvent, the intrinsic S_1 excited state lifetime is 1.4 ps. This almost doubles when the H atoms involved in intra-molecular hydrogen bonding are replaced with D atoms. The large kinetic isotope effect strongly points to the involvement of the H atoms in the dynamics on the S_1 excited state, confirming that the primary dynamics involves ESIPT. The isotope effect observed in the gas-phase is somewhat larger than in solution, but likely within the combined error of both experiments.[16] The primary process in the gas-phase is the same as in solution, in which the ESIPT can be identified from spectral signatures in the IR and has been shown to be independent on solvent.[14] Hence, it would appear that the ESIPT process in indigo is almost entirely independent of the environment.

The timescale for ESIPT in solution has been determined to be on the order of 600 fs.[15] In our experiment, no wavepacket motion can be discerned in the time-resolved spectra, suggesting that the PE spectra from the keto and mono-enol forms are very similar. As such, no timescale for this oscillatory motion can be directly determined. However, the excited state dynamics calculated by Cui and Thiel point to a similar timescale predicted in vacuum for the ESIPT.[8] These calculations were performed on the bispyrroleindigo derivative of indigo. They find that the ESIPT in the forward direction takes 600 fs. No significant back-reaction is observed in their simulations and the excited state evolves towards internal conversion geometries leading to an average predicted lifetime of 700 fs. This is in fair agreement with our observations. However, if we assume that the ESIPT for InC^{2-} in vacuum is similar to that in solution – which is justified given that the ESIPT is observed to be independent

on solvent – then there is sufficient time for the ESIPT back-reaction to be accessible in vacuum. Yamazaki *et al*. have shown that the potential energy surface for indigo and bispyrroleindigo have important differences.[6] In particular, no barrier to ESIPT is observed for bispyrroleindigo and the lowest conical intersection with the S_0 lies at an energy below the energy associated with the geometry at the Franck-Condon region by about 0.7 eV. In contrast, for indigo, a small 0.2 eV barrier was identified to access the mono-enol from the keto-form. After the mono-enol tautomer is formed, the system can evolve to a conical intersection that has been identified to be ~0.1 eV higher than this barrier. This is consistent with our observations and does indeed suggest that back-ESIPT will be possible on the S_1 state given that the excited state lifetime is 1.4 ps. This is also the case in solution where the S_1 lifetime exceeds the ESIPT process by orders of magnitude. The similarity between kinetic isotope effects suggests that the dynamics of ESIPT are similar in all environments and that the ESIPT motion on the S_1 proceeds via a similarly small barrier.

We point out that double ESIPT cannot be ruled out based on our data alone, but given the comparison with solution phase work, we can dismiss this with some confidence. This is in agreement with the large barrier calculated for this process and the results of the recent nonadiabatic dynamics simulations.[5, 6]

4.4.2 Effect of solvation on S_1 dynamics

Given the similarity between the ESIPT dynamics regardless of the environment, it seems surprising that the S_1 lifetime is affected so strongly by solvation. In solution, the decay of the S_1 state is multi-exponential and highly dependent on the solvent.[17] The slowest component of the decay ranges in lifetime from 2.7 ps in water, to 22 ps in methanol and 92 ps in DMSO, while the fastest component decays in 180 fs for H_2O, and around 500 fs in both methanol and DMSO. Based on the vibrational dynamics, the actual ESIPT mechanism in both protic methanol and aprotic DMSO takes around 600 fs for a full oscillation.[15] The individual timescales are difficult to assign; Franck-Condon factors and selection rules will affect the shape of the decays. In the gas-phase, the decay is mono-exponential. PE spectroscopy, unlike optical methods, does not have stringent selection rules and the probe step (photodetachment) is universally allowed. Hence, it is not unreasonable to consider that Franck-Condon factors and absorption/emission spectral shifts with time are at least partially responsible for the observed complex dynamics in solution. It is tempting to assign the shortest decay observed by Nagasawa *et al.* to the ESIPT process, because for both DMSO and methanol it has a lifetime that is approximately the same as the time for one complete

ESIPT cycle (~600 fs). However, given the complex multi-exponential nature of the decays, this assignment cannot be definitive. In particular, it seems unlikely that the time for ESIPT in aqueous solution is just 180 fs, with almost no kinetic isotope effect.[17]

Solvation has the effect of decreasing the rate of internal conversion relative to the gas-phase. Yamazaki *et al*. have briefly discussed solvation effects on the excited state.[6] The keto-form has no dipole moment while the mono-enol does. The effect of solvation will then be to lower the barrier as the mono-enol form is stabilised relative to the keto-tautomer and, hence, the rate of reaction is faster in more polar solvents. Although reasonable, this appears to be in contradiction with our observation that shows that the excited state lifetime is even faster if there is no solvent at all.

The reduced rate of internal conversion in solution points to a higher barrier to access conical intersections relative to the gas-phase. Indigo possesses a significant degree of solvatochromism, as evidenced by our gas phase absorption spectrum on InC^{2-}, as well as those on neutral indigo.[32, 34] In the vertical Franck-Condon region (of the keto-tautomer), the excited state is stabilized by 0.14 eV in methanol, however the effect on the mono-enol or conical intersection geometries is not known. Given the significant change in intra-molecular hydrogen bonding when going from the keto to the mono-enol, it is reasonable to expect that the solvent response will be different and for the effect of protic and aprotic solvents to be different. Protic solvents may raise the barrier to the conical intersections relative to the gas phase and aprotic solvents may raise it further. This hypothesis is supported by the findings from temperature dependant fluorescence that the deactivation of InC is a barrier crossing process, and that the barrier is larger in aprotic solvents than protic ones.[17] It is interesting to note that protic solvents tend to distort the structure of InC away from a planar geometry and we speculate that changes in the planarity of the molecule could be influential in modifying the ease with which the conical intersections can be accessed.[17] The conical intersection calculated by Yamazaki *et al.* were performed for indigo in a fixed planar geometry and it would be interesting to see how out-of-plane modes affect the potential energy surface.[6] On the other hand, Cui and Thiel had no such restrictions on their calculations and calculated the lowest energy conformation of bispyrroleindigo to be essentially planar, indicating that in the gas phase, out-of-plane motions are perhaps not especially important.[5]

One other potential cause for differences between the gas and solution phases is the presence of the two charged sulfate groups. Solvents, and particularly polar ones, will effectively shield the chromophore from these charges, whereas in the gas phase

no shielding is present. The perturbation caused by these charges may affect the potential energy surface leading to the observed lifetime changes. However, given the overall similarities in the absorption spectra and primary ESIPT processes, which one might anticipate to be more sensitive to this strong electrostatic interaction, it does not appear that this is the cause.

4.5 Conclusions

Using time-resolved photoelectron spectroscopy of the indigo carmine dianion in the gas-phase we have shown that, following excitation to the S_1 excited state, ESIPT is the primary mechanism occurring on the excited state. The ESIPT mechanism appears to be independent of the environment. On the other hand, the overall S_1 lifetime is highly solvent dependant, due to changes in the accessibility of the conical intersection between the S_1 excited state and the S_0 ground state. We have also measured a gas-phase absorption spectrum of InC^{2-}, which echoes neutral indigo well, supporting the suitability of studying it in place of the less soluble neutral indigo. Our data can be compared directly to recent theoretical efforts that have calculated the excited state potential energy surface as well as identified conical intersections that lead to internal conversion. Together, this provides a clear insight into the photo-stability of indigo and its derivatives.

4.6 References

1. G. Carr, *Oxford Journal of Archaeology*, 2005, **24**, 273.
2. E. S. B. Ferreira, A. N. H. Hulme, H. McNab and A. Quye, *Chem. Soc. Rev.*, 2004, **33**.
3. J. Seixas de Melo, R. Rondão, H. D. Burrows, M. J. Melo, S. Navaratnam, R. Edge and G. Voss, *ChemPhysChem*, 2006, **7**, 2303.
4. J. Seixas de Melo, A. P. Moura and M. J. Melo, *J. Phys. Chem. A*, 2004, **108**, 6975.
5. G. Cui and W. Thiel, *Phys. Chem. Chem. Phys.*, 2012, **14**, 12378.
6. S. Yamazaki, A. L. Sobolewski and W. Domcke, *Phys. Chem. Chem. Phys.*, 2011, **13**, 1618.
7. A. Cembran, F. Bernardi, M. Garavelli, L. Gagliardi and G. Orlandi, *J. Am. Chem. Soc.*, 2004, **126**, 3234.
8. G. Zimmerman, L.-Y. Chow and U.-J. Paik, *J. Am. Chem. Soc.*, 1958, **80**, 3528.
9. D. H. Waldeck, *Chem. Rev.*, 1991, **91**, 415.
10. G. M. Wyman, *Chem. Rev.*, 1955, **55**, 625.
11. G. M. Wyman, *J. Chem. Soc. D*, 1971, 1332.
12. G. M. Wyman and B. M. Zarnegar, *J. Phys. Chem.*, 1973, **77**, 1204.
13. T. Kobayashi and P. M. Rentzepis, *J. Chem. Phys.*, 1979, **70**, 886.
14. I. Iwakura, A. Yabushita and T. Kobayashi, *Bull. Chem. Soc. Jpn.*, 2011, **84**, 164.
15. I. Iwakura, A. Yabushita and T. Kobayashi, *Chem. Lett.*, 2009, **38**, 1020.
16. I. Iwakura, A. Yabushita and T. Kobayashi, *Chem. Phys. Lett.*, 2010, **484**, 354.
17. Y. Nagasawa, R. Taguri, H. Matsuda, M. Murakami, M. Ohama, T. Okada and H. Miyasaka, *Phys. Chem. Chem. Phys.*, 2004, **6**, 5370.
18. T. Suzuki, *Int. Rev. Phys. Chem.*, 2012, **31**, 265.
19. J. R. R. Verlet, *Chem. Soc. Rev.*, 2008, **37**, 505.

20. A. Stolow, A. E. Bragg and D. M. Neumark, *Chem. Rev.*, 2004, **104**, 1719.
21. A. Dreuw and L. S. Cederbaum, *Chem. Rev.*, 2001, **102**, 181.
22. X. B. Wang and L. S. Wang, *Annu. Rev. Phys. Chem.*, 2009, **60**, 105.
23. D. A. Horke, A. S. Chatterley and J. R. R. Verlet, *Phys. Rev. Lett.*, 2012, **108**, 083003.
24. P. J. Stephens, F. J. Devlin, C. F. Chabalowski and M. J. Frisch, *J. Phys. Chem.*, 1994, **98**, 11623.
25. R. Krishnan, J. S. Binkley, R. Seeger and J. A. Pople, *J. Chem. Phys.*, 1980, **72**, 650.
26. M. J. Frisch, G. W. Trucks, H. B. Schlegel, G. E. Scuseria, M. A. Robb, J. R. Cheeseman, G. Scalmani, V. Barone, B. Mennucci, G. A. Petersson, H. Nakatsuji, M. Caricato, X. Li, H. P. Hratchian, A. F. Izmaylov, J. Bloino, G. Zheng, J. L. Sonnenberg, M. Hada, M. Ehara, K. Toyota, R. Fukuda, J. Hasegawa, M. Ishida, T. Nakajima, Y. Honda, O. Kitao, H. Nakai, T. Vreven, J. A. Montgomery, J. E. Peralta, F. Ogliaro, M. Bearpark, J. J. Heyd, E. Brothers, K. N. Kudin, V. N. Staroverov, R. Kobayashi, J. Normand, K. Raghavachari, A. Rendell, J. C. Burant, S. S. Iyengar, J. Tomasi, M. Cossi, N. Rega, J. M. Millam, M. Klene, J. E. Knox, J. B. Cross, V. Bakken, C. Adamo, J. Jaramillo, R. Gomperts, R. E. Stratmann, O. Yazyev, A. J. Austin, R. Cammi, C. Pomelli, J. W. Ochterski, R. L. Martin, K. Morokuma, V. G. Zakrzewski, G. A. Voth, P. Salvador, J. J. Dannenberg, S. Dapprich, A. D. Daniels, Farkas, J. B. Foresman, J. V. Ortiz, J. Cioslowski and D. J. Fox, *Gaussian 09, Revision A.02*, Wallingford CT, 2009.
27. X.-P. Xing, X.-B. Wang and L.-S. Wang, *Phys. Rev. Lett.*, 2008, **101**, 083003.
28. X.-P. Xing, X.-B. Wang and L.-S. Wang, *J. Phys. Chem. A*, 2008, **113**, 945.
29. D. A. Horke, A. S. Chatterley and J. R. R. Verlet, *J. Chem. Phys.*, 2013, **139**, 084302.
30. D. A. Horke, A. S. Chatterley and J. R. R. Verlet, *J. Phys. Chem. Lett.*, 2012, **3**, 834.
31. S. E. Sheppard and P. T. Newsome, *J. Am. Chem. Soc.*, 1942, **64**, 2937.
32. G. Haucke and G. Graness, *Angew. Chem. Int. Ed.*, 1995, **34**, 67.
33. D. Jacquemin, J. Preat, V. Wathelet and E. A. Perpète, *J. Chem. Phys.*, 2006, **124**, 074104.
34. E. Wille and W. Lüttke, *Angew. Chem. Int. Ed.*, 1971, **10**, 803.
35. S. Dähne and D. Leupold, *Angew. Chem. Int. Ed.*, 1966, **5**, 984.
36. M. Klessinger and W. Luttke, *Tetrahedron*, 1963, **19**, 315.

5 Relaxation Dynamics of Gas Phase DNA Subunits

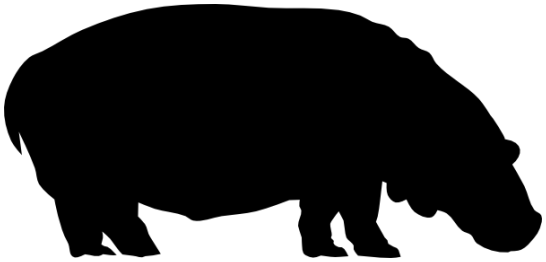

This chapter is based on the following publications:

A. S. Chatterley, A. S. Johns, V. G. Stavros and J. R. R. Verlet, Base-Specific Ionization of Deprotonated Nucleotides by Resonance Enhanced Two-Photon Detachment. *J. Phys. Chem. A,* 2013, **117,** 5299

A. S. Chatterley, C. W. West, G. M. Roberts, V. G. Stavros and J. R. R. Verlet, Mapping the ultrafast dynamics of adenine onto its nucleotide and oligonucleotides, **submitted**

The theory was performed by Gareth M. Roberts.

5.1 Introduction

The general topic of DNA relaxation dynamics was introduced in Chapter 1. These dynamics have implications for areas ranging from prebiotic evolution[1, 2] to modern day cancer science,[3] and hence there is a great deal of interest within the photoreaction dynamics community. In the gas phase, previous efforts have been for the most part limited to studying individual nucleobases[4, 5] – anything larger is too involatile to easily seed into a molecular beam. The complexity of even isolated nucleobases is high enough that experimental interpretation is non-trivial, and to assist in understanding experimental results, a large amount of theoretical chemistry studies have been performed,[5, 6] offering a multitude of explanations for the observed dynamics. With the increasing power of both computers and theoretical techniques, larger systems can be calculated, and the properties of systems too large to explore in the gas phase (as neutrals) can be computed.

In the solution phase, however, there is no practical limit on system size and so the dynamics of much more complex DNA subunits have been studied.[4, 7] The solution phase arguably resembles the natural environment of DNA better than the gas phase, and very complex systems can be studied. On the other hand, interpretation of solution phase data can be very difficult, as peaks are broadened by solvent and transient absorption and fluorescence upconversion (the most common techniques) results are

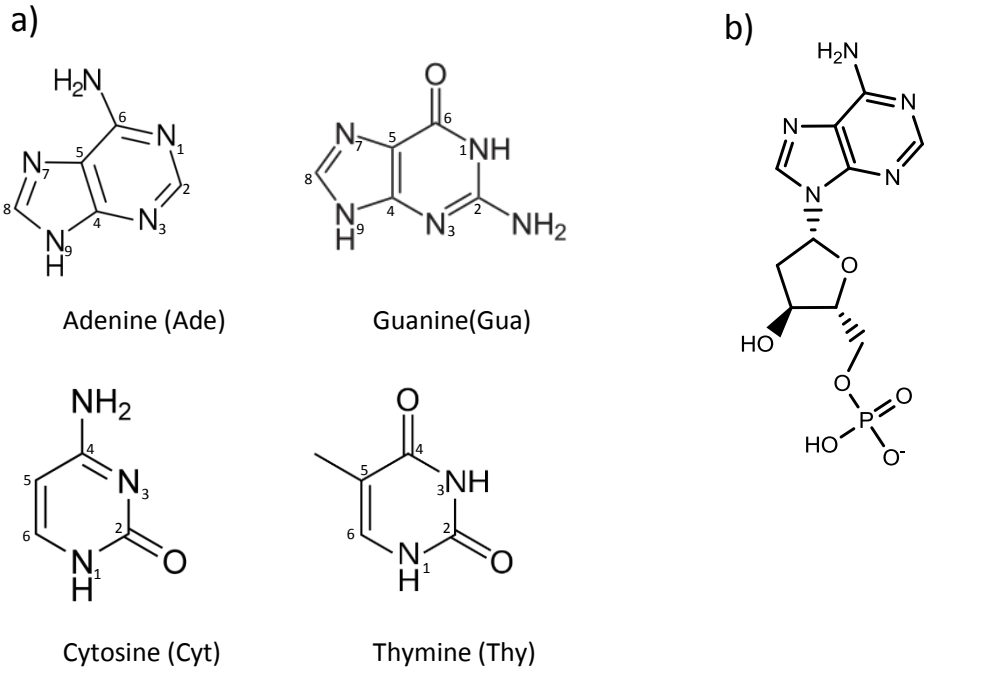

Figure 5.1 a) The chemical structure of the four nuclebases. The sugar/phosphate backbone attaches at the N^9 position for Ade and Gua, and N^1 position for Cyt and Thy. b) The chemical structure of 2'-deoxyadenosine 5'-monophosphate ($dAMP^-$) as an example of the structure of a nucleotide.

strongly influenced by selection rules and Franck-Condon factors.

Here, we demonstrate how the gap between neutral gas phase, solution phase and theory may be bridged by using electrospray to introduce large anionic DNA subunits into the gas phase. First, in section 5.3, we show how a novel resonance enhanced electron detachment scheme may be used to discern the ionization energy of a base chromophore from within a larger nucleotide structure (see Fig. 5.1(b)). An understanding of the ionization energies is crucial to interpretation of time resolved photoelectron (PE) experiments. The remainder of the chapter uses time resolved PE spectroscopy to measure the intrinsic dynamics of all four nucleotides for the first time. Finally, we demonstrate the scalability of the technique, and results from time resolved PE spectroscopy on oligonucleotide dimers and trimers is demonstrated. The results from isolated anion spectroscopy can be compared with those from theory and other DNA subunits in both the gas and solution phases, to give a more complete picture as to the mechanisms at play in photoexcited DNA relaxation.

5.2 Methods

5.2.1 Experimental Methods

The experiments were performed using the electrospray time-resolved photoelectron instrument in Durham (see Chapter 2). 2'-deoxythymidine 5'-monophospate ($dTMP^-$), 2'-deoxyadenosine 5'-monophospate ($dAMP^-$), 2'-deoxycytidine 5'-monophospate ($dCMP^-$) and 2'-deoxyguanosine 5'-monophospate ($dGMP^-$) is generated via electrospray ionization from a ~0.5 mM solution of dXMP or dXMP sodium salt (Sigma-Aldrich) in methanol and 2,2,2-trifluoroethanol (4:1 mixture). The oligonucleotide anions (Section 5.4.5) were generated from a ~0.5 mM solution of $d(A)_2$ or $d(A)_3$ (Sigma-Aldrich, desalted). To make up nucleotide solutions, ~1 mg of the solid nucleotide or nucleotide salt was dissolved in 4 mL of methanol. Additionally, 1 mL of 2,2,2-trifluorothenaol was added, this appears to enhance ion signal.[8] The oligonucleotides are generally provided in exceptionally small quantities, so they were dissolved in methanol directly from the tube they were provided in to make a stock solution, which was then diluted to the appropriate concentration for experiments. The ion signal does not seem to be particularly dependant on concentration; even into the μM regime reasonable ion signal was obtained.

For the base specific ionization work (section 5.3), a single 4.64 eV (267 nm) laser beam was used, whilst for the time-resolved work a 3.10 eV (400 nm) probe was used in addition to a 4.66 eV (266 nm) UV pump beam. As the 4.64 eV laser results in

significant background noise, for these experiments PE images were collected both in the presence and absence of ions, and were subtracted every 10 camera frames, removing background PE noise. The ion beam can be programmatically turned on and off by disabling or enabling the triggering of the ion trap from the digital delay generator.

All time resolved data were fitted using the global fitting algorithm, described in Chapter 2. Support plane analysis was used to estimate confidence intervals at the 95% level, and the greater of the upper and lower bounds has been reported as the error.

5.2.2 Theory Methods

Density functional theory (DFT) and time-dependent DFT (TD-DFT) calculations on $dAMP^-$ anions and adenine were performed using the PBE0 functional[9] in the Gaussian09 computational suite.[10] The functional has been selected for its balanced and robust description of both valence and Rydberg excited states in TD-DFT calculations.[11] All vertical excitation energies were calculated at the PBE0/aug-cc-pVDZ//TD-PBE0/aug-cc-pVTZ level of theory. Optimised ground state geometries were confirmed to be (local) minima, as verified through further harmonic frequency calculations (no imaginary frequencies). The effects of a water solvent were simulated using a polarisable continuum model (PCM).

5.3 Base-Specific Ionization of Nucleotides

5.3.1 Introduction

The interaction of electrons or high-energy photons with DNA is one of its main causes of damage which can ultimately lead to mutations and cell death.[12-16] From a molecular perspective, it is the ionization potentials of the DNA sub-units that are central to developing an understanding of how such damage may arise. In particular, the lowest (adiabatic) ionization energy of the nucleobases is of key importance as this is the lowest oxidation site in DNA and is an essential parameter in the conduction of holes through the polymer.[17, 18] This importance is reinforced by the burgeoning applications of DNA in molecular nanotechnology.[19-21] Developing robust methods to predict the ionization energy in any environment is therefore a major scientific goal, but this is reliant on experimental benchmark data. Here, we present the experimental determination of the adiabatic ionization energies of the nucleobases in all 4 nucleotides in the gas phase.

To help elucidate the ionization mechanisms, and the threshold at which these are observed, a 'bottom-up' approach has been employed, starting with the ionization of

isolated nucleobases in the gas-phase, which have been studied using PE spectroscopy,[22-27] electron attachment[28-30] and computational chemistry.[31-36] In the solution phase, ionization potentials have been determined using PE spectroscopy on liquid microjets[37] and with *ab initio*[38-41] or semi-empirical calculations.[42, 43] Building on the gas phase work, the PE spectroscopy of isolated nucleotides and oligonucleotides has recently been studied by the Wang group with the aim of understanding how the ionization energy changes with the introduction of the sugar and phosphate backbone.[44] Deprotonation of the nucleotide, which occurs on the phosphate,[45, 46] conveniently enables mass-selection prior to PE spectroscopy, and provides a protonation state analogous to that found in the natural environment. Although the gas phase is an alien environment for a biomolecule, isolated nucleotide anions are important model systems providing intrinsic electronic structure information, which is an essential starting point for comparisons with both theoretical calculations and experimental solvation studies, whether in bulk liquid or gas phase solvent clusters. In solution, it has been shown that in all cases the first ionization site is located on the base,[37, 42] as the solvent stabilizes the phosphate. Hence, the detachment energy of the phosphate is of little significance. In contrast, the determination of the intrinsic ionization energies of the *nucleobases* within nucleotides is significant and allows one to develop an understanding of the factors affecting the stabilization of the base in solution and ultimately in DNA. In the gas-phase, single-photon PE spectroscopy of nucleotides can lead to ionization from other parts of the molecule including the phosphate and sugar. As a result, ionization from the base could not be discerned from these additional ionization channels (see Fig. 5.2(a)). This was the case for $dTMP^-$, $dAMP^-$, $dCMP^-$. For $dGMP^-$, electron loss from the base could be identified by a feature at low electron binding energy (*eBE*) which was also observed in all G containing oligonucleotides.[44] Here, we overcome the limitations of single photon PE spectroscopy and experimentally determine the ionization energy of the base in the remaining deprotonated nucleotides.

Several techniques have been employed in an attempt to determine the site of the lowest binding energy in isolated oligonucleotides. The Kappes group has performed careful chemical substitution and PE spectroscopy of mass- and isomer-selected oligonucleotide anions to determine the binding sites in these polymeric systems.[47, 48] For the mononucleotides, however, theory has been the primary tool for settling this ambiguity. The Wang group carried out density functional theory (DFT) studies with their single-photon PE spectra, which gave the lowest binding site as the phosphate group for all nucleotides except $dGMP^-$.[44] More sophisticated theory has since been

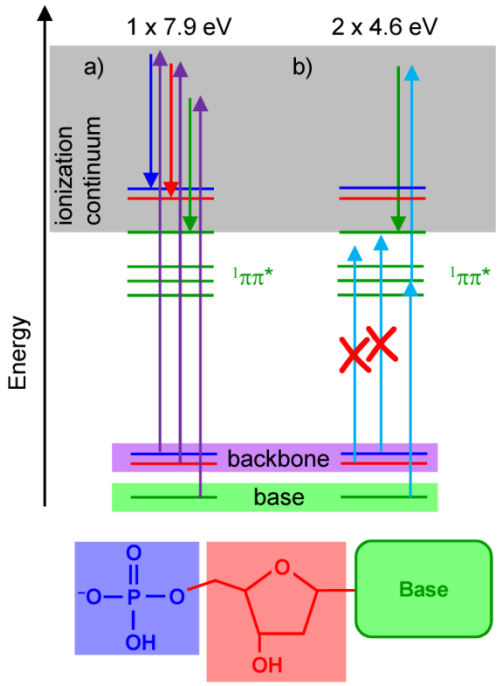

Figure 5.2 Schematic energy level and ionization scheme for a) one-photon vacuum ultraviolet PE spectroscopy, and b) resonance enhanced two-photon detachment (R2PD). The one-photon scheme leads to ionization from the base moiety and sugar-phosphate backbone. The R2PD scheme, on the other hand, leads to ionization specifically from the base moiety, and is insensitive to the backbone of the nucleotide.

performed, which has called this assignment into question. Both the partial third order self-energy approximation of the electron propagator (P3),[32, 49, 50] and complete active space with a perturbation theory correction (CASPT2)[51, 52] methods suggest that the first ionization is from the base in $dTMP^-$ and $dGMP^-$, with P3 also indicating that the phosphate is responsible for the first ionization from $dCMP^-$ and $dAMP^-$, although CASPT2 has not been performed on these systems. Here, we present a simple experimental methodology that provides direct and unique insight into the photodetachment energy of the base in nucleotides. Specifically, a resonance-enhanced two-photon detachment (R2PD) scheme is used that confirms the assignment of the low *eBE* feature in $dGMP^-$ and reveals, for the first time, that in $dCMP^-$, $dTMP^-$ and $dAMP^-$, the phosphate has the lowest ionization energy.

Single-photon PE spectroscopy is unable to determine *a priori* from where in the nucleotide the electron is detached, as the vacuum ultraviolet photon is sufficient to detach from the base, sugar and phosphate and all of these will contribute to the final PE spectrum (see Fig. 5.2(a)). For $dXMP^-$, this leads to broad and structureless bands. To circumvent this limitation, we exploit the fact that all four bases have a strong $^1\pi\pi^*$ transition in the UV around 4.6 eV (267 nm) and employ a two-photon excitation scheme. As shown in Fig. 5.2(b), a single 4.6 eV photon is insufficient to detach an

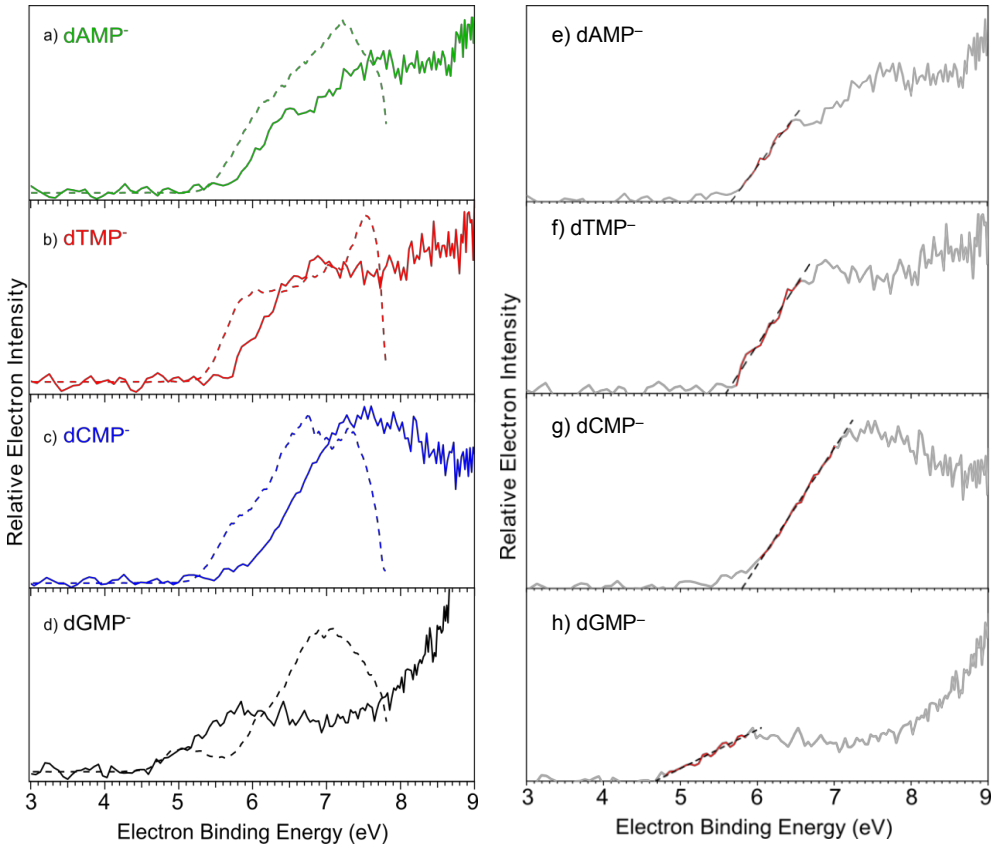

Figure 5.3 Comparison of one- and two-photon detachment spectra for a) $dAMP^-$ (green), b) $dTMP^-$ (red), c) $dCMP^-$ (blue) and d) $dGMP^-$ (black). One-photon spectra by Wang and co-workers are represented by dashed lines, whilst the solid lines present the two-photon detachment (R2PD) from the present work. The higher *eBE* onset in a) to c) indicate that phosphate detachment is the lowest ionization for these bases, whilst for $dGMP^-$ it is the base which detaches first. e) – h) show the procedure used to obtain the ADEs in this work. The steepest part (red) was fit by a straight line, and the intercept taken as the ADE. Adapted with permission from ref. 44.

electron from the base, sugar or phosphate moieties, but will excite it to the optically bright $^1\pi\pi^*$ states localized on the base. A second photon can subsequently remove the electron from the excited state, ionizing *only* the base. The time between the absorption of both photons must be minimized because the lifetimes of the $^1\pi\pi^*$ states in isolated bases have been shown to be very short.[7, 53-55] Hence, the use of femtosecond (fs) pulses is critical to the experimental scheme as they minimize detachment occurring from photo-products that can be formed following internal conversion.[56-59]

More formally, the mechanism whereby R2PD gives base selectivity can be explained using Koopmans' correlations and Franck-Condon factors (see Chapter 1). The concept of detachment from the base moiety is effectively a statement that the product radical neutral species has an electron hole in an orbital associated with the base. Conversely, detachment from the phosphate group results in a hole on an orbital associated with the phosphate. The resonance located around 4.6 eV promotes a π electron from the aromatic system of the base, and thus using this resonance a π^{-1}

neutral species can be obtained. The vertical nature of the transition means that electronic rearrangement cannot occur, and so a product with an electron hole on the phosphate is inaccessible, and all resonance enhanced detachment must correlate to detachment which leaves the base aromatic system with a hole.

5.3.2 Results and Discussion

The solid lines in Fig. 5.3(a-d) show the R2PD spectra taken at 4.64 eV for $dXMP^-$ with X = A, T, C and G, respectively, with the total photon energy corresponding to 9.28 eV (*i.e.* 2 × 4.64 eV). The R2PD spectra have broad asymmetric features with an onset of *eBE* ~5.7 eV observed for detachment from the base in $dAMP^-$, $dTMP^-$ and $dCMP^-$. In contrast, the onset in $dGMP^-$ is significantly lower at *eBE* = 4.65 eV, indicating that base-specific ionization in $dGMP^-$ occurs at significantly lower energy than in the other three nucleotides.

Also shown in Fig. 5.3(a-d), as dashed lines, are the single-photon PE spectra taken by the Wang group, with 7.866 eV photons.[44] For the four nucleotides, the single photon PE spectra show an intense, broad, and unresolved peak, with an onset of ~5.4 eV (see Table 5.1). The PE spectrum of $dGMP^-$ additionally shows a smaller feature separated from these intense features at lower binding energy with an onset at *eBE* = 4.61 eV. This PE feature was assigned to direct detachment from G in $dGMP^-$, with the large feature onset at 5.8 eV assigned to detachment from the backbone. Similarly, the onset of the broad features in $dAMP^-$, $dTMP^-$, and $dCMP^-$ were assigned to detachment from the backbone, with ionization of the base presumably convoluted in this peak. However, individual contributions due to the backbone and base cannot be unraveled in these spectra. This is exacerbated by the fact that the ionization cross-sections of the base and backbone may differ dramatically. For example, in $dGMP^-$ the feature assigned to detachment from the base is about 7 times smaller than the features believed to arise from ionization of the backbone. Hence, no experimental insight into the relative detachment channels could be gained.

Comparing the $dGMP^-$ spectra following one- and two-photon excitation, several important similarities and differences are apparent. Firstly, the onset at *eBE* = 4.65 eV in the R2PD scheme is in excellent agreement with the *eBE* = 4.61 eV measured with one photon. As the R2PD scheme ionizes only from the base moiety (the sugar and phosphate are optically dark), the original assignment of the lower binding energy peak to ionization of the Gua base has been confirmed experimentally. Moreover, the agreement in *eBE* onsets demonstrates that our methodology is a viable way of determining the onset of ionization of the base in a nucleotide. We recognize however,

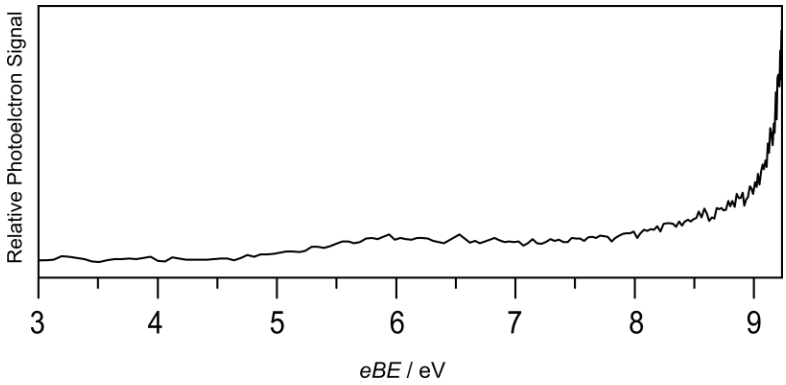

Figure 5.4 Complete R2PD spectrum of $dGMP^-$. The large signal >8 eV is the onset of photodetachment from the base with a single 4.64 eV photon.

that a number of final electronic states are potentially accessible following photodetachment. Specifically, we assume that the ground state of the neutral deprotonated nucleotide corresponds to one in which a hole resides on the base and an electron on the phosphate. As the phosphate anion has a considerably lower electron detachment energy than the ionization energy of a neutral base, this assumption may not necessarily hold. Regardless, we are still measuring the adiabatic detachment energy of the base itself, as per the Koopmans' correlation arguments above.

Secondly, the R2PD spectrum for $dGMP^-$ shows a very intense signal at high *eBE* (>8 eV), which is not present for the other nucleotides. This feature has been truncated above 8.8 eV, where it continues to rise sharply, dwarfing the R2PD base-selective ionization (see Fig. 5.4 for the full spectrum). This feature arises from single-photon ionization of the base; although the adiabatic ionization energy of $dGMP^-$ is 4.65 eV, both the initial internal temperature of the ions (≥ 300 K)[60] and the bandwidth of the femtosecond laser pulses will lead to a small fraction of molecules to be ionized with a single 4.64 eV photon. The relative intensity indicates that this process has a much larger cross section, as may be expected for a single-photon process compared to a R2PD process. Note that, with respect to the *eBE* axis shown in Fig. 5.4, the location of this feature is misleading, as this axis assumes a total absorbed energy of 9.28 eV (two photons of 267 nm).

Finally, the spectral profile of the PE spectra from $dGMP^-$ differs substantially between the one-photon and R2PD spectra. Specifically, the features due to detachment from the base have a maximum around 5.1 eV and 5.9 eV in the one-photon and R2PD spectra, respectively. There are two probable causes for this discrepancy. Firstly, the R2PD spectrum is dependent on both the cross section for excitation to the $^1\pi\pi^*$ state, and the subsequent ionization from this state. In contrast, direct one-photon ionization is solely dependent on the ionization cross section of the base. Thus, the Franck-

Table 5.1 Comparison of adiabatic detachment energies (*ADE*) for nucleotide anions and corresponding neutral nucleobases, measured using one-photon PE spectroscopy and base specific R2PD on the nucleotides. In $dGMP^-$, the lowest energy for single-photon ionization is from the base, whilst in the other nucleotides it is from the backbone. In all instances, the *ADE* of the base moiety in the nucleotide anion is ~3 eV lower than in the neutral base.

Mononucleotide	one-photon *ADE* /eV[a]	R2PD *ADE* / eV	nucleobase *ADE* /eV[b]
$dAMP^-$	5.55 ± 0.10	5.65 ± 0.15	8.26
$dTMP^-$	5.40 ± 0.10	5.60 ± 0.15	8.87
$dCMP^-$	5.30 ± 0.10	5.80 ± 0.15	8.68
$dGMP^-$	4.61 ± 0.10	4.65 ± 0.15	7.77

[a]Ref. 44, [b]Ref. 22

Condon factors for the two processes will be different, leading to different maxima observed in the PE spectra. Secondly, for the R2PD spectrum, the two photons must be absorbed within ~120 fs of each other (the laser pulse duration). Albeit short, this timescale is comparable to the fastest dynamics observed in neutral DNA bases by Stolow and co-workers using time-resolved PE spectroscopy.[53] For Ade, Cyt and Thy, the decay was observed to be bi-exponential with a sub-50 fs component and a slower picosecond component. The initially excited $^1\pi\pi^*$ state rapidly decays to lower lying states, believed to be $^1n\pi^*$ states. In the PE spectra, this manifests as a shift to higher *eBE* by ~1 eV in adenine, with similar shifts observed in the other bases. Unfortunately, no time-resolved PE data has been acquired for the isolated guanine base, although the lifetimes of integrated ion yield experiments show similar timescales and bi-exponential dynamics as those observed for the other bases.[55]

Additional insight into the early-time dynamics is given by the time resolved PE experiments presented in Section 5.4 of this chapter. Our results show a rapid red-shift in *eKE* of the signal maximum, which correlates to an increase in *eBE*. Hence, detachment from both the initial $^1\pi\pi^*$ state and the $^1\pi\pi^*$ at a lower energy geometry are likely to contribute to the R2PD spectrum. It is important to note that the presence of excited state dynamics, occurring on a timescale shorter than the experiment affords, invalidates an assignment of the vertical binding energy of the base in the nucleotide. In principle, using a much shorter excitation pulse would circumvent this issue and allow the vertical binding energy to be extracted. The ~50 fs dynamics (see below), however, would require pulses that are significantly shorter than this, which are non-trivial to generate with our current experimental setup.

We now discuss the remaining nucleotides, which display a higher *eBE* onset in the R2PD spectra than in the single-photon PE spectra. Table 5.1 presents the onset binding energies produced by extrapolating the steepest part of the onset, for both the single-photon and R2PD methods (see Fig. 5.3(e-h)). The base specific R2PD onsets show a clear blue shift for $dAMP^-$, $dTMP^-$ and $dCMP^-$. The higher *eBE* onsets in the

R2PD spectra confirm the assignment of Wang and co-workers that the lowest oxidation site on the nucleotides corresponds to electron loss from the backbone (deprotonated phosphate).[44] Presumably, in the one-photon PE spectra, the large phosphate peak obscures features arising from ionization of the base, as it is almost an order of magnitude larger (in $dGMP^-$). We note that ultrafast decay pathways are also present in Ade, Thy and Cyt bases[7, 53, 61] and the spectral shape of the R2PD spectra do not reflect the vertical Franck-Condon profile between the ground state bases and the ionized base.

The observed experimental results agree with DFT calculations performed by the Wang group, which assigned a phosphate moiety as the site of first electron detachment in all nucleotides except $dGMP^-$. The more recent P3 calculations,[32, 49, 50] as well as calculations using CASPT2,[51, 52] disagree with this and assign the first ionization to the base π system in $dTMP^-$ as well as $dGMP^-$. It is worth noting that these computational efforts have been to determine vertical, not adiabatic, detachment energies. It is feasible that, as the base and phosphate detachments are close together in energy (~0.1 eV in the case of $dAMP^-$), the ordering will switch between vertical and adiabatic detachment energies, especially as we may expect the geometric response to electron loss to be substantially different between the base and phosphate moieties. Thus, theory and experiment do not necessarily disagree and it would be particularly interesting to determine the adiabatic ionization energies of nucleotides using higher levels of theory. The discrepancy could also arise from the high temperature of the ions[45], meaning that a large variety of nuclear geometries will be sampled. The introduction of an ion-mobility cell prior to R2PD spectroscopy will be able to address these shortcomings.[62]

Calculated gas phase structures have shown that the most important factor in determining ionization energy ordering of the nucleotides is the degree of intra-molecular hydrogen bonding between the phosphate and base, which has been shown by theory and gas phase IR spectroscopy to differ greatly between $dGMP^-$ and the other bases.[45, 46, 50] The structure of $dGMP^-$ is considerably more compact, with a hydrogen bond between the base and phosphate, whilst the remaining three nucleotides form an open structure. This results in the Gua base residing significantly closer to the charge carrying phosphate and leads to a destabilization of the π system on the base through Coulomb interactions, which lowers the adiabatic detachment energy (*ADE*). The relation between phosphate-base distance and detachment energy is, to an extent, reflected in the differences between the nucleotide and neutral nucleobase *ADE*s (see

Table 5.1), which is >3 eV for Gua and Thy and <3 eV for Ade and Cyt. This may suggest that $dTMP^-$ also has a shorter base-phosphate distance, or samples such structures at the experimental internal temperature. It is important to note that structural considerations alone do not explain the very low base IP in $dGMP^-$; the extra destabilization induced by the nearby phosphate only accounts for a portion of the low *ADE*, and the fact that neutral Gua has a low *ADE* to be begin with must also be considered.[22] Calculations have the advantage that different ionization channels can be readily identified with specific molecular orbitals, whereas in experiment, this is non-trivial. The combination of one-photon and R2PD experiments overcomes some of these limitations, granting a larger wealth of benchmark data.

We now briefly turn to the comparison between the ionization of DNA components in the gas and solution phases. Recent liquid microjet experiments by Slavíček *et al.* have measured the PE spectra of aqueous nucleosides of Cyt and Thy.[37] Additionally, numerous estimates of the ionization energies in solution of DNA components have been made using either pure *ab initio* calculations,[37-41] or by adjusting gas phase ionization energies with calculated thermodynamic parameters.[42] In aqueous solution the adiabatic ionization energy of the base in the two nucleosides studied decreases by ~2 eV relative to that of the gas phase base.[37] This shift arises almost entirely from solvent reorganization following base ionization, both locally[29,62-65] and due to a more extensive rearrangement.[26,30] Our measurements indicate that the charged phosphate decreases the ionization energy of the base by ~3 eV (see Table 5.1) through strong Coulomb interactions with the base. In solution, however, calculations by Slavíček *et al.* show that this Coulombic interaction is completely screened[26,30] such that the adiabatic ionization energy of that in solution is effectively that of the base only.

It is important to recognize that neither full solvation nor full isolation accurately represents the biological environment of a nucleotide. In double helix DNA, the phosphate groups are surrounded by water and counter ions, but water is excluded from the bases which are paired through hydrogen bonding and experience extensive stacking interactions with their neighbors. Hence, the effective charge screening and the ionization energy of the base observed in solution may be very different in DNA. The *ADE* of the bases in isolated nucleotides determined here, combined with experiments on solvated nucleosides, presents key reference points towards building an understanding of the various factors that influence the lowest ionization energies DNA. In particular, gas phase data presents an important benchmark for theoretical calculations upon which solvation models can subsequently be built. This may allow for

the systematic prediction of the ionization energy in any environment. Further experiments will also play an important role in this. For example: incremental solvation of the phosphate will provide insight into the screening of the charge by water; the extension to oligonucleotides can begin to probe effects of π-stacking on the ionization energies;[47, 48] and extension to base-pairs allows exploration of the effect of the unique hydrogen bond interactions within DNA.[63-65]

The R2PD scheme presented here is in principle scalable to larger and more complex systems. The intramolecular hydrogen bonded geometry of $dGMP^-$, which is partly responsible for the lowering of the base-specific *ADE*, is a unique feature of isolated nucleotides and, while it persists for small oligonucleotides as demonstrated by the low ionization energy of Gua in all G-containing di- and tri-nucleotides,[44] it is clearly not a feature of DNA. Hence, although gas phase spectroscopy can provide useful insights into intramolecular effects, it is important to bear in mind that some of these interactions are not relevant in real biological environment. Nevertheless, the scalability of our approach in conjunction with chemical substitution and microsolvation techniques, may offer a wealth of information about charge location and state ordering of DNA.

5.4 Dynamics of Isolated Nucleotides

Time-resolved PE spectroscopy has been performed on anions of all four of the naturally occurring nucleotides, as well as on a di- and tri- oligonucleotide. We shall now consider each nucleotide in turn, beginning with a brief review of the dynamics of the isolated nucleobase from theory and experiment, as well as larger derivatives in solution. Time-resolved PE spectroscopy results are then presented, along with discussions of how these findings relate to previous work in an effort to elucidate the mechanism of DNA relaxation. It is important to note that these experiments, along with most dynamics work on DNA fragments, have been conducted using a 4.7 eV (266 nm) pump which is well above the absorption onset. These results then reflect the dynamics for vibrationally excited DNA bases, and mechanistic differences may arise as pump energy is increased or decreased. However, it should also be noted that the shape and position of the absorption band around 250 nm is very similar in the gas-phase to that in solution, at least for adenine.[66]

5.4.1 Adenine

Of the four naturally occurring nucleobases, adenine (Ade, see Fig. 5.1(a)) is by far the best studied in terms of its excited state dynamics. Adenine is found only in the

biological keto tautomer in molecular beams,[67] so it is ideally suited to gas phase experimentation.[53-55, 68-74] Simultaneously, a considerable number of *ab initio* computational studies have been performed to understand the excited states and relaxation dynamics of isolated Ade.[5, 6, 75-90] Despite the impressive body of work on Ade, there are still many fundamental questions is to its excited state dynamics, and especially how these results scale up to nucleotides and biological systems.

The electronic structure of Ade has been calculated by numerous techniques,[5, 6, 75-90] and measured using REMPI.[91-96] The first excited state is a dark state of $^1n\pi^*$ character, and lies slightly below the optically bright first $^1\pi\pi^*$ state (labelled ^1L_a). Higher in energy lies a second bright $^1\pi\pi^*$ state, labelled ^1L_b, although this state carries less oscillator strength than the ^1L_a state. The calculated state ordering, however, is very sensitive to theory method used for predictions.[90] Additionally, a $^1\pi\sigma^*$ state, corresponding to N^9-H bond dissociation (see Fig. 5.1(a) for atom labels), has been located,[79, 80, 83, 87, 97] along with another $^1\pi\sigma^*$ state localized on the N-H bond of the amino group on the C^6 atom.[80] These $^1\pi\sigma^*$ states form CIs with the ground state, as in phenols (see Chapter 3). The N^9 position is where the sugar/phosphate backbone attaches, and hence in biological systems the first $^1\pi\sigma^*$ state is much higher in energy. Many gas phase experiments have been performed on 9-methyladenine (Ade-9Me), a derivative where the N^9 position is methylated to better simulate adenine in biological systems.[68, 69, 72, 74]

Time-resolved ion yield experiments, exciting at 4.7 eV and employing multiphoton probes, found both Ade and Ade-9Me to decay biexponentially, with essentially equal time constants of 100 and 110 fs for the fast component, and 1.1 and 1.3 ps for the slower component in Ade and Ade-9Me, respectively.[55, 74] These results were interpreted with a two state mechanism, where the initially excited (^1L_a) $^1\pi\pi^*$ state rapidly decays into the $^1n\pi^*$ state, which then converts to the S_0 state via a CI on a ps timescale. Time-resolved PE spectroscopy, pumping at 266 nm and probing at 200 nm, globally fit in the same manner as the data presented here, was performed by Stolow and co-workers, on both Ade and Ade-9Me.[53, 68-70, 72] The two components of the biexponential decay could be resolved in the decay associated spectra, and are presented in Fig. 5.6(b) and (c). Although the timescales decay for Ade and Ade-9Me are extremely similar, the spectrum for the slower component in Ade-9Me shows a notable absence of signal around *eBE* = 9.8 eV, which is present in the corresponding spectrum for Ade. This was taken as an indication of involvement of the $^1\pi\sigma^*$ state in the relaxation of Ade, however more recent experiments have suggested that an H

atom loss channel does not switch on until 5.3 eV (233 nm) excitation, shedding some doubt on the involvement of the $^1\pi\sigma^*$ state in dissociation.[54, 71, 73] It is important to note that an absence of observed H atom yield does not necessarily mean that decay using the $^1\pi\sigma^*$ is inoperative – it is feasible that the quantum yield of H atoms crossing through the lower CI is negligible and so experiments which exclusively focus on H atoms are blind to it. This was observed in the indole system, which does not release H atoms when excited at 273 nm, despite strong evidence that the $^1\pi\sigma^*$ state is active.[98] The relaxation dynamics of Ade-9Me were then again explained using the $^1n\pi^*$ state as an intermediate in a two state mechanism, as the $^1\pi\sigma^*$ state is blocked.

Ab initio calculations have located two CIs with the ground state which are viable to drive relaxation, although many other CIs have been located.[75-87] Using the Boeyens classification scheme,[99] the approximate geometry of the six membered ring at each CI can be described, and these have been adopted as the labels for discussing the CIs in Ade. The first CI, ^{2}E, is a crossing between the ^1L_a ($^1\pi\pi^*$) and S_0 states. It is agreed to possess the lowest energy of all CIs, and has an 'envelop-like' geometry, puckered at the C^2 position. The second feasible relaxation CI is labelled $^1S_6$, found at a geometry where the amino group is out-of-plane. This CI is between the $^1n\pi^*$ and S_0 states, although outside of the equilibrium geometry significant mixing of characters occurs so that these labels no longer well describe the states. Other located CIs include a ring opening reaction, and the aforementioned $^1\pi\sigma^*$ states.[79, 80, 83] Both minimum energy paths[6, 78, 81, 82, 87] and adiabatic dynamics simulation techniques[84-86, 88-90] have been used in an attempt to understand which CI is utilized in Ade relaxation. Essentially, two mechanisms have been proposed. Firstly, there is a one state mechanism where relaxation is primarily through the ^{2}E CI, and all dynamics occur on the $^1\pi\pi^*$ states. Secondly, there has been proposed a two state mechanism, where the first step is population transfer to the $^1n\pi^*$, followed by decay to the ground state via the $^1S_6$ CI. In the one state mechanism, the rapid step of the experimentally observed biexponential decay is attributed to wavepacket motion on the $^1\pi\pi^*$ states, whilst in the two state mechanism it is caused by the initial $^1\pi\pi^* \rightarrow {}^1n\pi^*$ internal conversion. Which mechanism appears to be favoured is highly dependent on the level of theory employed – a recent study has shown that small variations in potential energy surface topography results in very different outcomes in adiabatic dynamics simulations.[90]

In the solution phase, a number of dynamics experiments have been performed on Ade, and $dAMP^-$ as in this work. Both fluorescence upconversion[4, 6, 100-102] and transient absorption[4, 6, 102-104] have been utilized, and $dAMP^-$ decays biexponentially when excited

at 4.7 eV. The most recent measurement gives the short timescale as < 100 fs, and the longer lifetime as 340 fs.[102] Recently, time-resolved PE spectroscopy has been performed on aqueous adenosine, pumped at 4.7 eV.[105] Within the time resolution of the experiment, only a monoexponential decay was observed, with a lifetime of ~220 fs, in reasonable agreement with other solution phase experiments. *Ab initio* theory in the solution phase found that the $^1n\pi^*$ state is significantly destabilized by solvation, whilst the $^1\pi\pi^*$ states are slightly stabilized.[106-109] Note that away from the vertical excitation geometry, significant state mixing occurs so that these diabatic labels no longer apply too well. Below we present TD-DFT calculations by our group which support these assignments, and also calculate the effect of the backbone and charge of a nucleotide on the states of gas phase $dAMP^-$. Most theory work has dismissed the two state mechanism in solution, due to the destabilization of the $^1n\pi^*$,[106-108, 110] however recent surface hopping results suggest that a two state mechanism may still be at play.[109] The authors of this work were careful to caution that such computations are highly sensitive to calculated potential energy surfaces, and so are not definitive.

In an attempt to unify the multiple approaches of Ade, and to build up towards biological DNA, we present the time-resolved photoelectron spectroscopy of the nucleotide of $dAMP^-$, which was generated using electrospray ionisation. We show that, by comparison of the dynamics of isolated $dAMP^-$ with those in solution and with Ade and derivatives of Ade, the relevant decay dynamics of the nucleobase in $dAMP^-$ can be understood.

Time-resolved photoelectron spectra (4.7 eV pump, 3.1 eV probe) are shown as a false colour plot for $dAMP^-$ in Fig. 5.5(a). In this, the two-photon contribution from the pump only has been subtracted, and as the probe is not resonant with any initial transition, this subtraction recovers the pump-probe excited state signal. An increase in photoelectron yield at $t = 0$ is observed as population is transferred to the optically bright $^1\pi\pi^*$ states by the pump. Inspection of the spectra shows two dominant features: at electron kinetic energies, $eKE < 0.7$ eV, there is a component which decays over the course of hundreds of femtoseconds, while between $1 < eKE < 2$ eV, a feature decays within the instrument response.

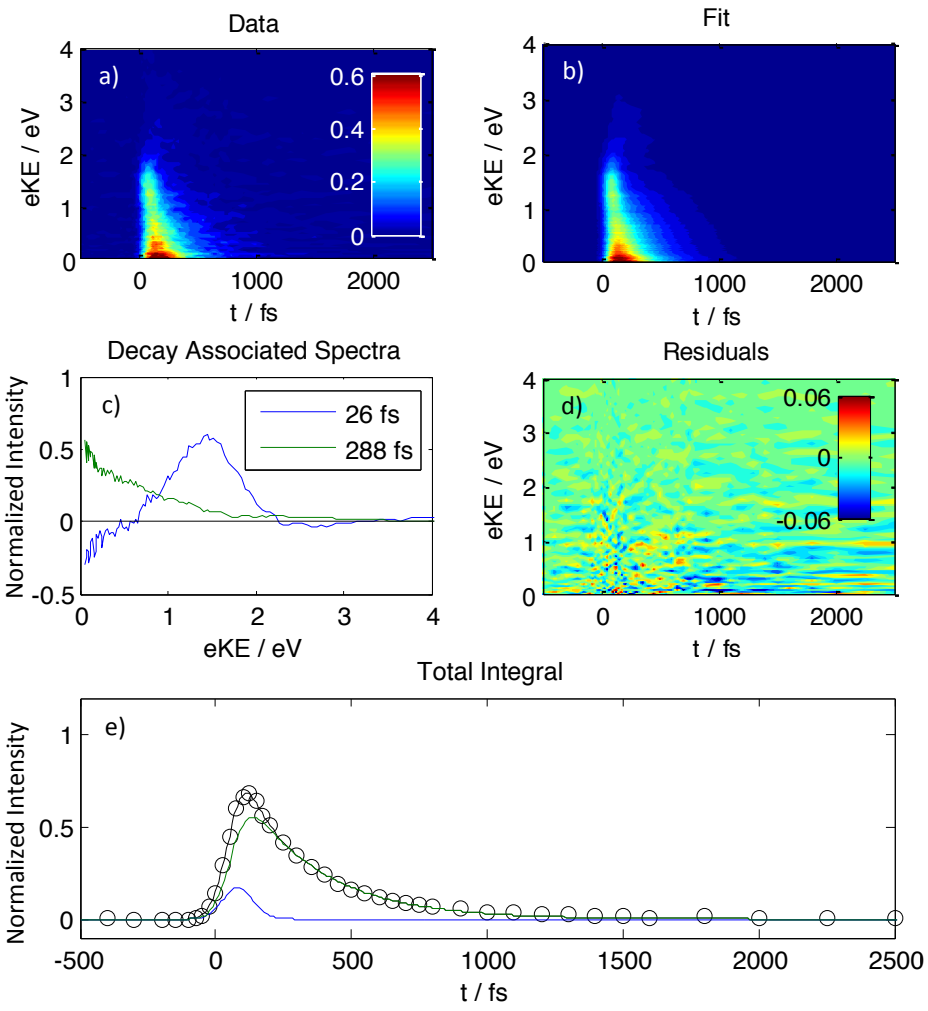

Figure 5.5 a) The time-resolved PE-spectrum of dAMP⁻, pumped at 4.7 eV, probed at 3.1 eV. b) Global fit of the experimental spectrum, using two exponential decay functions. c) Decay associated spectra from the global fit. d) Residuals from the fitting procedural. e) Total integrated PE counts as a function of time. Open circles show experimental points, coloured curves correspond to the integrals of the spectra shown in c), and the black curve is the total integral from the fitting procedure.

Quantitative insight can be gained by employing a global fitting procedure, see Chapter 2. The results of the global fit are shown in Fig. 5.5(b), and the residuals are in Fig. 5.5(d). Only two exponential functions with lifetimes τ_1 = 26 ± 37 fs and τ_2 = 288 ± 47 fs are required to fully recover the dynamics; the corresponding decay-associated spectra are shown in Fig. 5.5(c), and the time-integrated spectra are shown in Fig. 5.5(e). Lifetimes of less than 60 fs are beyond our time resolution so that τ_1 is only an estimate, as evidenced by the fact that the lower bound is 0 fs. The spectrum of the fast decay, $k_1(eKE)$, shows a peak between 0.7 < *eKE* < 2 eV, but is negative for *eKE* < 0.5 eV. Negative signals point to a concomitant exponential rise with a time-constant of τ_1; thus, signal that was initially contributing to the 0.7 < *eKE* < 2 eV is decaying *into* a feature at *eKE* < 0.5 eV. The dynamics is sequential and the initial spectral peak around

0.7 < *eKE* < 2 eV decays to form the decay-associated spectrum $k_2(eKE)$, which subsequently decays in a timescale of τ_2 = 290 fs.

The fitting procedure employed here was essentially identical to that used by Stolow and co-workers to fit the time-resolved PE spectra of Ade and Ade-9Me, and hence a direct comparison can be made.[53, 68, 72] Fig. 5.6(b-d) shows the decay-associated spectra of Ade, Ade-9Me and dAMP⁻ (plotted in *eBE*), revealing a striking similarity between Ade-9Me and dAMP⁻, which allows us to conclude that the dynamics are proceeding via similar pathways. The decay-associated spectra of Ade-9Me lacks a feature observed in that of Ade, which has been assigned to $^1\pi\sigma^*$ contributions, although this assignment has been extensively debated, as according to H atom dissociation experiments the $^1\pi\sigma^*$ channel does not appear to be open at 267 nm.[71] Regardless, these results show that dAMP⁻ follows the same dissociation dynamics as Ade-9Me, and that Ade alone is an insufficient model for the nucleotide. The observed lifetime is significantly shorter in dAMP⁻ than Ade-9Me. This is likely a temperature effect, as the nucleotide is at room temperature, whilst Ade-9Me was in a cold molecular beam, although we cannot rule out a smaller Franck-Condon window leading to the dynamics being lost track of more quickly.

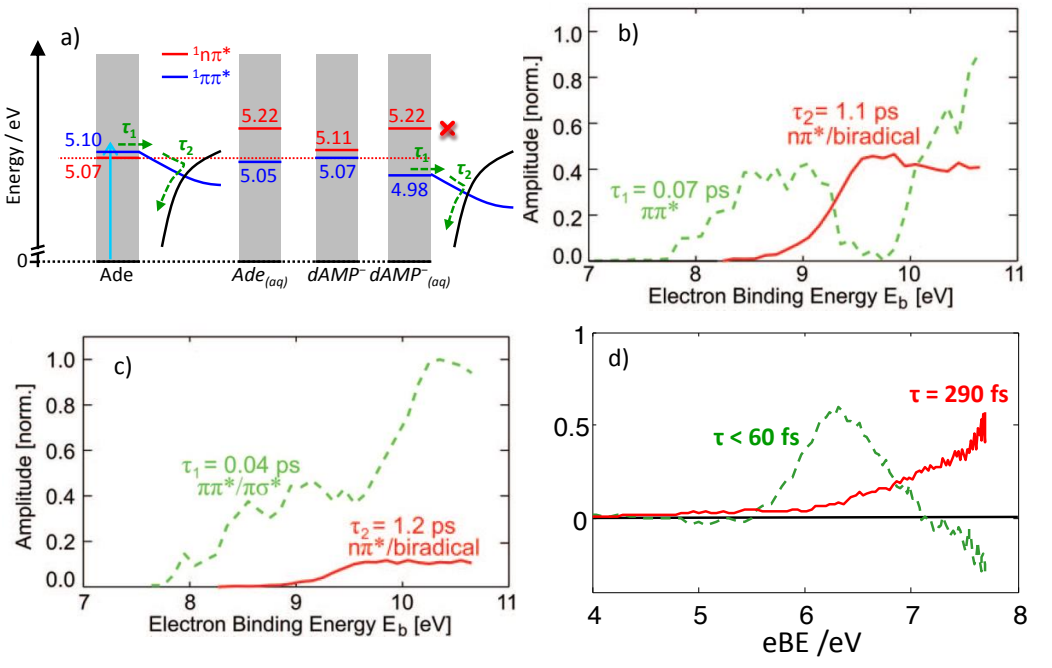

Figure 5.6 a) Sketch of the calculated energy levels for the ^1L_a and $^1n\pi^*$ states for Ade and dAMP⁻ either in aqueous solution or isolated. Changes to environment affect the $^1n\pi^*$ state greatly, but do not affect the ^1L_a state much, thus the similar dynamics in all enviornments indicate minimal influence of the $^1n\pi^*$ state. b) Decay associated spectra for Ade-9Me; c) Decay associated spectra for Ade; d) decay associated spectra for dAMP⁻. The spectra in b) and d) agree well, indicating a similar mechanism. Adapted with permission from ref. 70.

Table 5.2 Calculated vertical excitation energies (in eV) and oscillator strength of Ade and dAMP⁻ in both aqueous and isolated environments.

Adenine

Gas-phase				Aqueous solution (PCM)			
State	**Character**	**Energy**	***f***	**State**	**Character**	**Energy**	***f***
S_1	**$n_N\pi^*$**	**5.07**	**0.001**	**S_1**	**$\pi\pi^*$ ($1L_a$)**	**5.05**	**0.299**
S_2	**$\pi\pi^*$ ($1L_a$)**	**5.1**	**0.230**	**S_2**	**$n_N\pi^*$**	**5.22**	**0.001**
S_3	**$\pi\pi^*$ ($1L_b$)**	**5.34**	**0.030**	**S_3**	**$\pi\pi^*$ ($1L_b$)**	**5.28**	**0.044**
S_4	**$\pi\sigma^*$ (N9H)**	**5.4**	**0.007**	S_4	$\pi\sigma^*$ (N^6H)	5.6	0.009
S_5	$\pi\sigma^*$ (N^6H)	5.64	0.001	S_5	$n_N\pi^*$	5.79	0.002
S_6	$n_N\pi^*$	5.69	0.003	**S_6**	**$\pi\sigma^*$ (N9H)**	**6.08**	**0.000**

dAMP⁻

Gas-phase				Aqueous solution (PCM)			
State	**Character**	**Energy**	***f***	**State**	**Character**	**Energy**	***f***
S_1	$n_P\pi^*$	4.91	0.015	**S_1**	**$\pi\pi^*$**	**4.98**	**0.345**
S_2	**$\pi\pi^*$**	**4.95**	**0.028**	**S_2**	**$n_N\pi^*$**	**5.22**	**0.001**
S_3	**$\pi\pi^*$**	**5.07**	**0.205**	**S_3**	**$\pi\pi^*$**	**5.26**	**0.056**
S_4	**$n_N\pi^*$**	**5.11**	**0.002**	S_4	$\pi\sigma^*$ (N^6H)	5.63	0.008
S_5	$n_P\pi^*$	5.18	0.003	S_5	$n_N\pi^*$	5.79	0.006
S_6	$n_P\pi^*$	5.19	0.006	S_6	$n_P\pi^*$	5.83	0.049
$S_{n>20}$	**$\pi\sigma^*$ (N9C)**	**>5.63**		**$S_{n>20}$**	**$\pi\sigma^*$ (N^9C)**	**>6.36**	

In comparison with solution phase relaxation dynamics, the lifetime of dAMP⁻ in the gas phase agrees well, with both showing a biexponential decay with fast component, and a slower component, τ_2 ~300 fs.[4, 102] Given the dramatically different environments and experimental techniques, the agreement with our results is rather surprising. It suggests that the charge that is localised on the phosphate–which is completely screened in solution–has little or no effect on the dynamics of the base in the gas-phase. This is a key observation as it essentially allows us to view the charged phosphate as a spectator. Similarly, the hydration of the nucleobase appears to have little if any impact on the relaxation dynamics. Below we discuss the impact of base stacking, and find once again that, to a first approximation, the dynamics of adenine are not changed by the environment.

Based on the above arguments, we conclude that the dynamics of the nucleobase are relatively insensitive to the environment. However, what is the impact of the environment on the excited states? To gain some insight into this question, we have performed time-dependent density functional (TD-DFT) calculations. The choice of methodology is not to provide quantitative agreement with experiment, but rather to gain qualitative insight into the *relative* changes between Ade in the differing environments. The interaction with water is simulated using a polarisable continuum model. In Table 5.2, the energies of the relevant excited states are shown for Ade in: isolation, water, nucleotide, and aqueous nucleotide. These trends are in agreement with high-level *ab initio* calculations,[106-109] providing confidence that the TD-DFT

calculations have captured the underlying physics. A schematic of the first two states in both the vacuum and in solution is also shown in Fig. 5.6(a).

Firstly, our calculations clearly show that the energy of the $^1\pi\sigma^*$ state associated with the N^9 position increases in energy in $dAMP^-$ relative to Ade. Hence, the involvement of the $^1\pi\sigma^*$ state in the relaxation dynamics can be ruled out. However, it is the relative ordering between the $^1\pi\pi^*$ to $^1n\pi^*$ states that is most revealing about the probable decay mechanism. In Ade, the $^1n\pi^*$ state lies below the $^1\pi\pi^*$ state, whereas in $dAMP^-$ this ordering is reversed. The effect of solvation is to increase the energy gap between the $^1\pi\pi^*$ and $^1n\pi^*$ states in $dAMP^-$. One would anticipate that, if the $^1n\pi^*$ state was actively involved in the decay mechanism, the presence of the sugar and phosphate and the effect of solvation on the dynamics would be marked. But it is not, and so we conclude that the involvement of the $^1n\pi^*$ state in the decay dynamics is minor and the dynamics are dominated by a one excited state $^1\pi\pi^* \rightarrow S_0$ internal conversion mechanism, presumably using the ^2E CI. This is in agreement with some high-level calculations,[81, 87, 107, 108, 110] although we note that recent nonadiabatic dynamics simulations on solvated Ade have also invoked a second (mixed character) state, employing the $^1S_6$ CI .[109] The fast component biexponential dynamics observed is thus likely a consequence of motion on the $^1\pi\pi^*$ state from the Franck-Condon region towards the ^1L_a minimum. Similar dynamics were observed recently in the chromophore of the green fluorescent protein for which the dynamics were occurring on a single potential energy surface.[111] A key conclusion is that the dynamics of the Ade nucleobase appear to be the same regardless of the environment, be it in isolation or in a nucleotide and solvated. We anticipate that this restriction will enable theoretical models to be refined to gain a truly molecular level understanding of these processes.

5.4.2 Guanine

Studying the dynamics of the second purine base, guanine (Gua), presents a particular challenge, as Gua tends to decompose upon heating in a molecular beam apparatus,[112] and so gas phase experiments are especially difficult. Additionally, Gua can form multiple stable conformers in the gas phase,[113-116] which further complicates experiments. Ion yield experiments with mass selection are sensitive only to the product of interest, even in a beam which is unclean due to decomposition, and hence these are the only dynamics experiments which have been successfully performed on Gua.[55, 74] Exciting at 4.7 eV, a biexponential decay was observed, with lifetimes of 148 fs and 360 fs for the two components.[74]

Ab initio calculations reveal that at the ground state equilibrium geometry, the S_1 state is the ^1L_a ($^1\pi\pi^*$) state, and higher in energy lie the $^1n\pi^*$ and ^1L_b ($^1\pi\pi^*$) states, which are very close in energy.[117-124] The state ordering between the bright ^1L_a state and the dark $^1n\pi^*$ is reversed compared to Ade, which is significant as it suggests involvement of the $^1n\pi^*$ state to be less feasible. Calculations of CIs reveal a similar story to Ade: three CIs have been located which may be active in relaxation of Gua.[5, 6, 119, 121, 122, 124] The first two have a geometry puckered at the C^2 position, roughly equivalent to the ^2E CI in Ade. Both of these CIs, which differ only in the amino geometry, are between the ^1L_a and S_0 states. The third CI has a geometry with a C^6 pucker, again like in Ade, and this CI is associated with a state of mixed $^1n\pi^*$ and $^1\pi\pi^*$ character. There are also $^1\pi\sigma^*$ states associated with the N^1-H and $N^{(amino)}$-H bonds, which possess CIs like in phenols,[122] although most recent theory does not consider these states. Minimum energy path calculations suggested that the rapid decay observed was attributed to direct decay from the ^1L_a state through the ^2E CIs,[121] and the longer lived component was attributed to dynamics via the $^1n\pi^*/^1L_b$ mixed state. More recently, nonadiabatic dynamics simulations have been performed which indicate that dynamics occur almost exclusively on the first $^1\pi\pi^*$ state, with almost all population relaxing through the two ^2E CIs,[124] although an earlier simulation suggested that the C^6 pucker CI may also be involved.[125]

In the solution phase, Gua itself is rarely studied as it has poor solubility, although $dGMP^-$ has been studied in a number of experiments with transient absorption[4, 102, 126] and fluorescence upconversion.[101, 102, 127, 128] Like $dAMP^-$, when excited at around 4.7 eV, biexponential decay is observed.[4] Recent measurements give the short lifetime, $\tau_1 = 120$ fs and the longer lifetime, $\tau_2 = 680$ fs.[102] As in Ade and $dAMP^-$, solvation dramatically blue-shifts the first $^1n\pi^*$ state, to the extent where it is considered to be unlikely to have any substantial influence upon the dynamics.[125, 129] Instead, *ab initio* results have proposed that all dynamics occur upon the ^1L_a state, and any population on the ^1L_b state converts to the ^1L_a in < 20 fs.[129] The dynamics then once again proceed purely through CIs between the ^1L_a and S_0 states, although there are indications that the presence of the solvent influences which path – and ultimately which CI – is used to relax back to the ground state.

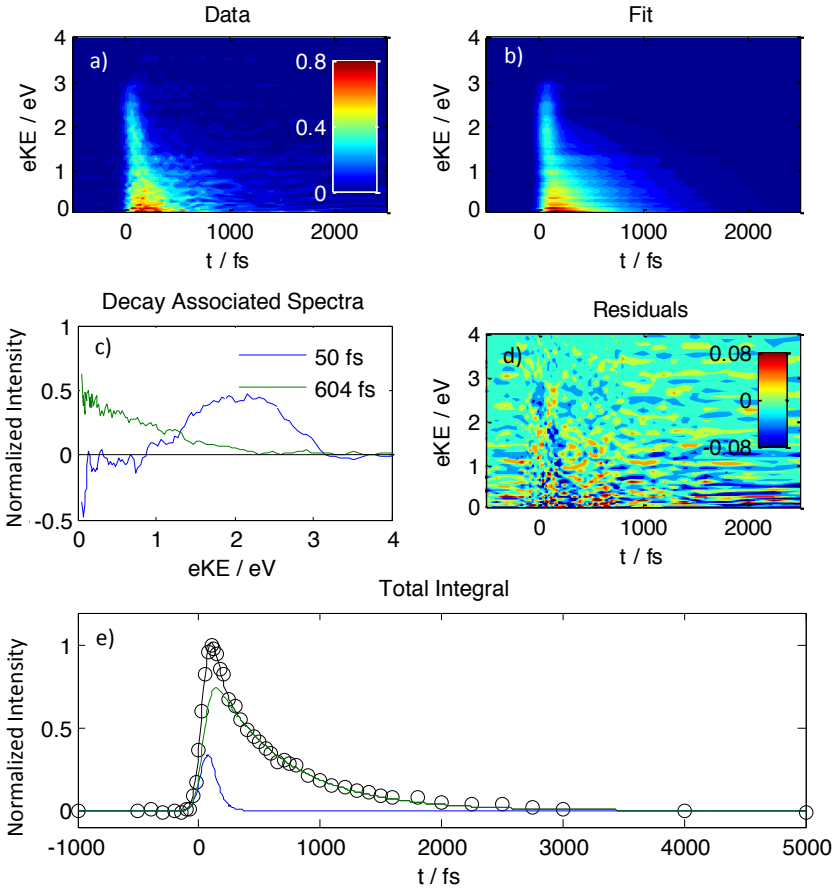

Figure 5.7 a) The time-resolved PE-spectrum of dGMP⁻, pumped at 4.7 eV, probed at 3.1 eV. b) Global fit of the experimental spectrum, using two exponential decay functions. c) Decay associated spectra from the global fit. d) Residuals from the fitting procedural. e) Total integrated PE counts as a function of time. Open circles show experimental points, coloured curves correspond to the integrals of the spectra shown in c), and the black curve is the total integral from the fitting procedure.

Time resolved PE spectroscopy on the nucleotide, performed in exactly the same manner as on dAMP⁻, gives further insight into the dynamics and allows the relaxation of isolated Gua to be tracked with a dispersed measurement for the first time. Fig. 5.7 shows the collected (background subtracted) data and global fit, along with decay associated spectra and time-integrated photoelectron spectra. Like dAMP⁻, only two timescales are required to fully fit the entire dynamics: τ_1 = 50 ± 60 fs and τ_2 = 604 ± 172 fs. In the decay-associated spectra, $k_1(eKE)$ and $k_2(eKE)$ are very similar to those for dAMP⁻, but spectrally shifted to higher *eKE* because of the lower ionisation energy of Gua relative to Ade in their deprotonated nucleotides (see Section 5.3). The quality of fit is also weaker for dGMP⁻ than dAMP⁻, as evidence by the much greater confidence intervals.

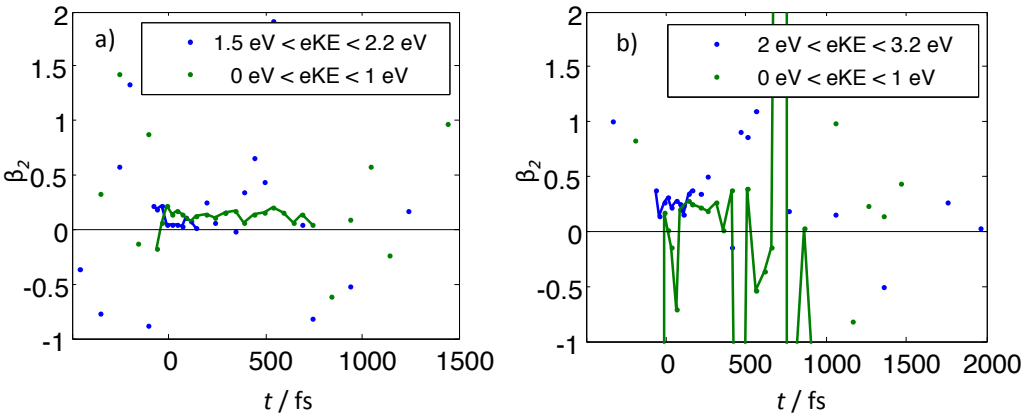

Figure 5.8 The β_2 components of the time-resolved PE images of a) dAMP$^-$ and b) dGMP$^-$. For each nucleotide, two energetic windows have been chosen, corresponding to the two components in the decay associated spectra, and the mean β_2 parameter is plotted as a function of *t*. A line has been added to the plots in the temporal regions where there is a great enough intensity for these values to be meaningful. All β_2 parameters are ~0, which is consistent with a decay mechanism where no change in electronic character occurs.

The main spectral difference between dAMP$^-$ and dGMP$^-$ is that the width of $k_1(eKE)$ is about twice as large in dGMP$^-$. This may reflect the flat potential energy surface that is predicted for the $^1\pi\pi^*$ state near the Franck-Condon region,[5, 121, 122] or it may be a consequence of the differences in the interactions of the base with the charged backbone. As explained above in Section 5.3, in the gas-phase, the lowest energy dGMP$^-$ structure is more compact than that of dAMP$^-$ due to an intramolecular hydrogen bond between the base and the phosphate.[45, 50] The reduced distance between the charge and the base may lead to changes of the excited states between the isolated Gua and that in the nucleotide. High level theoretical investigations should be able to shed additional light onto the excited state electronic structure, for which our data present an ideal benchmark, given that the photoelectron spectra associated with specific electronic states are sensitive to the potential energy landscapes.

The very strong similarity in time-resolved spectra between dAMP$^-$ and dGMP$^-$ serve as a strong indication that a similar relaxation mechanism is involved in both. Additional insight is available from studying the photoelectron angular distributions of the images (see Chapter 2), as a function of time and energy. Fig. 5.8 demonstrates that for both components of both dAMP$^-$ and dGMP$^-$, $\beta_2 \approx 0$. The slight positive value in all cases is well within the uncertainty for these measurements. Crucially, there is no observed change in angular distribution as a function of time or energy. This is consistent with a one-state mechanism, although it is not unequivocal.

As with dAMP$^-$, the evidence is that all dynamics occur on a single state, as with and in accordance with the *ab initio* findings. Excellent agreement with the solution phase is also observed. The experimental evidence suggests that the relaxation

dynamics of the purine bases may in fact be unified, although of course the specific CIs used will differ.

5.4.3 Thymine

The photophysics of thymine (Thy) are of particular interest as photoinitiated cycloaddition between two Thy groups is a leading form of DNA damage.[130] A number of experimental studies have focused on the decay dynamics of isolated Thy, when excited at 4.7 eV (266 nm). The dominant conformer in molecular beams is the biological keto tautomer.[131, 132] Time-resolved ion yield experiments using multiphoton probes show that isolated Thy has a much longer lived excited state than the other three nucleobases; they found there to be three decay constants associated with the relaxation, with lifetimes of approximately 100 fs and 5 ps for the first two decays.[55, 74, 133] The third feature has a lifetime of 2.8 ns, and has been assigned to an intersystem crossing onto the $^3\pi\pi^*$ state, by measurement of the vibrational spectrum of the transient species.[133] Time resolved PE spectra, using a 4.96 eV (250 nm) pump and a 6.20 eV (200 nm) probe, were fit using three time constants of < 50, 530 and 6400 fs.[53] Presumably owing to the differing pump energies, these data are not in perfect agreement with the ion yield data, however a strong pattern for the early dynamics of a fast decay, followed by a decay of ~5 ps emerges.

Numerous computational studies have been performed in an attempt to disentangle the initial dynamics of Thy. In the vertical excitation region, the S_1 is an optically dark state of $^1n\pi^*$ character, whilst the S_2 is the optically bright $^1\pi\pi^*$ state. CIs have been located between the $^1\pi\pi^*$ and both $^1n\pi^*$ and S_0 states, the former has a boat conformation, puckered at C^6 and C^3, while the latter is puckered at the C^5 atom.[6, 134-138] From the theory work performed, a number of possible explanations for the dynamics of Thy have emerged. Domcke and coworkers[134] calculated a barrierless reaction path to the $^1\pi\pi^*/S_0$ CI, responsible for the fast time constant, whilst the slower time constant was assigned to trapping on the dark $^1n\pi^*$ state. On the other hand, Merchan *et al.* attributed the slower dynamics to trapping on $^1\pi\pi^*$ state, without active contribution from the $^1n\pi^*$ state.[137] Interpretation of the time resolved PE spectra, using the *ab initio* multi spawning (AIMS) technique, concluded that the initial femtosecond component is resultant from motion on the $^1\pi\pi^*$ state, without any change of electronic character.[139] The slower component was then suggested to be borne from a barrier crossing at the $^1\pi\pi^*(S_2)/^1n\pi^*(S_1)$ CI, and a key observation was that many different CI pathways are available, rather than just a single decay mechanism.

In the solution phase, Hare *et al.* found that a wavepacket bifurcation occurs and Thy may decay via one of two mechanisms.[7, 140] The excited population mostly undergoes direct relaxation via a $^1\pi\pi^*/S_0$ CI with sub-picosecond timescales,[4, 103, 127, 141] while around 11% becomes trapped on the $^1n\pi^*$ state for 30 ps. They found that solvated dTMP displayed similar early time dynamics, but the slow component has a lifetime of 127 ps, indicating a much larger barrier to deactivation of the $^1n\pi^*$ state after ribosyl substitution. Similar to the purine bases, solvation destabilizes the $^1n\pi^*$ significantly more than the $^1\pi\pi^*$ state, so comparisons between gas and solution phases may not be valid in mechanisms where the $^1n\pi^*$ state plays a role.

Using time resolved anion PE spectroscopy we have measured the dynamics of isolated $dTMP^-$. The experiment was as above, with a 4.7 eV pump and a 3.1 eV probe. Fig. 5.9 shows the resultant data and global fit, after subtraction of one colour signal. Unlike the purine nucleotides, two decay components are not adequate to fit the 2D data: close inspection of Fig. 5.9(e) shows a small offset from the baseline at long time delays. The global fit was then performed with three decay components, with the lifetime of the third component arbitrarily set to τ_3 = 5 ps. The data are reminiscent of those for the purine bases, with a τ_2 = 211 ± 127 fs feature decreasing from 0 *eKE*, but remaining universally positive, and a faster τ_1 = 58 ± 111 fs feature which is positive around 1.5 eV, but negative < 1 eV. The large value for the confidence interval on τ_1 suggests that the global fit may not be perfectly recreating the experimental data, *i.e.* large amplitude motions are present. The picosecond component appears to mainly be found at low *eKE*, but the feature is too weak to make any comment about its spectrum. Above 2.1 eV, a feature is seen in both of the fast components. The *ADE* of the base with $dTMP^-$ is 5.6 eV, so the 4.7 + 3.1 eV input energy is insufficient detach electrons at these energies, and so detachment above ~2.2 eV must result from two-photon probing, *i.e.* 2×3.1 eV total probe energy. The appearance of the two-photon feature effectively extends the available probing window, although we note that convolution of the one- and two-probe photon peaks may complicate data analysis. In principle, the two photon peak could be amplified and inserted next to the one photon peak to extend the spectrum, although higher signal levels would be desirable before this could be performed.

The decay associated spectrum of the τ_1 fs component has considerable negative amplitude, and in fact the total integral of it is negative (see Fig. 5.9(e)). As with $dAMP^-$, negative amplitude indicates flow of population into a region, and positive amplitude is flow out. Hence, the overall negative integral indicates that we are observing

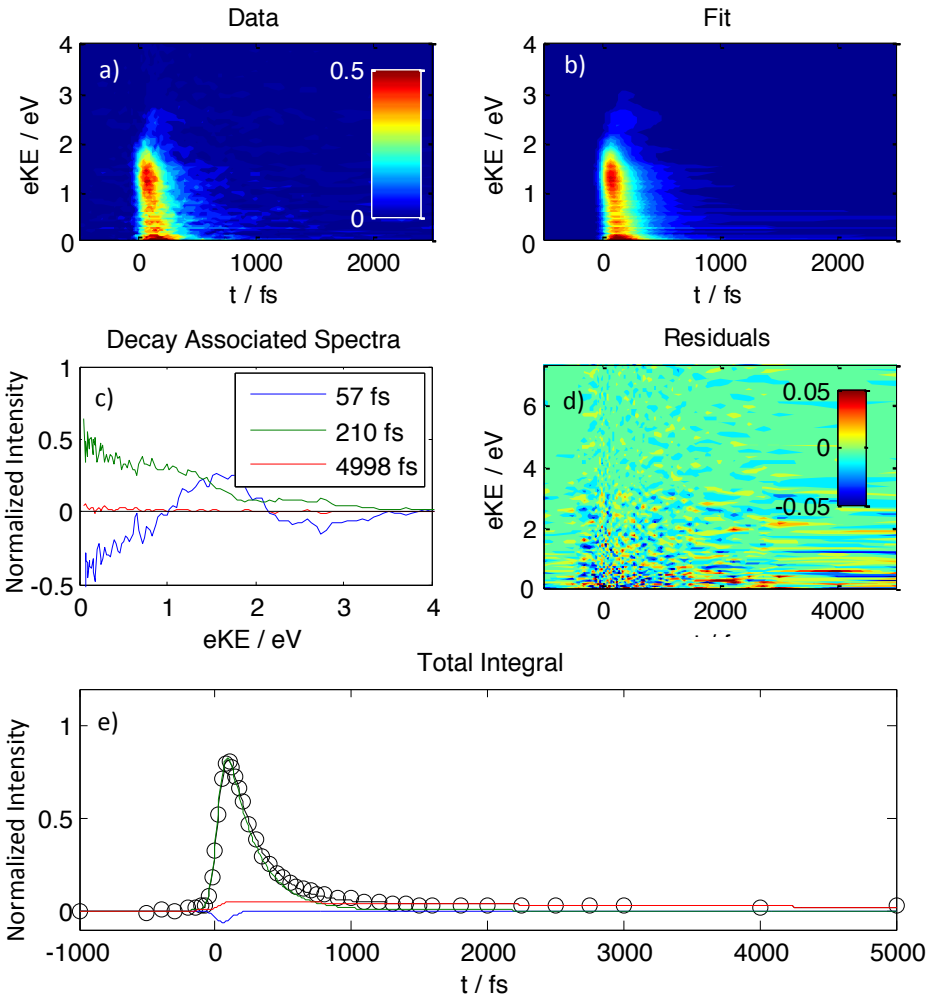

Figure 5.9 a) The time-resolved PE-spectrum of dTMP⁻, pumped at 4.7 eV, probed at 3.1 eV. b) Global fit of the experimental spectrum, using three exponential decay functions. c) Decay associated spectra from the global fit. d) Residuals from the fitting procedural. e) Total integrated PE counts as a function of time. Open circles show experimental points, coloured curves correspond to the integrals of the spectra shown in c), and the black curve is the total integral from the fitting procedure.

population flowing from some dark region into a brighter region. The two-photon peak does not appear to have a visible positive component; it is likely the absence of this feature which results in the overall negative integral. The large amount of negative signal in this feature is indicative of considerable population flow in the system; in the 2D spectra this flow is clearly manifested as a shift to later onset time for the *eKE* <1 eV feature and the two-photon feature.

A direct comparison of the nucleotide and nucleobase dynamics does not appear to be possible, and we do not at this time have a definitive assignment of the dynamics observed. As with dAMP⁻ and dGMP⁻, $\beta_2 \approx 0$, so no extra information is available from angular distributions. By analogy with the purine nucleotides, as well as with reference to the sizable body of work describing Thy's potential energy surface,[134-136, 138, 142] the initial τ_1 = 60 fs time constant can likely be assigned to motion of the wavepacket on

the S_2 $^1\pi\pi^*$ state, from the vertical Franck-Condon region to some local minimum. Assignment of the two slower features is much less straightforward, and we shall use the identity of the long lived component, τ_3, to guide this discussion. As this feature manifests as a flat offset on the timescale of our experiment, of too small intensity to accurately fit, we can only assign it a lifetime > 5 ps, and the lifetime could in principle stretch into the nanosecond regime. If this feature is indeed very long lived (nanoseconds), then it is likely a triplet feature, as seen in neutral Thy. If the long lived component is a triplet feature, then presumably the 210 fs component corresponds to ground state relaxation via a $^1\pi\pi^*/S_0$ CI. In this scenario, the $^1n\pi^*$ state does not appear to play an active role, and we must presume that the picosecond channel observed in both in isolated Thy and solvated dTMP has been quenched by either the presence of the charge or the unique geometry of the nucleotide.

A second possible assignment of the slower feature is to relaxation from the $^1n\pi^*$ state. In this scenario, the lifetime is likely on the order of picoseconds, as in neutral Thy. The τ_2 = 210 fs component would then correspond to $^1\pi\pi^* \rightarrow {}^1n\pi^*$ internal conversion. It is important to note that the 60 fs component has negligible (in fact negative) total amplitude, hence it would not be observed in a non-differential measurement such as ion yield experiments, and only the 210 fs component would be observed. This lifetime is longer than that observed in experiments on neutral Thy (~100 fs), although variations in the potential landscape due the addition of the sugar/phosphate backbone may well account for this. The very small amplitude of the picosecond component appears to disagree with this model, however we note that our spectral window is limited, and our 3.1 eV probe may be too low for the majority of detachment from the $^1n\pi^*$. In principle, two-photon detachment should assist in this this assignment, although we do not see any significant amplitude in the decay associated spectrum of the long lived component at *eKE* > 2.1 eV.

Finally, it is feasible that the long lived component is due to bifurcated population trapped on the $^1n\pi^*$ state, as is observed in solution,[140] and suggested by photoelectron spectroscopy and *ab initio* calculations.[139] If this were to be the case, the remaining dynamics are likely similar to those described for the triplet scenario. We note that solvation significantly destabilizes the $^1n\pi^*$ state (as in the purine bases), and hence this scenario is perhaps less likely in the gas phase.[134, 143] The short term dynamics are otherwise rather comparable with those in solution, perhaps again indicating a less active role of the $^1n\pi^*$ state that previously thought.

The above comparisons have all been between $dTMP^-$ and neutral Thy, and hence we may query whether substitution at the N^1 site has a great effect on the dynamics. The ion yield experiments of Brutschy and co-workers showed that almost identical dynamics are obtained for Thy and 1-methylthymine,[133] suggesting that the hydrogenated base is an acceptable model for the dynamics of Thy in more complex environments, however as this was a non-differential measurement, there may be additional masked features. Overall, it appears that although the specifics of the relaxation mechanism for $dTMP^-$ is debatable, these results represent a significant step towards a complete understanding of the process involved, and nicely illustrates how theory and small gas phase work can assist in building up to more complete systems.

5.4.4 Cytosine

The dynamics of cytosine (Cyt) in the gas phase have, until recently, been poorly understood. Early femtosecond experiments, using either time-resolved ion yield[55, 74] or time resolved PE spectroscopy[53] showed poor agreement. The ion yield experiments, performed with a 4.7 eV pump, gave biexponential decays with a fast component limited by the instrument response, and a slower component with a lifetime of 1.9 – 3.2 ps. [55, 74] The PE spectroscopy, performed with a 250 nm pump, resulted in a triexponential fit, with lifetimes of <50 fs, 820 fs and 3.2 ps (the latter lifetime fixed to the results by Kang *et al.*).[53]

The origin of this confusion is almost certainly due to multiple tautomers present in the molecular beam. Microwave[144] and high resolution IR[145, 146] spectroscopies reveal that there are three tautomers of Cyt present within a molecular beam, shown in Fig. 5.10. These are the biological keto tautomer, and the non-biological enol and imino tautomers, which are present in a ratio of ~1:1:0.25, respectively (from microwave experiments)[144]. In nucleotides, the sugar/phosphate backbone is attached on the N^1 site, and hence the enol tautomer is unavailable in biological systems, whilst the imino tautomer interferes with base pairing, and hence the primary biological tautomer is the keto form.[147]

Three recent experimental publications have sought to untangle the dynamics within Cyt to isolate the behaviour of each tautomer, and in particular to ascertain the nonadiabatic relaxation of the keto tautomer. Kosma *et al.* noted that the onset of absorption to the S_1 of the enol and imino tautomers is energetically higher than in the keto tautomer:[148] the keto-C onset is ~318 nm, whilst the enol-C origin is ~278 nm.[149, 150] Thus, by restricting pump wavelengths to $\lambda \geq 280$ nm, they could selectively observe only dynamics of the keto-C tautomer. Dynamics were tracked using time resolved ion

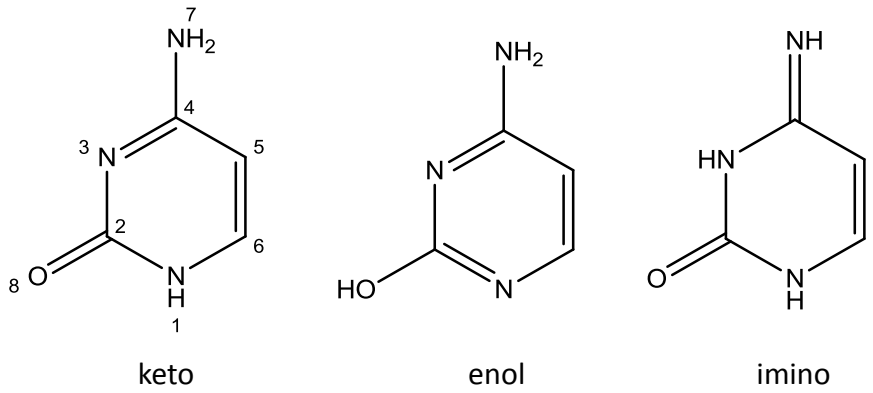

Figure 5.10 The structure of the three observed tautomers of neutral cytosine. In nucleotide systems, the sugar group attaches at the N^3 site. The keto tautomer is the biologically observed tautomer, although all three are found in molecular beams.

yield, pumped using either 280 or 290 nm (4.43 or 4.28 eV) radiation, and probed using 3 photons of the 800 nm (1.55 eV) fundamental. Three components were observed in the decay, with lifetimes of <100 fs, 1.1 (1.2) ps and >150 (55 ps) for excitation with 290 (280) nm. The proposed assignment was ultrafast motion away from the Franck-Condon region upon the $^1\pi\pi^*$ state, followed by internal conversion directly to the ground state. The long lived component was tentatively assigned to an excited state tautomerization.[148]

Ho *et al*. used chemical substitution to measure tautomer-specific behaviour:[151] methylation at the C^1 position (where the ribose group attaches) blocks keto-enol tautomerization, and also better represents the biological nucleotide. Time resolved ion yield experiments on Cyt-1Me with a range of pump wavelengths, 260 nm ≤ λ ≤ 300 nm, and an 800 nm probe, gave biexponential decays composed of an initial spike limited by the instrument response, and a decay with a lifetime of 0.4 - 1.3 ps (with shorter lifetimes at higher pump energies). Intriguingly, when pumped at 310 nm, the lifetime increases to 3.2 ps. The authors did not observe a slower component, and assigned that observed by Kosmas *et al.* to dynamics of fragments. Power dependency studies showed the initial spike to be primarily multi-photon in nature, although a one-photon component could not be ruled out.

Very recently, Lobsiger *et al*. have measured linewidths in frequency resolved REMPI experiments in order to determine the lifetime of keto-Cyt near the S_1 origin and shed light on the femtosecond measurements.[152] It was found that lifetime of Cyt is *not* ultrafast at the absorption onset, and rapid dynamics only appear after ~500 cm^{-1} of excess energy is imparted. The predominant vibrational progression was in an out-of-plane mode, and this was taken as evidence that relaxation occurs via a non-planar CI, as long as there is sufficient energy to access it.

On the theory side, there has been a considerable effort to understand the adiabatic dynamics of keto-C. It is generally agreed that in the ground state geometry the S_1 state is the $^1\pi\pi^*$ state, and the next two excited states are of $^1n\pi^*$ character, with the non-bonding orbital residing on either the N^3 ($^1n_N\pi^*$) or the O ($^1n_O\pi^*$) atom.[153-155] Several CIs with the ground state have been located, the three most accessible being a $^1\pi\pi^*/S_0$ CI from puckering on the C^6 atom, a $^1n_N\pi^*/S_0$ CI from puckering at the N^3 atom, or a semiplanar $^1n_O\pi^*/S_0$ CI.[6, 137, 153-158] Computations utilizing either minimum energy paths or surface hopping techniques have disagreed as to whether it is the C^6 pucker[137, 154] or the semiplanar[159, 160] CI which dominates, however very recently high level calculations have suggested that the $^1\pi\pi^*/S_0$ CI is the primary relaxation route, and that earlier calculations over-emphasized the importance of the $^1n_O\pi^*$ state.[153] This result is also supported by calculations on 5-fluorocytosine, which prevents facile state switching to the $^1n\pi^*$ states.[161, 162] A mechanism utilizing a puckered CI accords well with the findings that vibrational energy in out-of-plane modes is required before rapid relaxation will occur.[152]

In the solution phase, the dynamics of Cyt and CMP (the RNA nucleotide of C) when excited at 266 nm are very much reminiscent of those of Thy and dTMP.[7, 140]. Bifurcation of the population occurs between the bright $^1\pi\pi^*$ state and a dark state, presumably of $^1n\pi^*$ character. The dynamics of the rapid component are sub-picosecond,[4, 103, 127, 141] whilst the slow, dark, component decays in 12 ps.[140] As with Thy, moving to the nucleotide results in an increase in dark state lifetime, in this case to 34 ps, which indicates an increased barrier to relaxation. The dark state yield in CMP is considerably higher than in Cyt, at 41% and 9% respectively,[140] perhaps indicative of a decrease in rate of decay purely upon the $^1\pi\pi^*$ state, and a change in dynamics upon building up to the nucleotide.

Fig. 5.11 shows the time-resolved PE spectra and resultant global fit for the isolated $dCMP^-$ anion. As above, a 4.7 eV pump and 3.1 eV probe was employed, and one colour backgrounds were subtracted. As indicated by the large residuals, the signal to noise ratio for $dCMP^-$ is considerably worse than for the other three deoxynucleotides. This is partly because the ion signal of $dCMP^-$ was lower compared to the others, presumably because it does not electrospray as easily, and partly due to the reduced absorption (and perhaps ionization) cross section. As with the purine bases, two decay components are required to capture the dynamics, and unlike $dTMP^-$ there does not appear to be a long-time offset, although the poorer signal-to-noise may obscure it if it is present. The two features have lifetimes of τ_1 = 160 fs and τ_2 = 1.22 ps,

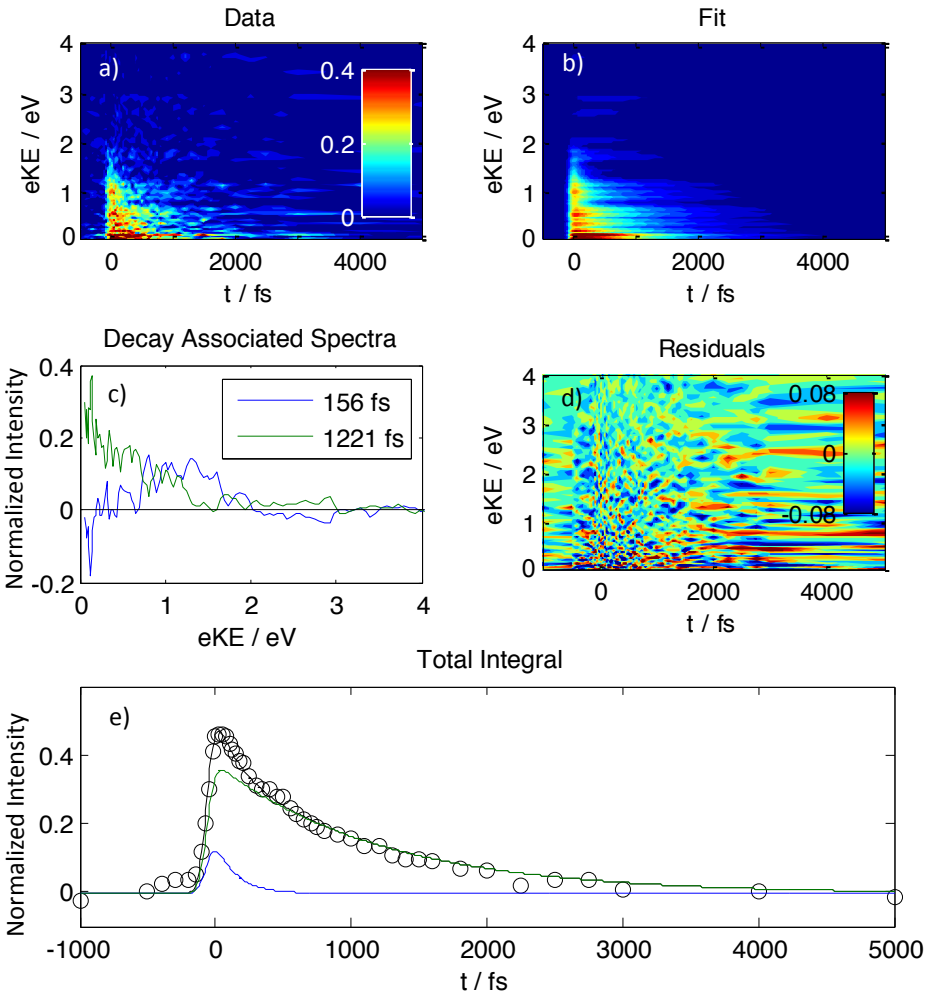

Figure 5.11 a) The time-resolved PE-spectrum of dCMP⁻, pumped at 4.7 eV, probed at 3.1 eV. b) Global fit of the experimental spectrum, using two exponential decay functions. c) Decay associated spectra from the global fit. d) Residuals from the fitting procedural. e) Total integrated PE counts as a function of time. Open circles show experimental points, coloured curves correspond to the integrals of the spectra shown in c), and the black curve is the total integral from the fitting procedure.

and the spectral profile resembles the other nucleotides, with the fast component found at higher *eKE*, and the slower decay increasing towards *eKE* = 0, however no evidence of sequential dynamics (negative decay associated spectra) is observed. The poor quality of these data mean they are considerably less reliable than for the other nucleotides, and so conclusions drawn from them are by necessity more tenuous. We have not assigned confidence intervals to the lifetimes extracted for dCMP⁻, because the support plane analysis revealed that the χ^2 landscape of the fit is exceedingly shallow, and so we cannot make any precise judgements on the uncertainties, or even validity of the model. Instead, we can only definitively state that dCMP⁻ is considerably longer lived than the other nucleotides.

dCMP⁻ is remarkable in that that it is the only nucleotide which possesses a significant component with a lifetime > 1 ps. In particular, it is the only example where

the hot nucleotide has longer lived dynamics than the isolated, cold base – Cyt-1Me has a lifetime of 0.5 ps when pumped at 270 nm.[151] There are two basic explanations for the increased lifetime of dCMP⁻ compared to Cyt-1Me. Firstly, the general mechanism may be the same, relaxation mediated by the $^1\pi\pi^*/S_0$ CI, but the nucleotide may not reach the CI as easily as the methylated base. The CI geometry is thought to involve a puckering of the ring at the C^6 atom,[128, 145] and it may be that inclusion of the sugar and phosphate impedes the required out of plane motion. In this scenario, all observed dynamics are borne from the $^1\pi\pi^*$ state, and the explanation follows that of the other bases, with initial motion from the Franck-Condon region, followed by slower relaxation via the CI.

Alternatively, the mechanism for relaxation of dCMP⁻ and Cyt-1Me need not be the same. The large difference in $^1n\pi^*$ utilization between Cyt and CMP in solution suggests that a significant modification to the electronic landscape of the chromophore may occur upon addition of the backbone.[140] Involvement of either of the $^1n\pi^*$ states cannot be ruled out. In fact, we could imagine that a bifurcation occurs, and that the two relaxation lifetimes reflect a split between relaxation using the $^1\pi\pi^*$ and $^1n\pi^*$ states. The lack of observed sequential dynamics supports this hypothesis, although of course the poor signal-to-noise of the data prevents anything but tenuous assignments.

Going forward, dCMP⁻ perhaps presents the greatest mystery of the nucleotides studied. It is the only nucleotide which shows dynamics slower than the corresponding isolated base, tentatively suggesting a change in relaxation mechanics as the system is built up. Future improvements to the instrument should hopefully help decrease the noise observed, so the dCMP⁻ can be studied more robustly. Additionally, it would be interesting to see how the dynamics of 5-fluoro-dCMP⁻ compare, echoing previous experiments and theory studies.[151, 161-163]

5.4.5 Oligonucleotides

As previously discussed in Section 1.4.2.2, a dramatic change is observed in the dynamics of DNA oligonucleotide chains compared to individual bases. DNA bases in a π-stacked arrangement possess exciton excited states, which rapidly decay into exciplex/excimer charge transfer states with lifetimes on the order of 100s of ps.[4, 5, 7] Recently there has been a great deal of activity aimed at understanding these long-lived dynamics, primarily through solution phase spectroscopy,[164-172] although a number of *ab initio* computations are also emerging.[173-179] The precise nature of these long lived states is still very much under debate, however gas phase spectroscopy may be able to assist in understanding these complex dynamics. Using electrospray, transportation of

oligonucleotides to the gas phase is readily achieved, and frequency resolved action spectroscopy has been performed on isolated oligonucleotide anions.[66, 170, 180] Here, we present the first time-resolved study of the oligonucleotides $d(A)_2^-$ and $d(A)_3^-$. The adenosine oligonucleotides were chosen because of our clearer understanding of the intrinsic dynamics of $dAMP^-$ and because these have previously shown the most dramatic effect of base-stacking on the lifetimes.[168] Additionally, time-resolved PE spectra of a stacked adenine dimer, stabilized by three water molecules, showed clear evidence of long lived dynamics.[181]

The chemical structures of $d(A)_2^-$ and $d(A)_3^-$ are shown in Fig. 5.12(a) and (e), together with their time-resolved photoelectron spectra and global fits. Although the ion currents for the mass-selected mono-, di-, and tri-nucleotides were progressively lower, the observed signal levels remained similar, with a small reduction in signal-to-noise for $d(A)_3^-$. This can be rationalised because, as the size increases, the number of absorbing chromophores also increases. A similar analysis of the time-resolved spectra yielded lifetimes of τ_1 = 26 ± 32 fs and τ_2 = 337 ± 90 fs for $d(A)_2^-$ and τ_1 = 28 ± 33 fs and τ_2 = 380 ± 116 fs for $d(A)_3^-$. The decay associated spectra are shown in Fig. 5.12(d) and (h) for $d(A)_2^-$ and $d(A)_3^-$, respectively. These show that the mechanism of the di- and tri-nucleotides is very similar to that of the mononucleotide, $dAMP^-$. Given that we have shown that the dynamics of the base are relatively unaffected by its environment, this observation is not wholly surprising, although no long-lived component is observed.

Comparing the spectra of the three species, $dAMP^-$, $d(A)_2^-$ and $d(A)_3^-$, small differences are observed. The high *eKE* cut-off for the oligonucleotides is ~2.0 eV, compared to ~2.3 eV in $dAMP^-$, and all other spectral features appear to be shifted accordingly. This has the result that no negative going signal is observed in the oligonucleotide decay associated spectra, however inspection of the 2D spectra reveal an offset in the two-photon peak, suggesting that sequential dynamics are still operative. The shift in PE energy likely indicates that the base-phosphate distance is increased, so the nucleobase is destabilized less. Compared to the spectra of $d(A)_2^-$, those of $d(A)_3^-$ are broadened somewhat. The number of distinct ionization sites in the trimer is greater, as the ionized base may not be adjacent to the charged phosphate, accounting for this observation.

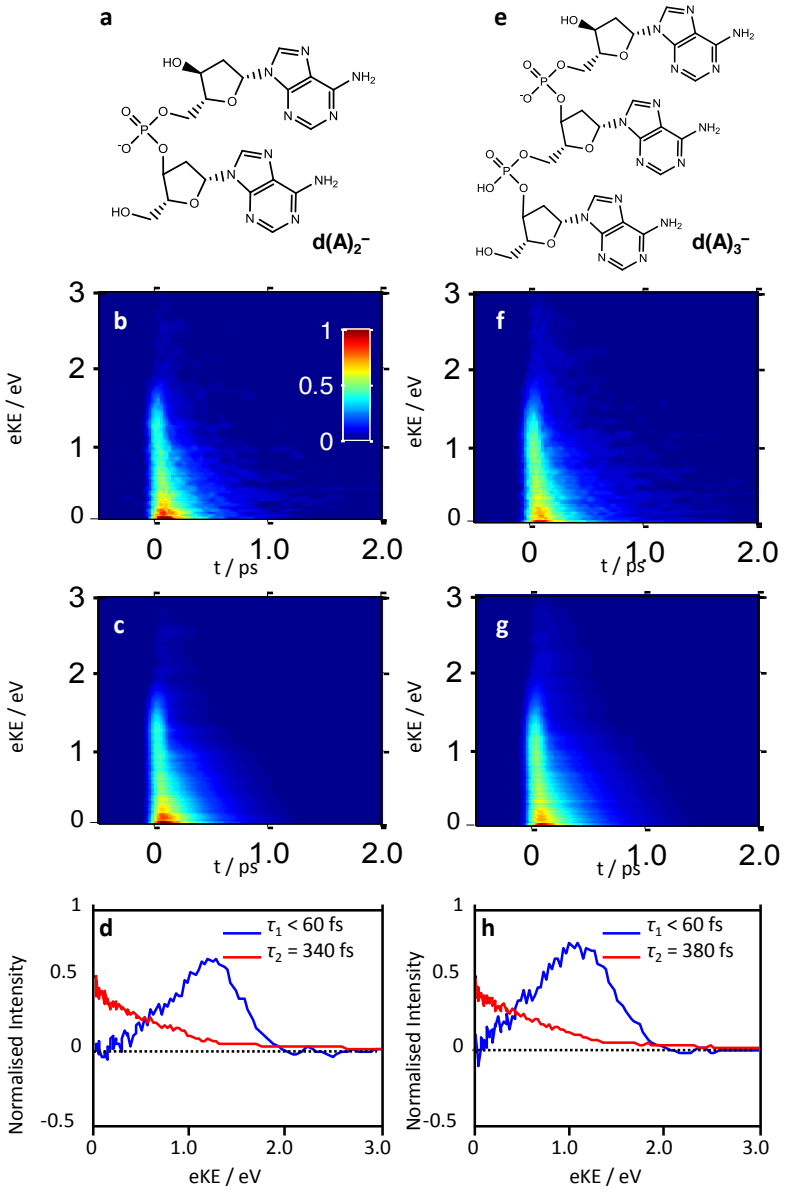

Figure 5.12 Time-resolved PE spectra of dA_2^- and dA_3^-. A) Chemical structure of $d(A)_2^-$; b), false-colour representation of the time-resolved PE spectra of $d(A)_2^-$ excited at 4.7 eV and probed at 3.1 eV; c), Global fit to the experimental data in b, modelled with two exponential decay functions (see text); d), Decay associated spectra from the global fit in c, showing the spectra of the two decay processes with associated lifetimes indicated. e) – h), same as above but for $d(A)_3^-$ instead of $d(A)_2^-$.

There may be several reasons for the lack of excimer dynamics observed: (i) The bases are simply not stacking. Even in solution, not all $d(A)_2^-$ is stacked and monomer-like dynamics are observed alongside excimer dynamics. The lack of stacking could simply be an entropic effect. Our experiments are performed with an internal energy of ~ 300 K and the entropic cost for stacking may be too high compared to the energy gain from π-stacking. In solution, stacking is favoured because of the unfavourable interaction of the nucleobase with water. The Bowers group have shown that 65 % of $d(A)_2^-$ were stacked at 80 K using ion mobility.[182] Hence, controlling the temperature

will be an important next step. This can be done using cryogenic ion traps as a storage device, which is currently being incorporated into our set-up. (ii) It is also possible that excimer states are formed but cannot be observed due to our limited detachment window with the 3.1 eV probe pulses. However, the work on the microhydrated Ade dimer would suggest that this is not a problem.[181] Moreover, our data show a weak but discernible 2-photon ionisation peak, which has a combined probe energy exceeding the ionisation energy of the base, however no long lived dynamics are observed in this either (iii) Finally, it is plausible that a sub-population of the ensemble is stacked but that the excimer states simply cannot form in the gas-phase because of the nearby charge on the phosphate. The excimer state has been predicted to have some charge-transfer character,[179] which may be destabilised by the strong Coulomb interaction with the charge. For sufficiently large oligonucleotides or for water-clustered oligonucleotides, this problem would be diminished because of the effective screening. Without further experiments, it is not possible to conclude why slower dynamics have not observed here, however the temperature is perhaps the most likely cause. Nevertheless, our results pave the way to performing time-resolved dynamical studies on much larger and biologically relevant systems and have shown the importance of environmental stabilisation of larger oligonucleotides. The base-stacked configuration leads to long-lived excited states but these can only be formed under suitable initial conditions. In double helix DNA, such base-stacking is enforced. An exciting prospect is that, in the gas-phase, conformation can be selected by, for example, ion mobility prior to the experiment. This will provide important insight into formation of these excited states.

5.5 Conclusions

The coupling of electrospray with femtosecond photoelectron spectroscopy provides new insight into the excited state dynamics of the fundamental building blocks of DNA. Using resonance enhanced two photon detachment, the adiabatic binding energy of the nucleobases has been determined, whilst they are in a larger nucleotide structure. It was found that the anionic phosphate group has the lowest detachment energy in all nucleotides except $dGMP^-$, for which the base moiety detaches first.

Time-resolved photoectron spectra have been recorded for all four nucleotide anions, exciting with 4.7 eV radiation. By comparison with gas and solution phase experiments, the decay mechanism of $dAMP^-$ was deduced to occur via a one-state mechanism, without any contribution from the much debated $^1n\pi^*$ state. The nucleotide of Gua, whose dynamics have been little studied in the gas phase, were

found to behave in a similar manner to $dAMP^-$, in line with theoretical predications. The two pyrimidine nucleotides, $dTMP^-$ and $dCMP^-$, show intriguing differences in dynamics, with $dTMP^-$ displaying a small amount long-lived population, and $dCMP^-$ demonstrating much slower dynamics than were expected based on the nucleobase alone. Finally, the power of the technique to expand to larger systems has been demonstrated, as the time-resolved photoelectron spectra of the oligonucleotides $d(A)_2^-$ and $d(A)_3^-$ have been recorded. Disappointingly, no evidence of long-lived dynamics from base stacking was observed, although this is likely a temperature effect, and future modifications to the instrument should hopefully allow these to be observed.

Outside of further experiment, a rigorous analysis of errors and confidence intervals is required to enable full interpretation of the existing data. This will likely be performed using the support plane analysis technique, outlined in Chapter 2. Prelimary efforts are underway towards these analyses.

5.6 References

1. C. Sagan, *J. Theor. Biol.*, 1973, **39**, 195.
2. N. Balucani, *Int. J. Mol. Sci.*, 2009, **10**, 2304.
3. A. Huijser, A. Pezzella and V. Sundstrom, *Phys. Chem. Chem. Phys.*, 2011, **13**, 9119.
4. C. E. Crespo-Hernández, B. Cohen, P. M. Hare and B. Kohler, *Chem. Rev.*, 2004, **104**, 1977.
5. K. Kleinermanns, D. Nachtigallová and M. S. de Vries, *Int. Rev. Phys. Chem.*, 2013, **32**, 308.
6. L. Serrano-Andrés and M. Merchán, *J. Photochem. Photobiol. C*, 2009, **10**, 21.
7. C. T. Middleton, K. de La Harpe, C. Su, Y. K. Law, C. E. Crespo-Hernández and B. Kohler, *Annu. Rev. Phys. Chem.*, 2009, **60**, 217.
8. Z. Wu, W. Gao, M. A. Phelps, D. Wu, D. D. Miller and J. T. Dalton, *Anal. Chem.*, 2004, **76**, 839.
9. C. Adamo and V. Barone, *J. Chem. Phys.*, 1999, **110**, 6158.
10. M. J. Frisch, G. W. Trucks, H. B. Schlegel, G. E. Scuseria, M. A. Robb, J. R. Cheeseman, G. Scalmani, V. Barone, B. Mennucci, G. A. Petersson, H. Nakatsuji, M. Caricato, X. Li, H. P. Hratchian, A. F. Izmaylov, J. Bloino, G. Zheng, J. L. Sonnenberg, M. Hada, M. Ehara, K. Toyota, R. Fukuda, J. Hasegawa, M. Ishida, T. Nakajima, Y. Honda, O. Kitao, H. Nakai, T. Vreven, J. A. Montgomery, J. E. Peralta, F. Ogliaro, M. Bearpark, J. J. Heyd, E. Brothers, K. N. Kudin, V. N. Staroverov, R. Kobayashi, J. Normand, K. Raghavachari, A. Rendell, J. C. Burant, S. S. Iyengar, J. Tomasi, M. Cossi, N. Rega, J. M. Millam, M. Klene, J. E. Knox, J. B. Cross, V. Bakken, C. Adamo, J. Jaramillo, R. Gomperts, R. E. Stratmann, O. Yazyev, A. J. Austin, R. Cammi, C. Pomelli, J. W. Ochterski, R. L. Martin, K. Morokuma, V. G. Zakrzewski, G. A. Voth, P. Salvador, J. J. Dannenberg, S. Dapprich, A. D. Daniels, Farkas, J. B. Foresman, J. V. Ortiz, J. Cioslowski and D. J. Fox, Wallingford CT, 2009.
11. S. S. Leang, F. Zahariev and M. S. Gordon, *J. Chem. Phys.*, 2012, **136**, 104101.
12. B. Boudaiffa, P. Cloutier, D. Hunting, M. A. Huels and L. Sanche, *Science*, 2000, **287**, 1658.
13. R. H. D. Lyngdoh and H. F. Schaefer, *Acc. Chem. Res.*, 2009, **42**, 563.
14. J.-L. Ravanat, T. Douki and J. Cadet, *J. Photochem. Photobiol., B*, 2001, **63**, 88.
15. L. Sanche, *European Physical Journal D*, 2005, **35**, 367.
16. P. Swiderek, *Angewandte Chemie-International Edition*, 2006, **45**, 4056.
17. D. B. Hall, R. E. Holmlin and J. K. Barton, *Nature*, 1996, **382**, 731.
18. Y. A. Berlin, A. L. Burin and M. A. Ratner, *J. Am. Chem. Soc.*, 2000, **123**, 260.
19. F. A. Aldaye, A. L. Palmer and H. F. Sleiman, *Science*, 2008, **321**, 1795.
20. A. V. Pinheiro, D. R. Han, W. M. Shih and H. Yan, *Nature Nanotechnology*, 2011, **6**, 763.
21. T. Torring, N. V. Voigt, J. Nangreave, H. Yan and K. V. Gothelf, *Chem. Soc. Rev.*, 2011, **40**, 5636.
22. V. M. Orlov, A. N. Smirnov and Y. M. Varshavsky, *Tetrahedron Lett.*, 1976, **17**, 4377.
23. S. T. Stokes, A. Grubisic, X. Li, Y. J. Ko and K. H. Bowen, *J. Chem. Phys.*, 2008, **128**, 044314.
24. A. B. Trofimov, J. Schirmer, V. B. Kobychev, A. W. Potts, D. M. P. Holland and L. Karlsson, *J. Phys. B: At. Mol. Opt. Phys.*, 2006, **39**, 305.
25. J. Lin, C. Yu, S. Peng, I. Akiyama, K. Li, L. K. Lee and P. R. LeBreton, *J. Phys. Chem.*, 1980, **84**, 1006.

26. B. F. Parsons, S. M. Sheehan, T. A. Yen, D. M. Neumark, N. Wehres and R. Weinkauf, *Phys. Chem. Chem. Phys.*, 2007, **9**, 3291.
27. J. H. Hendricks, S. A. Lyapustina, H. L. de Clercq, J. T. Snodgrass and K. H. Bowen, *J. Chem. Phys.*, 1996, **104**, 7788.
28. C. Desfrancois, H. Abdoul-Carime and J. Schermann, *J. Chem. Phys.*, 1996, **104**, 7792.
29. S. Denifl, S. Ptasinska, M. Cingel, S. Matejcik, P. Scheier and T. D. Märk, *Chem. Phys. Lett.*, 2003, **377**, 74.
30. M. A. Huels, I. Hahndorf, E. Illenberger and L. Sanche, *J. Chem. Phys.*, 1998, **108**, 1309.
31. N. A. Richardson, J. Gu, S. Wang, Y. Xie and H. F. Schaefer, *J. Am. Chem. Soc.*, 2004, **126**, 4404.
32. O. Dolgounitcheva, V. G. Zakrzewski and J. V. Ortiz, *Int. J. Quantum Chem*, 2002, **90**, 1547.
33. X. Li, Z. Cai and M. D. Sevilla, *J. Phys. Chem. A*, 2002, **106**, 1596.
34. S. D. Wetmore, R. J. Boyd and L. A. Eriksson, *Chem. Phys. Lett.*, 2000, **322**, 129.
35. D. M. Close and K. T. Ohman, *J. Phys. Chem. A*, 2008, **112**, 11207.
36. B. Pullman and A. Pullman, *Proc. Natl. Acad. Sci. USA*, 1958, **44**, 1197.
37. P. Slavicek, B. Winter, M. Faubel, S. E. Bradforth and P. Jungwirth, *J. Am. Chem. Soc.*, 2009, **131**, 6460.
38. C. E. Crespo-Hernández, R. Arce, Y. Ishikawa, L. Gorb, J. Leszczynski and D. M. Close, *J. Phys. Chem. A*, 2004, **108**, 6373.
39. E. Cauët, M. Valiev and J. H. Weare, *J. Phys. Chem. B*, 2010, **114**, 5886.
40. D. Ghosh, O. Isayev, L. V. Slipchenko and A. I. Krylov, *J. Phys. Chem. A*, 2011, **115**, 6028.
41. E. Pluhařová, P. Jungwirth, S. E. Bradforth and P. Slavíček, *J. Phys. Chem. B*, 2011, **115**, 1294.
42. H. Fernando, G. A. Papadantonakis, N. S. Kim and P. R. LeBreton, *Proc. Natl. Acad. Sci. USA*, 1998, **95**, 5550.
43. C. E. Crespo-Hernández, D. M. Close, L. Gorb and J. Leszczynski, *J. Phys. Chem. B*, 2007, **111**, 5386.
44. X. Yang, X.-B. Wang, E. R. Vorpagel and L.-S. Wang, *Proc. Natl. Acad. Sci. USA*, 2004, **101**, 17588.
45. Y.-w. Nei, N. Hallowita, J. D. Steill, J. Oomens and M. T. Rodgers, *J. Phys. Chem. A*, 2013, **117**, 1319.
46. J. Gidden and M. T. Bowers, *J. Phys. Chem. B*, 2003, **107**, 12829.
47. M. Vonderach, O. T. Ehrler, K. Matheis, P. Weis and M. M. Kappes, *J. Am. Chem. Soc.*, 2012, **134**, 7830.
48. J. M. Weber, I. N. Ioffe, K. M. Berndt, D. Löffler, J. Friedrich, O. T. Ehrler, A. S. Danell, J. H. Parks and M. M. Kappes, *J. Am. Chem. Soc.*, 2004, **126**, 8585.
49. D. M. Close and K. T. Øhman, *J. Phys. Chem. A*, 2008, **112**, 11207.
50. V. V. Zakjevskii, S. J. King, O. Dolgounitcheva, V. G. Zakrzewski and J. V. Ortiz, *J. Am. Chem. Soc.*, 2006, **128**, 13350.
51. M. Rubio, D. Roca-Sanjuán, L. Serrano-Andrés and M. Merchán, *J. Phys. Chem. B*, 2009, **113**, 2451.
52. M. Rubio, D. Roca-Sanjuán, M. Merchán and L. Serrano-Andrés, *J. Phys. Chem. B*, 2006, **110**, 10234.
53. S. Ullrich, T. Schultz, M. Z. Zgierski and A. Stolow, *Phys. Chem. Chem. Phys.*, 2004, **6**, 2796.
54. K. L. Wells, G. M. Roberts and V. G. Stavros, *Chem. Phys. Lett.*, 2007, **446**, 20.
55. H. Kang, K. T. Lee, B. Jung, Y. J. Ko and S. K. Kim, *J. Am. Chem. Soc.*, 2002, **124**, 12958.
56. S. Sunil Kumar, M. Pérot-Taillandier, B. Lucas, S. Soorkia, M. Barat and J. A. Fayeton, *J. Phys. Chem. A*, 2011, **115**, 10383.
57. G. Aravind, R. Antoine, B. Klaerke, J. Lemoine, A. Racaud, D. B. Rahbek, J. Rajput, P. Dugourd and L. H. Andersen, *Phys. Chem. Chem. Phys.*, 2010, **12**, 3486.
58. J. C. Marcum, A. Halevi and J. M. Weber, *Phys. Chem. Chem. Phys.*, 2009, **11**, 1740.
59. V. Gabelica, F. Rosu, T. Tabarin, C. Kinet, R. Antoine, M. Broyer, E. De Pauw and P. Dugourd, *J. Am. Chem. Soc.*, 2007, **129**, 4706.
60. D. A. Horke, A. S. Chatterley and J. R. R. Verlet, *J. Phys. Chem. Lett.*, 2012, **3**, 834.
61. K. L. Wells, D. J. Hadden, M. G. D. Nix and V. G. Stavros, *J. Phys. Chem. Lett.*, 2010, **1**, 993.
62. M. Vonderach, O. T. Ehrler, P. Weis and M. M. Kappes, *Anal. Chem.*, 2011, **83**, 1108.
63. D. Radisic, K. H. Bowen, I. Dąbkowska, P. Storoniak, J. Rak and M. Gutowski, *J. Am. Chem. Soc.*, 2005, **127**, 6443.
64. A. Szyperska, J. Rak, J. Leszczynski, X. Li, Y. J. Ko, H. Wang and K. H. Bowen, *ChemPhysChem*, 2010, **11**, 880.
65. Y. J. Ko, H. Wang, R. Cao, D. Radisic, S. N. Eustis, S. T. Stokes, S. Lyapustina, S. X. Tian and K. H. Bowen, *Phys. Chem. Chem. Phys.*, 2010, **12**, 3535.
66. L. M. Nielsen, S. O. Pedersen, M.-B. S. Kirketerp and S. B. Nielsen, *J. Chem. Phys.*, 2012, **136**, 064302.
67. R. D. Brown, P. D. Godfrey, D. McNaughton and A. P. Pierlot, *Chem. Phys. Lett.*, 1989, **156**, 61.
68. S. Ullrich, T. Schultz, M. Z. Zgierski and A. Stolow, *J. Am. Chem. Soc.*, 2004, **126**, 2262.
69. H. Satzger, D. Townsend and A. Stolow, *Chem. Phys. Lett.*, 2006, **430**, 144.
70. H. Satzger, D. Townsend, M. Z. Zgierski, S. Patchkovskii, S. Ullrich and A. Stolow, *Proc. Natl. Acad. Sci. USA*, 2006, **103**, 10196.
71. M. G. D. Nix, A. L. Devine, B. Cronin and M. N. R. Ashfold, *J. Chem. Phys.*, 2007, **126**, 124312.
72. C. Z. Bisgaard, H. Satzger, S. Ullrich and A. Stolow, *ChemPhysChem*, 2009, **10**, 101.
73. K. L. Wells, D. J. Hadden, M. G. D. Nix and V. G. Stavros, *J. Phys. Chem. Lett.*, 2010, **1**, 993.

74. C. Canuel, M. Mons, F. Piuzzi, B. Tardivel, I. Dimicoli and M. Elhanine, *J. Chem. Phys.*, 2005, **122**, 074316.
75. L. Blancafort, *J. Am. Chem. Soc.*, 2005, **128**, 210.
76. S. Brøndsted Nielsen and T. I. Sølling, *ChemPhysChem*, 2005, **6**, 1276.
77. H. Chen and S. Li, *J. Phys. Chem. A*, 2005, **109**, 8443.
78. C. M. Marian, *J. Chem. Phys.*, 2005, **122**, 104314.
79. S. Perun, A. L. Sobolewski and W. Domcke, *J. Am. Chem. Soc.*, 2005, **127**, 6257.
80. S. Perun, A. L. Sobolewski and W. Domcke, *Chem. Phys.*, 2005, **313**, 107.
81. L. Serrano-Andrés, M. Merchán and A. C. Borin, *Chemistry – A European Journal*, 2006, **12**, 6559.
82. L. Serrano-Andrés, M. Merchán and A. C. Borin, *Proc. Natl. Acad. Sci. USA*, 2006, **103**, 8691.
83. W. Credo Chung, Z. Lan, Y. Ohtsuki, N. Shimakura, W. Domcke and Y. Fujimura, *Phys. Chem. Chem. Phys.*, 2007, **9**, 2075.
84. M. Barbatti and H. Lischka, *J. Am. Chem. Soc.*, 2008, **130**, 6831.
85. E. Fabiano and W. Thiel, *J. Phys. Chem. A*, 2008, **112**, 6859.
86. Y. Lei, S. Yuan, Y. Dou, Y. Wang and Z. Wen, *J. Phys. Chem. A*, 2008, **112**, 8497.
87. I. Conti, M. Garavelli and G. Orlandi, *J. Am. Chem. Soc.*, 2009, **131**, 16108.
88. A. N. Alexandrova, J. C. Tully and G. Granucci, *J. Phys. Chem. B*, 2010, **114**, 12116.
89. M. Barbatti, A. J. A. Aquino, J. J. Szymczak, D. Nachtigallová, P. Hobza and H. Lischka, *Proc. Natl. Acad. Sci. USA*, 2010, **107**, 21453.
90. M. Barbatti, Z. Lan, R. Crespo-Otero, J. J. Szymczak, H. Lischka and W. Thiel, *J. Chem. Phys.*, 2012, **137**, 22A503.
91. N. J. Kim, G. Jeong, Y. S. Kim, J. Sung, S. K. Kim and Y. D. Park, *J. Chem. Phys.*, 2000, **113**, 10051.
92. D. C. Luhrs, J. Viallon and I. Fischer, *Phys. Chem. Chem. Phys.*, 2001, **3**, 1827.
93. E. Nir, K. Kleinermanns, L. Grace and M. S. de Vries, *J. Phys. Chem. A*, 2001, **105**, 5106.
94. C. Plutzer, E. Nir, M. S. de Vries and K. Kleinermanns, *Phys. Chem. Chem. Phys.*, 2001, **3**, 5466.
95. C. Plutzer and K. Kleinermanns, *Phys. Chem. Chem. Phys.*, 2002, **4**, 4877.
96. Y. Lee, M. Schmitt, K. Kleinermanns and B. Kim, *J. Phys. Chem. A*, 2006, **110**, 11819.
97. A. L. Sobolewski, W. Domcke, C. Dedonder-Lardeux and C. Jouvet, *Phys. Chem. Chem. Phys.*, 2002, **4**, 1093.
98. R. Livingstone, O. Schalk, A. E. Boguslavskiy, G. R. Wu, L. T. Bergendahl, A. Stolow, M. J. Paterson and D. Townsend, *J. Chem. Phys.*, 2011, **135**, 194307.
99. J. A. Boeyens, *Journal of Crystal and Molecular Structure*, 1978, **8**, 317.
100. T. Gustavsson, A. Sharonov, D. Onidas and D. Markovitsi, *Chem. Phys. Lett.*, 2002, **356**, 49.
101. D. Onidas, D. Markovitsi, S. Marguet, A. Sharonov and T. Gustavsson, *J. Phys. Chem. B*, 2002, **106**, 11367.
102. M. C. Stuhldreier and F. Temps, *Faraday Discuss.*, 2013, **163**, 173.
103. J.-M. L. Pecourt, J. Peon and B. Kohler, *J. Am. Chem. Soc.*, 2001, **123**, 10370.
104. B. Cohen, P. M. Hare and B. Kohler, *J. Am. Chem. Soc.*, 2003, **125**, 13594.
105. F. Buchner, H.-H. Ritze, J. Lahl and A. Lubcke, *Phys. Chem. Chem. Phys.*, 2013, **15**, 11402.
106. B. Mennucci, A. Toniolo and J. Tomasi, *J. Phys. Chem. A*, 2001, **105**, 4749.
107. S. Yamazaki and S. Kato, *J. Am. Chem. Soc.*, 2007, **129**, 2901.
108. V. Ludwig, Z. M. da Costa, M. S. do Amaral, A. C. Borin, S. Canuto and L. Serrano-Andrés, *Chem. Phys. Lett.*, 2010, **492**, 164.
109. Z. Lan, Y. Lu, E. Fabiano and W. Thiel, *ChemPhysChem*, 2011, **12**, 1989.
110. R. Mitrić, U. Werner, M. Wohlgemuth, G. Seifert and V. Bonačić-Koutecký, *J. Phys. Chem. A*, 2009, **113**, 12700.
111. C. R. S. Mooney, D. A. Horke, A. S. Chatterley, A. Simperler, H. H. Fielding and J. R. R. Verlet, *Chem. Sci.*, 2013, **4**, 921.
112. M. Smits, C. A. de Lange, S. Ullrich, T. Schultz, M. Schmitt, J. G. Underwood, J. P. Shaffer, D. M. Rayner and A. Stolow, *Rev. Sci. Instrum.*, 2003, **74**, 4812.
113. E. Nir, C. Janzen, P. Imhof, K. Kleinermanns and M. S. de Vries, *J. Chem. Phys.*, 2001, **115**, 4604.
114. W. Chin, M. Mons, I. Dimicoli, F. Piuzzi, B. Tardivel and M. Elhanine, *Eur. Phys. J. D*, 2002, **20**, 347.
115. M. Mons, I. Dimicoli, F. Piuzzi, B. Tardivel and M. Elhanine, *J. Phys. Chem. A*, 2002, **106**, 5088.
116. K. Seefeld, R. Brause, T. Häber and K. Kleinermanns, *J. Phys. Chem. A*, 2007, **111**, 6217.
117. H. Langer and N. L. Doltsinis, *Phys. Chem. Chem. Phys.*, 2004, **6**, 2742.
118. H. Langer, N. L. Doltsinis and D. Marx, *ChemPhysChem*, 2005, **6**, 1734.
119. H. Chen and S. Li, *J. Chem. Phys.*, 2006, **124**, 154315.
120. C. M. Marian, *J. Phys. Chem. A*, 2007, **111**, 1545.
121. L. Serrano-Andrés, M. Merchán and A. C. Borin, *J. Am. Chem. Soc.*, 2008, **130**, 2473.
122. S. Yamazaki, W. Domcke and A. L. Sobolewski, *J. Phys. Chem. A*, 2008, **112**, 11965.
123. Z. Lan, E. Fabiano and W. Thiel, *ChemPhysChem*, 2009, **10**, 1225.
124. M. Barbatti, J. J. Szymczak, A. J. A. Aquino, D. Nachtigallova and H. Lischka, *J. Chem. Phys.*, 2011, **134**, 014304.
125. M. Parac, M. Doerr, C. M. Marian and W. Thiel, *J. Comput. Chem.*, 2010, **31**, 90.
126. V. Karunakaran, K. Kleinermanns, R. Improta and S. A. Kovalenko, *J. Am. Chem. Soc.*, 2009, **131**, 5839.

127. J. Peon and A. H. Zewail, *Chem. Phys. Lett.*, 2001, **348**, 255.
128. F.-A. Miannay, T. Gustavsson, A. Banyasz and D. Markovitsi, *J. Phys. Chem. A*, 2010, **114**, 3256.
129. B. Heggen, Z. Lan and W. Thiel, *Phys. Chem. Chem. Phys.*, 2012, **14**, 8137.
130. D. S. Goodsell, *The Oncologist*, 2001, **6**, 298.
131. B. B. Brady, L. A. Peteanu and D. H. Levy, *Chem. Phys. Lett.*, 1988, **147**, 538.
132. M. K. Shukla and J. Leszczynski, *Wiley Interdisciplinary Reviews: Computational Molecular Science*, 2013, n/a.
133. M. Kunitski, Y. Nosenko and B. Brutschy, *ChemPhysChem*, 2011, **12**, 2024.
134. S. Perun, A. L. Sobolewski and W. Domcke, *J. Phys. Chem. A*, 2006, **110**, 13238.
135. G. Zechmann and M. Barbatti, *J. Phys. Chem. A*, 2008, **112**, 8273.
136. S. Yamazaki and T. Taketsugu, *J. Phys. Chem. A*, 2011, **116**, 491.
137. M. Merchán, R. González-Luque, T. Climent, L. Serrano-Andrés, E. Rodríguez, M. Reguero and D. Peláez, *J. Phys. Chem. B*, 2006, **110**, 26471.
138. D. Picconi, V. Barone, A. Lami, F. Santoro and R. Improta, *ChemPhysChem*, 2011, **12**, 1957.
139. H. R. Hudock, B. G. Levine, A. L. Thompson, H. Satzger, D. Townsend, N. Gador, S. Ullrich, A. Stolow and T. J. Martínez, *J. Phys. Chem. A*, 2007, **111**, 8500.
140. P. M. Hare, C. E. Crespo-Hernández and B. Kohler, *Proc. Natl. Acad. Sci. USA*, 2007, **104**, 435.
141. J.-M. L. Pecourt, J. Peon and B. Kohler, *J. Am. Chem. Soc.*, 2000, **122**, 9348.
142. J. Gonzalez-Vazquez, L. Gonzalez, E. Samoylova and T. Schultz, *Phys. Chem. Chem. Phys.*, 2009, **11**, 3927.
143. M. Etinski and C. M. Marian, *Phys. Chem. Chem. Phys.*, 2010, **12**, 4915.
144. R. D. Brown, P. D. Godfrey, D. McNaughton and A. P. Pierlot, *J. Am. Chem. Soc.*, 1989, **111**, 2308.
145. M. Szczesniak, K. Szczepaniak, J. S. Kwiatkowski, K. KuBulat and W. B. Person, *J. Am. Chem. Soc.*, 1988, **110**, 8319.
146. G. Bazso, G. Tarczay, G. Fogarasi and P. G. Szalay, *Phys. Chem. Chem. Phys.*, 2011, **13**, 6799.
147. D. L. Barker and R. E. Marsh, *Acta Crystallographica*, 1964, **17**, 1581.
148. K. Kosma, C. Schröter, E. Samoylova, I. V. Hertel and T. Schultz, *J. Am. Chem. Soc.*, 2009, **131**, 16939.
149. E. Nir, I. Hunig, K. Kleinermanns and M. S. de Vries, *Phys. Chem. Chem. Phys.*, 2003, **5**, 4780.
150. E. Nir, M. Müller, L. I. Grace and M. S. de Vries, *Chem. Phys. Lett.*, 2002, **355**, 59.
151. J.-W. Ho, H.-C. Yen, W.-K. Chou, C.-N. Weng, L.-H. Cheng, H.-Q. Shi, S.-H. Lai and P.-Y. Cheng, *J. Phys. Chem. A*, 2011, **115**, 8406.
152. S. Lobsiger, M. A. Trachsel, H.-M. Frey and S. Leutwyler, *J. Phys. Chem. B*, 2013, **117**, 6106.
153. A. Nakayama, Y. Harabuchi, S. Yamazaki and T. Taketsugu, *Phys. Chem. Chem. Phys.*, 2013, **15**, 12322.
154. M. Merchán and L. Serrano-Andrés, *J. Am. Chem. Soc.*, 2003, **125**, 8108.
155. K. Tomić, J. Tatchen and C. M. Marian, *J. Phys. Chem. A*, 2005, **109**, 8410.
156. K. A. Kistler and S. Matsika, *J. Chem. Phys.*, 2008, **128**, 215102.
157. K. A. Kistler and S. Matsika, *J. Phys. Chem. A*, 2007, **111**, 2650.
158. N. Ismail, L. Blancafort, M. Olivucci, B. Kohler and M. A. Robb, *J. Am. Chem. Soc.*, 2002, **124**, 6818.
159. H. R. Hudock and T. J. Martínez, *ChemPhysChem*, 2008, **9**, 2486.
160. M. Barbatti, A. J. A. Aquino, J. J. Szymczak, D. Nachtigallova and H. Lischka, *Phys. Chem. Chem. Phys.*, 2011, **13**, 6145.
161. M. Z. Zgierski, S. Patchkovskii and E. C. Lim, *J. Chem. Phys.*, 2005, **123**, 081101.
162. M. Z. Zgierski, S. Patchkovskii, T. Fujiwara and E. C. Lim, *J. Phys. Chem. A*, 2005, **109**, 9384.
163. L. Blancafort, B. Cohen, P. M. Hare, B. Kohler and M. A. Robb, *J. Phys. Chem. A*, 2005, **109**, 4431.
164. C. E. Crespo-Hernandez, B. Cohen and B. Kohler, *Nature*, 2005, **436**, 1141.
165. I. Buchvarov, Q. Wang, M. Raytchev, A. Trifonov and T. Fiebig, *Proc. Natl. Acad. Sci. USA*, 2007, **104**, 4794.
166. T. Takaya, C. Su, K. de La Harpe, C. E. Crespo-Hernández and B. Kohler, *Proc. Natl. Acad. Sci. USA*, 2008, **105**, 10285.
167. K. de La Harpe and B. Kohler, *J. Phys. Chem. Lett.*, 2011, **2**, 133.
168. C. Su, C. T. Middleton and B. Kohler, *J. Phys. Chem. B*, 2012, **116**, 10266.
169. I. Vayá, T. Gustavsson, T. Douki, Y. Berlin and D. Markovitsi, *J. Am. Chem. Soc.*, 2012, **134**, 11366.
170. L. M. Nielsen, S. V. Hoffmann and S. B. Nielsen, *Photochemical & Photobiological Sciences*, 2013, **12**, 1273.
171. M. C. Stuhldreier and F. Temps, *Faraday Discuss.*, 2013.
172. G. W. Doorley, M. Wojdyla, G. W. Watson, M. Towrie, A. W. Parker, J. M. Kelly and S. J. Quinn, *J. Phys. Chem. Lett.*, 2013, **4**, 2739.
173. J. M. Jean and K. B. Hall, *Biochemistry*, 2002, **41**, 13152.
174. B. Bouvier, J.-P. Dognon, R. Lavery, D. Markovitsi, P. Millié, D. Onidas and K. Zakrzewska, *J. Phys. Chem. B*, 2003, **107**, 13512.
175. E. Emanuele, K. Zakrzewska, D. Markovitsi, R. Lavery and P. Millié, *J. Phys. Chem. B*, 2005, **109**, 16109.
176. G. Olaso-González, M. Merchán and L. Serrano-Andrés, *J. Am. Chem. Soc.*, 2009, **131**, 4368.
177. Y. Dou, W. Zhao, S. Yuan, W. Zhang and H. Tang, *Science China Chemistry*, 2012, **55**, 1377.

178. F. Plasser, A. J. A. Aquino, W. L. Hase and H. Lischka, *J. Phys. Chem. A*, 2012, **116**, 11151.
179. F. Plasser and H. Lischka, *Journal of Chemical Theory and Computation*, 2012, **8**, 2777.
180. F. Rosu, V. Gabelica, E. De Pauw, R. Antoine, M. Broyer and P. Dugourd, *J. Phys. Chem. A*, 2012, **116**, 5383.
181. V. R. Smith, E. Samoylova, H. H. Ritze, W. Radloff and T. Schultz, *Phys. Chem. Chem. Phys.*, 2010, **12**, 9632.
182. J. Gidden and M. T. Bowers, *Eur. Phys. J. D*, 2002, **20**, 409.

6 Construction of a New Instrument for VMI and Laser Desorption

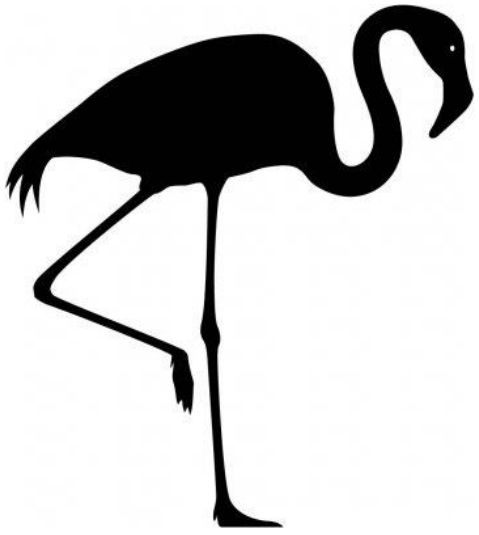

6.1 Introduction

The central theme of this thesis has been 'building-up' – that is extending gas phase time domain measurements to ever larger systems. Although the electrospray ion source in Durham allows for very large systems to be studied, there is the stipulation that they must be charged, and neutral species cannot be studied. Using a simple heated pulsed valve, as in the presented experiment in Warwick, there is a limit on the size of system which can be studied before decomposition occurs.

One technique to circumvent the size limit of molecular beams is to use laser desorption techniques.[1] In these, a laser pulse is used to rapidly transfer energy into a solid sample, desorbing it into the gas phase. The desorbed sampled can then be studied directly, or seeded into a molecular beam for cooling. Desorption sources coupled with frequency resolved laser spectroscopy have been used to study a number of systems, such as peptides[2-7] and nucleobases.[8-12] On the other hand, desorption sources have been more rarely used for dynamics studies, although examples do exist.[6, 13, 14]

To study dynamics of large neutral systems, a laser desorption system is being developed in Warwick. The intended desorption source design is similar to that of Stolow and co-workers,[12] although at the time of writing it is still in preliminary stages. Essentially, the design consists of a rotating graphite rod, onto which the analyte is pressed. A nanosecond laser ablates material from the graphite rod, seeding it into a molecular beam of buffer gas from the pulsed valve. To ensure fresh sample is always used, the rod rotates on a motorized screw system.

This chapter describes the design of a second generation instrument for studying gas phase dynamics with VMI in Warwick, which has the capability to be fitted with a desorption source. Fig. 6.1 shows a computer render of the entire assembly of the instrument. There are two regions, the source region and the interaction region, separated by a gate valve. The design and operation of each region shall be considered in turn. Technical drawings for the main chambers are presented in Appendix C. As signal levels may be anticipated to be very low in the desorption system, the instrument is designed to give the minimum possible distance between the molecular beam source and the VMI system. This should ensure the greatest possible sample density in the interaction region.

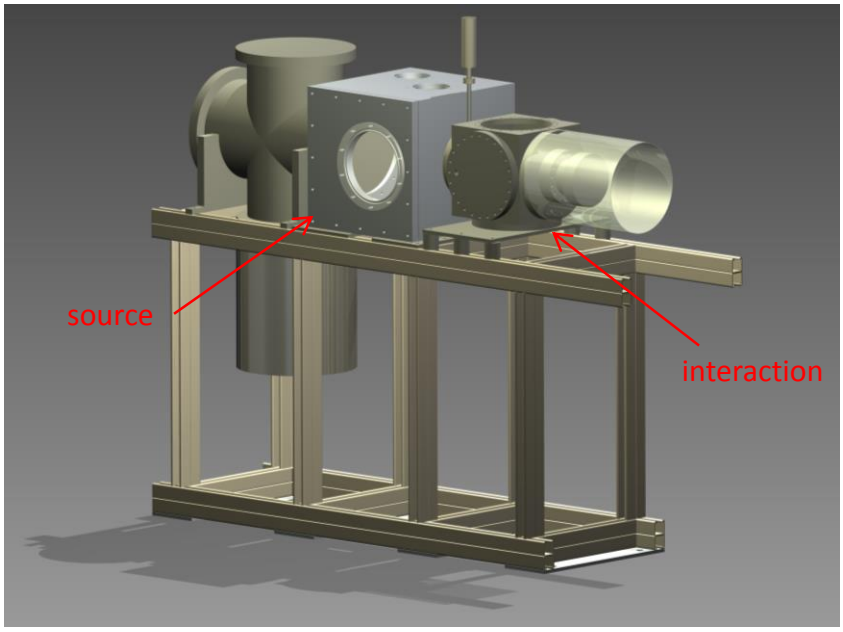

Figure 6.1 CAD rendering of the completed instrument. The machine is broadly divided into two region, the source region which consists of a cross and a large cube, and the interaction region composed of a smaller cube and a time-of-flight tube. The outer mu-metal magnetic shield has been rendered transparent for visibility purposes.

6.2 Source Chamber

6.2.1 Chamber Specifications

The source region is composed of two chambers. The first serves only to mount a turbomolecular pump whilst the second houses the molecular beam source.

The first chamber is a cross, with four 13¼ inch CF ports. The bottom port holds a 2200 L s^{-1} turbo-pump (Oerlikon Leybold Mag W 2200), and the right port mates to the cube containing the beam source. The remaining two ports are blanked off.

The source cube is custom designed, and was constructed by Lewvac LLP. It is 400 mm long on each axis. A rendered cross section of the cube is shown in Fig. 6.2. The cube is constructed from six welded stainless steel plates. With reference to the face labelling in Fig. 6.2, each face is detailed as follows.

i) The left face mates to the cross holding the turbo-pump with a 13¼ inch CF port. Internally, there is a ring (308.9 mm diameter) of 15 tapped M8 bolt holes, which can be used for mounting.

ii) The top face has two ISO 100 ports. The leftmost port is used for gas, thermocouple and power feedthroughs for the pulsed valve. A borosilicate window (Lewvac VP-100LF) may be placed on the right port to give access from above for a desorption laser. The inside of the top face is undetailed.

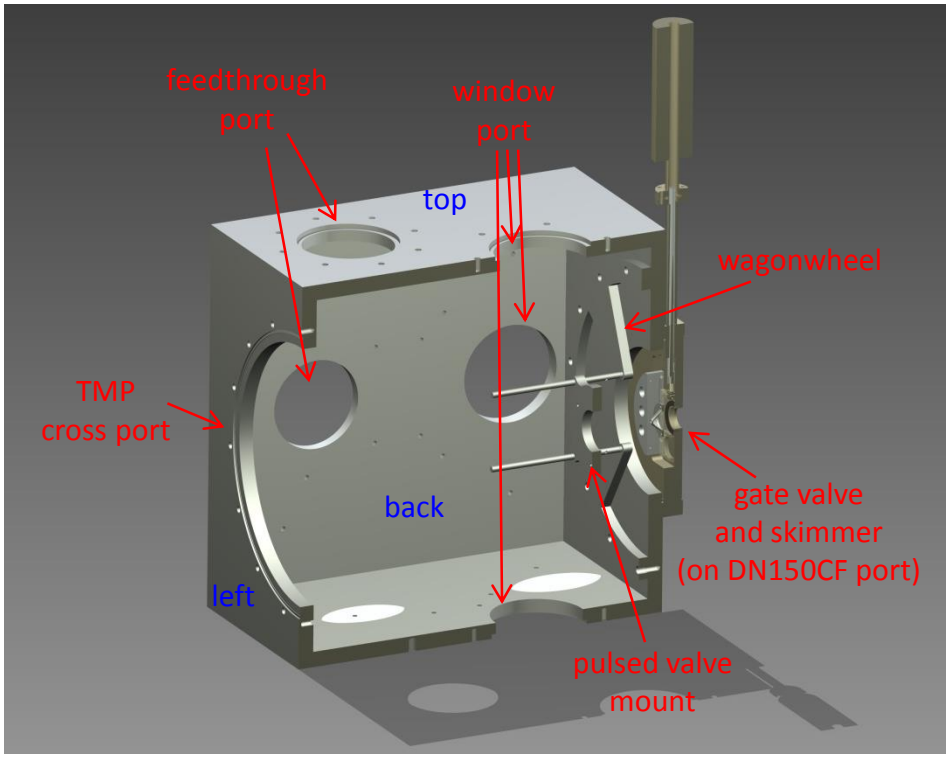

Figure 6.2 Rendering of a cross section of the source cube. The pulsed valve is mounted to a holder which slides along four rods. The near-side face (not shown) is a fully detachable square flange, sealed with a rubber O-ring. The majority of ports are reserved for laser desorption usage. Internal tapped holes are for mounting laser desorption components.

iii) The back face has two ports on it. On the left is an ISO 100 port, on which feedthroughs may be mounted, and on the right is a DN100CF port, with a fused silica window (Lewvac FSPP-UV-100CF) on it. A CF port is used rather than ISO as this allows the window to be as close as possible to the desorption source, which may be important to maximize the throughput of a desorption system. Internally, the back face has a series of tapped M6 holes, for mounting.

iv) The bottom face has a single ISO 100 port on it, onto which a window may be placed for vertical laser access, as with the top face. Internally, the bottom face has a series of tapped M6 bolt holes, spaced such that a standard optical breadboard may be mounted to the bottom surface.

v) The front face of the cube holds a detachable square aluminium flange (made in-house). The flange covers the front face entirely, and holds a Perspex window, and handles for ease of transportation. The flange is sealed by a rubber O-ring which is kept on the cube, and held in place by M8 bolts. The internal face of the flange is featureless.

vi) The right face mates to the gate valve, via a DN150CF port. Internally, this face holds the mounting for the pulsed valve. The mounting is achieved as followed: an aluminium 'wagon wheel' is mounted to the internal face via a ring (308.9 mm diameter) of 15 M8 bolts. The wagon wheel has four spokes, into which mount four

rods (6.0 mm diameter). The valve mount slides onto these four rods, allowing the distance to the skimmer to be adjusted. The valve mount is secured to the rods using grub screws. The pulsed valve used in an Even-Lavie valve[15] (see Chapter 2).

Pressure in the source region is measured using a magnetron gauge. Typically, the pressure is $\sim 5\times10^{-7}$ mbar when the pulsed valve is off, and $\sim 1\times10^{-5}$ mbar during experiments when the valve is running.

6.2.2 Gate Valve

To change over samples in the pulsed valve, the source region must be vented to atmosphere. If the interaction region is also vented, this results in a long wait before acceptable pressures are obtained and experiments can be run. A gate valve circumvents the pressure problem, however it imposes a new difficulty in mounting a skimmer between the two regions. For the coldest possible beams a skimmer should be used between the two differentially pumped regions, however most commercially available gate valves have no capacity to mount a skimmer to them. An additional problem with commercial gate valves is one of width – for maximum signal we required the shortest possible distance between the valve and desorption source, and so the minimum possible width of gate valve in required, which in practice is the width of a CF flange.

To overcome these problems, a home built gate valve was used. The gate valve is a slight modification of the design of Pittman and O'Conner,[16] and was constructed in-house. The gate valve is composed of a DN150CF flange, which has been milled out to accommodate the mechanics. A blade, affixed to PTFE runners, moves up and down within a guide rail, which curves in at both ends to seal the blade against a rubber O-ring. Motion is provided by a linear motion feedthrough (Caburn-MDC). Mounted to the blade is a stainless steel skimmer with a 2 mm opening, machined in-house. Moving the linear feedthrough allows the blade to be moved between the two sealing positions, one where a solid blade seals the two regions from each other, and the other where the skimmer is sealed into place. The gate valve is visible on the right hand side of Fig. 6.2.

6.3 Interaction Chamber

The interaction region is composed of two CF chambers, a custom cube to house the ion optics, and a short nipple to serve as a time-of-flight tube. We shall first detail the specifications of the components, followed by simulations and details of the ion optics.

6.3.1 Chamber Specifications

The interaction cube is a custom design, and was constructed by Lewvac LLP. It is 258.4 mm long on all axes. On five faces of the cube is a standard DN200CF port. The sixth face is for mounting to the gate valve, and consists of a welded nipple, followed by a rotatable DN150CF port. There is a 15.0 mm gap between the cube face and the interior face of the flange, which is the shortest length possible to still allow nuts to be inserted and tightened to mate the flanges. On the interior of the face with the nipple is a set of tapped M4 holes for mounting ion optics to. There are four sets, each composed of four holes in a square configuration. The diagonal dimensions of the squares are 110.0, 130.0, 150.0 and 170.0 mm for the four sets.

On the opposing face to that with the nipple is a DN200CF to DN100CF reducer flange, with four M4 holes drilled and tapped into it (125 mm diameter bolt circle) to mount a mu-metal shield. This flange is mated to a DN100CF flange which holds the deflectors (see below), and to this flange is mounted the 90.0 mm time-of-flight tube. At the end of the time-of-flight tube is the VMI detector (Photek, see Chapter 2).

Above the cube, a 700 L s^{-1} turbomolecular pump (Oerlikon Leybold Turbovac Mag W 700) is mounted. On either side is a flange with a CaF_2 window. The window is placed on the side of the flange, in line with the VMI optics, and is sealed by a rubber O-ring. The windows are otherwise unsupported – they rely on atmospheric pressure to keep them on the flanges.

Pressure in the interaction region is measured using a magnetron gauge, on an extension nipple mounted to one of the window flanges. Typically, the pressure is $\sim 7\times10^{-9}$ mbar when the pulsed valve is off, and $\sim 1\times10^{-7}$ mbar during experiments.

6.3.2 Ion Optics

6.3.2.1 Design

The ion optic setup is a direct replica of Eppink and Parker's original on-axis velocity map imaging arrangement.[17-19] The setup has been designed so that both ions and electrons may be velocity mapped, with a kinetic energy upper limit of ~7 eV, although the magnification factor of the arrangement may be varied depending on the energetic region of interest. A rendered cross section of the interaction region is shown in Fig. 6.3.

The VMI plates are all made of mu-metal, and are 2.0 mm thick, spaced 15.0 mm centre-to-centre (13.0 mm between plates). The plates are 135.0 mm in diameter. The extractor and ground plates have a 20.0 mm central hole. The repeller plate has a

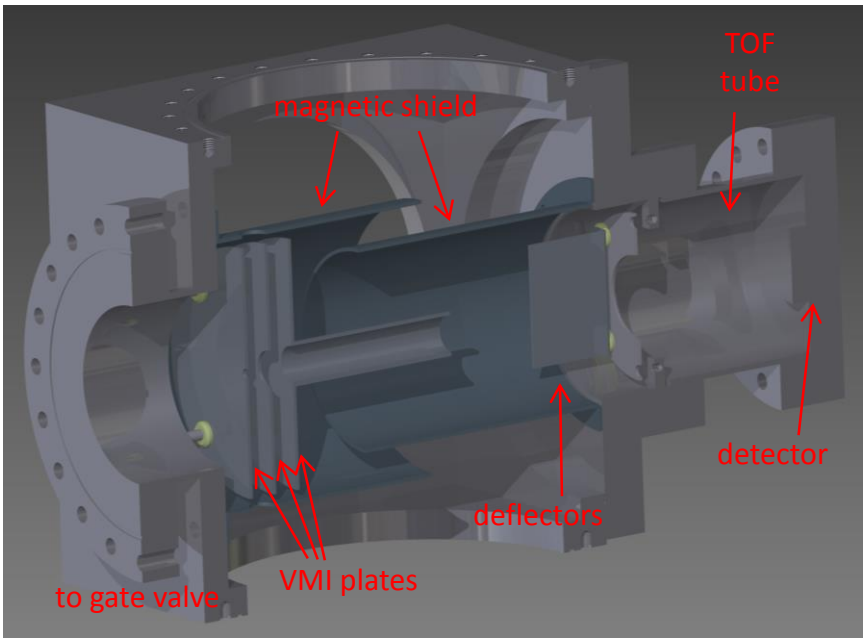

Figure 6.3 Rendered cross section of the interaction region. Shown are ion optics, and magnetic shields.

5.0 mm central hole to allow access by the molecular beam. The ground plate has a tube welded to the front of it, 100 mm long, to reduce the impact of stray fields whilst ions are in early flight. The VMI plates are mounted to four 4.0 diameter mm rods which screw into holes on the front face of the cube, with a 110.0 mm bolt circle. Electrical isolation is achieved by a pair of ceramic split bushes (Lewvac), and the appropriate spacing is achieved from a set of metal spacers. The spacers between the plates are 1.85 mm long, and between the repeller and the cube face they are 12.3 mm long. Electrical connections to the plates employ a 2 mm hole on the outer corner (behind the mounting rod).

The detector is re-used from the first generation instrument, composed of a stack of two MCPs coupled to a phosphor screen (Photek). The front surface of the detector is 40 mm in diameter, and it is separated from the centre of the ground plate by 320 mm of time-of-flight space.

As in the first generation instrument, when imaging cations (such as protons), a large background of parent$^+$ ions will strike the detector, causing burns. To avoid this eventuality, a pair of deflector plates are mounted to the interaction cube. A time dependant voltage may be pulsed onto one plate, to deflect any ions heavier than those of interest. The deflector plates are composed of two pieces of bent steel, placed 40 mm apart. The deflectors are held to a stainless steel mounting ring by two M4 screws, and electrically isolated with ceramic split bushes. The bolt holes on the mounting ring are on an 80 mm diameter bolt circle. The mounting ring itself is connected to a DN100CF

flange, by means of four welded mounting rods with M6 tapped holes, also on an 80 mm diameter bolt circle.

To facilitate measurement of photoelectron spectra, it is imperative that interference from magnetic fields is kept to an absolute minimum. Magnetic shielding is provided in the form of internal mu-metal shields around the VMI optics, and external mu-metal shield around the time-of-flight tube, and the VMI plates themselves are made of mu-metal (all mu-metal pieces provided custom from Magnetic Shields Ltd.). The first shield is located around the VMI plates. It mounts to the rear face of the cube with M4 screws on a 170.0 mm diameter bolt circle. It extends out 130 mm, and has a 145.0 mm internal bore. On either side are 15.0 mm holes, aligned with the centre of the space between the repeller and extractor. The holes allow for laser access. There

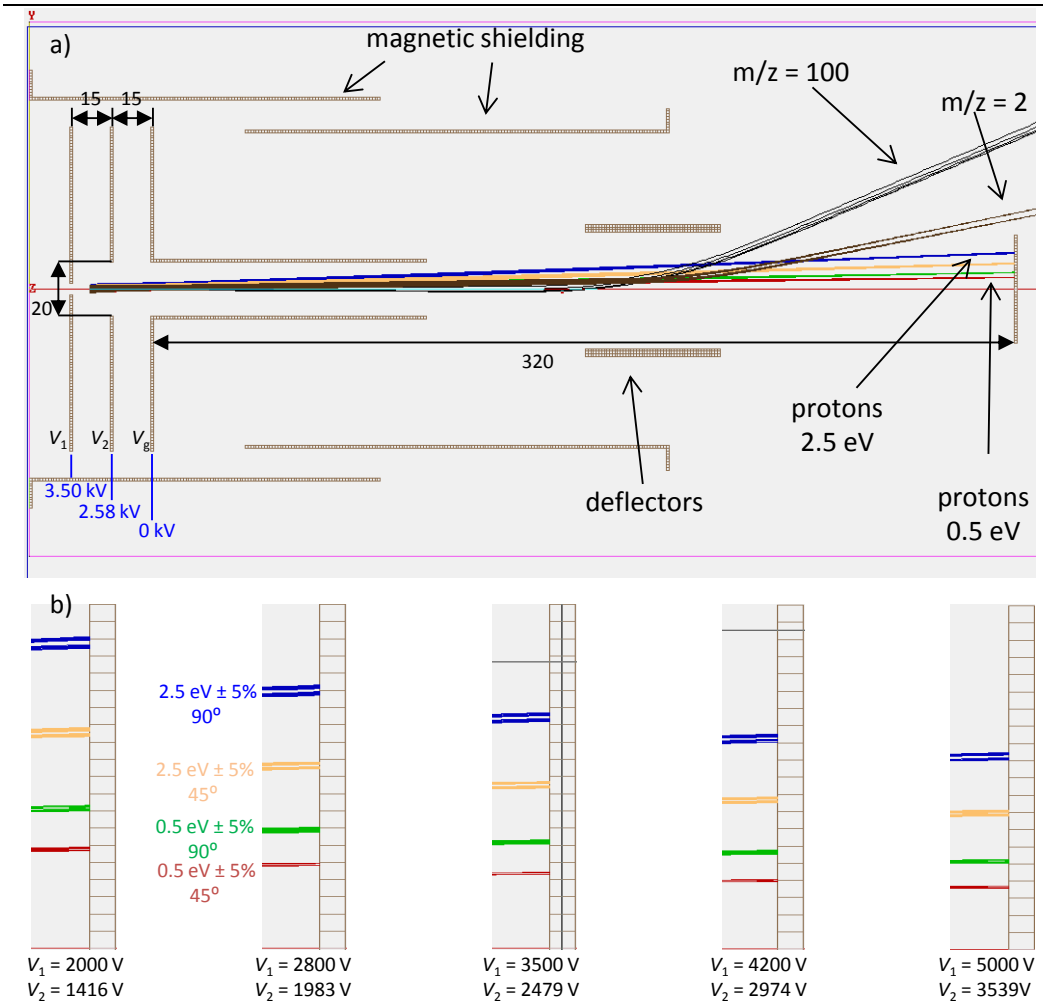

Figure 6.4 a) Simulation of an H^+ imaging experiment, from a 100 amu parent molecule. Four different proton bunches are simulated, with energies of either 2.5 eV or 0.5 eV, and spawned with velocities at either 90° or 45° to the axis of flight. Also shown are ions with a mass of 2 and 100 amu, which are deflected away from the detector by a time dependant high voltage pulse on the deflector plates. b) Expanded view of the detector at five different repeller voltages. The ions are as above, except in each case there are two bunches separated by ±5 %, to show the achievable resolution.

is a small slot at the rear of the shield to allow connector wires to be passed through. The second shield is mounted to the reducer flange at the other end of the instrument. It is connected by M4 bolts on a 125,0 mm diameter bolt circle, and it extends out 150 mm. The final shield is external, it sits over the time of flight tube, with a 256 mm internal bore and is 350 mm long. There is a slot cut in so that the connectors for the deflector plates may protrude.

6.3.2.2 Simulation

The ion optics were designed and simulated using the SIMION 8.1 program. Fig. 6.4(a) shows a simulated experiment where H^+ ions are imaged from a parent species with a mass of 100 amu. Coloured lines striking the detector correspond to protons, with kinetic energies of either 2.5 or 0.5 eV. The black, deflected, ion trace corresponds to 100 amu $parent^+$ ions, which are deflected by 1 kV applied to the lower deflector, after the protons have passed. To demonstrate the selectivity of the deflector plates, cations with a mass of 2 amu (deuterium ions) are also deflected, by turning on the deflector very soon after the protons have passed.

The VMI arrangement is designed such that the voltages on the repeller and extractor plates may be varied, to allow a range of kinetic energy windows to be monitored. If the ratio V_E / V_R is kept at 0.708 (found empirically by simulation), then any potential up to 5 kV may be applied to the repeller, in order to image higher energy particles. Fig. 6.4(b) shows expanded views of the detector, with five different sets of potentials on the VMI optics. In each case simulated protons are shown, either 2.5 or 0.5 eV of energy, and ejected at an angle of either 90° or 45° to the axis of propagation. Two sets of each energy of ions were simulated, separated by 5% kinetic energy. The visible gap between these in Fig. 6.4(b) then shows that a resolution of at least 5% should be obtained by this arrangement.

6.4 Conclusions

A second generation VMI imaging machine has been developed, with the capacity to be upgraded to include a laser desorption source. A gate valve separates the source and interaction regions of the instrument, greatly decreasing the time required to change samples. The instrument is designed for maximal signal, with the shortest possible distance between the molecular beam source and the ion optics. Once a desorption source is incorporated into the system, it should be capable of performing time resolved VMI experiments on large neutral systems, complementary to the electrospray machine in Durham.

6.5 References

1. M. Staniforth and V. G. Stavros, *Proceedings of the Royal Society A: Mathematical, Physical and Engineering Science*, 2013, **469**.
2. J. R. Cable, M. J. Tubergen and D. H. Levy, *J. Am. Chem. Soc.*, 1987, **109**, 6198.
3. R. Cohen, B. Brauer, E. Nir, L. Grace and M. S. de Vries, *J. Phys. Chem. A*, 2000, **104**, 6351.
4. F. Piuzzi, I. Dimicoli, M. Mons, B. Tardivel and Q. Zhao, *Chem. Phys. Lett.*, 2000, **320**, 282.
5. I. Hunig and K. Kleinermanns, *Phys. Chem. Chem. Phys.*, 2004, **6**, 2650.
6. L. Belshaw, F. Calegari, M. J. Duffy, A. Trabattoni, L. Poletto, M. Nisoli and J. B. Greenwood, *J. Phys. Chem. Lett.*, 2012, **3**, 3751.
7. M. Taherkhani, M. Riese, M. BenYezzar and K. Muller-Dethlefs, *Rev. Sci. Instrum.*, 2010, **81**, 063101.
8. L. Li and D. M. Lubman, *Int. J. Mass Spectrom. Ion Processes*, 1989, **88**, 197.
9. E. Nir, P. Imhof and K. Kleinermanns, *J. Am. Chem. Soc.*, 2000, **122**, 8091.
10. E. Nir, K. Kleinermanns and M. S. de Vries, *Nature*, 2000, **408**, 949.
11. E. Nir, K. Kleinermanns, L. Grace and M. S. de Vries, *J. Phys. Chem. A*, 2001, **105**, 5106.
12. M. Smits, C. A. de Lange, S. Ullrich, T. Schultz, M. Schmitt, J. G. Underwood, J. P. Shaffer, D. M. Rayner and A. Stolow, *Rev. Sci. Instrum.*, 2003, **74**, 4812.
13. Z. Gengeliczki, M. P. Callahan, N. Svadlenak, C. I. Pongor, B. Sztaray, L. Meerts, D. Nachtigallova, P. Hobza, M. Barbatti, H. Lischka and M. S. de Vries, *Phys. Chem. Chem. Phys.*, 2010, **12**, 5375.
14. D. Nachtigallova, H. Lischka, J. J. Szymczak, M. Barbatti, P. Hobza, Z. Gengeliczki, G. Pino, M. P. Callahan and M. S. de Vries, *Phys. Chem. Chem. Phys.*, 2010, **12**, 4924.
15. U. Even, J. Jortner, D. Noy, N. Lavie and C. Cossart-Magos, *J. Chem. Phys.*, 2000, **112**, 8068.
16. J. Pittman and P. O'Connor, *J. Am. Soc. Mass. Spectrom.*, 2005, **16**, 441.
17. A. T. J. B. Eppink and D. H. Parker, *Rev. Sci. Instrum.*, 1997, **68**, 3477.
18. D. H. Parker and A. T. J. B. Eppink, *J. Chem. Phys.*, 1997, **107**, 2357.
19. B. Whitaker, ed., *Imaging in Molecular Dynamics: Technology and Applications*, Cambridge University Press, New York, 2003.

7 Conclusions and Outlook

7.1 Summary

The overall theme of this thesis is of 'bottom-up' gas phase spectroscopy – that is, starting with simple systems and gradually adding complexity. The techniques of time-resolved photoelectron and photofragment imaging give unprecedented insight into the excited state dynamics of molecular systems. Ultimately, the aim is to understand the photophysics of biomolecules, which are generally very large and complex. By methodically increasing the size and complexity of the systems studied, even very large systems can be understood in great detail. The work on nucleotide dynamics (Chapter 5) represents an important milestone in the move to understanding the dynamics of very large biomolecules in the gas phase.

The first chapter of this thesis gave a general overview of the vast topic of gas phase femtochemistry. The introduction first reviewed the fundamental concepts behind excited state dynamics, before moving to consider experimental techniques. The two techniques used in this thesis, time-resolved photoelectron and photofragment spectroscopies, were discussed. Finally, a very brief overview was given of the current state of the art in the application of gas phase femtochemistry to biomolecules, with a view to understanding how biological systems can withstand constant solar irradiation.

Chapter two was devoted to the describing the experiments, both in Warwick and Durham. The detection scheme used in both, velocity map imaging, was discussed, along with the femtosecond laser system which is essentially the same in both laboratories. Following this, each experiment was explained in detail, with a description firstly of the source technique (molecular beams or electrospray), followed by overviews of the instruments themselves.

Chapter three began by demonstrating results of time-resolved H atom imaging from phenol. A clear signature of dissociation via a $^1\pi\sigma^*$ state was observed, on a slow timescale. The phenol results tentatively suggested that H atom dissociation occurs via tunnelling, although they were in no way definitive. A phenol derivative, catechol, provided firm evidence that phenolic systems do indeed lose H atoms by tunnelling. In particular, a combination of studying the dynamics of both H^+ and parent catechol$^+$, along with isotopic and chemical substitution, allowed the dynamics to be definitively assigned. In this instance, slightly increasing the complexity of phenol (by adding an extra hydroxyl group) afforded new data and allowed the decay mechanisms in both phenol and catechol to be understood.

In Chapter four, a yet more complex system was studied in the form of the indigo carmine dianion. Time-resolved photoelectron spectroscopy allowed the dynamics to be tracked. Deuteration, as with catechol, allowed the decay mechanism to be assigned, in this case to an excited state intramolecular proton transfer. This is a simple example of the concept of 'bottom-up' spectroscopy, where understanding of a simple system allows a more complex one to be better assigned. Additionally, intriguing effects on the photoelectron angular distributions from the doubly charged nature of the ion were observed.

The dynamics of real biological systems, in the form of DNA nucleotides and oligonucleotides, were shown in Chapter 5. First, a resonance enhanced electron detachment scheme was used to determine the ionization energy of nucleobases *inside* a larger nucleotide framework. This served as an important first step for the measurement of time-resolved photoelectron spectra, which was performed on all four naturally occurring nucleotides. For the first time, the intrinsic dynamics of large DNA subunits were measured, showing that in all cases ultrafast relaxation occurs. In the case of deoxyadenosine-monophosphate, whose nucleobase has previously been well studied, comparison with the dynamics of the nucleotide and nucleobase in gas and solution allowed the dynamics to be assigned. This is a clear example where a bottom-up approach leads to greater understanding of complex systems. Finally, the technique was extended to a dimer and trimer of deoxyadenosine, demonstrating the ability to build up to even larger and more realistic systems.

Finally, the designs for a new instrument in Warwick were presented. This machine will have a desorption source fitted, to allow for the studying of the dynamics of large neutral species in the gas phase. The ability to study larger systems with the techniques of time-resolved photofragment and photoelectron imaging will allow many biomolecule systems to be studied, and furthers the bottom-up methodology.

7.2 Outlook

Going forward, there is huge potential in both laboratories to study larger, more complex and more biologically relevant systems. There are a number of very exciting possibilities for future research, and a very brief selection of possibilities shall be explored. Additionally, further collaboration between the two laboratories could result in extremely detailed new insights.

7.2.1 Dynamics of Large Neutral Species

The new instrument outlined in Chapter 6 will soon be adapted to include a laser desorption source. Additionally, the new instrument should be capable of time-resolved photoelectron imaging, which allows an additional perspective on molecular dynamics. As an initial experiment, the time-resolved photoelectron or photofragment spectra of isolated guanine (and 9-methyl guanine) can be performed, filling in a conspicuous hole in current knowledge of the isolated bases. Continuing on from the work presented here, another important species to study is DNA nucleosides (a nucelobase with sugar attached). This would build on from the work presented in Chapter 5, as it would allow the influence on the charged phosphate group on the intrinsic dynamics of DNA fragments to be determined. A complementary ion and neutral study could be especially fruitful in gaining a wider understanding of DNA photodynamics.

7.2.2 Cooling and Control of Ions

The electrospray photoelectron imaging instrument in Durham capable of studying dynamics of very large isolated systems, but at current it produces ions which are (at minimum) at room temperature. The limitations of high temperatures were already observed in Chapter 5, where excimer dynamics were not observed in di- or tri-oligonucleotides. Presumably, if the ions had been cooled to a lower temperature then a stacked configuration would be induced,[1] and excimer dynamics observed. In addition, cooled ions will have less conformers thermally accessible, so spectra should be simplified.[2]

Cooling ions would require a redesign of the ion trap in the instrument. Currently, the trap is at room temperature, with no facility for cooling. A secondary issue with the current trap is when ions are pulsed out of it, numerous collisions with buffer gas will occur, which will heat the ions. A new trap design would require both these issues be solved. The temperature can be reduced by designing the trap so that the buffer gas is in contact with a surface cooled by a cryogenic liquid, and ions will thus thermalize to this temperature. More precise control could be achieved using, for example, a thermoelectric cooling system. To solve the problem of heating upon ion exit, collisions with buffer gas need to be minimized.

A cryogenic ion trap design in use by several groups uses a circle of 22 poles for radial confinement, with a radio frequency high voltage, 180° out of phase on alternating poles. DC endcaps provide confinement in the linear direction. The choice of 22 poles is to ensure the electric field is effectively circular, and minimize heating

caused by the trap. Cooling and trapping is facilitated by cooled helium gas, which is pulsed into the trap. The helium is pumped away again before emptying the trap, to minimize collisional heating.[2-5] A trap of similar design may work for the Durham instrument, although the frequency of the experiment (500 Hz) may be too high to allow for complete trapping and subsequent pumping away of buffer gas.

Cooling ions will freeze out conformers, although in itself it does not allow for selection of conformers. To achieve this additional level of control, an ion mobility cell could be added to the instrument.[6, 7] Ion mobility is effectively a form of ion chromatography, sorting ions by their shape. This allows individual conformers to be selected for, and experiments performed on each one for complete control.

7.2.3 Solution Phase Collaboration

Finally, future experiments could lean towards an understanding of the effect solvent has on dynamics. There are two main approaches available: firstly direct collaboration with solution phase experimentalists allow comparative studies to be performed. In both laboratories, solution phase femtosecond experiments have been constructed, so many fruitful collaborations should be possible.

Secondly, solvent effects can be measured in the gas phase, by performing clustering experiments. In these, the molecule or ion of interest is clustered with a small number of solvent molecules, allowing the effect of sequential solvation to be measured.[8] The Durham experiment is particularly suited to clustering experiments, because mass selection allows complete control of the number of solvent molecules clustered with the ion. At current, temperatures are too high to form stable ion-solvent complexes, however the addition of a cold trap would in principal make is facile.

7.3 References

1. J. Gidden and M. T. Bowers, *Eur. Phys. J. D*, 2002, **20**, 409.
2. T. R. Rizzo, J. A. Stearns and O. V. Boyarkin, *Int. Rev. Phys. Chem.*, 2009, **28**, 481.
3. G. Dieter, *Phys. Scr.*, 1995, **1995**, 256.
4. A. Dzhonson, D. Gerlich, E. J. Bieske and J. P. Maier, *J. Mol. Struct.*, 2006, **795**, 93.
5. S. Schlemmer, E. Lescop, J. von Richthofen, D. Gerlich and M. A. Smith, *J. Chem. Phys.*, 2002, **117**, 2068.
6. A. B. Kanu, P. Dwivedi, M. Tam, L. Matz and H. H. Hill, *J. Mass Spectrom.*, 2008, **43**, 1.
7. G. Papadopoulos, A. Svendsen, O. V. Boyarkin and T. R. Rizzo, *Faraday Discuss.*, 2011, **150**, 243.
8. J. R. R. Verlet, *Chem. Soc. Rev.*, 2008, **37**, 505.

Appendix A: List of Abbreviations

ADE	adiabatic detachment energy
BBO	beta barium oxide
BO	Born-Oppenheimer
CI	conical intersection
DAS	decay associated spectra
DNA	deoxyribonucleic acid
DFT	density functional theory
eBE	electron binding energy
eKE	electron kinetic energy
ESI	electrospray ionization
ESIPT	excited state intramolecular proton transfer
FC	Franck-Condon
FWHM	full width (at) half maximum
IC	internal conversion
ISC	inter-system crossing
IVR	intramolecular vibrational energy redistribution
OPA	optical parametric amplifier
PAD	photoelectron angular distribution
PCM	polarization continuum model
PE	photoelectron
PEPICO	photoelectron-photoion coincidence spectroscopy
PES	potential energy surface
POP	polar onion peeling
RCB	repulsive Coulomb barrier
REMPI	resonance enhanced multi-photon ionization
SFG	sum frequency generation
SHG	second harmonic generation
TDM	transition dipole moment
TKER	total kinetic energy release
TOF	time-of-flight
TRPES	time-resolved photoelectron spectroscopy
vFC	vertical Franck-Condon
VMI	velocity map imaging
WKB	Wentzel–Kramers–Brillouin
ZPE	zero-point energy
InC	indigo carmine
A / Ade	adenine

G / Gua	guanine
C / Cyt	cytosine
T / Thy	thymine
dAMP	5'-deoxyadenosine 3'-monophosphate
dGMP	5'-deoxyguanosine 3'-monophosphate
dCMP	5'-deoxycytidine 3'-monophosphate
dTMP	5'-deoxythymidine 3'-monophosphate
DMF	dimethyl formamide
DMSO	dimethyl sulfoxide

Appendix B: Global Fitting MATLAB code

GlobalFitDecay.m

```
function [DAS, taus, decays, fit, residuals, t0, FWHM, y0] =
GlobalFitDecay(tau, IRFFWHM, delays, eKE, TRPES, fig)
%%GlobalFitDecay
%Perform a global fit on a TRPES matrix.

% INPUTS:
% tau = row vector of initial guesses for time constants
% IRFFWHM = intial guess for FWHM of the IRF
% delays = row vector of delays data were sampled at
% eKE = column vector of energies data were sampled at
% TRPES = matrix of TRPES data, in the format described by delays
and eKE
% fig = no. of figure to output to.

% OUTPUTS:
% DAS = matrix of decay associated spectra, one column for each
component
% taus = vector of time constants
% decays = matrix of time-integrated signals. First n columns are
the
%          decays for each n componenets, followed by the
experimental data, then
%          the total fit
% fit = matrix of fitted TRPES
% residuals = matrix of experiment - fit
% t0 = fitted t0
% FWHM = fitted FWHM
% y0 = fitted linear offset (accounts for noise)

rebinPES = TRPES;
eScale = eKE;
sigma = IRFFWHM / 2.35;

persistent cstring;

figure(fig);
subplot(3,2,1);
[cha,cha] = contourf(delays, eScale, rebinPES , 25);
set(cha,'linestyle','none');
ax = caxis;
title('Data');
xlabel('t / fs');
ylabel('eKE / eV');
%axis([-500 2500 binSize max(eScale)]);
colorbar;
drawnow;

x0 = ones(length(eScale)+4, length(tau))*0.1;
x0(1,:) = tau;
x0(2,1) = 0; %t0
x0(3,1) = 0; %y0
x0(4,1) = sigma;
```

```
%uncomment these and change the fit line to use limits.

% lower = ones(length(eScale)+3, length(tau))*-5;
% lower(1,:) = 20; %tau
% lower(2,1) = -100; %t0
% lower(3,1) = -1; %y0
% lower(4,1) = 80/2.35; %FWHM

% upper = ones(length(eScale)+3, length(tau))*5;
% upper(1,:) = 8000;
% upper(2,1) = 100; %t0
% upper(2,2) = 1; %y0
% upper(3,1) = 180/2.35; %FWHM


%generate weights (to account for non-linear eKE axis)
%N.B. the *10 factor is to get the residuals into a regime the
fitter
%likes. Tweaking this can change the tolerance and fitting speed
weight = repmat(diff(eKE)',1,length(delays));
weight = [weight; repmat(weight(end,1), 1, length(delays))]*100;

%% Start with the default options
options = optimset;
%% Modify options setting
options = optimset(options,'Display', 'iter-detailed');
options = optimset(options,'ScaleProblem', 'Jacobian');
options = optimset(options,'PlotFcns', { @outfun });
[x,resnorm,residual,exitflag,output,lambda,jacobian] = ...
lsqnonlin(@(x)((GenerateTRPES(delays,eScale,x(1,:),x(5:end,:),x(2,1)
,x(4,1),x(3,1))-rebinPES).*weight).*1,x0,[],[],options);

%% if limits are required, replace the [], [], above with lower,
upper - and fill out the matricies above.

taus = x(1,:)
t0 = x(2,1)
y0 = x(3,1)
FWHM = x(4,1)*2.35

fitTRPES = GenerateTRPES(delays, eScale, taus, x(5:end,:), t0,
FWHM/2.35, y0);
fit = fitTRPES;

figure(fig);
subplot(3,2,2);
[chb,chb] = contourf(delays, eScale, fitTRPES, 25);
set(chb,'linestyle','none');
caxis(ax);
title('Fit');
xlabel('t / fs');
ylabel('eKE / eV');
colorbar;
drawnow;

%% plot DAS
subplot(3,2,3);
cla;
DAS = plotDAS(x);
```

```
drawnow;

%% plot residuals
subplot(3,2,4);
residuals = (fitTRPES - rebinPES);
[chc,chc] = contourf(delays, eScale, residuals, 25);
set(chc,'linestyle','none');
caxis(ax - max(ax)/2);
title('Residuals');
xlabel('t / fs');
ylabel('eKE / eV');
colorbar;
drawnow;

%% plot decays
subplot(3,1,3);
cla;
decays = plotDecays(x);


%% function to plot the DAS
    function DAS = plotDAS(xc)
        cstring=[];

        DAS = zeros(length(eScale), length(xc(1,:)));
        for i=(1:length(xc(1,:)))
            plot(eScale, xc(5:end,i));
            DAS(:,i) = xc(5:end,i);

            %legend(sprintf('%0.1f fs', x(1,i)));
            cstring{end+1} = sprintf('%0.0f fs', xc(1,i));
            hold all;
        end
        hold off;
        title('Decay Associated Spectra');
        xlabel('eKE / eV');
        hline = refline([0 0]);
        set(hline, 'Color', 'k');
        legend(cstring);

    end

%%function to plot total integrals
    function decays = plotDecays(xc)
        decays = zeros(length(xc(1,:)) + 2, length(delays));
        decays(length(xc(1,:)) + 2, :) = trapz(eScale,
GenerateTRPES(delays, eScale, xc(1,:), xc(5:end,:),xc(2,1), xc(4,1),
xc(3,1)));
        decays(length(xc(1,:)) + 1, :) = trapz(eScale, rebinPES);

        plot((delays(1):10:delays(end)), trapz(eScale,
GenerateTRPES((delays(1):10:delays(end)), eScale, xc(1,:),
xc(5:end,:),xc(2,1), xc(4,1), xc(3,1))), 'k');
        hold all;
        plot(delays, trapz(eScale, rebinPES), 'ok');
        for i=(1:length(xc(1,:)))
            singleComp = zeros(length(eScale), length(tau));
            singleComp(:,i) = xc(5:end,i);
```

```
            plot((delays(1):10:delays(end)), trapz(eScale,
GenerateTRPES((delays(1):10:delays(end)), eScale, xc(1,:),
singleComp,xc(2,1), xc(4,1), xc(3,1))));
            decays(i,:) = trapz(eScale, GenerateTRPES(delays,
eScale, xc(1,:), singleComp, xc(2,1), xc(4,1), xc(3,1)));
        end

        title('Total Integral');
        xlabel('t / fs');
        legend(sprintf('xcor FWHM = %0.0f fs', xc(4,1)*2.35),
sprintf('t0 = %0.0f fs', xc(2,1)));
        hold off;
    end

%%function to plot real time fit results
    function stop = outfun(xc,optimvalues, state)
        stop = false;
        switch state
            case 'iter'
                subplot(2,1,1);
                plotDAS(xc);

                subplot(2,1,2);
                plotDecays(xc);
                %plot fit

            otherwise
                hold off;
        end

    end
end
```

GenerateTRPES.m

```
function [ TRPES ] = GenerateTRPES( delays, eKE, tau, DAS, t0,
sigma, y0 )
%GenerateTRPES
%This function generates a full TRPES matrix, given the delays,
energy
%scale, decay assoc. spectra, etc.

TRPES = zeros(length(DAS), length(tau));


for i=(1:length(delays))
    TRPES(:,i) = GeneratePES(DAS, tau, delays(i), t0, sigma, y0);

end

end
```

GeneratePES.m

```
function [ PES ] = GeneratePES(DAS, tau, t, t0, sigma, y0 )
%Returns the convoluted and decayed spectra at time t, given a decay
%associated spectra matrix, DAS, t0; the cross correlation,
%sigma; and an offset factor y0

%N.B. The A, B & C factors are for the convoluted fit found in Dan's
thesis
%Here, A = DAS(i)

%initialize the PES vector
PES = ones(length(DAS(:,1)), 1) * y0;

%loop through each decay component
for i=(1:length(tau))
    B = (sigma^2/(2*tau(i)^2)) - (t - t0)/tau(i);
    C = erfc( (-1/sqrt(2)) .* ((t-t0)/sigma - sigma/tau(i)) );

    PES = PES + (DAS(:,i) .* exp(B) .* C);

end

end
```

Appendix C: Drawings for New Instrument

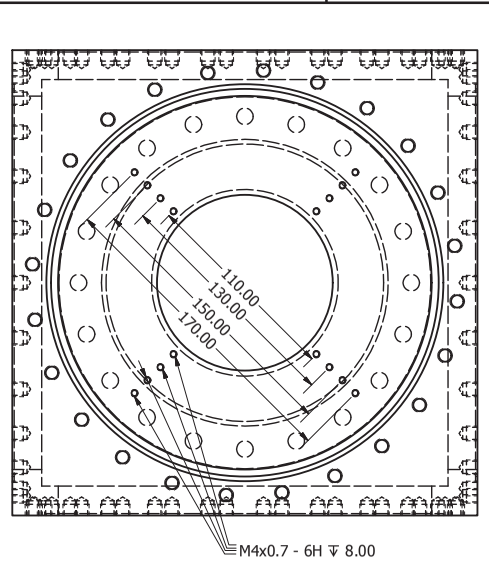

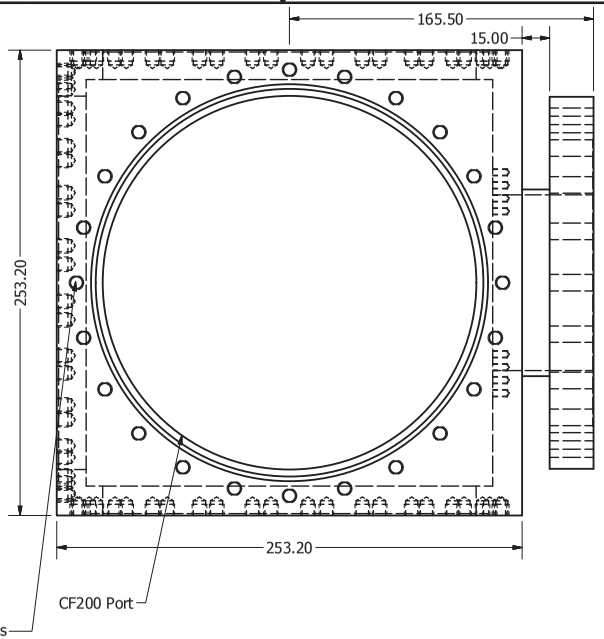

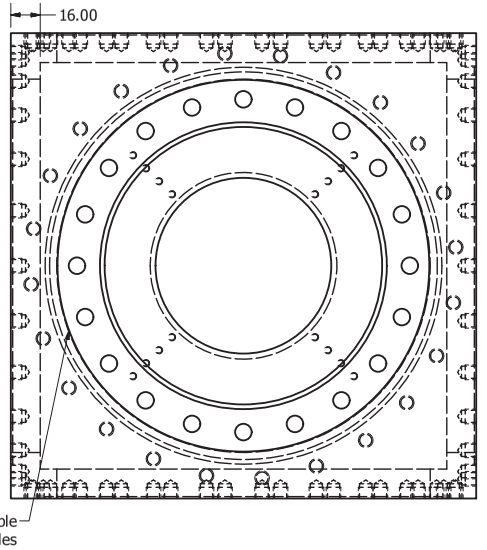

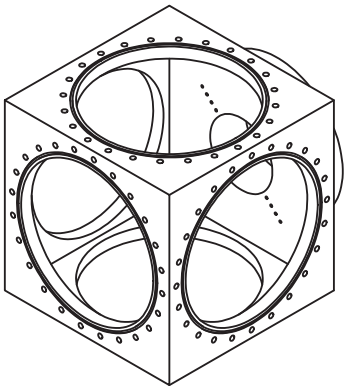

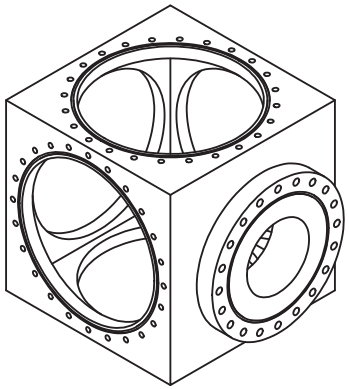

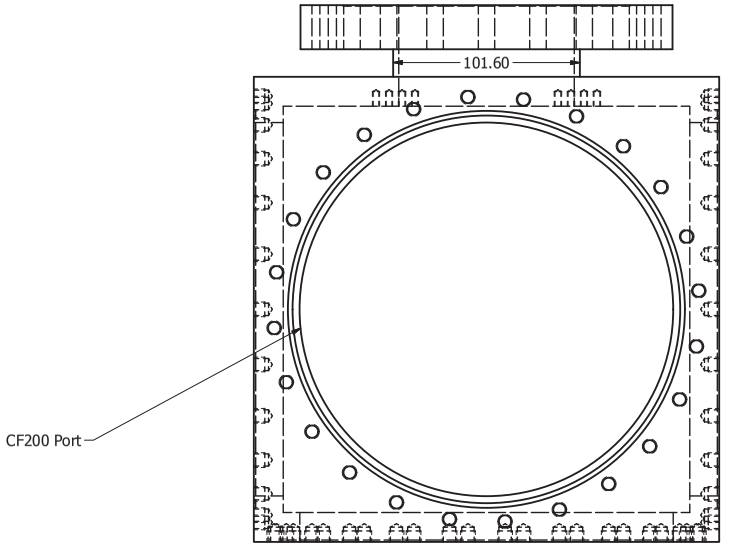

DRAWN chemist	28/11/2012			
CHECKED		TITLE		
QA				
MFG				
APPROVED		SIZE C	DWG NO Cube	REV
		SCALE	SHEET 1 OF 1	

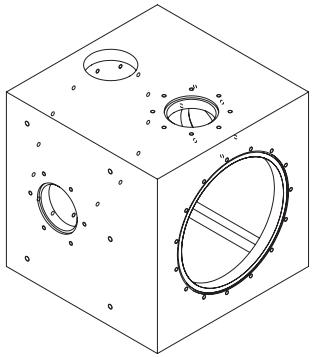

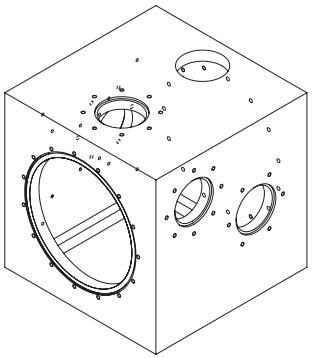

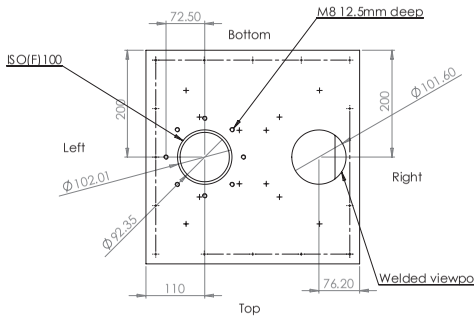

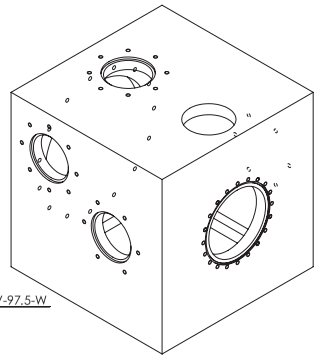

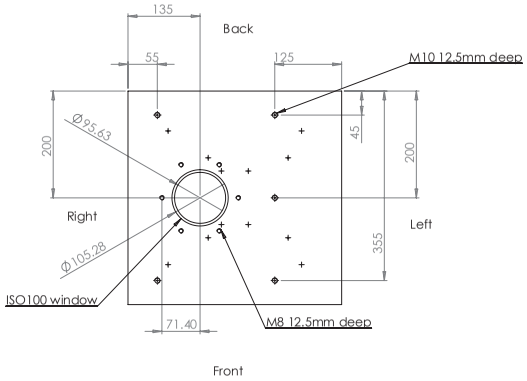

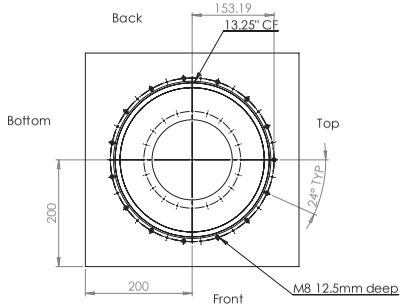

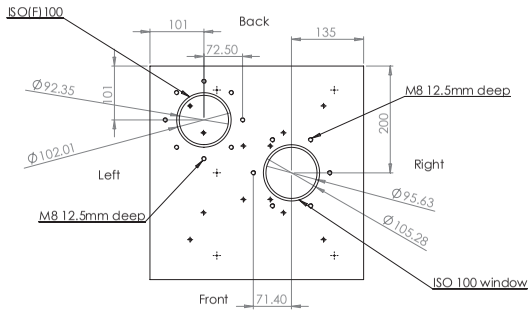

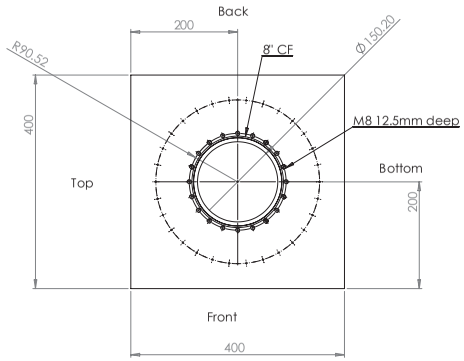

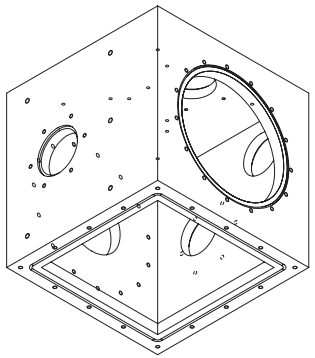

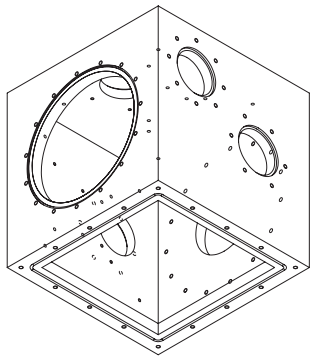

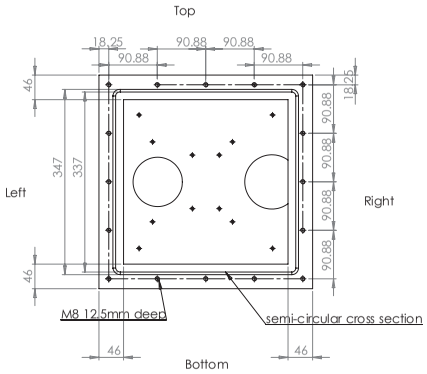

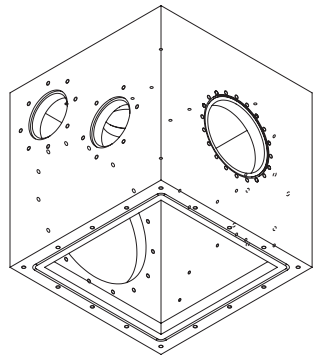

UNLESS OTHERWISE SPECIFIED DIMENSIONS ARE IN MILLIMETERS SURFACE FINISH: TOLERANCES LINEAR: ANGULAR:			FINISH:				DEBUR AND BREAK SHARP EDGES	DO NOT SCALE DRAWING	REVISION
	NAME	SIGNATURE	DATE						
DRAWN								TITLE:	
CHK'D									
APP'V'D									
MFG									
Q.A.									
				MATERIAL:				DWG NO. lowvacchambex1	A1
				WEIGHT:				SCALE:1:5	SHEET1 OF 1

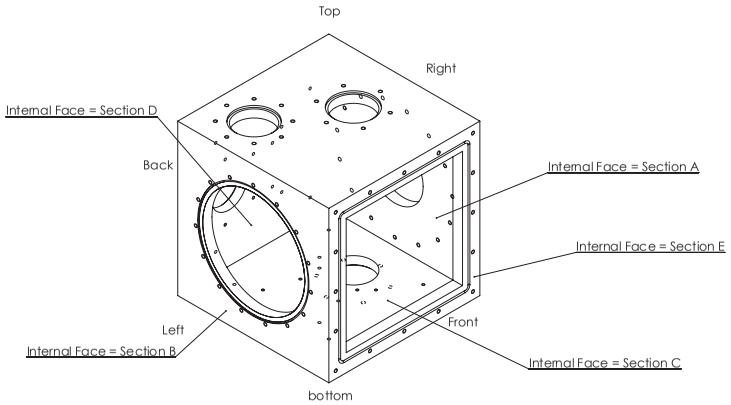

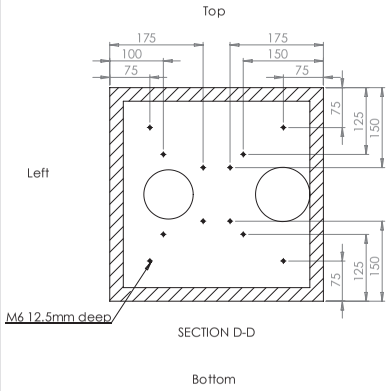

SECTION D-D

Bottom

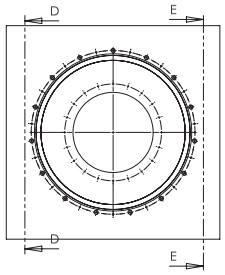

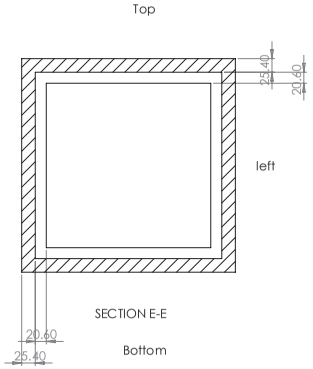

SECTION E-E

Bottom

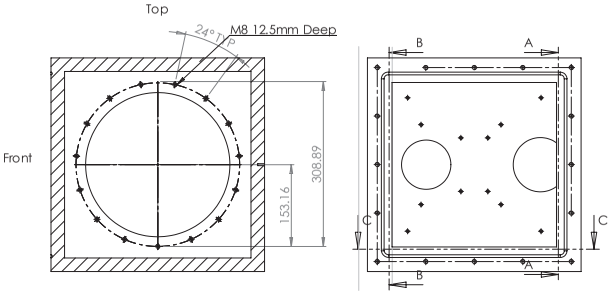

SECTION B-B

Bottom

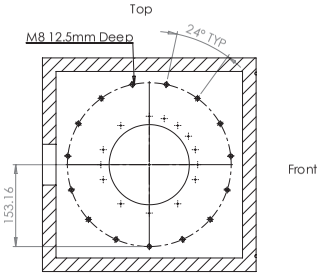

SECTION A-A

Bottom

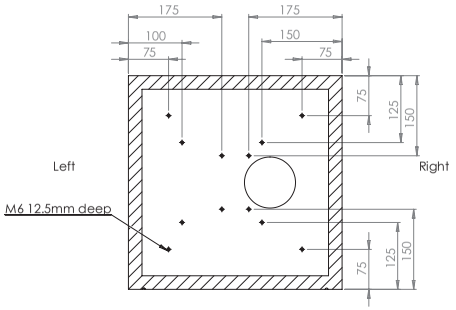

SECTION C-C

Front

UNLESS OTHERWISE SPECIFIED: DIMENSIONS ARE IN MILLIMETERS SURFACE FINISH: TOLERANCES LINEAR: ANGULAR:			FINISH:			DEBUR AND BREAK SHARP EDGES	DO NOT SCALE DRAWING	REVISION
	NAME	SIGNATURE	DATE					
DRAWN							TITLE:	
CHK'D								
APPV'D								
MFG								
Q.A				MATERIAL:			DWG NO. lowvacchambint	A1
				WEIGHT:			SCALE:1:5	SHEET1 OF 1